

Université
de Toulouse

THÈSE

En vue de l'obtention du

DOCTORAT DE L'UNIVERSITÉ DE TOULOUSE

Délivré par :

Institut Supérieur de l'Aéronautique et de l'Espace (ISAE)

Présentée et soutenue par :
Paulo Alexandre FERREIRA ESTEVES

le mardi 27 mai 2014

Titre :

Techniques d'acquisition à haute sensibilité des signaux GNSS

École doctorale et discipline ou spécialité :

ED MITT : Signal, image, acoustique et optimisation

Unité de recherche :

Équipe d'accueil ISAE-ONERA SCANR

Directeur(s) de Thèse :

Mme. Marie-Laure BOUCHERET (directrice de thèse)

M. Mohamed SAHMOUDI (co-directeur de thèse)

Jury :

M. Karim ABED MERAÏM - Rapporteur

M. Fabio DOVIS - Rapporteur

M. Michel BOUSQUET - Examineur

M. René LANDRY - Examineur

M. Paul GROVES - Examineur

Mme. Marie-Laure BOUCHERET - Directrice de thèse

M. Mohamed SAHMOUDI - Codirecteur de thèse

That which does not kill us makes us stronger.

~Friedrich Nietzsche

Abstract

Satellite navigation (GNSS) is a constant in our days. The number of applications that depend on it is already remarkable and is constantly increasing. With new applications, new challenges have also risen: much of the new demand for signals comes from urban areas where GNSS signal processing is highly complex. In this thesis the issue of weak GNSS signal processing is addressed, in particular at the first phase of the receiver processing, known as signal acquisition. The first axe of research pursued deals with the analysis and compensation of the Doppler effect in acquisition. The Doppler shift that is experienced by a user is one of the main design drivers for the acquisition module and solutions are proposed to improve the sensitivity-complexity trade-off typical of the acquisition process. The second axe of research deals with the characterization of differential GNSS detectors. After a first step of coherent integration, transition to postcoherent (noncoherent or differential) integration is required for acquiring weak signals. The quantification of the sensitivity of differential detectors was not found in literature and is the objective of this part of the research. Finally, the third axe of research is devoted to multi-constellation Collective Detection (CD). CD is an innovative approach for the simultaneous processing of all signals in view. Several issues related to CD are addressed, including the improvement of the CD search process and the hybridization with standard acquisition. Finally, the application of this methodology in the context of a multi-constellation receiver is also addressed, by processing simultaneously real GPS and Galileo signals.

Résumé

Les systèmes de navigation par satellite (GNSS) font partie de notre quotidien. On peut présentement les trouver dans un ensemble d'applications. Avec les nouveaux besoins, des nouveaux enjeux sont aussi apparus : le traitement du signal dans les environnements urbains est extrêmement complexe. Dans cette thèse, le traitement des signaux GNSS à faible puissance est abordé, en particulier dans la première phase du traitement, nommé acquisition de signal. Le premier axe de recherche porte sur l'analyse et la compensation de l'effet Doppler dans l'acquisition. Le décalage Doppler perçu par l'utilisateur est un des paramètres principaux pour la configuration du module d'acquisition. Dans cette étude, des solutions sont proposées pour trouver le meilleur compromis sensibilité-complexité propre à l'acquisition. En deuxième axe, la caractérisation des détecteurs différentiels est abordée, en particulier la quantification de sa sensibilité. Pour l'acquisition des signaux faibles, après une première phase d'intégration cohérente, il faut passer par une intégration «postcohérente» (noncohérente ou différentielle.) L'analyse exécutée ici permet de mieux identifier le meilleur choix entre les deux possibilités. Le troisième axe de recherche est consacré à la méthode de Détection Collective (CD), une innovation qui fait l'acquisition simultanée de tous les signaux visible par le récepteur. Plusieurs analyses sont réalisées incluant l'amélioration de la procédure de recherche de la CD, et l'hybridisation avec l'acquisition standard. Enfin on effectue l'analyse de la CD dans un contexte multi-constellation, en utilisant simultanément des vrais signaux GPS et Galileo.

Acknowledgement

No man is an island, and no achievement can ever be the result of a purely individual effort. This thesis does not escape this paradigm.

First and foremost, many thanks are due to my supervisor, Dr. Mohamed Sahmoudi, for the many hours of discussion spent together and the many lessons I have learned during these three years. My appreciation is also expressed to the jury of this thesis, especially to Prof. Fabio Dovis and Prof. Kareem Abed-Meraim, who kindly accepted to review this work and took the time to propose ways of making it more complete. Many thanks are also due to TESA and CNES, in particular Prof. Corinne Mailhes and Lionel Ries, that have provided me with all the necessary conditions to successfully carry this research.

I would also like to express my appreciation to Prof. Michel Bousquet for having made this PhD possible and for his crucial support. I am equally grateful to Prof. Nesreen Ziedan for her contribution to one of the main scientific contributions of this thesis and for her continued support. Furthermore, I would like to thank Cillian O'Driscoll and Daniele Borio for setting the high quality standards that this thesis tried to follow.

At this time of reflection, I cannot forget my colleagues and friends at ISAE who were there during these three years, day after day, providing me with their essential support, good mood, friendship, and distractions, Aude, Syed, Khairol, Cheng, Azeddine, Remy, Benoît, Gael, and Vincent. Likewise, I am very happy to have been part of the "Toulouse GNSS PhD group", together with Myriam, Seb R., Seb C., Leslie, and Jérôme (still counts). A special thanks is due to Myriam (code name "M") for her incredible support and all the good moments we shared.

It is impossible also not to mention my friends in Toulouse, in particular Gianluca and Sara who were always there ensuring my sanity and good mood; Luca, Gerardo, and Tiziana, composing the rest of my Italian Toulouse family; the Portuguese gang, always present to remind me of how great our home is; the Greek party animals, with whom so many good moments were spent; and last, but not least, my wonderful Lia, whose support was so important in the final year. A big thanks also to Jean-Luc for his outstanding support during the final sprint.

Even if mostly at a distance, the support and friendship of Nuno, Fred, and Tatiana was also essential as it has been for so long now. My appreciation goes also to all those who have contributed for keeping my spirits high during these three years.

Por último, para a minha família, em particular os meus pais e a minha irmã, qualquer tentativa de expressão da minha felicidade pelo vosso apoio e carinho será sempre uma obra falhada, pelo que não o ousarei nem tentar.

CONTENTS

| | |
|---|-----------|
| Nomenclature | ix |
| Résumé des Travaux en Français | xv |
| 1 Introduction | 1 |
| 1.1 GNSS Systems Overview | 1 |
| 1.1.1 Working Principle | 1 |
| 1.1.2 GNSS Systems Worldwide | 2 |
| 1.2 The Role of Acquisition in a GNSS Receiver | 6 |
| 1.3 21st Century Challenges for GNSS Applications | 6 |
| 1.4 Thesis Objectives and Overview | 7 |
| 1.5 List of Publications | 9 |
| 2 Principles of GNSS Signal Acquisition | 11 |
| 2.1 Problem Formulation | 11 |
| 2.1.1 Acquisition as an Estimation Problem | 14 |
| 2.1.2 Acquisition as a Detection Problem | 15 |
| 2.1.3 Fundamental Structure of GNSS Acquisition Schemes | 17 |
| 2.2 Correlation Methods | 18 |
| 2.2.1 Time-Domain Acquisition | 22 |
| 2.2.2 Frequency-Domain Acquisition | 23 |
| 2.2.3 Methods Comparison | 31 |
| 2.3 Detection Schemes | 33 |
| 2.3.1 Coherent Detector | 33 |
| 2.3.2 Noncoherent Detector | 38 |
| 2.3.3 Differential Detectors | 40 |
| 2.4 Assisted GNSS | 42 |
| 2.4.1 Snap-Shot Positioning | 43 |

| | | |
|----------|---|-----------|
| 2.4.2 | Collective Detection | 43 |
| 2.5 | Modern Signals Impact in Acquisition | 44 |
| 2.5.1 | Binary Offset Carrier Modulations | 45 |
| 2.5.2 | Composite Signals Acquisition | 48 |
| 2.5.3 | Handling Secondary Codes | 49 |
| 2.6 | Combined Acquisition Approaches | 50 |
| 2.7 | Discussion | 52 |
| 3 | Analysis and Compensation of Doppler Shift Effect in GNSS Acquisition | 55 |
| 3.1 | Doppler Effect Compensation in Low-Dynamics | 58 |
| 3.1.1 | Fine Frequency Estimation in Acquisition | 59 |
| 3.1.2 | Fine Frequency Estimation using Spectral Peak Location Algorithms | 60 |
| 3.1.3 | Application of SPL Algorithms in GNSS Acquisition | 63 |
| 3.1.4 | Performance Analysis | 65 |
| 3.1.5 | Real Signals Acquisition | 69 |
| 3.1.6 | Scenario of Application: Mass-market receivers | 72 |
| 3.2 | Doppler Effect Analysis in Medium-Dynamics | 74 |
| 3.2.1 | Coherent Integration - Single Output | 74 |
| 3.2.2 | Coherent Integration - Multiple Outputs | 79 |
| 3.2.3 | Postcoherent Integration | 82 |
| 3.2.4 | Scenarios of Application: Low Earth Orbit and Geostationary Satellites & Urban environments | 84 |
| 3.3 | Doppler Effect Compensation in High-Dynamics | 86 |
| 3.3.1 | Staircase Frequency Update | 87 |
| 3.3.2 | Chirp Frequency Update | 89 |
| 3.3.3 | Approaches Comparison | 90 |
| 3.3.4 | Comparison with Medium-Dynamics Assumption | 92 |
| 3.3.5 | Scenario of Application: Deep urban & Indoor environments | 94 |
| 3.4 | Conclusion | 96 |
| 4 | Sensitivity Characterization of Differential GNSS Detectors | 99 |
| 4.1 | Background | 100 |
| 4.2 | Statistical Characterization of the PWD Detector | 101 |
| 4.2.1 | Characterization under Noise-only Hypothesis (H_0) | 102 |
| 4.2.2 | Characterization under Signal and Noise Hypothesis (H_1) | 105 |
| 4.2.3 | Limitations of the PWD Detector | 108 |
| 4.3 | Evaluation of the Sensitivity Loss of a Nonoptimal Detector | 110 |

| | | |
|----------|--|------------|
| 4.3.1 | Optimal Detector and Sensitivity Loss Definition | 110 |
| 4.3.2 | Sensitivity Loss of the Squaring Operation | 112 |
| 4.3.3 | Sensitivity Loss of the Differential Operation | 115 |
| 4.3.4 | Sensitivity Loss of the NCDD Detector | 118 |
| 4.4 | Applications of the NCDD Detector Sensitivity Loss Formula | 120 |
| 4.5 | Differential and Noncoherent Detection Schemes Theoretical Comparison | 121 |
| 4.5.1 | Comparison in Absence of Doppler Sensitivity Losses | 122 |
| 4.5.2 | Comparison in Presence of Doppler Sensitivity Losses | 126 |
| 4.6 | Differential and Noncoherent Detection Schemes Comparison in Real Data Acquisition | 128 |
| 4.6.1 | Sensitivity Comparison | 128 |
| 4.6.2 | Performance in Weak Signal Acquisition | 129 |
| 4.7 | Conclusion | 131 |
| 5 | Systematic and Efficient Collective Acquisition of Multi-Constellation GNSS Signals | 133 |
| 5.1 | Background on Prior Works | 133 |
| 5.2 | Collective Detection Overview | 137 |
| 5.2.1 | Working Principle | 137 |
| 5.2.2 | Methodology of Application | 139 |
| 5.2.3 | Collective Detection as a Direct Positioning Method | 140 |
| 5.2.4 | Collective Detection as a High-Sensitivity Acquisition Method | 141 |
| 5.2.5 | Search Grid Influence | 142 |
| 5.3 | Systematic and Efficient Collective Acquisition (SECA) | 143 |
| 5.3.1 | Redefinition of Local Horizontal Plane | 143 |
| 5.3.2 | Search Grid Definition | 145 |
| 5.3.3 | Generation of Individual Detection Metrics | 148 |
| 5.3.4 | Search Grid Iterative Update | 149 |
| 5.4 | Performance of the SECA Approach | 152 |
| 5.4.1 | Influence of the Vertical Component | 155 |
| 5.5 | Hybridized Sequential-Vectorial SECA | 156 |
| 5.5.1 | Near-Far Problem in Acquisition | 156 |
| 5.5.2 | Hybrid SECA in Presence of 1 Strong Signal | 157 |
| 5.5.3 | Hybrid SECA in Presence of 2 Strong Signals | 158 |
| 5.5.4 | Hybrid SECA in Presence of 3 or more Strong Signals | 159 |
| 5.5.5 | Performance of Hybridized Algorithms | 160 |
| 5.6 | Combined GPS-Galileo SECA | 162 |
| 5.6.1 | Considerations for Multi-GNSS Collective Detection | 162 |
| 5.6.2 | Real Data Results | 163 |

| | | |
|----------|---|------------|
| 5.7 | Conclusion | 170 |
| 6 | Conclusion and Future Work | 171 |
| 6.1 | Thesis Research Conclusions | 171 |
| 6.2 | Future Work Recommendations | 173 |
| A | GPS and Galileo Civil Signals Structure | 175 |
| B | Normal-Laplace Approximation of Coherent Differential Detector Output under H_1 for | |
| | $N_{DC} = 1$ | 179 |
| | Bibliography | 181 |

NOMENCLATURE

| | |
|------------------------|---|
| α | Doppler offset change rate |
| β | Maximum tolerable code phase estimation error in SECA algorithm |
| $\Delta\rho$ | Differential pseudorange |
| $\Delta\zeta$ | Code Phase estimation error |
| $\delta\zeta$ | Code Phase search grid resolution |
| Δb | User clock bias |
| Δf_d | Doppler offset |
| δf_d | Doppler offset search grid resolution |
| $\Delta R_{dimension}$ | User uncertainty radius in SECA algorithm |
| γ | Sweep factor |
| μ_0 | Initial Doppler frequency offset-to-Doppler bin width ratio |
| ρ | Pseudorange |
| τ | Signal travel time |
| sinc | Sinus cardinal |
| SNR | Signal-to-Noise Ratio |
| ζ | Code phase offset |
| c | Speed of light |
| C/N_0 | Carrier-to-Noise Ratio |

| | |
|------------|--|
| f_s | Sampling frequency |
| N_{code} | Number of samples per code period |
| P_d | Probability of Detection |
| P_{fa} | Probability of False Alarm |
| $R(\zeta)$ | PRN signal autocorrelation function |
| T_s | Sampling period |
| T_{coh} | Coherent integration time (ms) |
| w_{bias} | Weight allocated to bias component in SECA algorithm |
| A-GNSS | Assisted-GNSS |
| AltBOC | Alternative BOC Modulation |
| AWGN | Additive White Gaussian Noise |
| BDSS | BeiDou Navigation Satellite System (Chinese GNSS System) |
| BOC | Binary Offset Carrier Modulation |
| BPS | Bidimensional Parallel Search (Correlation Method) |
| BPSK | Binary Phase Shift Keying Modulation |
| BS | Base Station (A-GNSS context) |
| C/A | Coarse Acquisition (GPS Signal) |
| CBOC | Composite BOC Modulation |
| CD | Coherent Detector |
| CDD | Coherent Differential Detector |
| CDF | Cumulative Density Function |
| CDMA | Code Division Multiple Access |
| CLT | Central Limit Theorem |
| CS | Commercial Service (Galileo Service) |
| DBZP | Double Block Zero Padding (Correlation Method) |

| | |
|---------|--|
| DFT | Discrete Fourier Transform |
| dof | Degrees of Freedom |
| DP | Direct Positioning (from acquisition) |
| DSSS | Direct Sequence Spread Spectrum |
| FDMA | Frequency Division Multiple Access |
| FFT | Fast (Discrete) Fourier Transform |
| FOC | Frequency Offset Correction |
| FT | Fourier Transform |
| GEO | Geostationary Orbit |
| GGTO | GPS-Galileo Time Offset |
| GLONASS | GLOBAL Navigation Satellite System (Russian GNSS System) |
| GLRT | Generalized Likelihood Ratio Test |
| GNSS | Global Navigation Satellite Systems |
| GPS | Global Positioning System (US GNSS System) |
| GSO | Geosynchronous Orbit |
| HS | High-Sensitivity |
| I&Q | In-phase and Quadrature |
| INS | Inertial Navigation Sensor |
| IRNSS | Indian Regional Navigational Satellite System |
| ISAE | Institut Supérieur de l'Aéronautique et de l'Espace |
| LEO | Low Earth Orbit |
| LEX | L-band Experiment (QZSS Signal) |
| LoS | Line of Sight |
| LRT | Likelihood Ratio Test |
| MBOC | Multiplexed BOC Modulation |

| | |
|------|---|
| MEO | Medium Earth Orbit |
| ML | Maximum Likelihood |
| MS | Mobile Station (A-GNSS context) |
| NCD | Noncoherent Detector |
| NCDD | Noncoherent Differential Detector |
| NED | North-East-Down (referential) |
| OS | Open Service (Galileo Service) |
| osf | Oversampling Factor |
| PCS | Parallel Code Search (Correlation Method) |
| PDF | Probability Density Function |
| PFS | Parallel Frequency Search |
| PRN | Pseudorandom Noise (spreading code) |
| PRS | Public Regulated Service (Galileo Service) |
| PWD | Pair-Wise Detector |
| QZSS | Quasi-Zenith Satellite System |
| ROC | Receiver Operating Characteristic |
| SAIF | Submeter-class Augmentation with Integrity Function (QZSS Signal) |
| SDR | Software Defined Receiver |
| SECA | Systematic and Efficient Collective Acquisition |
| SIC | Successive Interference Cancellation |
| SLD | Square-Law Detector |
| SNR | Signal-to-Noise Ratio |
| SPL | Spectral-Peak Location (algorithm) |
| SS | Serial Search |
| SVD | Singular Value Decomposition |

TMBOC Time Multiplexed BOC Modulation

TTFF Time To First Fix

RÉSUMÉ DES TRAVAUX EN FRANÇAIS

La navigation par satellite est une technologie très présente dans nos jours. Le nombre d'applications qui dépendent de ces signaux est déjà remarquable et chaque année des nouveaux marchés, tant pour les masses comme spécialisés, font leur apparition dans lesquels cette technologie devient très utile. Les systèmes qui offrent ce service sont connus comme des systèmes globaux de navigation par satellite (*Global Navigation Satellite Systems*, GNSS), y compris le notoirement célèbre *Global Positioning System* (GPS) des États-Unis, le système russe GLONASS, le système européen Galileo, et le système chinois Beidou. Avec les nouvelles applications qui ont été conçues, des nouveaux défis sont également apparus qui n'avaient pas été prévus dans les débuts du GNSS: beaucoup de la nouvelle demande de signaux provienne des milieux urbains où le traitement du signal est beaucoup plus complexe que dans les environnements dégagés. Dans cette thèse, le problème de traitement des signaux à faible puissance est approché, en particulier lors de la première phase de la chaîne de traitement du signal reçu, nommé *acquisition de signal*.

1. Principe de Fonctionnement GNSS et Structure du Signal

Même si la navigation par satellite est une technologie assez récente et complexe, le concept mathématique sur lequel elle est basée est assez ancien et simple. Le principe sous-jacent est la *trilatération*, qui suggère qu'une position dans un espace géométrique donné peut être déduite par le calcul de distances à un certain nombre de points avec une position connue dans ce même espace. L'équation clé dans la navigation par satellite, connu sous le nom *équation de navigation*, est alors:

$$\rho_i = r_i + c \cdot \Delta b = \sqrt{(x_1 - x_u)^2 + (y_1 - y_u)^2 + (z_1 - z_u)^2} + c \cdot \Delta b \quad (1)$$

où ρ_i représente la *pseudo-distance* de l'utilisateur au satellite i , exprimée comme la somme de la distance géométrique entre l'utilisateur et le satellite, r_i , et le produit du biais d'horloge de l'utilisateur par rapport au temps de la constellation GNSS, Δb , par la vitesse de la lumière dans le vide, c . Les termes (x_i, y_i, z_i) et (x_u, y_u, z_u) représentent les coordonnées 3D pour le satellite et l'utilisateur, re-

spectivement. L'inclusion de Δb dans (1) est essentielle compte tenu de la façon par laquelle la pseudo-distance est calculée:

$$\rho_i = c \cdot \tau_i \quad (2)$$

où τ_i représente le temps de voyage du signal entre le satellite et l'utilisateur. Cette équation fournira seulement la distance entre l'utilisateur et le satellite si le récepteur est déjà synchronisé avec les satellites en avance. Comme cette condition ne peut pas être assurée a priori, il est donc nécessaire d'introduire le biais d'horloge du récepteur dans (1) comme une inconnue supplémentaire à déterminer. Par conséquent, le nombre minimal de satellites nécessaires pour déterminer la solution de navigation de positionnement et biais d'horloge est quatre.

L'estimation du temps de voyage des signaux pour le calcul des pseudo-distances est effectuée grâce à des techniques d'étalement de spectre à séquence directe (*Direct Sequence Spread Spectrum*, DSSS). Un code pseudo-aléatoire (*Pseudorandom Noise*, PRN) est transmis par chaque satellite et c'est au récepteur d'atteindre la synchronisation avec les satellites, en alignant ses répliques de code locaux avec les codes contenus dans le signal d'entrée. La démodulation des données contenues dans ces signaux permet ensuite d'établir la position des satellites au moment de la transmission du signal, de calculer des termes de correction à inclure aussi dans (1), et enfin à résoudre le système d'équations de navigation.

Pour le traitement d'un signal GPS L1 *Coarse Acquisition* (C/A), le signal le plus largement utilisé au monde ainsi que la base de la plupart des signaux GNSS actuels et prévus, la sortie échantillonnée d'un *front-end* d'un récepteur, $r[n]$, peut être écrite comme:

$$r[n] = \sqrt{P[nT_s]} \cdot d[(n - \zeta)T_s] \cdot c[(n - \zeta)T_s] \cdot e^{j\{2\pi(f_{IF} + f_d)nT_s + \phi\}} + w[nT_s] \quad (3)$$

où $P[\cdot]$ est la puissance instantanée du signal reçu, T_s est la période d'échantillonnage du signal, $d[\cdot]$ est la séquence des données de navigation binaires contenues dans le signal, ζ est la phase de décalage de code mesurée en échantillons et qui peut prendre n'importe quelle valeur dans l'intervalle $[0, n_s - 1]$, n_s étant le nombre d'échantillons dans un délai de code, $c[\cdot]$ est le code PRN contenu dans le signal, f_{IF} est la fréquence de démodulation intermédiaire, f_d est le décalage Doppler du signal perçu par le récepteur, ϕ est la phase de la porteuse du signal au début de l'observation du signal, et $w[\cdot]$ est la composante de bruit dans le signal reçu, généralement modélisé comme bruit blanc

gaussien additif (*Additive White Gaussian Noise*, AWGN). Compte tenu de l'orthogonalité des codes PRN typiquement utilisés dans les systèmes GNSS, lors de la focalisation sur le traitement d'un seul signal provenant d'un satellite spécifique, tous les autres signaux provenant des différents satellites peuvent être considérés comme une composante additionnelle de bruit.

Beaucoup plus d'informations sur le principe de fonctionnement des systèmes GNSS et les différentes structures de signal peuvent être trouvées, par exemple, dans [1–4].

2. Introduction à l'Acquisition de Signal GNSS

La première phase dans le processus de synchronisation récepteur-satellite est connu comme *acquisition de signal*. L'acquisition est une phase de synchronisation grossière qui a traditionnellement comme objectif de fournir des estimations approximatives de deux paramètres inconnus du signal entrant, en particulier sa *phase de code* et son *décalage Doppler*. En outre, sachant que le récepteur ne peut avoir aucune information a priori sur la présence d'un signal provenant d'un satellite spécifique, le processus d'acquisition est formulé comme un problème combinée *estimation/détection*. La structure de base d'un système d'acquisition GNSS est composée de deux blocs principaux [5–7] comme on décrit plus loin.

Méthode de Corrélation La méthode de corrélation est chargée de l'analyse de l'espace de recherche des paramètres inconnus, générant pour chaque pair de candidats phase de code/décalage Doppler une métrique qui est en fonction de ces valeurs. La métrique qui doit être calculée, connue sous le nom *sortie de corrélation*, correspond à la démodulation du signal d'entrée par une porteuse affectée au décalage Doppler, \hat{f}_d , et à la corrélation du code du signal d'entrée avec une réplique locale décalée circulairement par la phase de code candidat, $\hat{\zeta}$ (Figure 1). Le processus de corrélation est alors représenté comme:

$$S(\hat{\zeta}, \hat{f}_d) = \sum_{n=0}^{N-1} r[n] \cdot c[(n - \hat{\zeta})T_s] e^{-j2\pi(f_{IF} + \hat{f}_d)nT_s} \quad (4)$$

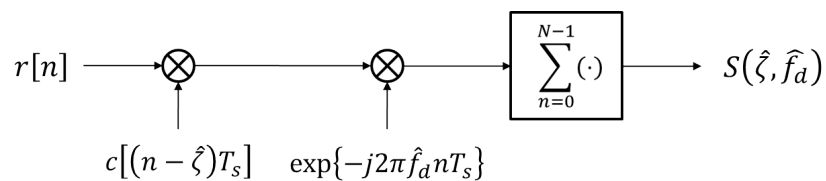


Figure 1 – Corrélation dans le domaine temporel (implémentation filtre adapté (*matched-filter*))

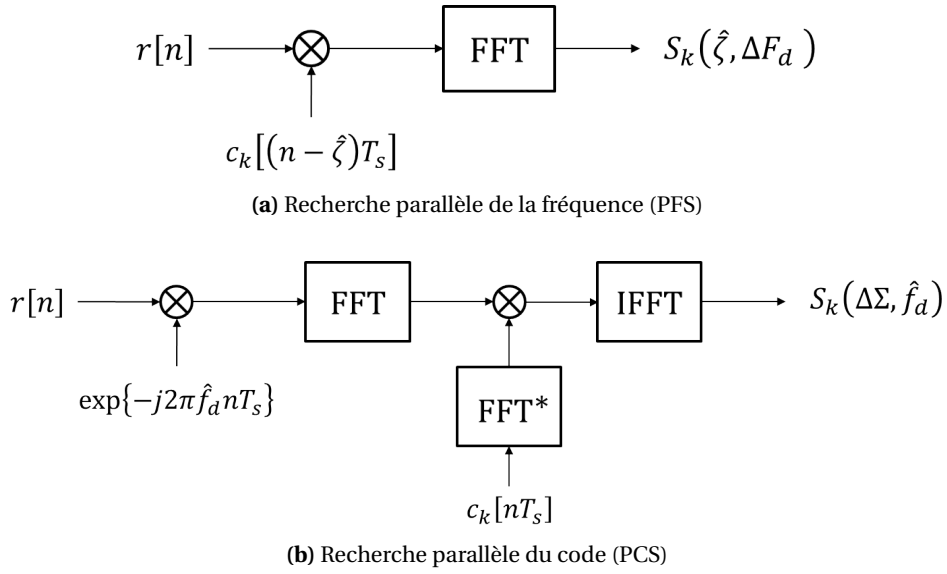


Figure 2 – Méthodes de corrélation dans le domaine fréquentiel

où $S(\hat{\zeta}, \hat{f}_d)$ représente la sortie de corrélation obtenue pour l'ensemble des paramètres candidats $\hat{\zeta}$ et \hat{f}_d et N est le nombre d'échantillons utilisés dans ce processus. Compte tenu du nombre des combinaisons phase de code/décalage Doppler typiquement très grand qui doivent être considérées, ainsi que les typiquement également grands valeurs de N , le processus de corrélation est la phase de l'acquisition la plus exigeante en termes de charge de calculs requis. Par conséquent, plusieurs méthodes de corrélation ont été développées pour tenter de minimiser le nombre d'opérations nécessaires pour analyser l'espace de l'incertitude de l'ensemble des paramètres. Ce résultat est obtenu grâce à l'utilisation de la *transformée de Fourier rapide* (Fast Fourier Transform, FFT), qui conduit à ce que ces méthodes soient communément appelées de *méthodes d'acquisition dans le domaine fréquentiel* (Figure 2).

Deux exemples bien connus sont: la méthode de recherche parallèle de la fréquence (*Parallel Frequency Search*, PFS, Figure 2a) et la méthode de recherche parallèle du code (*Parallel Code Search*, PCS, Figure 2b) [3, 4, 8]. Ces méthodes de corrélation produisent le même résultat que la méthode de corrélation dans le domaine temporel, mais simplement optimisent le nombre d'opérations nécessaires pour obtenir le résultat final. Une exécution de la méthode PFS calcule toutes les sorties de corrélation pour une phase de code candidat donné, c'est à dire:

$$S_{PFS}(\hat{\zeta}) = S(\hat{\zeta}, :) = \text{FFT}\{r[n] \cdot c[(n - \hat{\zeta})T_s]\} \quad (5)$$

Il est à noter que cette méthode impose la résolution de recherche en fréquence à cause de l'application de la FFT pour l'analyse spectrale du signal. Ce n'est pas le cas avec l'acquisition dans le domaine temporel ou avec la méthode PCS. Une exécution de la méthode PCS, d'autre part, fournit tous les résultats de corrélation pour une fréquence Doppler candidate donnée:

$$S_{PCS}(\hat{f}_d) = S(:, \hat{f}_d) = \text{IFFT}\{\text{FFT}\{r[n] \cdot e^{-j2\pi(f_{IF} + \hat{f}_d)nT_s}\}\text{FFT}^*\{c[n]\}\} \quad (6)$$

Deux autres méthodes de corrélation bien connus sont le *Double-Block Zero-Padding* (DBZP) [9–12] et le *Spectral Shift with Doppler Preprocessing ou Bidimensional Parallel Search* (BPS) [13–15]. Bien que n'étant pas une des contributions principales de cette thèse, une comparaison détaillée de ces quatre méthodes de corrélation est incluse dans la thèse, non seulement en termes de complexité d'application, mais aussi considérant leurs limites de sensibilité inhérentes (voir le chapitre 2 de la partie en anglais).

Détecteur ou Schéma de Détection Le rôle du détecteur est de générer une *métrique de détection* à partir de la sortie (ou de plusieurs sorties) du bloc de corrélation, ce qui permet de décider la présence ou l'absence du signal provenant du satellite en cours de test. Différents schémas de détection peuvent être utilisés dans la recherche des signaux GNSS faibles, qui seront plus ou moins efficaces en fonction de la structure du signal ainsi que ses paramètres. Un système de détection est caractérisé par [5, 6, 16]:

1. La probabilité de fausse signalisation de la présence du signal lorsque celui-ci est, en effet, absent (probabilité de fausse alarme, P_{fa}); et
2. La probabilité de détection correcte lorsque le signal est effectivement présent (probabilité de détection, P_d).

Le critère de décision de Neyman-Pearson est typiquement appliqué à l'acquisition GNSS, à travers lequel un seuil de détection, η , est réglé selon la P_{fa} souhaitée et la distribution de la sortie du détecteur dans l'hypothèse d'absence de signal (hypothèse H_0). Ensuite, la probabilité de détection correspond à la probabilité que la métrique de détection dépasse η compte tenu de sa distribution dans la présence de signal (hypothèse H_1) et les paramètres de ce signal d'entrée.

La différence principale entre les différents systèmes de détection trouvés dans la littérature est la façon dont les sorties de corrélation consécutives sont traitées, ou *intégrés*. Les trois techniques d'intégration de signaux les plus connus sont l'intégration *cohérente*, *non-cohérente* et *différentielle*. Exemples de détecteurs utilisant ces techniques d'intégration sont présentés dans la

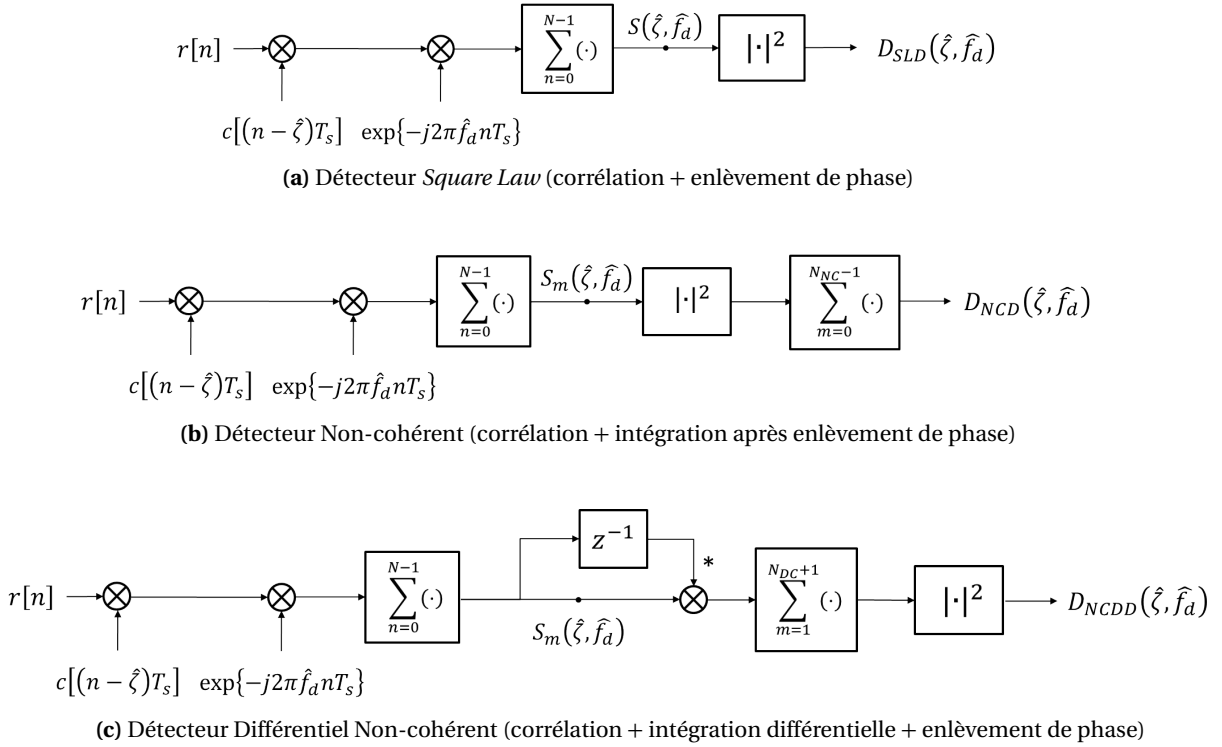


Figure 3 – Schémas de détection GNSS

Figure 3. Il convient de noter que l'opération d'enlèvement de phase (modulo carré) est nécessaire dans chaque détecteur sachant que la phase du signal d'entrée est normalement inconnue.

L'intégration cohérente de plusieurs périodes de code correspond dans la pratique à la corrélation au cours de ce même nombre de périodes de code. Par conséquent, la sortie de corrélation est aussi parfois appelée par la *sortie d'intégration cohérente*. Pour cette même raison, les trois techniques d'intégrations présentées peuvent être regroupées comme les techniques d'intégration cohérentes et post-cohérentes, comme le traitement de signal cohérent (voir corrélation) est une étape obligatoire pour tous les schémas de détection.

L'intégration cohérente est bien connue comme étant la stratégie d'intégration de signal la plus efficace, car c'est elle qui maximise le gain d'intégration du signal. Toutefois, la mesure dans laquelle l'intégration cohérente peut être étendue est limitée par plusieurs facteurs, tels que le décalage Doppler résiduel, et la transition de bits de données, entre autres. Par conséquent, la transition à des techniques d'intégration post-cohérente est souvent nécessaire pour atteindre une plus haute sensibilité. Il convient également de noter, que la structure de détection non-cohérente est toujours celle représentée sur la Figure 3, plusieurs détecteurs peuvent être conçus pour appliquer l'intégration différentielle.

Comme il a été mentionné précédemment, la combinaison de la méthode de corrélation et le système de détection représente le noyau d'un système d'acquisition GNSS. Néanmoins, beaucoup plus de complexités et d'axes de recherche peuvent naturellement être ajoutés à l'étude de l'acquisition des signaux GNSS, et un examen approfondi de l'état de l'art de ce sujet est présenté dans la thèse. *Pour plus de détails, référez-vous au chapitre 2 de cette thèse.*

3. Contributions Scientifiques de la Thèse

En vue de l'examen de l'état de l'art qui a été très brièvement présenté ici et qui est décrit en détail dans le Chapitre 2 de cette thèse, le nombre d'aspects intéressants qui pourraient avoir été ciblés au cours de cette recherche doctorale est considérablement grand. Pour cette raison, les choix effectués concernant les sujets sur lesquels se concentre cette recherche, étaient l'objet d'un examen attentif tout au long de la période de recherche. Enfin, les angles de recherche qui ont été définis comme étant pertinents à l'état actuel des techniques d'acquisition GNSS, d'un point de vue technique et scientifique comme pratique, et qui sont analysées en détail dans la thèse sont:

- Analyse et Compensation du Décalage Doppler dans l'Acquisition;
- Caractérisation de la Sensibilité des Détecteurs GNSS Différentiels; et
- Détection Collective Multi-Constellation: Analyse des Performances et Optimisation de Complexité.

Ces choix ont été motivés par la pertinence de ces thèmes et les possibilités de contributions significatives, réalisables pendant la période limitée de recherche de cette thèse. Les sections suivantes présentent brièvement les contributions développées dans cette thèse.

3.1. Analyse et Compensation du Décalage Doppler dans l'Acquisition

L'un des principaux critères pour la conception des systèmes d'acquisition GNSS est le décalage Doppler qui est attendu par l'utilisateur lors de la réception du signal. Trois scénarios d'application ont été définis pour évaluer l'évaluation :

- Le décalage Doppler reste à peu près inchangé au cours du temps d'acquisition - *dynamique basse*;
- Le décalage Doppler change légèrement pendant la période d'acquisition et une compensation dynamique de ce changement n'est pas nécessaire pour répondre aux besoins des utilisateurs - *dynamique moyenne*; et
- Le décalage Doppler change significativement pendant la période d'acquisition et une compensation dynamique de ce changement est nécessaire pour répondre aux besoins des utilisateurs - *dynamique haute*.

3.1.1. Compensation du Décalage Doppler dans Dynamique Basse

Tel que défini précédemment, nous considérons un utilisateur étant en dynamique basse quand le décalage Doppler des signaux entrants peut être considéré comme constante pendant toute la durée d'acquisition. C'est, en fait, l'une des hypothèses les plus communes pour la conception des schémas d'acquisition GNSS. Dans cette hypothèse et selon (4), le décalage Doppler du signal aura alors un impact sur l'amplitude de la sortie de corrélation comme une atténuation de $\text{sinc}(\Delta f_d N T_s)$ où $\Delta f_d = f_d - \hat{f}_d$ est l'erreur d'estimation de la fréquence candidate.

Lorsqu'on utilise des méthodes de corrélation qui permettent de fixer librement la résolution de la fréquence, tel que le PCS, une atténuation maximale admissible de la sortie de corrélation peut être définie et la résolution de recherche de fréquence est calculée à partir de cette atténuation. Cependant, les méthodes qui parallélisent la recherche de la fréquence par FFT, comme le PFS, BPS, et DBZP, imposent intrinsèquement une résolution de recherche de fréquence de $1/(N T_s)$, ne permettant donc pas la flexibilité qui est vérifiée avec le PCS. Néanmoins, comme indiqué dans cette thèse et d'autres sources, les méthodes DBZP et BPS sont plus efficaces en termes de nombre d'opérations requises, donc désirables d'être employées dans les récepteurs GNSS. L'objectif de cette partie du travail était donc de développer une méthodologie pour atteindre une méthode de corrélation capable de combiner les pertes de sensibilité moins élevées de la méthode PCS avec l'efficacité de calcul de la méthode BPS (Figure 4).

La solution qui a été trouvée c'est d'appliquer des algorithmes de *Spectral Peak Location*(SPL)

afin d'affiner l'estimation de la fréquence avant la détection du signal. La représentation schématique de la solution proposée est présentée dans la Figure 5. L'amélioration de la robustesse au décalage Doppler de la nouvelle méthodologie par rapport à son homologue simple (sans application des algorithmes SPL) est démontrée par des simulations ainsi que par l'acquisition de signaux réels. *Pour plus de détails, référez-vous à la section 3.1 de cette thèse.*

3.1.2. Analyse du Décalage Doppler dans Dynamique Moyenne

Dans certaines applications, il peut être clair que l'hypothèse d'un décalage Doppler constant pendant toute la durée d'acquisition ne peut pas tenir. En tous cas, au lieu d'essayer directement une compensation de ce décalage Doppler variable, il peut être suffisant de quantifier l'impact de la variation de ce décalage Doppler dans la sensibilité des différents détecteurs et, à partir de cette analyse, déduire les conditions pour la variation Doppler maximale admissible pendant le temps d'acquisition. Pour atteindre cet objectif, une métrique pour quantifier le changement de Doppler totale dans une cellule de Doppler (équivalent à la résolution de la recherche Doppler), appelé le *facteur de balayage* (γ dans la Figure 6), est d'abord présentée. Le facteur de balayage est défini comme le rapport entre la variation totale du décalage Doppler au cours de la période d'intégration cohérente et la largeur de la cellule Doppler, et, ainsi, il représente la fraction de la cellule Doppler qui est *balayé* par le Doppler variable pendant le temps d'intégration cohérente. À titre d'exemple, envisager un changement de Doppler total de 10 Hz dans une cellule Doppler de dimension 1000 Hz ou 100 Hz. Pour le premier cas $\gamma = 1\%$ et pour le second $\gamma = 10\%$.

En modélisant la fréquence d'entrée de signal comme une fonction linéaire, le signal à traiter

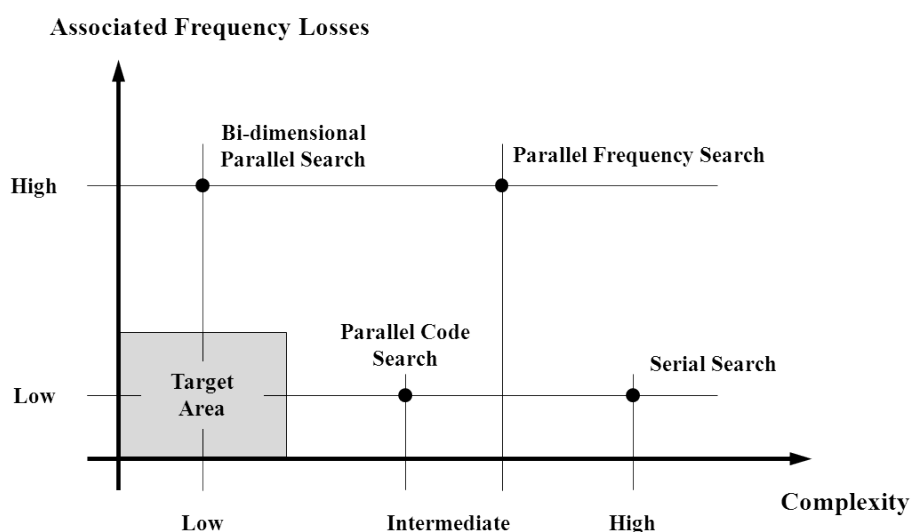


Figure 4 – Comparaison qualitative des méthodes de corrélation

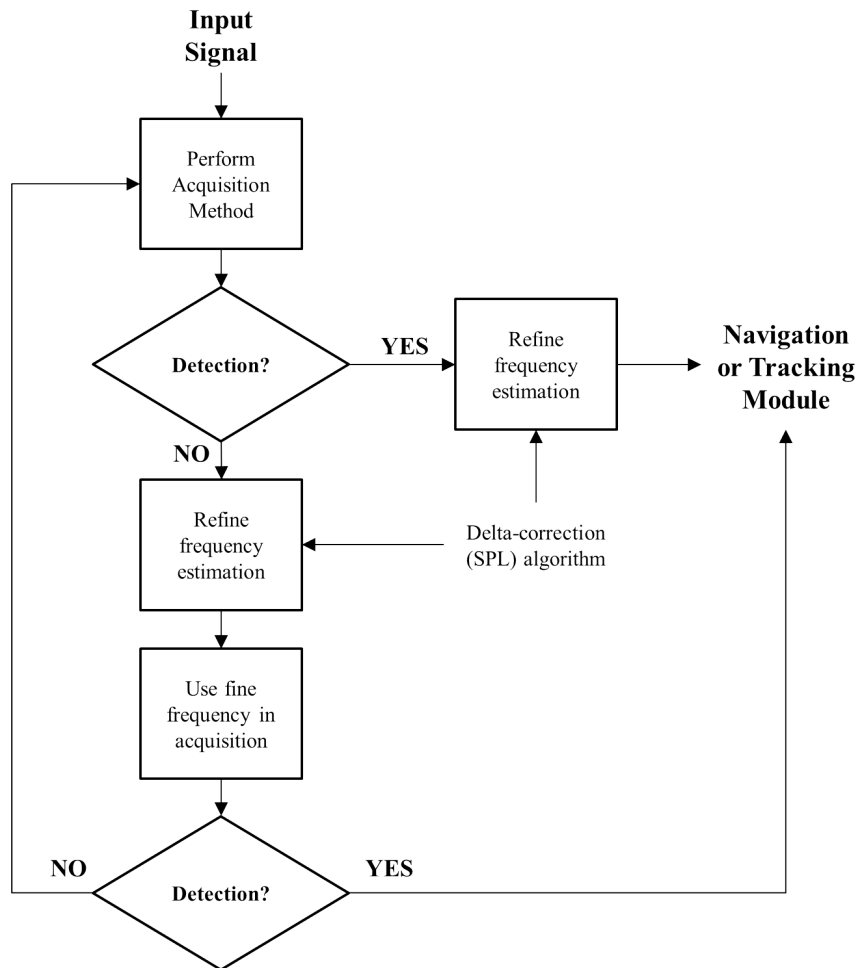


Figure 5 – SPL-corrected acquisition method diagram

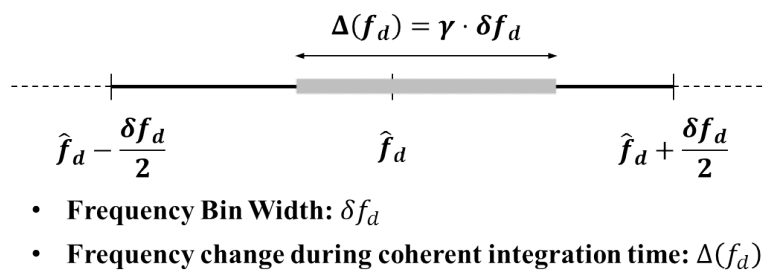


Figure 6 – Définition du facteur de balayage

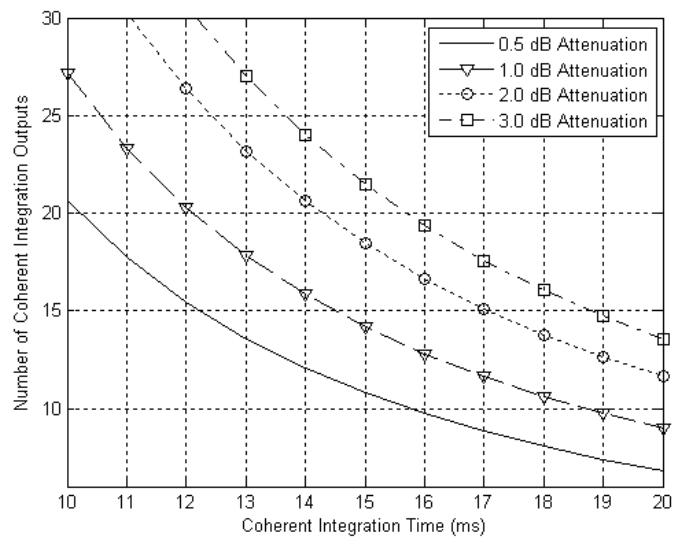


Figure 7 – Exemple obtenu avec la formule proposée pour des dynamiques moyennes pour le compromis du temps d’intégration cohérente et le nombre total de sorties cohérentes pour des différentes atténuations maximales admissibles des sorties cohérentes, pour un taux de changement de Doppler de 50 Hz/s (application dans un signal GPS L1 C/A)

devient un signal *chirp*, et, par approximation des résultats des simulations, une formule est proposée, permettant de mettre en relation le temps d’intégration cohérente et le temps totale d’observation du signal avec le niveau de la dynamique attendue et l’atténuation maximale souhaitée pour les sorties cohérentes (Figure 7) *Pour plus de détails, référez-vous à la section 3.2 de cette thèse.*

3.1.3. Compensation du Décalage Doppler dans Dynamique Haute

Lorsqu’il est prévu que le décalage Doppler change considérablement pendant la période d’acquisition, ce que veut dire, les dynamiques attendues sont trop élevées pour permettre des temps d’intégration de signal assez longs sans subir des atténuations trop élevées, une compensation dynamique doit être mise en place. Une approche possible consiste à obtenir une estimation de la fréquence Doppler à partir d’un résultat intermédiaire du traitement du signal et de créer une boucle de correction de décalage de fréquence (*Frequency Offset Correction*, FOC) qui met à jour de façon dynamique la fréquence de démodulation du signal d’entrée (Figure 8).

Un tel système d’acquisition a été identifié dans la littérature, en particulier dans [17], qui estime le décalage Doppler par l’argument de la sortie de l’intégration différentielle. Dans l’étude décrite dans cette thèse, une méthode alternative pour exécuter la boucle FOC est proposée, tout simplement en mesurant la phase des sorties d’intégration cohérentes consécutives et de différencier les résultats pour obtenir le taux de changement de Doppler. Les résultats obtenus montrent que

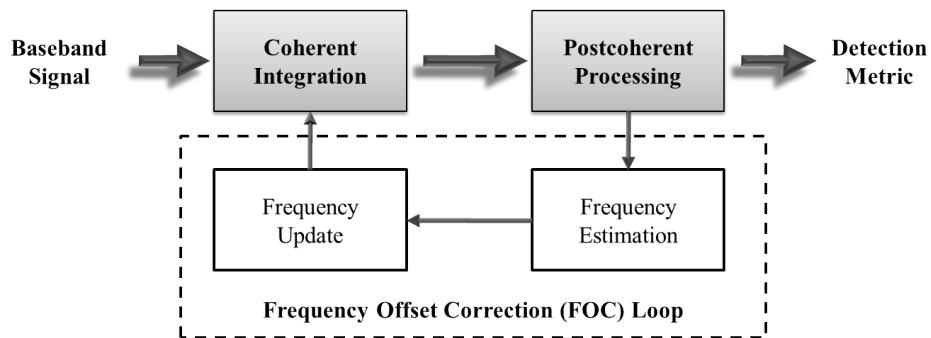


Figure 8 – Structure générale d'un schéma d'acquisition incluant une boucle FOC

l'architecture proposée apporte des avantages par rapport à celle de [17] et qu'elle apporte plus de robustesse pour l'application dans des scénarios considérés comme étant des dynamiques hautes. Les limites de l'approche développée sont également décrites. *Pour plus de détails, référez-vous à la section 3.3 de cette thèse.*

3.2. Caractérisation de la Sensibilité des Détecteurs GNSS Différentiels

Pour l'acquisition des signaux dans des environnements difficiles, l'utilisation des techniques de traitement de signal capables de détecter la présence de ces signaux, même à des puissances beaucoup plus faibles que ses valeurs nominales, est indispensable. Ces techniques sont connues comme des *techniques d'acquisition à haute sensibilité*. Selon les trois types de détecteurs présentés dans la section 2, une sensibilité accrue peut être obtenue par l'application d'intégrations cohérentes exclusivement ou aussi par l'application d'intégrations post-cohérentes. Même si l'intégration cohérente a le potentiel de maximiser le gain de sensibilité atteignable, la mesure dans laquelle le temps d'intégration cohérente peut être augmentée est limitée par plusieurs facteurs, tels que le décalage Doppler résiduel, la transition de bits de données, et les propres capacités de calcul du récepteur. Par conséquent, après un certain nombre d'accumulations cohérentes, la transition vers des stratégies d'intégration post-cohérentes est généralement choisie pour continuer à augmenter la sensibilité de l'acquisition.

La stratégie d'intégration post-cohérente la plus connue, est généralement appliquée, c'est l'intégration *non-cohérente*, dans laquelle les phases des sorties cohérentes sont enlevées avant des accumulations additionnelles (Figure 3b). La métrique de détection du détecteur non-cohérent (*Noncoherent Detector*, NCD) est alors obtenue par:

$$D_{NCD}(\hat{\zeta}, \hat{f}_d) = \sum_{m=0}^{N_{NC}-1} |S_m(\hat{\zeta}, \hat{f}_d)|^2 \quad (7)$$

où S_m représente la sortie cohérente numéro m et N_{NC} est le nombre total d'intégrations non-cohérentes à réaliser. Il est également bien connu, néanmoins, que l'intégration non-cohérente est moins efficace que l'intégration cohérente en termes de gain de sensibilité, à cause de l'opération d'enlèvement de phase qui subit une perte, communément appelé de *squaring loss*, qui réduit le rapport signal-bruit (*Signal-to-Noise Ratio*, SNR) du signal en cours de traitement.

L'autre approche d'intégration post-cohérente est l'intégration *différentielle*. Dans cette approche, chaque sortie cohérente est corrélée avec une sortie précédente, ce qui résultera à une phase constante de ce produit si le décalage Doppler reste constant. Cette approche est préférable par rapport à l'enlèvement de phase, car le produit des deux sorties indépendantes est statistiquement moins préjudiciable en raison de l'indépendance entre les termes de bruit des différentes sorties cohérentes. La métrique de détection du détecteur différentiel non-cohérent (*Noncoherent Differential Detector*, NCDD), représentée sur la Figure 3c, est donné par:

$$D_{NCDD}(\hat{\zeta}, \hat{f}_d) = \left| \sum_{m=1}^{N_{DC}+1} S_m(\hat{\zeta}, \hat{f}_d) \cdot S_{m-1}^*(\hat{\zeta}, \hat{f}_d) \right|^2 \quad (8)$$

où N_{DC} est le nombre total d'intégrations différentielles exécutées. Il a été rapporté dans plusieurs publications que le détecteur NCDD est préférable pour l'acquisition des signaux faibles par rapport au détecteur NCD, mais une comparaison formelle entre la sensibilité des deux détecteurs n'a pas été trouvée dans la littérature. Cela est essentiel afin d'optimiser les ressources du récepteur impliquées dans l'acquisition, premièrement décidant quelle stratégie d'intégration post-cohérente doit être adoptée, et puis calculer le nombre d'intégrations nécessaires pour atteindre le *point de travail* (*working point*, le pair (P_d, P_{fa})) souhaité, pour arriver à atteindre la sensibilité ciblée. Ceci, c'est la base pour un système d'acquisition haute sensibilité *adaptatif*.

Une formule capable de prédire la perte de sensibilité du détecteur NCD, résultant de l'exécution d'un nombre N_{NC} d'intégrations non-cohérentes du même nombre d'intégrations cohérentes, a été développé pour les systèmes de radar dans [18], mais une formule similaire n'a pas pu être trouvée pour les détecteurs différentiels. Ainsi, celui-ci était l'objectif principal de cette phase de recherche.

L'approche classique pour évaluer le gain SNR d'une opération sur un signal est basée sur la comparaison du SNR du signal avant et après cette opération. Cependant, cette approche est montrée dans [19, 20] comme n'étant pas applicable aux opérations non-cohérentes et différentielles. L'approche suivie dans [18] est donc également adoptée dans ce travail. Cette approche suggère de caractériser une stratégie d'intégration non-optimale par rapport à la solution optimale (cohérente). Par conséquent, la perte de sensibilité de l'approche non-optimale est définie comme la puissance supplémentaire pour le signal d'entrée, qui est requis par le détecteur qui utilise l'approche envisagée pour atteindre le même point de fonctionnement que le détecteur qui emploie exclusivement l'intégration cohérente.

Cette étude commence par la caractérisation statistique de l'opération différentielle, pour arriver à la sensibilité des différents détecteurs différentiels. Un des résultats finaux est la formule souhaitée pour la caractérisation de la sensibilité du détecteur NCDD, en fonction de N_{DC} , P_d , et P_{fa} qui permet d'effectuer la comparaison souhaitée entre les détecteurs NCD et NCDD. Un exemple des résultats qui peuvent être obtenus avec cette nouvelle formule est montré dans le Tableau 1. *Pour plus de détails, référez-vous au chapitre 4 de cette thèse.*

Table 1 – Nombre d'intégrations post-cohérentes requises pour atteindre $10 \cdot \log_{10}(20) = 13\text{dB}$ de gain de sensibilité pour un point de travail $(P_d, P_{fa}) = (0.9, 10^{-5})$ (application à un signal GPS L1 C/A)

| Temps d'Intégration Cohérente (ms) | Nombre de Sorties Cohérentes Requises | |
|------------------------------------|---------------------------------------|----------------|
| | Détecteur NCD | Détecteur NCDD |
| 1 | 64 | 40 |
| 2 | 21 | 16 |
| 4 | 8 | 7 |
| 5 | 6 | 6 |
| 10 | 3 | 3 |
| 20 | - | - |

3.3. Détection Collective Multi-Constellation: Analyse des Performances et Optimisation de Complexité

Une des techniques les plus efficaces pour le traitement des signaux GNSS à faible puissance dans la phase qui généralement suit l'acquisition, connue comme la *poursuite*, c'est de traiter tous les signaux visibles conjointement, de sorte que les signaux plus faibles puissent profiter de la présence des signaux plus forts. Le même concept, connu sous le nom de traitement de signal *vectoriel*, a été récemment transposé à l'acquisition, dans ce qui est connu comme *détection collective* [21–23]. Ce concept s'appuie sur des informations d'assistance (information fournie par d'autres sources que les satellites GNSS), pour que l'utilisateur puisse définir une incertitude dans sa position et biais d'horloge, à partir de laquelle une grille de recherche est établie. Chaque combinaison position et biais d'horloge (point 4D) est ensuite utilisée pour estimer la phase de code pour chaque satellite et une seule métrique de détection est générée en fonction de cette position et biais d'horloge (Figures 9 et 10).

La Détection Collective est simultanément une méthode d'acquisition haute sensibilité, par l'application de l'acquisition vectorielle, et une méthode de positionnement directe, étant capable de générer une estimation de position/biais d'horloge directement à partir de l'acquisition. Comme une méthode d'acquisition de haute sensibilité, la détection collective est caractérisée par 1) sa sensibilité et 2) sa complexité d'exécution, et comme une méthode de positionnement directe, elle est caractérisée par 1) l'erreur de position, 2) le temps pour obtenir une première solution de navigation (*Time to First Fix*, TTFF) et aussi, dans une certaine mesure, par sa complexité d'exécution, qui peut devenir problématique si c'est trop élevée. Comme le montre le Tableau 2, toutes ces mesures de performance peuvent être en quelque sorte liées à la résolution de la grille de recherche choisie.

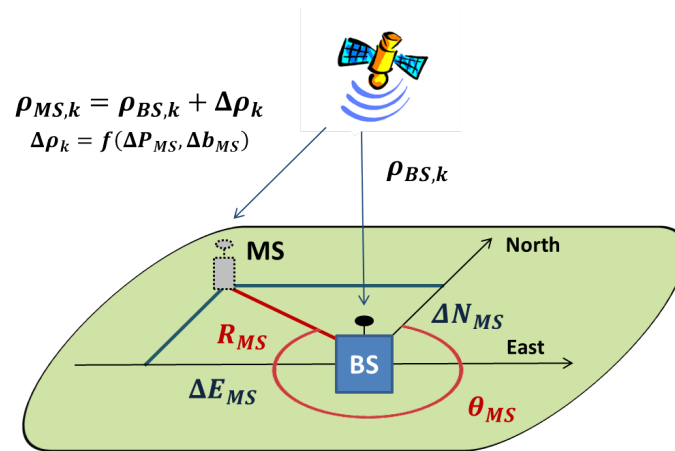


Figure 9 – Translation de la recherche de la phase du code de la station mobile (*Mobile Station*, MS) au domaine position-biais d’horloge par rapport à une station de base (*Base Station*, BS) appliquée dans la Détection Collective

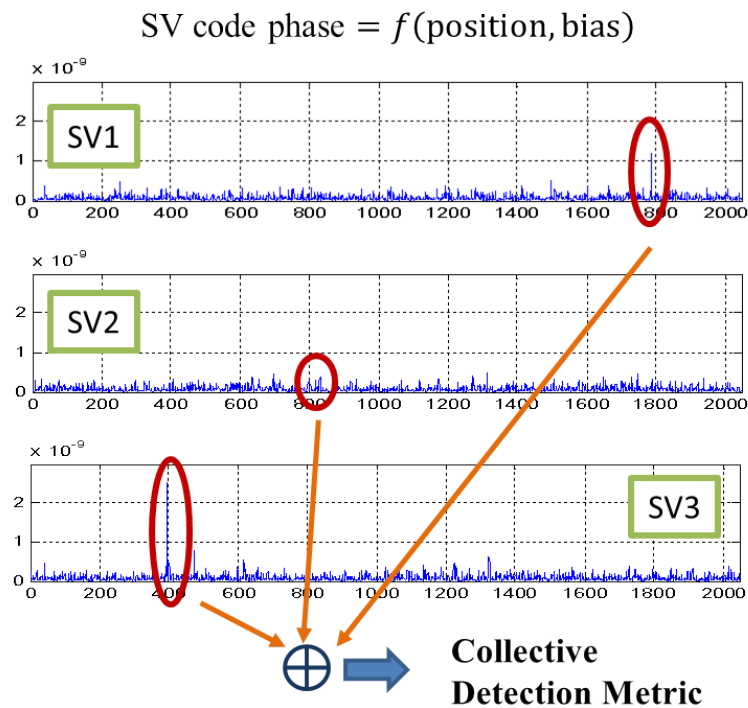


Figure 10 – Génération de la métrique de détection pour la Détection Collective

Table 2 – Métriques de performance pour la Détection Collective

| Métrique de Performance | Dépend de | Lié à |
|-------------------------|--|--------------------------------------|
| Sensibilité | Résolution dans la recherche de la phase du code | |
| Complexité | Nombre de points à considérer | Résolution de la grille de recherche |
| Erreur de Position | Résolution dans la recherche de la phase du code | |
| TTFF | Nombre de points à considérer | |

Donc, l'un des plus grands défis pour la Détection Collective est le compromis entre la résolution de la grille de recherche, qui doit être assez fine pour permettre des bonnes performances de sensibilité et d'erreur de position, et le nombre total de points à analyser, qui a des répercussions directes sur la complexité et TTFF de l'algorithme. La résolution idéale de la grille de recherche, cependant, n'a pas été pleinement évaluée dans la littérature. L'objectif principal de cette recherche était alors la proposition d'une méthodologie pour l'application du processus de recherche de la Détection Collective répondant aux exigences suivantes:

- **Systematique:** la résolution de la grille à employer dans les recherches pour la position et le biais d'horloge est déterminée selon un ensemble de paramètres d'entrée; et
- **Efficace:** les étapes de la recherche assurent que les vraies phases de code des signaux d'entrée ne sont pas manquées tout en évitant des grilles de recherche trop fines qui apportent des charges de calculs inutilement lourds.

Cet objectif est obtenu grâce à l'analyse de l'impact de la résolution de recherche de la grille dans l'erreur maximale d'estimation de phase de code, en tenant aussi compte de la géométrie de la constellation de satellites visibles. En outre, nous abordons également la question de l'hybridation de l'acquisition vectorielle et séquentielle pour accélérer le processus de recherche de la Détection Collective. Enfin, nous développons une méthodologie pour l'application de la détection collective dans un récepteur combiné GPS + Galileo travaillant à la bande E1/L1, validé avec des signaux réels des deux constellations. *Pour plus de détails, référez-vous au chapitre 5 de cette thèse.*

4. Conclusions et Perspectives

La navigation par satellite joue un rôle de plus en plus important dans la société moderne. Néanmoins, avec les nouvelles applications, des nouveaux défis sont aussi apparus. Dans cette thèse, l'une des phases les plus importantes de la chaîne de traitement du signal dans un récepteur GNSS a été étudiée, *l'acquisition de signal*. Après une introduction exhaustive et approfondie au sujet de l'acquisition GNSS dans le chapitre 2, les trois chapitres suivants présentent les contributions principales de cette recherche. Ces contributions sont résumées ci-dessous, ainsi que quelques recommandations pour l'avenir de suivi de ces travaux.

4.1. Conclusions de la Recherche de la Thèse

Analyse et Compensation de l'effet Doppler dans l'Acquisition des Signaux GNSS Dans le chapitre 3, le décalage Doppler a été reconnu comme l'un des principaux critères de conception du module d'acquisition pour des différentes applications GNSS. En particulier, non seulement sa valeur, mais également sa variation au cours du temps d'observation du signal est importante. Trois scénarios d'application ont été pris en considération pour l'évaluation, considérés comme dynamique basse, moyenne, et haute.

Pour le cas de dynamique basse, lorsque le décalage Doppler peut être considéré comme constant pendant le temps d'acquisition, la résolution de la grille de recherche pour la recherche Doppler doit être pondérée avec l'efficacité de calcul de la méthode de corrélation souhaitée. On a vu que les méthodes les plus efficaces pour le calcul de la corrélation sont soumises à des atténuations Doppler potentiellement plus élevées que ceux des méthodes moins efficaces, et une méthodologie pour atténuer ces pertes a été proposée. En appliquant un algorithme nommé de *Spectral Peak Location* (SPL), le décalage entre le vrai décalage Doppler et la fréquence candidate le plus proche peut être estimé, et une grille de recherche fine peut ensuite être émulée avec les méthodes autrement moins robustes au décalage Doppler. Une nouvelle méthodologie d'acquisition a été développée pour l'application des algorithmes SPL dans l'acquisition GNSS, et ses mérites ont été prouvés dans l'acquisition des signaux GNSS à la fois réels et simulés. Les résultats obtenus et la simplicité de la technique SPL montrent que cette proposition est une solution prometteuse pour optimiser le compromis sensibilité/complexité dans la conception des récepteurs GNSS.

Pour le cas de la dynamique moyenne, définie comme la situation dans laquelle le taux de changement de Doppler n'est pas assez élevée pour justifier des solutions de complexité plus élevées pour tenter la compensation dynamique, l'analyse de ce taux de changement sur des différents détecteurs a été évaluée. Dans le cas du détecteur *Square-Law Detector* (SLD, Figure 3a), il a été établi

une limite pour la durée d'intégration cohérente qui garantit que les atténuations de la métrique de détection finale ne sont pas plus élevées que celles qu'on obtiendrait pour un Doppler stationnaire. Selon (3.17), cette limite est de $T_{coh} = \sqrt{\alpha^{-1}}$. Pour les détecteurs NCD et NCDD, une formule qui permet de mettre en relation la durée maximale de l'intégration cohérente avec le nombre totale de sorties cohérentes, en fonction de la dynamique attendue et de l'atténuation maximale admissible pour les sorties cohérentes est aussi proposée (équation (3.21)). C'était également vu que dans l'hypothèse d'un signal d'entrée du type *chirp* et d'un décalage de fréquence initial proche de zéro, le détecteur NCD est un choix plus fiable que le NCDD. La deuxième solution est plus indiquée pour des temps d'intégration cohérente relativement bas (10-20ms), de façon à être applicable dans les récepteurs autonomes, tandis que la première vise à des temps d'intégration cohérentes très longs (> 100 ms).

Enfin, lorsque le taux de changement de Doppler est considéré comme significatif par rapport à la durée de l'intégration cohérente, il a été montré que l'inclusion d'une boucle FOC dans le détecteur NCD est capable de fournir plusieurs dBs de sensibilité supplémentaire par rapport au détecteur non corrigée (Figure 3.28 et Figure 3.29). Cependant, l'accroissement de la sensibilité de la solution proposée est limité par la capacité de l'estimateur choisi de produire des bonnes estimations à faibles SNR d'entrée. On a remarqué que pour des valeurs du facteur de balayage (γ) entre 5 et 15 %, la solution proposée peut offrir une fiabilité accrue par rapport à l'hypothèse de dynamique moyenne. Table 3.6 montre la solution préférable et le détecteur à appliquer en fonction de γ .

Caractérisation de la Sensibilité des Détecteurs GNSS Différentiels Dans le chapitre 4, la performance des détecteurs différentiels dans l'acquisition des signaux GNSS faibles a été étudiée. En premier, nous avons caractérisé statistiquement le détecteur *Pair-wise Detector* (PWD). Sous l'hypothèse de signal absent, on a fait usage du fait que la sortie de l'intégration différentielle *pair-wise* correspond à une somme de variables aléatoires Laplaciennes indépendantes pour proposer une nouvelle expression pour sa caractérisation. Dans l'hypothèse où tous les deux, signal et bruit, sont présents, il a été montré que l'approximation de la sortie de ce détecteur par une variable aléatoire gaussienne produit un résultat très proche de la distribution réelle, et une expression pour la probabilité de détection de ce détecteur a donc été proposée.

Compte tenu de la complexité de la suite d'une procédure similaire pour le détecteur NCDD, nous avons opté pour caractériser ce détecteur par sa perte de sensibilité par rapport au détecteur SLD. Premièrement, la méthode pour caractériser un détecteur de cette manière a été décrite, et par la suite, une formule pour l'évaluation de la perte de la sensibilité du détecteur NCDD (combinant les pertes différentielles et non-cohérentes) a été proposée. Les résultats théoriques ont

été validés par des simulations, ce qui montre qu'il s'agit d'une approche valable à suivre dans tels cas, lorsque l'analyse statistique des détecteurs est trop complexe. Les résultats obtenus ont permis la comparaison des détecteurs NCDD et NCD, ce qui permet de décider quelle stratégie d'intégration est la plus adéquate pour atteindre un niveau de sensibilité ciblé. Il a été confirmé que l'intégration différentielle a en effet le potentiel d'être préférable à l'intégration non-cohérente dans l'acquisition des signaux faibles. Toutefois, la dynamique de l'utilisateur doit également être prise en considération, comme était remarqué dans le chapitre 3. Les conclusions théoriques ont été confirmées par l'acquisition des signaux GPS L1 C/A réels, soulignant le potentiel du détecteur NCDD pour l'acquisition des signaux faibles.

Détection Collective Multi-Constellation: Analyse des Performances et Optimisation de Complexité Dans le chapitre 5, une nouvelle méthodologie pour une application systématique et efficace de la Détection Collective a été proposée. Ce chapitre suppose la disponibilité d'un second récepteur utilisé comme une station de base et un lien d'assistance fournissant les données requises par la station mobile. Le nouvel algorithme définit une grille de recherche couvrant l'incertitude dans la position de l'utilisateur sur une zone circulaire (pendant que les études précédentes utilisaient une zone d'incertitude carrée) et prend en compte l'angle d'élévation le plus bas de l'ensemble des satellites visibles, ainsi que deux paramètres définis par l'utilisateur: l'erreur maximum admissible pour l'estimation de la phase de code pendant le processus de recherche de la détection collective et la portée maximale de la station de base. Le nouvel algorithme a été montré comme étant plus efficace en termes de charge de calcul qu'une méthode utilisant une grille carrée avec une résolution de recherche prédéfinie, et plus fiable, en gardant sa performance indépendante de la vraie position de l'utilisateur et de son biais d'horloge (Figures 5.11 et 6.1).

Deux approches pour l'hybridation de l'algorithme proposées avec l'acquisition séquentielle classique ont également été présentées. On a vu que ces approches hybrides sont plus efficaces pour atteindre une sensibilité plus élevée que la version uniquement vectorielle, compte tenu des limites imposées sur la grille de recherche pour l'incertitude 4D de l'utilisateur. En outre, les algorithmes proposés ont également été testés dans l'acquisition de signaux réels GPS et Galileo, démontrant ainsi la faisabilité de la détection collective multi-constellation. Les résultats obtenus dans les deux scénarios considérés (à ciel ouvert avec bruit supplémentaire ajoutée et à l'intérieure d'un bâtiment) témoignent la capacité du principe d'acquisition vectoriel pour acquérir des signaux plus faibles que les algorithmes séquentiels. En outre, les résultats présentés pour les données intérieures montrent la capacité des algorithmes hybrides de fournir une estimation de la position approximative de l'utilisateur, même avec seulement deux signaux détectables par l'acquisition

séquentielle. Une analyse plus approfondie sera réalisée dans le groupe de recherche pour consolider les résultats présentés ici.

4.2. Perspectives du Travail

En ligne avec les résultats de la recherche présentés ici, plusieurs questions peuvent également être posées pour des travaux futurs:

- L'analyse menée sur les scénarios dynamiques dans le chapitre 3 suppose que les signaux d'entrée sont bien modélisés par un signal *chirp* avec un taux de changement constant, ce qui n'est certainement pas le cas pour l'acquisition de signaux très atténués, nécessitant des temps d'intégration très longs. Le moyen le plus fiable pour tester les algorithmes proposés serait de créer un dispositif expérimental de travail avec des signaux réels et permettant la démonstration de la performance réelle de l'algorithme dans de tels scénarios.
 - Également dans l'analyse des scénarios dynamiques dans le chapitre 3, on a vu que la performance du système d'acquisition assisté par la boucle FOC est très dépendante de la capacité de l'estimateur de fréquence de produire le bon résultat à des faible SNR d'entrée. De cette façon, d'autres estimateurs, plus fiables que celui employé ici, pourraient être envisagés d'être utilisés dans cette architecture, lui rendant ainsi encore plus fiable.
 - Pour la caractérisation des détecteurs différentiels effectué dans le chapitre 4, l'une des hypothèses fondamentales c'est que l'effet de bits de données est correctement corrigé. Toutefois, si ce n'est pas le cas, les détecteurs différentiels ne peuvent plus être considérés comme toujours préférables au détecteur NCD. Ce fait est particulièrement relevant pour l'acquisition des signaux modernes dans lesquelles les périodes de ses codes PRN sont égales aux périodes des bits de données. Néanmoins, ces signaux comprennent également un canal pilote qui peut être utilisé pour remédier à cet effet, sachant la phase de code secondaire. L'évaluation de la performance des détecteurs différentiels dans ce cas n'a pas été considérée dans cette thèse et, par conséquent, est également recommandé pour les travaux futurs.
 - En ce qui concerne la Détection Collective et les algorithmes proposés dans le chapitre 5, une analyse plus exhaustive de leurs performances véritables est encore nécessaire, en particulier dans des scénarios multi-constellation, car les résultats présentés ne peuvent pas être considérés comme entièrement concluants. Une analyse plus approfondie sera poursuivie au sein du groupe de recherche.
-

Également à prendre en considération dans l'avenir, c'est la combinaison des signaux dans des bandes de fréquences différentes.

- En ce qui concerne les algorithmes proposés pour la Détection Collective, il est également noté que les paramètres de configuration utilisés pour exécuter les algorithmes ont une influence importante sur leur performance globale (complexité, sensibilité, et erreur de positionnement). Une étude pour déterminer le meilleur choix des valeurs de ces paramètres de configuration doit également être effectuée pour le réglage optimal des algorithmes.

INTRODUCTION

Satellite navigation is a widespread technology in our days. The number of applications that depend on these signals is already remarkable and each year new markets, both for the masses and specialized, are appearing in which this technology becomes ingeniously useful. The systems that deliver this service are known as Global Navigation Satellite Systems (GNSS), including the United States' owned and notoriously famous Global Positioning System (GPS), the Russian GLONASS, and the European Galileo, among others. With the new applications that have been devised, new challenges have also risen which had not been foreseen in the beginnings of GPS and GNSS in general: much of the new demand for signals comes from urban environments where signal processing is outstandingly more complex than in open-air environments. In this thesis the issue of weak signal processing is analyzed, in particular at the first phase of the receiver signal processing chain, known as *signal acquisition*. The acquisition process is responsible for detecting the satellites visible to the receiver, therefore, if a missed detection occurs, the whole receiver processing can be affected, ultimately resulting in a failure in computing the user position.

The introduction to the thesis work starts by providing a brief overview of GNSS systems, including their working principle and a description of the currently available and future planned systems worldwide. Next, the role of acquisition within a GNSS receiver is briefly introduced, as well as the challenges that are currently faced by acquisition modules. In light of this, the thesis structure is described, highlighting the contributions provided at each chapter.

1.1 GNSS Systems Overview

1.1.1 Working Principle

Even though satellite navigation is a rather recent and complex technology, the mathematical concept on which it is based is fairly ancient and simple. The underlying principle is *trilateration*,

which suggests that a position in a given geometric space can be inferred by calculating distances to a number of points with a known position in this same space. The key equation in satellite navigation, known as the *navigation equation*, is then [1–4,24]:

$$\rho_i = r_i + c \cdot \Delta b = \sqrt{(x_i - x_u)^2 + (y_i - y_u)^2 + (z_i - z_u)^2} + c \cdot \Delta b \quad (1.1)$$

where ρ_i is known as the user's *pseudorange* to the satellite i , expressed as the sum of the geometric range between the user and the satellite, r_i , and the product of the user clock bias with respect to the GNSS constellation time, Δb , with the speed of light in the vacuum, c . The terms (x_i, y_i, z_i) and (x_u, y_u, z_u) stand for the satellite and user 3D coordinates, respectively. The inclusion of Δb in (1.1) is essential given the way through which the pseudorange is calculated:

$$\rho_i = c \cdot \tau_i \quad (1.2)$$

where τ_i represents the signal travel time between the satellite and the user. This equation will only provide directly the satellite-user geometric range if the receiver is synchronized with the satellites beforehand. As this condition cannot be assured to be met a priori, it is then necessary to introduce the receiver clock bias in (1.1) as an additional unknown to be determined. Therefore, the minimum number of satellites needed to determine the combined positioning + timing navigation solution is famously known as being four.

The estimation of the signal travel time for the calculation of the pseudoranges, is performed recurring to Direct Sequence Spread Spectrum (DSSS) techniques. A given Pseudorandom Noise (PRN) code is transmitted by each satellite and it is then up to the receiver to achieve synchronization with the satellites, by aligning its local code replicas with the codes contained in the incoming signal. The demodulation of the data contained in these signals then allows establishing the satellites' position at the signal time of transmission, compute correction terms to (1.1), and finally solve the set of navigation equations either through least-squares estimation or Kalman filtering [1–4,24].

1.1.2 GNSS Systems Worldwide

Various GNSS systems are operational and under deployment around the globe. These include the United States' (US) Global Positioning System (GPS), the Russian GLObal NAVigation Satellite System (GLONASS), the European Galileo, the Chinese BeiDou, the Japanese Quasi-Zenith Satellite System (QZSS), and the Indian Regional Navigational Satellite System (IRNSS). A brief overview of these systems, and their services and signals is provided next.

Global Positioning System (GPS) GPS is undisputedly the most well-known GNSS system worldwide. Launched in 1973 as a military program under the United States' (US) Department of Defense, it became fully operational in 1995. Until May 2000, civilian usage of the GPS signals was restricted due to the presence of Selective Availability, which was then discontinued by presidential mandate. Since then, the number of civilian GPS units has rapidly grown.

As of beginning 2014, the GPS constellation consists of 32 satellites arranged into 6 equally-spaced orbital planes at an altitude of approximately 20,200 km corresponding to a Medium Earth Orbit (MEO), which circle the Earth twice per day (Figure 1.1). Currently, three civil signals are being transmitted by GPS satellites, in three different frequency bands, and a fourth one will be included in the new generation of GPS satellites (these signals are described in detail in Tables A.1-A.4 in Annex A).

The most commonly used GPS signal is known as the GPS Coarse/Acquisition (C/A) signal, transmitted at the L1 spectrum band (1575.42 MHz). This signal is transmitted by all GPS satellites currently in orbit and is available for public use. Each satellite transmits a unique PRN Gold code of length 1023 chips, repeating itself every 1 ms. The navigation data contained in this signal is transmitted at a rate 20 times lower than the code period, meaning that each navigation data bit spans over 20 code periods of the PRN code.

One other signal that has also been transmitted since the origins of the GPS program, and is known as the Precise (P) code signal. Given that the actual P code is not directly transmitted, but a modified version by a Y code, this signal is usually referred to as the P(Y) signal. This code is not available for civilian users and is primarily used by the US military. This code is transmitted both on the L1 and L2 (1227.6 MHz) bands.

Three new civil signals have been conceived in the modernization phase of GPS undertaken since the early 2000s. The second civil signal, transmitted in the L2 band, and known as L2 Civil

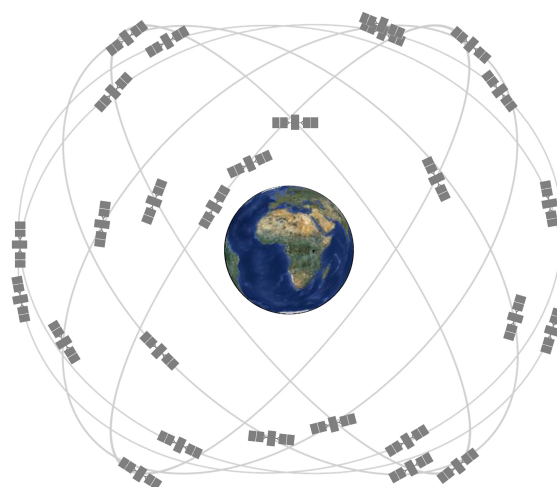


Figure 1.1 – Artist's impression of the GPS constellation [25]

(L2C) signal, started being transmitted in 2005 and as of December 2013 was broadcast by 11 satellites. The third civil signal is intended for support of safety-critical civil aviation operations and is transmitted at the L5 band (1176.45 MHz), a band highly protected for Aeronautical Radio Navigation Services. This signal started transmission in 2010 and is currently being transmitted by four GPS satellites. The fourth civil signal, also transmitted in the L1 band, and known as L1 Civil (L1C) was designed to enable interoperability between GPS and other GNSS systems. This signal is intended to start transmission in 2015.

All this and much more information about GPS can be found, for example, in [1–4, 24–28]

Global Navigation Satellite System (GLONASS) The GLONASS system was initially developed in the 1970s, simultaneously as GPS, and equally as a military program. After a first initial full operation capability of 24 satellites by 1995, the lack of funding by the Russian government led to a decay of the number of operational satellites, which reached a minimum of eight operational satellites by 2001. Renovated efforts by the Russian government to fund the GLONASS program reestablished a total of 23 operational spacecraft by April 2013. These satellites are placed in three orbital planes at an altitude of approximately 19,100 km (MEO).

While the legacy GLONASS satellites broadcast navigation signals in the L1 (standard and high accuracy signals) and L2 (high accuracy signal) bands, the modernized satellites will transmit in the L3/L5 band as well. Several signals are currently planned for these bands, both employing Frequency Division Multiple Access (FDMA) and Code Division Multiple Access (CDMA) for the shared spectrum between the different satellites [1, 29–31].

Galileo Recognizing the key role of GNSS applications in the present and future of European industry, the European Commission engaged itself on developing its own system, Galileo, the first system to be conceived and developed under civilian control. Once it is fully deployed, the complete Galileo constellation will consist of 30 satellites in three orbital planes at an approximate altitude of 23,200 km, completing an orbit around the Earth every 14 hours (Figure 1.2). As of the beginning of 2014, the Galileo constellation consists of four operational satellites.

Three main services will be provided by Galileo. The Galileo Open Service (OS) is a free-of-charge service suitable for mass-market applications and is accessible at the L1/E1 and E5 (1191.795 MHz) bands. This service can be used in single- or dual-frequency mode, providing enhanced accuracy in dual-frequency mode. The Public Regulate Service (PRS) shall provide position and timing restricted to government-authorized users and is intended for security and strategic infrastructure. This service is broadcast in the E1 and E6 (1278.75 MHz) bands. The third service, Commercial Service (CS), is aimed at market applications requiring higher performance than offered by the OS, providing added services as well, on payment of a fee. This service is based on the OS and is complemented by two signals at the E6 band (1278.75 MHz) (these signals are described in detail in

Tables A.1-A.4 in Annex A) [32–34].

BeiDou Navigation Satellite System (BDSS) The BDSS is equally a global system which in its full operating capability will incorporate 35 satellites (five in Geostationary orbit (GEO), 37 in MEO at an altitude of 21.528 km, and three in an inclined Geosynchronous orbit (GSO)). Two civil signals are currently described in the BDSS Interface Control Document, the B1I and B2I signals in the E2 (1561.098 MHz) and E5B (1207.14 MHz) bands. With a constellation of 14 operational systems, the system has been declared fully operational over the Asia-Pacific region since December 2012 [35, 36].

Indian Regional Navigational Satellite System (IRNSS) The IRNSS is an independent regional navigation satellite system that will consist of seven satellites (three satellites in GEO, and two satellites in GSO). The IRNSS will provide two signals in the L5 and S (2492.03 MHz) bands providing two services: the Standard Positioning Service for common civilian users, and the Restricted Service for special authorized users. The first satellite has been launched in July 2013 and the full constellation is expected to be deployed by 2016 [37, 38].

Quasi-Zenith Satellite System (QZSS) The QZSS system is under development by Japan and will be composed of satellites in quasi-zenith orbits, appropriate for signal reception over Japan. This system is intended to at first augment GPS with a four-satellite constellation by 2018, and to have in the future a full constellation of seven satellites. The QZSS system will provide signals similar to GPS's L1 C/A, L1C, L2C, and L5, as well as two augmentation signals, the Submeter-class Augmentation with Integrity Function (SAIF) in the L1 band and the L-band Experiment (LEX) in the L6/E6 band [39, 40].

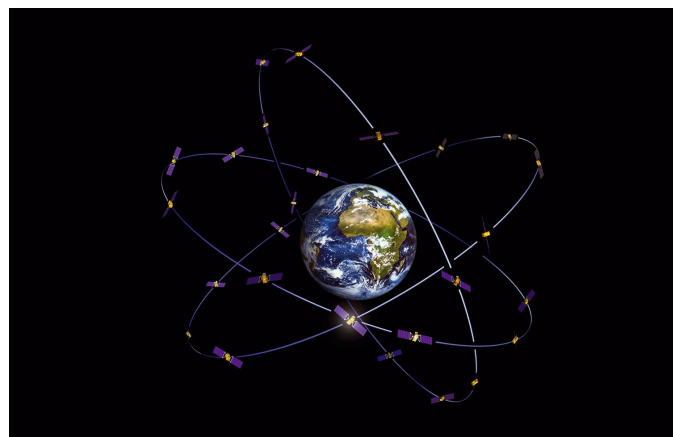


Figure 1.2 – Artist's impression of the Galileo constellation [32]

1.2 The Role of Acquisition in a GNSS Receiver

It was mentioned in section 1.1.1 that at the basis of the working principle of GNSS systems is the synchronization between the receiver and the different satellites. This synchronization is achieved through DSSS techniques, meaning that each satellite transmits a unique PRN code, which is locally generated at the receiver as well. For the demodulation of the data contained in the GNSS signals, it is essential that the locally generated replica be synchronized or *aligned* with the incoming signals with a maximum error of a small fraction of code chip. However, as seen in Tables A.1-A.4 in Annex A, the length of the codes employed in both GPS and Galileo signals is in the order of thousands of chips. If no apriori information is available to the receiver regarding the approximate phase of the incoming signals' codes, the code phase uncertainty to be considered by the receiver is the same as the code length. If a search for the correct phase is carried targeting directly the code alignment requirement for the data demodulation, the total number of possibilities will turn out to be excessively high.

One other option is that, instead of searching for the actual code phase directly employing the *fine* resolution, a first *coarse* search can be performed which is still capable of detecting the signal presence and estimating its approximate code phase. This way, the total number of possibilities will be more tractable, and after this first coarse signal detection, a fine synchronization system can be employed to initially refine the code phase estimation and subsequently maintain the alignment throughout the receiver operating time. The first coarse phase is commonly known as code or signal *acquisition*, and the second one as *tracking*.

One particularity of GNSS systems, with respect to other DSSS systems, is the fact that there is implicitly a large relative transmitter-receiver motion caused by the satellites orbital paths, which induces a *Doppler shift* on the received signal. For the synchronization to occur, it is also required that the receiver be able to demodulate the incoming signal with a frequency estimation error much lower than the uncertainty which is induced by the relative motion between the two communication ends. Once again, a coarse frequency search is employed in acquisition, prior to the refinement and maintenance through a loop in tracking.

This way, the main role of acquisition schemes in GNSS receivers is to provide coarse code phase and Doppler shift estimates of the incoming signals' true values. An in-depth introduction to the acquisition of GNSS signals is provided in Chapter 2 of this thesis.

1.3 21st Century Challenges for GNSS Applications

When GPS was first envisaged in the 1970s, it must surely have been impossible for its designers to foresee the challenges that would be raised to this technology more than 30 years later. What started off as a military project, is nowadays a vulgarized name among the general public, with millions of

users worldwide, who are generally unaware of the challenges of making this technology work in all kind of environments. From open-sky environments, with good visibility of the satellites and little or none obstructions to signal reception, the demand for GNSS signals is coming today from locations such as urban canyons, where not only the satellite visibility is impaired, but also the obstacles to the signal propagation are significant.

For the case of acquisition, in particular, what is most concerning is the *attenuation* of the signals prior to their reception. In Figure 1.3, a general illustration of the problem of signal reception in different environments is presented [41–43]. As can be seen in this image, the typical Carrier-to-Noise ratios (C/N_0), a measure of the signal power available to the receiver, is highly dependent on the signal reception scenario. As an example, a decrease by 30dB-Hz which can be verified going from a Line-of-Sight (LoS) environment (outdoors) to an indoor scenario, represents a drop of 1000 times in signal power.

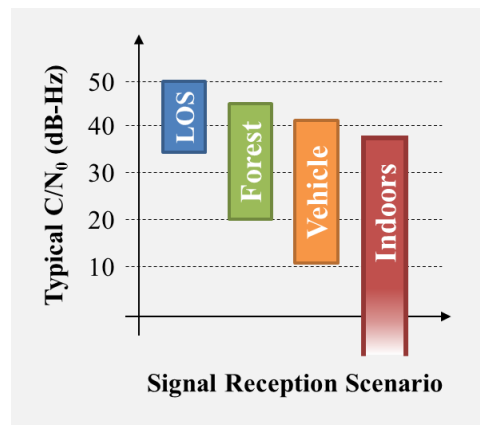


Figure 1.3 – Expected GNSS signal powers in different reception environments

These new requirements in the processing of signals weaker than their nominal signal powers have fostered research and innovation in the development of solutions for the various phases of GNSS signal processing within a receiver.

1.4 Thesis Objectives and Overview

This thesis addresses the acquisition of GNSS signals at signal powers lower than their nominal values, also known as *weak* signals. The techniques developed for the acquisition of weak signals are commonly referred to as *high-sensitivity* acquisition techniques.

The main objective of the research here described is to propose innovative solutions to the problems encountered in the state-of-the-art review which is carried in Chapter 2. Contributions in three different aspects of GNSS acquisition are presented in this thesis.

Analysis and Compensation of the Doppler Effect in GNSS Acquisition The Doppler shift that is expected to be experienced by a user is one of the main design drivers for the acquisition module for different GNSS applications. In particular, not only its value, but also its variation during the signal observation time is important. Three separate scenarios of application are considered for evaluation:

- The Doppler shift remains approximately unchanged during the acquisition time - *low-dynamics*;
- The Doppler shift changes during the acquisition time and a dynamic compensation of this change is not required to meet the user requirements - *medium-dynamics*;
- The Doppler shift changes during the acquisition time and a dynamic compensation of this change is required to meet the user requirements - *high-dynamics*;

For the first case, linked with receivers in which the receiver power constraints and the user's requirements dictate a fast acquisition time, a methodology to reduce the Doppler-induced sensitivity losses that are inherent of the fastest GNSS acquisition methods is proposed. For the second case, the analysis of a changing input Doppler frequency in the acquisition performance is assessed, and a formula to adapt the acquisition time to the expected user dynamics is proposed. The scenarios of application envisaged are space-based GNSS receivers, as well as urban environments. In fact, both scenarios have totally different characteristics, but they are shown to fall in the same category. Lastly, when the Doppler changes are significant to the point of impacting the user requirements, such as the case of indoor positioning, a proposal for a dynamic compensation of the incoming signal Doppler shift is described.

Sensitivity Characterization of Differential GNSS Detectors It will be seen that to reach the sensitivity levels required for some applications, different types of signal processing techniques will be required. After a first step of *coherent* signal integration, transition to post-coherent integration techniques is necessary. Two main postcoherent integration strategies are found in literature: *non-coherent* and *differential* integration. Differential integration has often been mentioned in literature as being the preferable choice, but an appropriate quantification of the sensitivity of detectors employing this structure was not found. Therefore, the main objective of this part of the research was the development of a formula which can be employed to fulfill this objective. The analysis carried confirms the previous results that differential detectors have the capacity to outperform noncoherent detectors in the acquisition of weak signals.

Systematic and Efficient Collective Acquisition of Multi-Constellation GNSS Signals The first two contributions of this thesis fall in the category of *standard* acquisition methods, implying that the acquisition of each signal visible to the receiver is carried independently of any other signal.

Collective Detection is an innovative approach for the simultaneous or *collective* processing of all signals in view to receiver. The base for this approach is that the search for satellites is carried in the user position-clock bias dimensions, mapping a candidate 4D point into the code phase search for each satellite. Several issues related to Collective Detection are addressed in this research. First, a methodology to improve the Collective Detection search process is proposed, by ensuring that a systematic and efficient search grid is established. Next, an hybridization of the proposed method with the standard (*sequential*) acquisition approach is also described, highlighting its potential in the acceleration of the Collective Detection method and in increasing its sensitivity. Finally, the application of this methodology in the context of a multi-constellation receiver is also addressed, by processing simultaneously GPS L1 C/A and Galileo E1 signals.

Thesis Structure The remainder of thesis is organized in 5 chapters. In Chapter 2, the problem of GNSS signals acquisition is formulated and a thorough review of the existing approaches in several different aspects of acquisition are analyzed. In light of this state-of-the-art review, the research objectives are also justified.

In chapters 3 to 5, the main contributions of this thesis are described. Finally, Chapter 6 concludes this thesis, and provides considerations about directions for future work based on the algorithms developed.

1.5 List of Publications

Publications in International Conferences

- P1** Sahmoudi, M., Esteves, P., Bousquet, M., Ries, L. and others. A New Frequency Offset Correction Approach for Enhancing Sensitivity of GNSS Receivers. In *Proceedings of the 24th International Technical Meeting of the Satellite Division of The Institute of Navigation (ION GNSS 2011)*, Portland, OR, USA, 2011.
- P2** Esteves, P., Sahmoudi, M., Ziedan, N. and Boucheret, M.-L. A New Adaptive Scheme of High-Sensitivity GNSS Acquisition in Presence of Large Doppler Shifts. In *Proceedings of the 25th International Technical Meeting of The Satellite Division of the Institute of Navigation (ION GNSS 2012)*, Nashville, TN, USA, 2012.
- P3** Esteves, P., Sahmoudi, M., Ries, L. and Boucheret, M.-L. Accurate Doppler-Shift Estimation for Increased Sensitivity of Computationally Efficient GNSS Acquisition. In *Proceedings of the European Navigation Conference (ENC 2013)*, Vienna, Austria, 2013.
- P4** Esteves, P. An Innovative and Efficient Frequency Estimation Method for GNSS Signals Acquisition. In *Proceedings of the 26th International Technical Meeting of The Satellite Division of*
-

the Institute of Navigation (ION GNSS 2013), Nashville, TN, USA, 2013.

P5 Esteves, P., Sahmoudi, M., Ries, L. and Boucheret, M.-L. An Efficient Implementation of Collective Detection Applied in a Combined GPS-Galileo Receiver. In *Proceedings of the 6th European Workshop on GNSS Signals and Signal Processing (SIGNALS 2013)*, Neubiberg, Germany, 2013.

Publications in International Journals/Magazines

P6 Esteves, P., Sahmoudi, M. and Boucheret, M.-L. Sensitivity Characterization of Differential Detectors for Acquisition of Weak GNSS Signals. *Submitted (March 2013) to IEEE Transactions in Aerospace and Electronic Systems*. In second revision.

P7 Esteves, P., Sahmoudi, M. and Ries, L. Vector Acquisition for Improving Sensitivity and Combining Multi-GNSS Signals. *To appear in Inside GNSS in 2014*.

Awards in International Conferences

- Best Young Scientist Presentation Award (ENC 2013) for publication P3
- Best Student Paper Award (ION GNSS 2013) for publication P4

PRINCIPLES OF GNSS SIGNAL ACQUISITION

In this section, the principles of GNSS Signal Acquisition are discussed. In section 2.1, the acquisition problem is formulated, describing its role within the receiver signal processing chain, and posing it as a combined estimation/detection problem, from which the fundamental structure of GNSS acquisition schemes is derived. In sections 2.2 and 2.3, the two main building blocks of the fundamental acquisition structure, the correlation and detector blocks, are discussed in detail, reviewing the state-of-the-art of each one and providing a comparison of the main existing approaches. The remainder of this chapter deals with other important aspects to consider in GNSS signal acquisition, such as Assisted-GNSS techniques (section 2.4), the impact of the modern signals in acquisition (section 2.5), and approaches for sensitivity enhancement by making use of (combining) more than one channel in acquisition (section 2.6). Section 2.7 justifies, in the light of the state-of-the-art debated in this section, the research topics that were pursued during this doctoral research.

2.1 Problem Formulation

Satellite-receiver synchronization in GNSS systems is achieved through a Direct Sequence Spread Spectrum (DSSS) link [1–4]. In DSSS communication systems, a waveform $c(t)$, known as the *direct sequence modulation*, is obtained by linear modulation of a Pseudorandom Noise (PRN) code, c_n , over a sequence of pulses, $p(\cdot)$, commonly known as chips, with a duration T_{chip} [5, 16]:

$$c(t) = \sum_n c_n p(t - nT_{chip}) \quad (2.1)$$

This waveform is then used to modulate a binary data sequence, $d(t) = \pm 1$, typically at a much lower rate than $c(t)$, and the resulting sequence is modulated into a carrier at a carrier frequency, f_c , and power P_t :

$$s(t) = \sqrt{2P_t} d(t) c(t) \cos(2\pi f_c t) \quad (2.2)$$

This modulation form is known as *binary phase-shift keying* (BPSK), and this signal structure is widely recognized as the structure of the GPS L1 C/A signal [1–4]. This signal structure is the basis for most of current and planned GNSS signals, and is considered as the signal model to be treated in this section. From (2.2), the complex signal at the output of a GNSS receiver front-end, $r(t)$, can be written as:

$$r(t) = \sum_{i \in \mathcal{S}_v} \sqrt{P_i(t)} d_i(t - \tau_i) c_i(t - \tau_i) e^{j\{2\pi(f_{IF} + f_{d_i})t + \phi_i\}} + w(t) \quad (2.3)$$

where \mathcal{S}_v represents the set of all satellites in view, $P_i(t)$ is the received instantaneous signal power from satellite i , τ_i is the signal time delay due to its transit between the satellite and the receiver, f_{IF} is the receiver intermediate frequency set by its front-end, f_{d_i} is the signal Doppler shift perceived by the receiver, ϕ_i is the signal carrier phase, and $w(t)$ is the noise component in the received signal.

For the great majority of GNSS signals, including the current and planned GPS and Galileo ones, the PRN codes adopted are also chosen in order to provide multiple-access communication in the code domain (Code Division Multiple Access, CDMA) capabilities [1–4]. This way, all satellites in a given constellation transmit at the same central frequencies, and the satellite identification at the receiver is achieved through the despreading of the satellites' unique assigned PRN code. The auto- and cross-correlation properties of the PRN codes employed define the reliability of correct identification of the present signal. Except for the case when the signal strengths from different satellites are highly disproportionate, the different signals within the same band can be considered orthogonal and when focusing on the processing of a single received signal, k , (2.3) can be rewritten as:

$$r(t) = \sqrt{P_k(t)} d_k(t - \tau_k) c_k(t - \tau_k) e^{j\{2\pi(f_{IF} + f_{d_k})t + \phi_k\}} + \tilde{w}(t) \quad (2.4)$$

The new noise term, $\tilde{w}(t)$, comprises both the thermal noise component, $w(t)$, and the results of cross-correlation between $c_k(t)$ and the codes of signals of other satellites in visibility. For most of the cases, nevertheless, the additional cross-correlation noise term can be disregarded with respect to the thermal noise component due to the extremely low power of the incoming signals. This way, throughout this thesis, $w(t)$ is assumed to be a zero-mean additive white Gaussian (AWGN) process. In reality $w(t)$ is neither Gaussian nor white, but the Gaussian approximation is justified by the central limit theorem and is found to be accurate in practice for the acquisition purpose of

coarse estimation of signal parameters [6].

The main focus of this thesis is on signal processing in software-defined receivers (SDR), so the digital counterpart of (2.4) will instead be considered. By sampling the incoming signal at a sampling frequency f_s this equation becomes:

$$r[n] = \sqrt{P_k[nT_s]} d_k[nT_s - \tau_k] c_k[nT_s - \tau_k] e^{j2\pi(f_{IF} + f_{d_k})nT_s + \phi_k} + w[nT_s] \quad (2.5)$$

where $T_s = 1/f_s$ is the sampling period. This way, the probability distribution of the sampled complex noise term, $w[nT_s]$, is given by:

$$p(\Re\{w\}, \Im\{w\}) = \frac{1}{2\pi\sigma^2} \exp\left(-\frac{\Re\{w\}}{2\sigma^2} - \frac{\Im\{w\}}{2\sigma^2}\right) \quad (2.6)$$

where $\Re\{w\}$ and $\Im\{w\}$ denote, respectively, the real and imaginary parts of $w[\cdot]$, and the noise variance, σ^2 , is given by:

$$\sigma^2 = E\{\Re\{w\}^2\} = E\{\Im\{w\}^2\} = \mathcal{N}_0 B \quad (2.7)$$

with $E\{\cdot\}$ the operator for the expectation value, $\mathcal{N}_0 = k_B T_0$ the single-sided noise power spectral density, with k_B the Boltzmann constant and T_0 the noise temperature, and $B \approx f_s$ the front-end filter bandwidth [16, 17]. The signal transit time can also be expressed as function of the sampling period as:

$$\tau_k = N_{codes} T_{code} + \zeta_k T_s \quad (2.8)$$

where N_{codes} represents the number of code periods occurring during the signal transit time, T_{code} is the PRN code duration, and ζ_k is the code phase offset measured in samples and that can take any value in the range $[0, N_s - 1]$, N_s being the number of samples within a code period. In (2.8) there are two unknowns, N_{codes} and ζ_k , however, given the periodicity of the PRN code, the receiver does not need to calculate the number of code repetitions in the signal propagation path to achieve synchronization with the satellite (it may, nevertheless, require this number of repetitions in further phases of the signal processing chain). Finally, the received signal can be rewritten as:

$$r[n] = \sqrt{P_k[nT_s]} d_k[(n - \zeta_k)T_s] c_k[(n - \zeta_k)T_s] e^{j2\pi(f_{IF} + f_{d_k})nT_s + \phi_k} + w[nT_s] \quad (2.9)$$

According to this signal model, upon reception of a given GNSS signal, the unknown signal parameters to the receiver are:

1. The satellite ID, k ;
2. The instantaneous signal power, P_k ;
3. The current data bit value, d_k ;
4. The code phase offset, ζ_k ;
5. The Doppler offset, f_{d_k} ; and
6. The signal phase, ϕ_k .

Estimation of these parameters is required for the satellite-receiver synchronization to happen and in typical GNSS receivers takes place in two phases. The first phase is a coarse synchronization phase, *acquisition*, and the second a fine tuning process, *tracking*. Within the acquisition phase the receiver must generate estimates of the unknown parameters with limited or no a priori information about their values, and the acquisition process can be seen as an estimation problem. Furthermore, in the search for the satellite identifier, the receiver may have no a priori information about the presence of the signal from this particular satellite. This way, acquisition becomes a combined *estimation/detection* problem [6, 7, 44].

The next sections detail the estimation and detection formulations of the GNSS acquisition problem, and, based on these categorizations, the fundamental structure of GNSS acquisition schemes is introduced at the last section.

2.1.1 Acquisition as an Estimation Problem

From the unknown signal parameters previously listed, only the code phases, ζ , and Doppler offsets, f_d , of the incoming signals are usually attempted to be estimated at the acquisition stage, jointly with the satellite IDs. Let $\boldsymbol{\theta} = [\zeta, f_d]$ represent this set of parameters, and $\hat{\boldsymbol{\theta}}$ its estimates. Given that the signal model is known, but not its parameters, in GNSS SDR receivers these estimates are generated through the analysis of a sequence of observations of the input signal, $\mathbf{r} = \{r_0, r_1, \dots, r_{N-1}\}$, where N denotes the number of observations or *samples*. A cost function suitable for this purpose can be derived from the Probability Density Function (PDF) of the received signal conditioned on its estimated parameters, $f_{\mathbf{r}|\hat{\boldsymbol{\theta}}}(\mathbf{r}|\hat{\boldsymbol{\theta}})$. This PDF is effectively a measure of the likelihood that the true parameter vector is $\hat{\boldsymbol{\theta}}$ given that the observation vector is \mathbf{r} , and as so it is referred to as the *likelihood function*. The most straightforward estimation technique in this case is *Maximum Likelihood (ML) estimation*, through which the estimate, $\hat{\boldsymbol{\theta}}_{ML}$, is obtained as [6, 16]:

$$\hat{\boldsymbol{\theta}}_{ML} = \arg \max_{\hat{\boldsymbol{\theta}}} f_{\mathbf{r}|\hat{\boldsymbol{\theta}}}(\mathbf{r}|\hat{\boldsymbol{\theta}}) \quad (2.10)$$

From the likelihood function, a sufficient statistic, $D_k(\hat{\boldsymbol{\theta}})$, can be defined, containing the same information as this one and that is maximum for the same set of parameters, $\hat{\boldsymbol{\theta}}_{ML}$ [6, 16]. A suitable expression for $D_k(\hat{\boldsymbol{\theta}})$ for the GNSS acquisition estimation problem was derived in [44] for an analogue receiver, and its discrete-time equivalent is shown in [6] to be given by:

$$D_k(\hat{\boldsymbol{\theta}}) = |\mathbf{r} \cdot \mathbf{s}_k(\hat{\boldsymbol{\theta}})|^2 \quad (2.11)$$

where $\mathbf{s}_k(\hat{\boldsymbol{\theta}}) = \{c_k[(n - \hat{\zeta}_k)T_s] \exp\{-j2\pi(f_{IF} + \hat{f}_{d_k})nT_s\}\}$. The operation of multiplying the incoming signal with a replica of its presumed code represents a *correlation* operation and is a fundamental operation in DSSS communications [5, 16]. Historically, the correlation operation is performed by *matched filters*, which, by definition, is the optimal linear filter for maximizing the Signal-to-Noise Ratio (SNR) in the presence of additive noise [5, 16]. The process of correlation in GNSS signal acquisition is analyzed in detail in section 2.2.

Nevertheless, if acquisition is treated merely as an estimation problem, there is no guarantee that the ML estimate corresponds to the best approximation to the true signal parameters, as the signal under test may not even be present, in which case this estimate corresponds simply to the noise peak. A second step is then necessary which evaluates if this estimate can be reliably associated to a signal, by testing the presence or absence of this same signal.

2.1.2 Acquisition as a Detection Problem

Once the sufficient statistic has been generated for the code phase and Doppler offset combinations under test, these statistics are then used to decide on the presence or absence of signal. In this case, the sufficient statistic is known as the *detection metric*, as it is fed into a detection scheme, or detector, that performs a binary hypothesis test. Let H_0 denote the *null hypothesis*, corresponding to the situation in which the signal is absent, and H_1 the *alternate hypothesis*, corresponding to the situation in which the signal is actually present [5, 6, 16]. According to these hypotheses, the detector can take one of two decisions:

- Decision D_0 – the decision that H_0 is true; and
- Decision D_1 – the decision that H_1 is true.

From these decisions, there are four possible outcomes of the detection test:

1. Correct rejection – Decision D_0 given that H_0 is true;
-

-
2. Missed detection – Decision D_0 given that H_1 is true;
 3. False alarm – Decision D_1 given that H_0 is true; and
 4. Correct detection – Decision D_1 given that H_1 is true.

Correspondingly, four probabilities are defined, which represent the main measures of performance of a detection scheme:

1. Probability of correct rejection – P_r ;
2. Probability of missed detection – P_m ;
3. Probability of false alarm – P_{fa} ; and
4. Probability of correct detection – P_d .

For an optimal choice between the two possible decisions, several criteria can be employed. These include the Neyman-Pearson criterion, in which the detection is made to maximize the probability of detection under the constraint that the probability of false alarm does not exceed a predefined value, the Bayes minimum cost criterion, and maximization of the probability of correct decision, among others [45]. Regardless, optimization under any of these criteria leads to the Likelihood Ratio Test (LRT) [45]:

$$\Lambda(\mathbf{r}) = \frac{f_{\mathbf{r}|H_1}(\mathbf{r}|H_1)}{f_{\mathbf{r}|H_0}(\mathbf{r}|H_0)} \underset{D_0}{\overset{D_1}{\gtrless}} \eta \quad (2.12)$$

where $\Lambda(\mathbf{r})$ is known as the likelihood ratio of vector \mathbf{r} and, if its value exceeds the detection threshold η , then the decision D_1 is made, while if it does not, the decision D_0 is instead chosen.

At this point the detection and estimation natures of the acquisition process converge as the likelihood function of \mathbf{r} conditioned to the H_1 hypothesis, $f_{\mathbf{r}|H_1}(\mathbf{r}|H_1)$ is inherently dependent of the estimate of the unknown signal parameters, $\hat{\boldsymbol{\theta}}$. In this case the Generalized Likelihood Ratio Test (GLRT) is employed, which can be expressed as [6]:

$$\Lambda_g(\mathbf{r}) = \max_{\hat{\boldsymbol{\theta}}} \frac{f_{\mathbf{r}|H_1, \hat{\boldsymbol{\theta}}}(\mathbf{r}|H_1, \hat{\boldsymbol{\theta}})}{f_{\mathbf{r}|H_0}(\mathbf{r}|H_0)} = \max_{\hat{\boldsymbol{\theta}}} \Lambda(\mathbf{r}|\hat{\boldsymbol{\theta}}) = \Lambda(\mathbf{r}|\hat{\boldsymbol{\theta}}_{ML}) \quad (2.13)$$

Given that the distribution of the received signal vector under H_0 is independent of the signal parameter vector, the evaluation of the LRT can be directly related to the detection metric as:

$$D_k(\hat{\boldsymbol{\theta}}_{ML}) \underset{D_0}{\overset{D_1}{\gtrless}} \eta \quad (2.14)$$

According to (2.13) and (2.14), acquisition of GNSS signals can be seen as a two-step process. First, the detection metric is calculated for all the unknown parameters' combinations in the uncertainty search space of interest, and the combination which provides the highest detection metric is chosen as $\hat{\boldsymbol{\theta}}_{ML}$. Then, this value is compared to a predefined threshold and, based on the result of this comparison, a decision about signal presence is made.

The threshold setting process in GNSS acquisition is usually done according to the Neyman-Pearson criterion, that is, the probability of detection is attempted to be maximized for a given, fixed false alarm probability. For this, knowledge of the PDF of the detection metric under both hypotheses is required. The detection threshold can then be calculated according to [5, 6, 16]:

$$P_{fa} = \int_{\eta}^{\infty} f_{D_k(\hat{\boldsymbol{\theta}}|H_0)}(x|H_0) \cdot dx \quad (2.15)$$

and the probability of detecting a given signal is subsequently given by:

$$P_d = \int_{\eta}^{\infty} f_{D_k(\hat{\boldsymbol{\theta}}|H_1)}(x|H_1) \cdot dx \quad (2.16)$$

These two equations are the basis for the comparison of the performance of different detector forms in the presence of a given signal, as will be seen in section 2.3. One other approach that is often followed in the detection of GNSS signals is to define a *peak-to-peak ratio* detection threshold [4, 46, 47]. Although the peak-to-peak ratio approach offers a quick and intuitive method for deciding on signal presence, it is not as widespread as the threshold setting through 2.15, and it is also shown in [47] not to offer advantages over this one.

2.1.3 Fundamental Structure of GNSS Acquisition Schemes

According to the estimation/detection formulation of the GNSS acquisition problem described in the previous sections, the core or fundamental structure of GNSS acquisition schemes can now be introduced. The two main building blocks of GNSS acquisition schemes are shown in the diagram of Figure 2.1 [5–7]. The blocks shown in this figure are:

- **Correlation block** - this block is responsible for scanning the whole unknown parameters search space, generating for each different candidate set of parameters a metric that is function of its values. The metric to be generated, also known as the correlation output, corresponds to the product of the two vectors \mathbf{r}_n and $\mathbf{s}_{k,n}(\hat{\boldsymbol{\theta}})$ in 2.11, representing the demodulation of the input signal, and the correlation of its code with a locally generated and circularly-
-

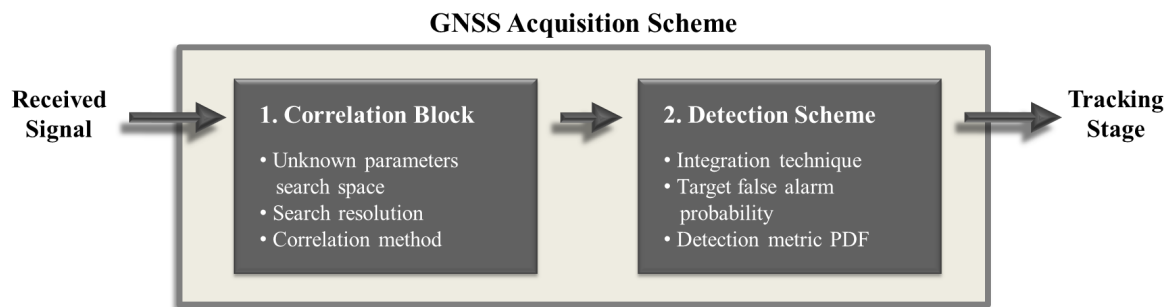


Figure 2.1 – Fundamental GNSS acquisition scheme structure

shifted replica. The search space scanning can be performed in several different ways, employing for this different correlation or acquisition methods. This block is analyzed in detail in section 2.2.

- **Detector or Detection Scheme** - the detector generates a test or detection metric from the output of the correlation block, which allows deciding on the presence of the signal from the satellite under test. Different types of signal integration techniques can be applied in the search for signals at a lower signal strength than at the nominal case (weak signals), which may be more or less effective depending on the signal structure and expected parameters. This block is analyzed in detail in section 2.3.

Naturally, most GNSS acquisition schemes found in literature include additional features, such as data preprocessing [9, 48–50], multi-trial detection [1, 5, 51], feedback loops [17, 52], fusion with other data sources [53, 54], inclusion of additional blocks to refine the coarse estimates before the handover to tracking [3, 55], among others. Nevertheless, the core elements of these acquisition schemes are invariably the ones represented in Figure 2.1.

As so, the following sections are dedicated to the analysis of these two fundamental blocks and the specific variations of interest will be addressed later on. Given the specific function carried by each block, different metrics are defined to characterize their performance. Therefore, instead of characterizing the performance of the GNSS acquisition scheme as a whole, it is more appropriate to characterize each block individually. Sections 2.2 and 2.3 describe in detail these two blocks, defining their individual metrics of performance, and reviewing the most relevant approaches proposed for each one in literature.

2.2 Correlation Methods

The acquisition of GNSS signals implies the coarse estimation of the available signals' code phase and Doppler offset, in what is the first step of the synchronization between the receiver and the

satellites in view. These parameters are continuous variables, and therefore the 2-dimensional (2D) search space of all their possible combinations consists of an infinity of options. The approach usually followed is to define a search grid to cover this 2D space in which only a finite number of points are evaluated, as shown in Figure 2.2. The possible combinations of ζ and f_d in this search grid are denoted as *search cells*, and the search cell which best approximates the true parameters' values is referred to as the correct, or H_1 , cell. In Figure 2.2, $\Delta\Sigma$ and ΔF_d represent the code phase and Doppler offset uncertainty range, respectively, and $\delta\zeta$ and δf_d are the search grid resolution for each parameter. Each search cell consists then of a candidate code phase, $\hat{\zeta}_i = i \cdot \delta\zeta$, and Doppler shift, $\hat{f}_{d_j} = j \cdot \delta f_d - \Delta F_d/2$.

When no a priori information about the true values of these parameters is available, all search cells covering their entire uncertainty range must be tested in the estimation process. This survey of the search grid is accomplished by the *correlation* block. According to 2.11, the correlation output for satellite k for a given candidate set of parameters, $\hat{\zeta}$ and \hat{f}_d , is obtained as:

$$S_k(\hat{\zeta}, \hat{f}_d) = \mathbf{r} \cdot \mathbf{s}_k(\hat{\zeta}, \hat{f}_d) = \sum_{n=0}^{N-1} r[n] \cdot c_k[(n - \hat{\zeta})T_s] e^{-j2\pi(f_{IF} + \hat{f}_d)nT_s} \quad (2.17)$$

As this operation must be repeated for each search cell, and given the typical lengths of the PRN codes present in GNSS signals, the correlation process is the most computationally demanding operation within acquisition. It is therefore desirable to execute the correlation operations by performing the least number of operations possible, both optimizing the computational effort and reducing the delay introduced by this search process. This is the main objective of the different *correlation methods* that are found in literature.

In the definition of the acquisition search grid it must be ensured that a search cell *sufficiently close* to the true parameter values is included. Denoting by $\Delta\zeta = \zeta - \hat{\zeta}$ and $\Delta f_d = f_d - \hat{f}_d$ the errors in the estimation of the two parameters, the maximum estimation error that may be incurred at the

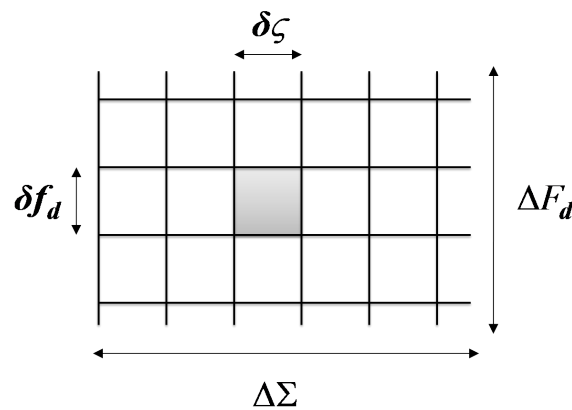


Figure 2.2 – Acquisition Search Grid

H_1 search cell is half of the search grid resolution, that is, $\Delta x_{H_1, \max} = \delta x/2$. Therefore, the search resolutions for each parameter must be decided taking into account the effect of their worst-case estimation errors on the correlation output at the H_1 search cell. This constraint in acquisition represents a well-known trade-off between computational complexity and associated sensitivity losses that will be constantly referred to throughout this thesis.

Code Search For the code phase dimension, the number of code phases to be tested, N_ζ , is equal to the number of samples per code period, N_s , typically a multiple of the number of chips per code, N_{code} . The ratio between N_s and N_{code} is known as the oversampling factor, osf , and is an important design parameter in GNSS receivers. The oversampling factor is directly the inverse of the resolution in the code delay, so $\Delta \zeta_{H_1, \max} = 1/(2 \cdot osf)$. This relation implies that the oversampling factor must be chosen according to the autocorrelation function of the signals under test, in order to constrain the attenuation of the correlation output at the H_1 cell to tolerable values. In Figure 2.3, the autocorrelation functions of the BPSK and BOC(1,1) modulations are shown [1, 4, 33, 56].

In this figure, the much sharper correlation peak of BOC(1,1) with respect to the one of BPSK is clearly remarked. This way, while an oversampling factor of 2 (corresponding to $\Delta \zeta_{H_1, \max} = 1/4$ chip) may be employed in acquisition of signals employing the BPSK modulation (GPS L1 C/A, for example), this oversampling factor will hardly be considered appropriate for the acquisition of signals employing BOC(1,1), as an estimation error of 1/4 of chip leads to a significant attenuation of the correlation output, and higher values of osf must be chosen. According to the autocorrelation functions depicted in Figure 2.3, an osf of 4 ensures roughly the same attenuation of the correlation peak as an osf of 2 for the BPSK modulation. Further discussion about new signal modulations is provided in section 2.5.

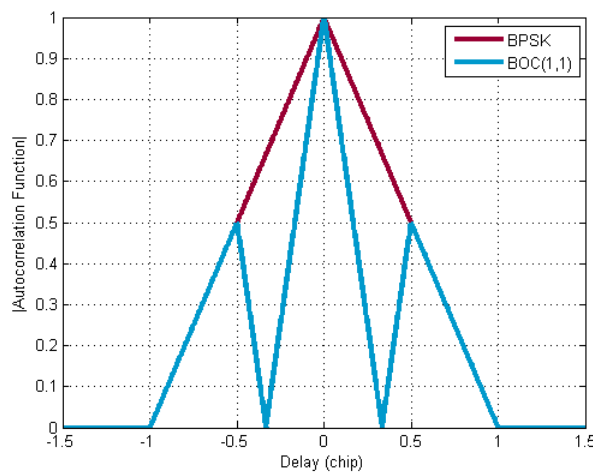


Figure 2.3 – BPSK and BOC(1,1) autocorrelation function (absolute value)

Frequency Search For the Doppler offset search the same approach as for the code phase is followed. That is, the search grid resolution is defined according to the maximum tolerable attenuation of the correlation output due to the maximum estimation error of the Doppler shift at the H_1 cell, $\Delta f_{d,H_1,\max}$. According to (2.17), assuming that the navigation data bit and signal power remain constant throughout the observation time, the module of $S_k(\hat{\zeta}, \hat{f}_d)$ results as:

$$\begin{aligned}
|S_k(\hat{\zeta}, \hat{f}_d)| &= \left| \sum_{n=0}^{N-1} r[n] \cdot c_k[(n - \hat{\zeta})T_s] e^{\{-j2\pi(f_{IF} + \hat{f}_d)nT_s\}} \right| \quad (2.18) \\
&= \sqrt{P_k} \left| \sum_{n=0}^{N-1} c_k[(n - \zeta)T_s] c_k[(n - \hat{\zeta})T_s] \cdot e^{\{j2\pi(f_c + f_{d_k})nT_s + \phi_k\}} e^{\{-j2\pi(f_c + \hat{f}_d)nT_s\}} + \tilde{w}[n] \right| \\
&= \sqrt{P_k} \left| \sum_{n=0}^{N-1} c_k[(n - \zeta_k)T_s] c_k[(n - \hat{\zeta})T_s] e^{\{j2\pi(\Delta f_d)nT_s\}} + \tilde{w}[n] \right| \\
&\approx \sqrt{P_k} N |R(\Delta\zeta)| \left| \text{sinc}(\Delta f_d N T_s) \right| + \tilde{w}_N
\end{aligned}$$

where $R(\Delta\zeta)$ represents the autocorrelation function of $c_k[n]$ evaluated at the relative code phase offset $\Delta\zeta$, and $\text{sinc}(x) = \sin(\pi x)/(\pi x)$. It should be noted that the last passage is an approximation only valid in the vicinity of the signal's true parameters [57].

According to (2.18), any frequency estimation error is translated into the correlation output as an attenuation through the sinc function. Therefore, the maximum loss of the correlation output due to the Doppler estimation error at search cell H_1 is:

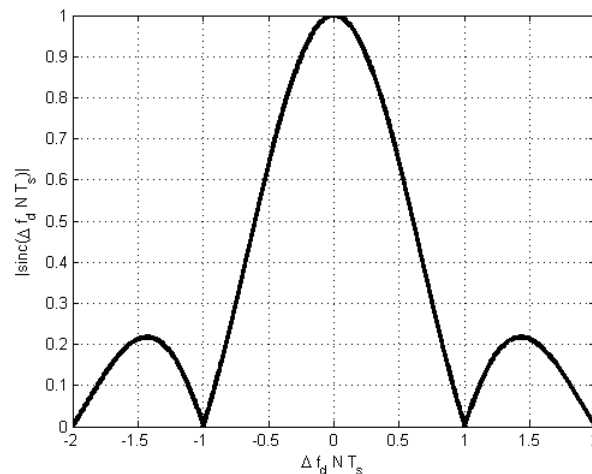


Figure 2.4 – Correlation output frequency response as function of the Doppler estimation error - $|\text{sinc}(\Delta f_d N T_s)|$

$$L_{\Delta f_d, H_1, \max} = 10 \log_{10} \left| \text{sinc}(\delta f_d / 2 \cdot N T_s) \right| \quad (2.19)$$

where $\delta f_d / 2$ (half of the Doppler bin) represents the maximum Doppler estimation error at the H_1 cell. This loss is shown in Figure 2.4 as function of the product $\Delta f_d N T_s$. This relation implies that the maximum allowable Doppler offset estimation error must be weighed with the product $N T_s$. Some rules of thumb for choosing the Doppler search resolution are:

- $L_{\Delta f_d, H_1, \max} = 0.45 \text{ dB} \Rightarrow \delta f_d = 1 / (2 N T_s)$
- $L_{\Delta f_d, H_1, \max} = 0.81 \text{ dB} \Rightarrow \delta f_d = 2 / (3 N T_s)$
- $L_{\Delta f_d, H_1, \max} = 1.96 \text{ dB} \Rightarrow \delta f_d = 1 / (N T_s)$

The number of search bins to be scanned in the Doppler search, N_{f_d} , is finally obtained as the ratio between the uncertainty in the Doppler dimension and the chosen grid resolution. The total number of search cells to be scanned within acquisition is therefore $N_{f_d} \times N_s$, and can reach values in the order of 10^6 points in the most current GNSS applications. Emphasis is then placed on the receiver's processor capability to scan this large search space as quickly as possible. This way, for each correlation method presented, its computational complexity will be assessed for the comparison in the last section. It will also be seen that in some correlation methods the flexibility to freely set the Doppler frequency search resolution is lost, which may pose an issue when dealing with signals at a lower signal strength. This will therefore also be taken into account in the comparison between the different methods.

The correlation methods presented next are: Serial Search (SS), Parallel Frequency Search (PFS), Parallel Code Search (PCS) [3, 4, 8], Spectral Shifting with Doppler Pre-processing (here referred to as Bi-Dimensional Parallel Search, BPS) [13–15], and the Double Block Zero Padding (DBZP) [9–12]. Although other correlation methods can be found in literature, such as [58–67], these are considered as representative of the state-of-the-art. These methods can be divided in two categories: the SS method is a Time-Domain acquisition method, while all others are grouped as Frequency-Domain acquisition methods, as they make use of the Fast Fourier Transform (FFT) for computational complexity reduction. The next two sections will detail the algorithm of these correlation methods, and their relative performance compared afterwards. The results shown in this section have been published in [68].

2.2.1 Time-Domain Acquisition

The simplest GNSS correlation method is the so-called Serial Search (SS) or time-domain acquisition method, corresponding to the direct implementation of (2.17) [3, 4, 7]. The block diagram

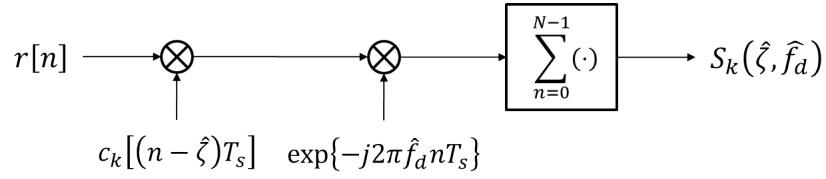


Figure 2.5 – Serial Search Correlation Method Architecture

of this method is shown in Figure 2.5. The SS method tests the different search cells sequentially one at a time, employing the above structure. As so, the total number of operations required to scan the entire search space with this method is of the order of $N_{f_d}N_s^2$ operations. Given that $N_{f_d} = \Delta F_d / \delta f_d \propto N_s$, it results that the number of operations required to evaluate all possible code phases employing time-domain acquisition is of the order of N_s^3 . This cubic dependence with the number of samples per code period is highly undesirable, given the typical values of N_s . In order to reduce the acquisition search complexity, frequency-domain acquisition techniques have been developed and are introduced next.

2.2.2 Frequency-Domain Acquisition

Frequency-domain acquisition methods rely on the Fast Fourier Transform (FFT) for reducing the number of operations required to search the whole uncertainty region for the two unknown parameters [3, 4, 7, 8]. These methods can be further sub-divided into three groups:

1. FFT taken over data blocks longer than the equivalent to one code period;
2. FFT taken over data blocks equivalent to one code period;
3. FFT taken over data blocks shorter than the equivalent to one code period;

The need for analyzing data blocks longer than the equivalent to one period of the PRN spreading code rises when the signals to be detected are at a signal strength lower than its nominal value (weak signals), and will be further justified in section 2.3. For the moment, we focus exclusively on the need of processing (correlating) signal observation blocks whose length, N , is a multiple of N_s . Well-known correlation methods found in literature and representative of each of the three sub-groups are described next.

1. FFT over multiple code periods Two main frequency-domain acquisition methods fall in this category, in particular the Parallel Frequency Search (PFS) and Parallel Code Search (PCS) methods [3, 4, 7, 8]. As the names point out, these correlation methods perform the search in one dimension serially, and the search in the other dimension in parallel, through usage of the FFT.

A schematic representation of the PFS acquisition method is shown in Figure 2.6. According to

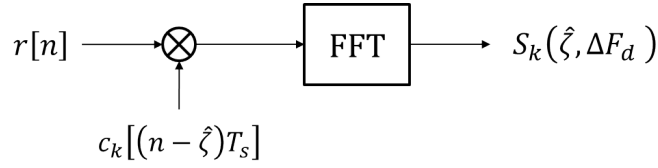


Figure 2.6 – Parallel Frequency Search method block diagram

the block diagram shown in this figure, the PFS scheme starts by despreading the incoming signal code, and, once the correct code phase is used at this operation, the resulting waveform consists exclusively of a carrier at the Doppler-affected frequency, which can be perceived through analysis by FFT. The step-by-step execution of the PFS method and the number of operations required for each step are shown in Table 2.1. The number of operations required for the execution of a FFT of size N is considered to be approximately $5N \cdot \log_2(N)$, requiring for that that N be zero-padded until the next power of 2 [15].

According to the number of operations required for each of the execution steps shown in Table 2.1, a computational gain with respect to the SS scheme is obtained with this method, as its dependency with N_s is $N_s^2 \cdot \log_2(N_s)$, therefore lower than N_s^3 . It should also be noted that, by performing the frequency estimation through FFT, the frequency resolution obtained with this method is intrinsically limited to:

$$\delta f_d = \frac{f_s}{N} = \frac{1}{NT_s} \quad (2.20)$$

which means that, unlike the case of the SS scheme, the frequency grid resolution for this method is automatically fixed by the data set length. According to the formula for the correlation output attenuation due to the Doppler offset estimation error, it then results that the maximum Doppler-induced attenuation losses of the PFS method at the H_1 cell are:

$$L_{\Delta f_d, H_1, \max, \text{PFS}} = 10 \log_{10} \left| \text{sinc}(\delta f_d / 2 \cdot NT_s) \right| = 10 \log_{10} |\text{sinc}(1/2)| = 1.96 \text{dB} \quad (2.21)$$

Table 2.1 – Step-by-step execution of the PFS method

| Step | Number of Operations |
|---|---------------------------------|
| 1 - Code despreading | N |
| 2 - FFT over whole data block | $5N \cdot \log_2(N)$ |
| 3 - Repeat step 1 and 2 for each code phase | $N_s \times (1 \text{ and } 2)$ |

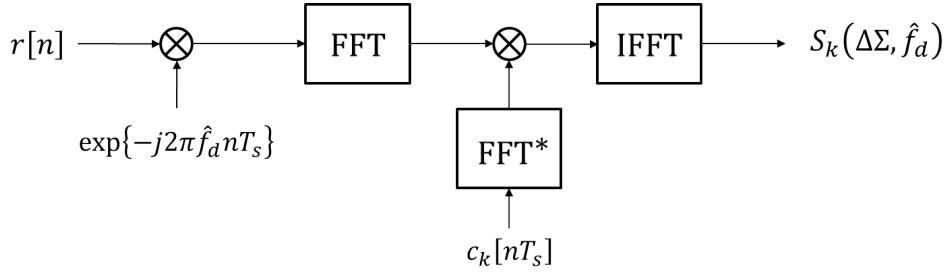


Figure 2.7 – Parallel Code Search method block diagram

This worst-case situation occurs when the Doppler offset falls exactly in the middle of two consecutive frequency bins, and is commonly known in signal processing as the *FFT scalloping loss* [69, 70]. This maximum Doppler-induced loss is common to all methods that perform frequency search through spectral analysis as in the PFS method, if no measures to attenuate its effects are taken.

The block diagram of the PCS acquisition method is shown in Figure 2.7. The PCS method employs the convolution theorem which states that the convolution of two sequences in the time-domain (equivalent to the correlation at all code phases) can be obtained through multiplication of these sequences in the frequency-domain. The correlation between two general sequences, \mathbf{y} and \mathbf{c} , is obtained as [15]:

$$h[m] = \sum_{n=0}^{N-1} y[n]c[n+m] \quad (2.22)$$

where $h[m]$ is the correlation result for the relative shift index m . Recalling the definition of the inverse Discrete Fourier Transform (IFFT, in the case of an FFT implementation), the sequences \mathbf{y} and \mathbf{c} can also be written as:

$$x[n] = \frac{1}{N} \sum_{k=0}^{N-1} X(k) \cdot e^{j2\pi nk/N} \Leftrightarrow \mathbf{x}[\cdot] = \text{IFFT}\{\mathbf{X}(\cdot)\} \quad (2.23)$$

where:

$$\mathbf{X}(\cdot) = \text{FFT}\{\mathbf{x}[\cdot]\} \Leftrightarrow X(k) = \sum_{n=0}^{N-1} x[n] \cdot e^{-j2\pi nk/N}$$

stands for the Fourier transform of $x[n]$. Noting the shifting property of the Fourier transform, through which:

$$\text{FFT}\{\text{SHIFT}_m\{\mathbf{x}[\cdot]\}\} = \mathbf{X}(\cdot)e^{j2\pi mk/N}$$

with $\text{SHIFT}_m\{x[n]\} = x[n + m]$, the correlation operation in (2.22) can be rewritten as:

$$\begin{aligned}
h[m] &= \sum_{n=0}^{N-1} \frac{1}{N^2} \sum_{k,l=0}^{N-1} Y(k)C(l) e^{j2\pi(nk+l(n+m))/N} \\
&= \frac{1}{N^2} \sum_{k,l=0}^{N-1} Y(k)C(l) e^{j2\pi ml/N} \sum_{n=0}^{N-1} e^{j2\pi n(k+l)/N} \\
&= \frac{1}{N^2} \sum_{k,l=0}^{N-1} Y(k)C(l) e^{j2\pi ml/N} \cdot N \delta_{k,-l} \\
&= \frac{1}{N} \sum_{k=0}^{N-1} Y(k)C(-k) e^{j2\pi mk/N}
\end{aligned} \tag{2.24}$$

where $\delta_{k,-l}$ is the Kronecker delta, which evaluates to 1 if $k = -l$ or to 0 otherwise. This way, the sequence $\mathbf{h} = \{h[0], \dots, h[N-1]\}$ corresponding to the correlation results over all possible N shift indexes of the local code replica can be obtained as [15]:

$$\mathbf{h}[\cdot] = \text{IFFT}\{\mathbf{Y}(\cdot)\text{FLIP}\{\mathbf{C}(\cdot)\}\} \tag{2.25}$$

where the $\text{FLIP}\{x[n]\}$ operation inverts the positions of the entries of the $x[n]$ sequence (the last entry goes to the first place, and so on). For real-valued sequences, it results that $\text{FLIP}\{\text{FFT}\{\mathbf{c}[\cdot]\}\} = \text{FFT}^*\{\mathbf{c}[\cdot]\}$, from which the structure shown in Figure 2.7 is finally obtained, with $y[n] = r[n] \cdot e^{-j2\pi \hat{f}_d n T_s}$. The step-by-step execution of this method and the number of operations required are shown in Table 2.2.

According to the complexity of execution of each step for the PCS method, the number of operations required to execute this method is in the order of $N_{f_d} \times N \cdot \log_2(N)$. Given that in most cases $N_{f_d} \ll N_s$, the PCS scheme is computationally more efficient than the PFS one. Furthermore, as the frequency search is done serially in this method, the frequency search resolution can be freely set, potentially allowing frequency-derived correlation losses lower than those of the PFS method.

Table 2.2 – Step-by-step execution of the PCS method

| Step | Number of Operations |
|--|------------------------|
| 1 - Demodulation of whole data block with candidate Doppler offset | N |
| 2 - FFT of output of 1 | $5N \cdot \log_2(N)$ |
| 3 - Multiplication of output of 2 with FFT of local code replica | N |
| 4 - Inverse FFT of output of 3 | $5N \cdot \log_2(N)$ |
| 5 - Repeat step 1-4 for each Doppler offset | $N_{f_d} \times (1-4)$ |

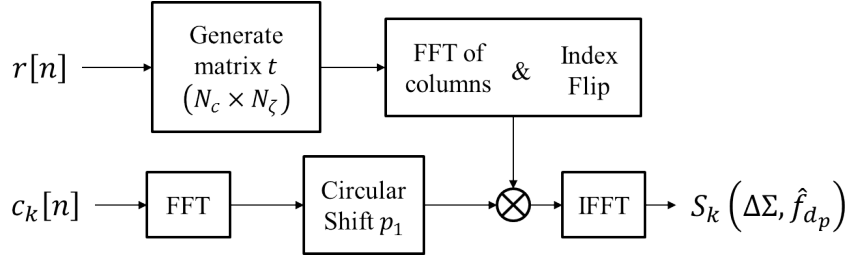


Figure 2.8 – Bi-dimensional Parallel Search (BPS) method block diagram

2. FFT over one code period The biggest disadvantage in terms of complexity of execution of the PCS method is the fact that the required FFTs are taken over the whole data blocks. In [13], an acquisition method is developed in which the whole data block is broke down into sub-blocks equivalent in length to the number of samples per code period, N_s . This acquisition method is given the name of "spectral shifting with Doppler preprocessing" in [15], and is referred to here as Bi-dimensional Parallel Search (BPS) method, as it improves the search algorithm in both dimensions. The block diagram of the BPS method is shown in Figure 2.8.

The BPS acquisition method starts by breaking down the whole data block into the equivalent to one code period blocks, averaging the incoming signal over the total number of code periods contained in the signal, N_c . The result of this averaging is the matrix denoted in [15] as T :

$$T(p_2, a_1) = \sum_{a_2=0}^{N_c-1} r[a_1 + a_2 N_s] \exp \left\{ -j2\pi \frac{(a_1 + a_2 N_s) p_2}{N_c N_s} \right\} \quad (2.26)$$

The row index of this matrix, p_2 , is associated with a fine frequency index, and the column index a_1 corresponds to a sample index. The number of fine frequencies in this algorithm is made equal to N_c , so the final matrix is $N_c \times N_s$. The processing of the local code is done as shown in Figure 2.8. At first its FFT is taken and the result is circularly shifted, which in the frequency domain is equivalent to a multiplication by a carrier in the time domain. The code despreading is done by point-wise multiplication of each of the rows of T with a code replica spectrally shifted by an index p_1 , termed as coarse frequency index. The correlation output is then obtained as:

$$S(\Delta\Sigma, \hat{f}_{d_p}) = \text{IFFT} \left\{ \text{FLIP} \left\{ \text{FFT} \{ t(p_2, :) \} \right\} \cdot \text{SHIFT}_{p_1} \left\{ \text{FFT} \{ c \} \right\} \right\} \cdot e^{-j2\pi \frac{(m_2 N_s + m_1) p_2}{N}} \quad (2.27)$$

where $m_1 \in [0, N_s - 1]$ represents the sample index within the code period and $m_2 \in [0, N_c - 1]$ the code period index. One execution of (2.27) generates the correlation output for all possible code delays at the Doppler shift $p = p_1 N_c + p_2$. For the full derivation of (2.27) refer to [15] or [13]. The steps for execution of the BPS method, together with the corresponding number of operations

required, is shown in Table 2.3.

As can be seen in Table 2.3, all FFT operations in the BPS method are executed over code blocks of dimension N_s exclusively. The process of spectral shifting of the FFT of the local code grants the same frequency resolution as the spectral analysis, that is, $\delta f_{d,BPS} = f_s/N_s$, so the total number of shifts p_1 to be tested should be made equal to $\Delta F_d/\delta f_d + 1$. In the case that the signal corresponds to only one code period, the BPS method is equivalent to the PCS method, with the difference that the frequency search is made by shifting the FFT of one of the waveforms prior to their multiplication.

3. FFT over fractions of code period The complexity reduction of the BPS method with respect to the PCS one is mostly due to the reduction by a factor N_c in the size of the blocks over which the FFT operations are executed. Other correlation methods were proposed in literature which attempt to further reduce the complexity of the acquisition search process, by breaking the incoming data block into a number of blocks higher than N_c , corresponding to fractions of the spreading code period. The most well-known correlation method that follows this approach is the Double Block Zero Padding (DBZP) method [9–12]. The DBZP method is schematically represented in Figure 2.9. The first operation within the DBZP method is to bring the input signal to baseband, which is achieved by demodulation by a carrier at the receiver IF. Subsequently, the division into the fractional blocks is performed. In [11] it is suggested to do this breakdown according to two parameters: the total number of code periods in the whole signal block and the Doppler uncertainty range. The number of blocks is then given by [11]:

$$N_{blocks} = 2\Delta F_d \cdot T_{code} \cdot N_c \quad (2.28)$$

which corresponds to blocks of size:

$$S_{block} = \frac{N_c \cdot N_s}{N_{blocks}} = \frac{N_s}{2\Delta F_d \cdot T_{code}} \quad (2.29)$$

Table 2.3 – Step-by-step execution of the BPS method

| Step | Number of Operations |
|--|-------------------------------------|
| 1 - Average input signal into T matrix (eq. (2.26)) | $N_c^2 \cdot N_s$ |
| 2 - Take FFT of the N_c rows of T | $N_c \cdot 5N_s \cdot \log_2(N_s)$ |
| 3 - Multiplication of output of 2 with shifted FFT of code replica | $N_c \cdot N_s$ |
| 4 - Inverse FFT of output of 3 | $N_c \cdot 5N_s \cdot \log_2(N_s)$ |
| 5 - Repeat step 3-4 for each coarse frequency index | $N_{f_d} \times (3 \text{ and } 4)$ |

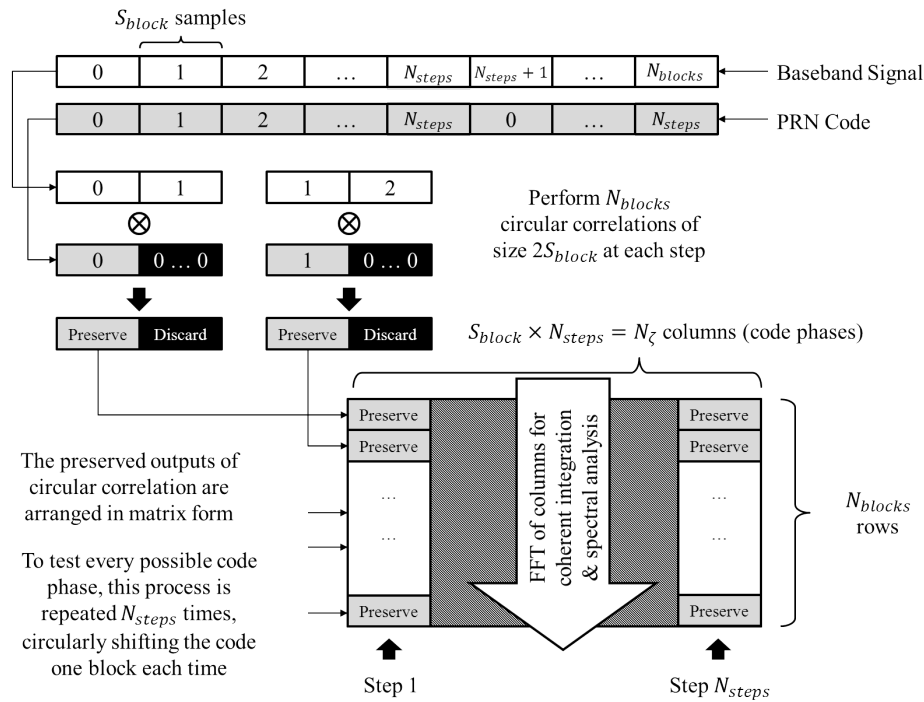


Figure 2.9 – Double Block Zero Padding (DBZP) method block diagram

Each of the resulting signal blocks is then joined with the following, while the local code replica blocks are padded with zeros as shown in Figure 2.9. This process of the doubling in size of the data blocks assures that the correlation operation produces the desired peak at the H_1 estimated code phase, regardless of the true value of this code phase. If this processing is not done prior to the correlation operation, when the true code phase is not a multiple of S_{block} , the correlation peak is reduced, the worst case scenario occurring when the true code phase is at the middle of one of the code blocks.

Circular correlation is then performed for each signal block with the (zero-padded) local code block, and only the first S_{block} values are preserved, as these are the ones containing the useful information. The procedure is repeated for each of the N_{blocks} blocks to generate a $N_{blocks} \times S_{block}$ matrix. In order to test every possible code phase this procedure is repeated $N_{steps} = N_{blocks}/N_c$ times, where a circularly shifted version of the local code is employed, resulting in a $N_{blocks} \times N_s$ matrix. The correlation output is finally found by spectral analysis (through FFT) of each one of the columns in this matrix.

The steps required to execute this method, together with the corresponding number of operations required is shown in Table 2.4.

This way, all FFT operations in the DBZP method are executed over data blocks shorter than N_s . Given that the frequency search is done through FFT, the DBZP method will also be affected by

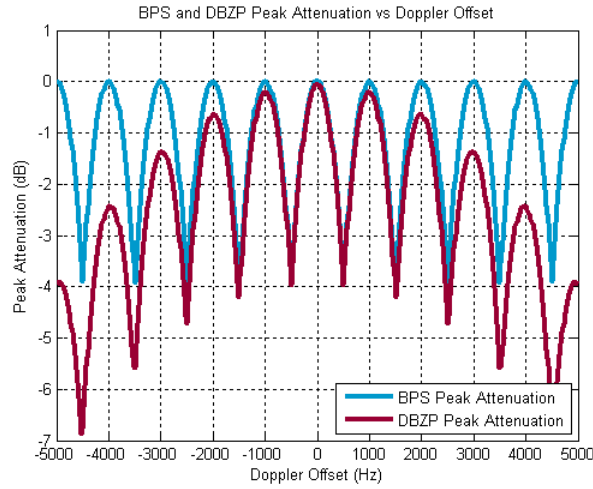


Figure 2.10 – Frequency response of the DBZP and BPS methods to Doppler offsets within a $\pm 5\text{kHz}$ uncertainty range for a 1ms GPS L1 C/A data block

the scalloping loss as the PFS and BPS methods. An additional frequency-related attenuation of the correlation output is also verified with the DBZP method, given that the correlation operation (steps 3 and 4) is done prior to the frequency search (step 6) and, this way, the effect of the Doppler offset on the DBZP correlation output is two-fold. In Figure 2.10 the attenuation of the correlation output of the DBZP method in the acquisition of a 1ms-long simulated GPS L1 C/A signal as function of the Doppler offset in a $\pm 5\text{kHz}$ uncertainty range is shown. The attenuation of the correlation output of the BPS method is also shown for comparison.

From the plot shown in Figure 2.10, it is clear the accentuated influence of the Doppler offset in the attenuation of the correlation output of the DBZP method as the frequency offset approaches the limits of the uncertainty range. It should be noticed that this profile is independent of the Doppler uncertainty range, given the definition of the block size as in 2.29. One possible way to circumvent this secondary effect is to extend the Doppler uncertainty range to values beyond the

Table 2.4 – Step-by-step execution of the DBZP method

| Step | Number of Operations |
|--|--|
| 1 - Demodulation of input signal to baseband | $N_c \cdot N_s$ |
| 2 - Take FFT of N_{blocks} double-sized blocks of data | $N_{blocks} \cdot 5 \cdot 2S_{block} \cdot \log_2(2S_{block})$ |
| 3 - Multiplication of output of 2 with local code blocks | $N_{blocks} \cdot 2S_{block}$ |
| 4 - Inverse FFT of output of 3 | $N_{blocks} \cdot 5 \cdot 2S_{block} \cdot \log_2(2S_{block})$ |
| 5 - Repeat 3 and 4 for each step | $N_{steps} \times (3 \text{ and } 4)$ |
| 6 - Take FFT of columns of resulting matrix | $N_s \cdot 5 \cdot N_{blocks} \cdot \log_2(N_{blocks})$ |

ones expected, at the price of an increased computational cost given the larger search space.

2.2.3 Methods Comparison

Having introduced the correlation methods representative of the state-of-the-art, a comparison between them can now be carried. Table 2.5 summarizes the main characteristics of the correlation methods previously described. From the values shown in Table 2.5, the lowest complexity correlation methods appear to be the PCS, BPS, and DBZP. However, as the number of code periods in the whole data block, N_c , increases, the size of the FFT operations within the PCS method will gradually increase as well, while for the BPS and DBZP methods they still remain of the same, fixed dimension. This effect can be observed in the comparison of the mean execution time for each of the three methods, as function of the number of code periods in the whole data block, shown in Figure 2.11. The Doppler range chosen is $\pm 5\text{kHz}$ and the PCS frequency resolution is set to be the same as for the BPS and DBZP methods, $\delta f_d = f_s/N = 1/(N_c T_{period})$.

From the plot shown in Figure 2.11, the effect of the variable size FFTs on the execution of the

Table 2.5 – Summary of Correlation Methods Characteristics

| Correlation Method | Dependence with N_s | Frequency Resolution |
|--------------------------------|--------------------------|----------------------|
| Serial Search | N_s^3 | Nonimposed |
| Parallel Frequency Search | $N_s^2 \cdot \log_2 N_s$ | Imposed |
| Parallel Code Search | $N_s \cdot \log_2 N_s$ | Nonimposed |
| Bi-dimensional Parallel Search | $N_s \cdot \log_2 N_s$ | Imposed |
| Double-Block Zero Padding | $N_s \cdot \log_2 N_s$ | Imposed |

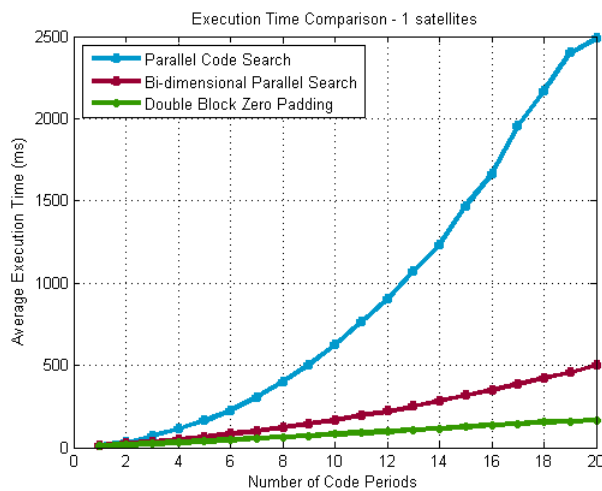


Figure 2.11 – Execution time comparison of PCS, BPS and DBZP methods for the acquisition of one signal as function of the number of code periods present for the GPS L1 C/A signal

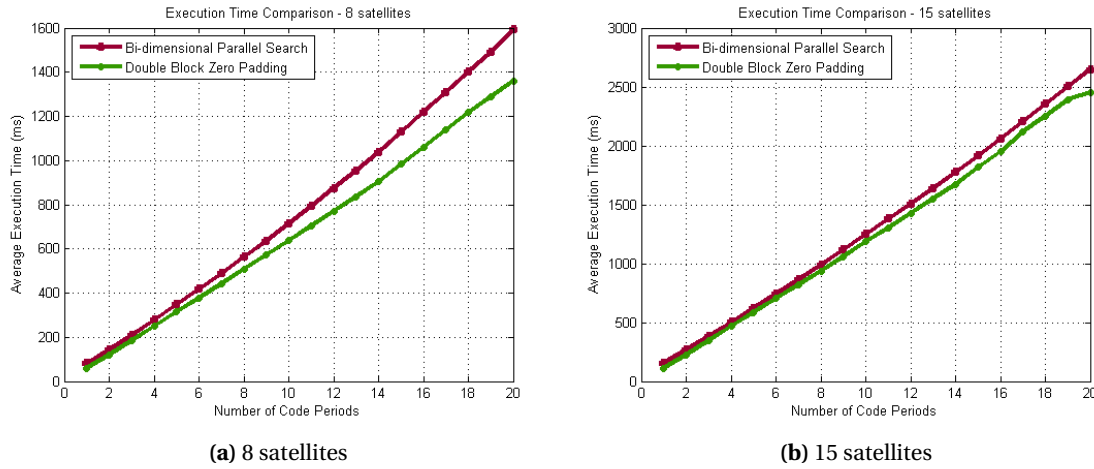


Figure 2.12 – Execution time comparison of BPS and DBZP methods for the acquisition of 8 (left) and 15 (right) signals as function of the number of code periods present for the GPS L1 C/A signal

PCS method becomes noticeable, from $N_c > 3$. One more conclusion that can be drawn from this plot is that the DBZP method appears to be computationally advantageous with respect to BPS. This is due to the fact that the number of computations required by the BPS method are proportional to N_c^2 (step 1 in Table 2.3), while this dependence is linear for the DBZP method. Nevertheless, it should be noted that the step 1 in the execution of the BPS method only needs to be performed once for all satellites in view, and all other operations are linearly dependent of N_c . This way, in Figure 2.12, the comparison of the execution time of the two methods in the acquisition of several satellites is shown, also considering a DBZP implementation optimized for the acquisition of several satellites. Through the plots in Figure 2.12, it can be seen that the gap between the mean execution time of the BPS and DBZP methods becomes narrower if the BPS execution is optimized for the acquisition of signals from several satellites at once.

As a result of the comparison carried in this section of the different GNSS correlation methods presented, it can be concluded that the DBZP appears to be the most computationally efficient method, but that the BPS can reach a similar efficiency if it is executed taking into account the acquisition of more than one signal. In what concerns the frequency search, the SS and PCS methods are the only methods from the ones presented that allow flexibility in the setting of the search resolution, while the DBZP is the one which is inherently more sensitive to the Doppler offset value. This analysis provides the basis for the choice of the most adequate correlation method based on the desired weight of each component in the complexity vs. sensitivity trade-off typical of GNSS acquisition schemes.

2.3 Detection Schemes

Once the correlation process for one or more search cells has been concluded, signal detection can take place. As described in section 2.1.2, a *detection scheme*, or *detector*, is characterized by [5, 6, 16]:

1. the probability of falsely signaling signal presence when this one is, in fact, absent (probability of false alarm, P_{fa}); and
2. the probability of correct detection when the signal is effectively present (probability of detection, P_d).

The Neyman-Pearson decision criterion is typically applied in GNSS acquisition, through which a detection threshold, η or V_{th} , is set according to the desired P_{fa} and the distribution of the detector output, i.e. its *detection metric*, in the absence of signal (hypothesis H_0). The probability of detection then corresponds to the probability of this same detection metric crossing η given its distribution in the presence of signal (hypothesis H_1) and the signal parameters [5, 6, 16].

Three main types of GNSS detection schemes can be found in literature and are introduced in this section. The main difference between these detection schemes is the way in which the consecutive correlation outputs are combined, or *integrated*. The three signal integration techniques analyzed are *coherent*, *noncoherent*, and *differential* integration. As coherent integration of multiple code periods, corresponds in practice to correlation over this same number of code periods, the correlation output is also sometimes referred to as the *coherent integration output*. For this same reason, these integration techniques can also be grouped as coherent and post-coherent integration techniques, as coherent signal processing (correlation) is a required step in any detection scheme.

2.3.1 Coherent Detector

As mentioned at the end of the previous section, coherent integration is equivalent to correlation over more than one code period. A suitable detection metric for a detector that performs only the correlation operation is simply the detection metric of (2.11), through which $D(\hat{\zeta}, \hat{f}_d) = |S(\hat{\zeta}, \hat{f}_d)|^2$, where the index k is dropped for simplicity of notation [6, 45]. It should be noted that this detection metric, however, does not correspond to a purely coherent detector, as the input signal phase is unknown and, therefore, phase removal is required prior to the detection test. This way, to avoid the naming inaccuracy, this detector is referred here to as the *square-law detector* (SLD), following the nomenclature in [45], and its detection metric is $D_{SLD}(\hat{\zeta}, \hat{f}_d)$. The block diagram of the SLD detector is shown in Figure 2.13.

The distribution of $D_{SLD}(\hat{\zeta}, \hat{f}_d)$ under H_0 and H_1 can be directly inferred from the distribution of the correlation output conditioned to these hypotheses. Under H_0 , the signal is absent so

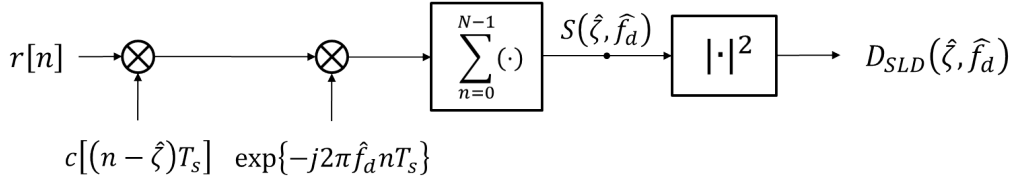


Figure 2.13 – Square-law detector block diagram

$r[n] = w[n]$, and in this case $S(\hat{\zeta}, \hat{f}_d)$ results as :

$$S(\hat{\zeta}, \hat{f}_d) = \sum_{n=0}^{N-1} w[n] \cdot c[(n - \hat{\zeta})T_s] e^{-j2\pi(f_{IF} + \hat{f}_d)nT_s} \quad (2.30)$$

which corresponds exclusively to the sum of the products of a random variable by a deterministic component. The code term can only take the values ± 1 and, assuming independence between the real and imaginary (in-phase and quadrature, I&Q) terms of $w[n]$, its multiplication by a complex exponential does not affect its PDF [6]. Therefore, the product of the two components will have the same distribution as $w[n]$, which, according to the assumptions described in section 2.1, corresponds to a zero-mean complex Gaussian random variable with variance σ^2 . This way, $S(\hat{\zeta}, \hat{f}_d|H_0)$ is also characterized as a zero-mean complex Gaussian random variable with variance $\sigma_N^2 = N \cdot \sigma^2$. This implies that $D_{SLD}(\hat{\zeta}, \hat{f}_d|H_0)$ has a central χ^2 distribution with two degrees of freedom (dof) and its PDF is given by [6]:

$$f_{D_{SLD}(\hat{\zeta}, \hat{f}_d|H_0)}(x|H_0) = \frac{1}{2\sigma_N^2} \exp\left(-\frac{x}{2\sigma_N^2}\right) \quad (2.31)$$

for $x \geq 0$, and 0 otherwise. According to (2.15) and (2.31), the threshold, η , for decision over signal presence is then obtained from:

$$P_{fa} = \int_{\eta}^{\infty} f_{D_{SLD}(\hat{\zeta}, \hat{f}_d|H_0)}(x|H_0) \cdot dx = \exp\left(-\frac{\eta}{2\sigma_N^2}\right) \quad (2.32)$$

Under H_1 , the incoming signal consists of both signal and noise, and the correlation output corresponds to the sum of the correlation output under H_0 with a deterministic component, $S_{\text{mean}}(\hat{\zeta}, \hat{f}_d|H_1)$, given by:

$$S_{\text{mean}}(\hat{\zeta}, \hat{f}_d|H_1) = \sum_{n=0}^{N-1} r_{\text{signal}}[n] \cdot c[(n - \hat{\zeta})T_s] e^{-j2\pi(f_{IF} + \hat{f}_d)nT_s} \quad (2.33)$$

where $r_{signal}[n]$ corresponds to the deterministic component of the received signal. According to (2.33), under H_1 the SLD detection metric has a noncentral χ^2 distribution with two dof and non-centrality parameter, $\lambda = |S_{\text{mean}}(\hat{\zeta}, \hat{f}_d|H_1)|^2$. The probability of detection is then given by:

$$P_d = \int_{\eta}^{\infty} f_{D_{SLD}(\hat{\zeta}, \hat{f}_d|H_1)}(x|H_1) \cdot dx = Q_1\left(\frac{\sqrt{\lambda}}{\sigma_N}, \frac{\sqrt{\eta}}{\sigma_N}\right) \quad (2.34)$$

where $Q_K(a, b)$ is the K^{th} order Marcum Q-function [16]. In the particular case of this detector, the expressions for P_{fa} and P_d can be easily intertwined by writing η as function of P_{fa} , thus obtaining:

$$P_d = Q_1\left(\frac{\sqrt{\lambda}}{\sigma_N}, \sqrt{-2\ln(P_{fa})}\right) = Q_1\left(\sqrt{2N\text{SNR}_{in}}, \sqrt{-2\ln(P_{fa})}\right) \quad (2.35)$$

where the last equality is verified in the case of a perfect time-frequency alignment between the incoming signal and the local replicas, so that $\lambda = N^2P$, and $\text{SNR}_{in} = P/2\sigma^2$ represents the Signal-to-Noise Ratio prior to the signal correlation.

According to (2.35), two types of analysis can be followed in the performance evaluation of this detection scheme (and of all detection schemes, in general). Either P_{fa} is kept constant and the evolution of P_d with the input SNR is assessed, or on the other hand the SNR is fixed and P_{fa} varied. The first analysis is known as *sensitivity analysis* and the second one as *Receiver Operation Characteristic (ROC) analysis*. Examples of both analysis are shown in Figure 2.14. The simulations shown are obtained for the acquisition of a 1ms-long GPS C/A signal, sampled at twice the chip rate, and considering a perfect time-frequency alignment so as to isolate the effect of (2.35).

Throughout this thesis the focus will mostly be placed on the sensitivity analysis rather than

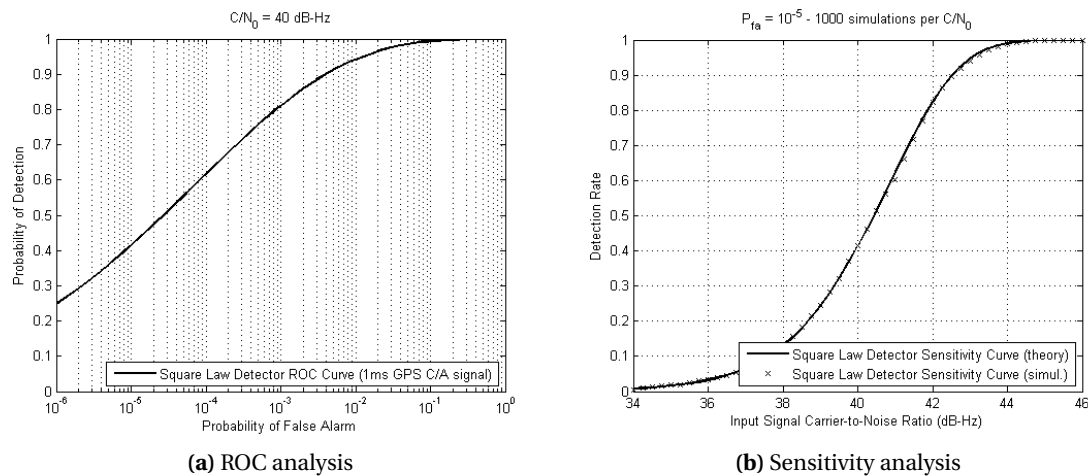


Figure 2.14 – Examples of ROC and sensitivity analysis for the SLD detector

on the ROC one, as in the cases of interest the P_{fa} is usually contained within a restricted range of values, so the different detectors' relative performance will remain unaltered within this short range of values. In Figure 2.14b, it is seen the evolution of the probability of detection of the SLD detector with the increasingly higher signal strength of the input signal, represented by the signal Carrier-to-Noise Ratio (C/N_0). The C/N_0 relates to the SNR through [3, 16]:

$$C/N_0 = \text{SNR}_{in} \cdot B = \frac{P}{2\sigma^2} \cdot B = \frac{P}{2\mathcal{N}_0} \quad (2.36)$$

where B was seen previously to be the receiver front-end bandwidth. According to this definition, the C/N_0 is independent of the receiver bandwidth and it is commonly used to quantify the input signal powers in GNSS signal processing.

According to the plot in Figure 2.14b, the input C/N_0 required to achieve $P_d = 0.9$ at $P_{fa} = 1E-5$, is of approximately 42.5dB-Hz. A given target pair (P_d, P_{fa}) is known as the *receiver working point*, and the C/N_0 at which this point is achieved with a given detector and detector configuration represents the detector sensitivity.

If the same receiver working point is desired with this detector, but with an improved sensitivity, that is, achieving the desired working point at a lower C/N_0 , the only option available is to increase the noncentrality parameter, λ , of the distribution of $D(\hat{\zeta}, \hat{f}_d | H_1)$. This can be achieved by increasing the number of samples in the correlation process, without increasing the sampling frequency, which means using more than N_s samples in the correlation process. This is typically achieved by jointly processing, or coherently integrating, more than one code period. In the case that N_c code periods are used, the noncentrality parameter will be increased by a factor of N_c^2 , while the noise variance will only be increased by a factor of N_c . The maximum achievable coherent integration gain in the presence of N_c code periods is thus given by:

$$G_{coherent,dB}(N_c) = 10 \cdot \log_{10}(N_c) \quad (2.37)$$

The coherent integration gain given by (2.37) is the maximum theoretical gain achievable with any integration technique. Naturally, this gain is equally the ideal gain of the correlation operation, even if in reality several nonidealities should also be taken into account, such as quantization, filtering or other losses imposed by the receiver frontend [4, 71]. As an example, the ideal sensitivity gain drawn from coherent integration over two code periods of a GPS L1 C/A signal sampled at twice the chip rate is then:

$$G_{total,dB} = G_{correlation,dB}(2 \cdot 1023) + G_{coherent,dB}(2) = 36.1\text{dB}$$

Even if this is the optimal gain achievable, the extent to which the coherent integration time, $T_{coh} = N_c \cdot T_{code}$, can be extended is limited by several factors:

Navigation data bit transition The navigation data bit has been considered constant in every example so far, but this assumption cannot be considered valid when several code periods are processed. The effect on the correlation output of a data bit transition between one code period to another is an inversion of 180 degrees in the correlation output phase. In the worst-case scenario, the sum of two consecutive correlation outputs in the presence of data bit transition may result in complete cancellation of both code periods, given their 180 degrees phase difference.

In [72], two of the most commonly employed methods for dealing with the acquisition of GPS L1 C/A data blocks of the same duration of (or longer than) this signal's navigation data bit are developed. These are known as the *full-bit* and *alternate half-bit* acquisition methods. The full-bit method (Figure 2.15a) consists of keeping twenty parallel 20ms coherent integrations (equivalent to the duration of a data bit), each one shifted by one code period with respect to the previous one, so that one of these coherent integrations is correctly aligned with the data bit start. A similar approach is also proposed in [64], in which twenty coherent integrations are also kept, but with successive bit sign reversal (Figure 2.15b). On the other hand, the alternate half-bit (Figure 2.15c) method breaks each 20ms data block into two 10ms blocks, and coherently integrates over each half bit. Given that one of the blocks is assured to be transition free, one of the two coherent integrations is also free of this effect. One other solution is to receive the navigation data stream through an alternative channel and cancel its effect, through the usage of the assistance data link described in section 2.4.

While such techniques are well suited for the acquisition of the GPS L1 C/A signal, given the relatively long data bit duration with respect to the code period, the issue of navigation data bit

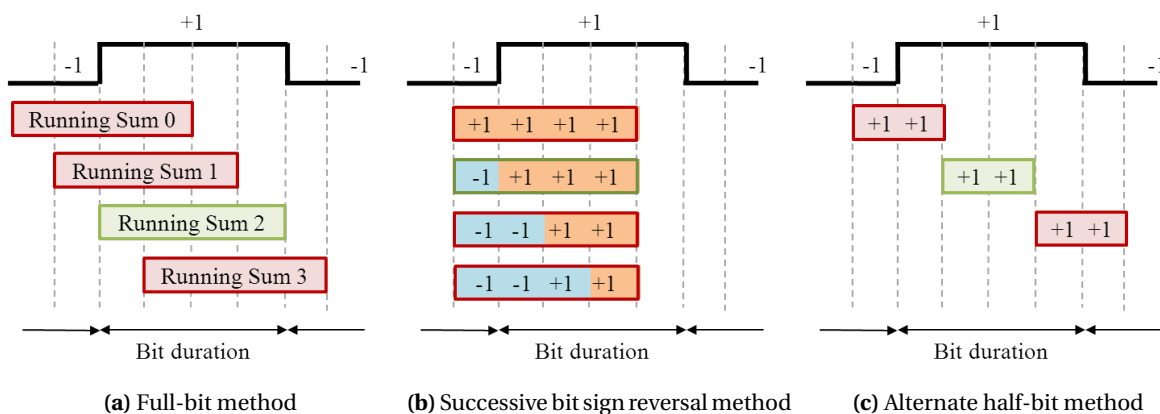


Figure 2.15 – Methods for handling navigation data bit transition for GPS L1 C/A signals [72]

transition becomes particularly critical when considering the modernized GNSS signals. In many of the new GNSS signals, the data bit period is often the same as the spreading code period, so data bit transitions can occur *at each* code period [27, 28, 34]. While several techniques can be employed to efficiently minimize the effect of the data bit transition during a single code period [12, 73–75], the only reliable approach to coherent summation of consecutive correlation outputs in standalone receivers is by testing each possible combination of relative sign change between code periods. That is, once the correlation output for the 2nd code period is obtained, two sums are performed, corresponding to the hypotheses that data bit transition has, or has not, occurred. The total number of running sums to keep in this case is 2^{N_c-1} . Once again, this issue may be avoided in the presence of an alternative assistance channel. The equivalent problem of secondary code acquisition is addressed in section 2.5.3.

Frequency-induced losses In section 2.2 it was seen that any frequency estimation error is translated into the correlation output as an attenuation of its amplitude through a sinc function. Recalling (2.18), the argument of this sinc function is product of the frequency estimation error with the coherent integration time. This way, a frequency error that may be negligible for the coherent processing of only one code period, may no longer be negligible when considering $N_c > 1$.

This condition imposes restrictions not only on the frequency search grid, but also on the user dynamics and the receiver oscillator stability, as these parameters also contribute to the Doppler shift perceived by the receiver [3, 76–82]. With respect to the search grid, if a finer grid is defined in order to limit the maximum frequency-induced attenuation, the side effect will be that the number of Doppler bins to be scanned will also increase, thus increasing the complexity of the correlation process, as seen in section 2.2.

One other factor that should be considered as limiting the extent of coherent integration, is *code Doppler* [3, 83], even if in a lower scale than the two previously mentioned ones. Still, some approaches for handling this effect can be found in literature [13, 15, 84].

Given the limitations to the efficient application of coherent integration over extended signal observation times, post-coherent integration techniques are recurrently applied in order to continue enhancing acquisition sensitivity. The two existing post-coherent integration alternatives are presented in the following sections.

2.3.2 Noncoherent Detector

Given the limitations of coherent integration referred at the end of the previous section, post-coherent integration techniques have been developed to further continue increasing sensitivity of GNSS acquisition schemes once coherent integration has achieved its limit of applicability. The post-

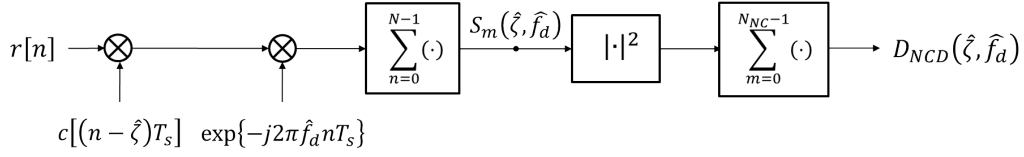


Figure 2.16 – Noncoherent Detector block diagram

coherent integration approach most commonly applied in GNSS receivers is *noncoherent integration* [3, 4, 6, 45, 85, 86]. Noncoherent detectors circumvent the limitations of coherent integration by removing the phase of the coherent output prior to further accumulation. The block diagram of the Noncoherent Detector (NCD) is shown in Figure 2.16. According to this block diagram, the NCD detection metric is obtained as:

$$D_{NCD}(\hat{\zeta}, \hat{f}_d) = \sum_{m=0}^{N_{NC}-1} |S_m(\hat{\zeta}, \hat{f}_d)|^2 = \sum_{m=0}^{N_{NC}-1} D_{SLD,m}(\hat{\zeta}, \hat{f}_d) \quad (2.38)$$

That is, $D_{NCD}(\hat{\zeta}, \hat{f}_d)$ is the result of the sum of N_{NC} consecutive detection metrics for the SLD detector. Considering the analysis of the previous section, it results that the NCD detection metric is a central χ^2 distribution under H_0 , and noncentral under H_1 , with $2N_{NC}$ dof. The expressions for P_{fa} and P_d for the NCD detector are then [6]:

$$P_{fa} = \tilde{\Gamma}_{N_{NC}}\left(\frac{\eta}{2\sigma_N^2}\right) \quad (2.39)$$

$$P_d = Q_{N_{NC}}\left(\frac{\sqrt{\lambda}}{\sigma_N}, \frac{\sqrt{\eta}}{\sigma_N}\right) \quad (2.40)$$

where $\tilde{\Gamma}_{N_{NC}}$ is the regularized incomplete gamma function of order N_{NC} [87]. The noncentrality parameter of the distribution of $D_{NCD}(\hat{\zeta}, \hat{f}_d|H_1)$ is obtained as the sum of the noncentrality parameters of each $D_{SLD}(\hat{\zeta}, \hat{f}_d|H_1)$.

While this detector form is effectively capable of addressing the limitations of the coherent detector, by removing the phase and frequency offset dependency over periods longer than T_{coh} , it is well-known that its sensitivity gain with the number of noncoherent integrations is not as high as the one obtained with coherent integration. This is due to the fact that the phase removal operation performed prior to the noncoherent accumulations has the undesirable effect of increasing the noise component, which results in a sensitivity loss usually known as the *squaring loss* [3, 18, 61, 86, 88].

Several different analysis of the squaring loss can be found in literature, and are addressed and compared in [19] and [20]. One approach that is usually followed in the evaluation of this loss is through the so-called *deflection coefficient*. However, in [19], its inapplicability on the evaluation of

the sensitivity loss of noncoherent, differential or any other type of detectors employing nonlinear operations is explicitly demonstrated, so this approach is not detailed here. A more suitable alternative for quantifying the sensitivity loss of noncoherent integration with respect to the coherent integration gain was developed in [18] for radar systems, and was applied to GNSS acquisition in [3]. This approach consists of determining a sensitivity loss factor which is incurred when N_{NC} noncoherent integrations are performed, instead of the equal number of coherent integrations, considering that the ideal coherent integration gain would be achieved through these. The formula proposed in [18] for the sensitivity loss of the noncoherent detector, L_{NCD} is:

$$L_{NCD}(N_{NC}) = 10 \cdot \log_{10} \left(\frac{1 + \sqrt{1 + 9.2 \cdot N_{NC} / D_c(P_d, P_{fa})}}{1 + \sqrt{1 + 9.2 / D_c(P_d, P_{fa})}} \right) \quad (2.41)$$

where D_c is known as the *detectability factor*, and is calculated as [18]:

$$D_c(P_d, P_{fa}) = [\text{erfc}^{-1}(2 P_{fa}) - \text{erfc}^{-1}(2 P_d)]^2 \quad (2.42)$$

with $\text{erfc}(\cdot)$ the complementary error function, representing the tail of the standard normal distribution. This formula for L_{NCD} is obtained through a polynomial approximation of the squaring loss, and will be discussed in detail in Chapter 4. This way, the sensitivity gain of the NCD detector can be expressed as:

$$G_{NCD} = 10 \cdot \log_{10}(N_c) + \left(10 \cdot \log_{10}(N_{NC}) - L_{NCD}(N_{NC}) \right) \quad (2.43)$$

where the terms between brackets correspond to the noncoherent integration gain. Apart from noncoherent integration, one more post-coherent integration technique is found associated with GNSS signals acquisition. This technique is presented next.

2.3.3 Differential Detectors

In the previous section noncoherent integration was seen as a technique that effectively address the limitations of coherent integration, but is incapable of achieving a similar sensitivity gain due to the effect of the so-called squaring loss. An alternative post-coherent integration technique for the acquisition of DSSS CDMA signals was proposed in [89]. Within this approach, known as *differential integration*, the coherent outputs are not squared, but rather correlated with the previous output [6, 17, 45, 90–107]. The product of these two uncorrelated coherent outputs is statistically less detrimental to the signal SNR than the squaring operation, given the assumed independence of the noise terms. An example of a differential detector, here referred to as Noncoherent Differential De-

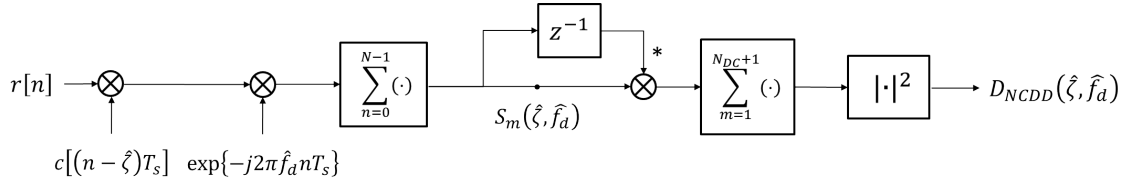


Figure 2.17 – Noncoherent Differential Detector block diagram

detector (NCDD) given the phase removal operation at the end, is shown in Figure 2.17. According to this block diagram, the NCDD detection metric is obtained as [90]:

$$D_{NCDD}(\hat{\zeta}, \hat{f}_d) = \left| \sum_{m=1}^{N_{DC}+1} S_m(\hat{\zeta}, \hat{f}_d) \cdot S_{m-1}^*(\hat{\zeta}, \hat{f}_d) \right|^2 \quad (2.44)$$

with $N_{DC} = N_C - 1$ the number of differential integrations that can be performed with this approach, having N_C coherent outputs available. This differential detector form, nevertheless, is only one of the few developed since the original proposal in [89]. One of the two main factors that distinguish the differential detectors found in literature is the generation of the differential outputs. Given the nature of the differential operation, each coherent output (except the first and the last) may be used more than one time in the differential correlation. This results in a dependency between consecutive differential outputs which is remarkably difficult to characterize statistically. Closed form PDFs for the detection metric of (2.44) were developed in [6], but, as the author notes, while exact, the expressions derived are of limited application due to the presence of functions which easily become both burdensome and inaccurate for a high number of differential accumulations. One approach to overcome the dependency problem was proposed in [104], in which only each second differential integration output is integrated. This approach is referred to in [6] as *pair-wise integration*, and the corresponding detection metric of the Pair-Wise Detector (PWD) is given by:

$$D_{PWD}(\hat{\zeta}, \hat{f}_d) = \Re \left\{ \sum_{m=1}^{N_{DC}^{PW}} S_{2m}(\hat{\zeta}, \hat{f}_d) \cdot S_{2m-1}^*(\hat{\zeta}, \hat{f}_d) \right\} \quad (2.45)$$

with $N_{DC}^{PW} = \lfloor N_C/2 \rfloor$ the number of differential integrations achievable with this detector having N_C coherent outputs available.

The second main factor that distinguishes differential detectors is the formulation of the detection metric from the differential integration outputs. The original proposal for the post-coherent differential detector considers only the in-phase part of the differential integration output, as shown in (2.45). Nevertheless, a posterior evaluation of this detection metric carried in [90] noted that a residual Doppler offset leads to a partition of the useful signal power between the I&Q components of the differential integration output. The authors of [90] then proposed a Doppler-robust differ-

entially noncoherent form, in which the detection metric is obtained as the squared magnitude of the differential integration output. This detection form corresponds to the NCDD detector shown in Figure 2.17. It should be noted that, although this form significantly improves the differential detection scheme performance in the presence of an unknown Doppler offset, its detection metric is obtained as the sum of two dependent random variables, which means that even if the pair-wise integration approach is employed, the theoretical analysis of the detector output will once again be complex.

The approach which is frequently followed in the analysis of differential detectors is to resort to the Central Limit Theorem, through which the noise terms resulting from differential integration can be approximated by a Gaussian distribution for a sufficiently high enough number of integrations [6, 17]. In [6], the author develops a Gaussian approximation for both the NCCD and PWD detector forms and points out the risk of employing this approximation for a low number of accumulations, resulting from the fact that the actual distributions of the I&Q components of the differential operation output have heavy tails and are clearly not Gaussian. This way, the Gaussian approximation may lead to large inaccuracies in the threshold setting process for few accumulations.

The multitude of differential detector forms existing, together with the complexity of their statistical characterization, have been obstacles to the comparison of differential and noncoherent detectors. Although in several publications it has been observed that differential detectors are a preferable choice for weak signals acquisition, it was not until [106] that a formal comparison between the sensitivity losses of the squaring and differential operations was encountered. The approach developed in [106] was consolidated in [107], and is the main focus of Chapter 4 of this thesis.

2.4 Assisted GNSS

Assisted-GNSS (A-GNSS) improves on standard GNSS performance by providing information to the user receiver through an alternative communication channel [71, 76, 108, 109]. The main goal of the assistance data supplied by a Base Station (BS) is to improve the Time to First Fix (TTFF) and sensitivity of the user receiver, or Mobile Station (MS). There are two main approaches to A-GNSS: MS-Based, in which the position is calculated in the receiver itself, and MS-Assisted, in which the position is calculated at a server. These two approaches naturally have different requirements in the type and amount of data to be shared between the MS and the BS. The MS-Based approach requires more data to be supplied to the MS but also presents several advantages, such as better position accuracy, and possibility of integration of improved navigation filters (Kalman), among others [110, 111]. In Chapter 5 of this thesis an acquisition algorithm based on the MS-Based approach is presented.

The required assistance data to be supplied to the MS for the application of the MS-Based A-GNSS approach is [71]:

- Coarse time and ephemeris – for computation of the expected satellite azimuth and elevation angles, as well as their velocity for compensation of the Doppler offset component due to satellite motion;
- Reference frequency – for calibration of the MS oscillator, enables compensation of most of oscillator Doppler offset component; and
- BS position – for reducing the initial MS spatial uncertainty;

By compensating both for the oscillator and satellite motion Doppler offset components, the source which most influences the Doppler perceived by the receiver is the user motion, which is typically the least significant source from the three [71, 77]. Apart from the items listed, the receiver may also be supplied with fine timing information (less than 1ms accuracy) which may allow considerably reducing its clock bias uncertainty. This, however, is not necessarily the general case [71].

Through the usage of the assistance parameters listed, the TTF of A-GNSS receivers can be reduced to the order of magnitude of a standalone receiver in a “hot start”, when acquisition is performed only a few minutes after the receiver was last turned off. Depending on the signal power levels of the signal received this reduced TTF can be as short as 1s, as opposed to the 1min required in a “cold start” (no a priori information) [71, 76, 108].

2.4.1 Snap-Shot Positioning

One technique that became possible with A-GNSS is known as snap-shot (or single-shot) positioning [112–116]. Snap-shot receivers use the estimated code phase for each visible satellite to obtain a direct position solution, thus eliminating the need for tracking loops. This technique is particularly useful when dealing with strongly attenuated signals that do not permit the navigation message extraction by the tracking loops. Snap-shot positioning allows positioning with increased observation times thus yielding enhanced reception sensitivity. This technique, nevertheless, implies that each signal is acquired individually, and then used in the navigation equation to compute the estimated receiver position.

2.4.2 Collective Detection

The overall processing of GNSS signals in harsh environments is a challenging task, given the low signal powers characteristic of these environments. An approach that is recurrently employed in weak signal tracking algorithms is to handle all signals collectively, in what is commonly known

as *vector tracking* [24, 117, 118]. The main rationale behind this approach is that the processing of weaker signals is facilitated by the presence of stronger ones.

The application of the vectorial concept to acquisition has been envisaged in [24] but it was not until [21], that an approach to do so was introduced. The proposal in [21] is to coherently combine the detection metrics from all satellites in view in order to improve the overall acquisition sensitivity. This concept relies on assistance information, for the user to define a position and clock bias uncertainty range from which a search grid is established. Each position and clock bias combination (4D point) is then mapped to the code phase for each satellite and a single detection metric is generated as function of the expected user position and clock bias (Figure 2.18). This approach was the subject of other recent studies, in particular [22, 23, 119–122], where it got the name of Collective Detection. These studies refined the concept introduced in [21] and further improved upon it in several ways. The proposal of a new approach to Collective Detection is the subject of Chapter 5, so the detailed analysis of this technique is provided in that chapter.

2.5 Modern Signals Impact in Acquisition

Most of the literature developed for GNSS signal processing until the first years of this century was produced having per basis the GPS L1 C/A signal structure. This is a natural consequence of this having been for many years the only GNSS signal open to the public, thus fostering research in the topic. Nevertheless, in the last decade significant advances have been made in the development of not only new signals but also whole new GNSS systems all around the world. These advances have brought new angles to exploit in the research of GNSS signal processing, and signal acquisition in particular, as they have a natural impact in receiver design and optimization. The structure of the

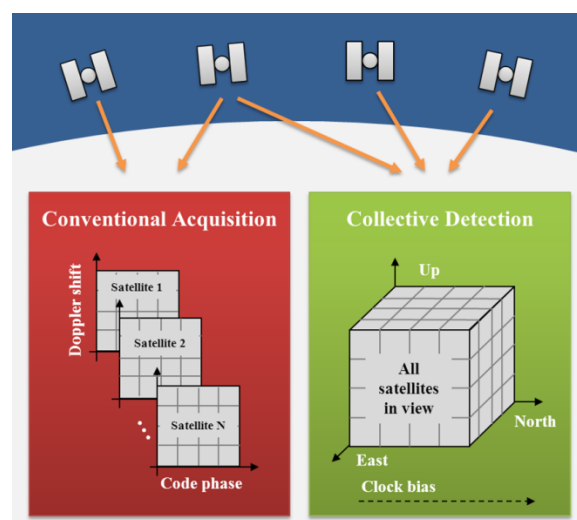


Figure 2.18 – Collective Detection principle

modern GPS and Galileo signals, and their effects on acquisition are reviewed in this section.

2.5.1 Binary Offset Carrier Modulations

Two of the key drivers for the design of the Galileo signals were the assurance of both *compatibility* and *interoperability* with the GPS signals also present in the shared transmission bands [123]. In the E1/L1 band, in particular, the multitude of signals that are planned for this band required that the Galileo Open Service (OS) and Public Regulated Service (PRS) signal modulations be designed in order to occupy the less crowded areas of the spectrum [33, 124, 125]. The innovative solution that was found was to split the power of these signals around the peak of the GPS L1 C/A signal. This is achieved through the usage of *Binary Offset Carrier (BOC) modulations* [33, 56]. These modulations are characterized by two independent design parameters:

- subcarrier frequency, f_{sc} ; and
- PRN code rate, f_{code} .

These parameters provide freedom to concentrate the signal power within specific parts of the allocated band, thus enabling reduced interference with other signals. A $BOC(f_{sc}, f_{code})$ modulation is the result of the product of a PRN spreading code with the subcarrier which is equal to sign of a sine (or cosine) waveform:

$$s_{BOC_{\sin/\cos}}(t) = c(t) \text{sign}[\sin / \cos(2\pi f_{sc} t)] \quad (2.46)$$

where $c(t)$ is the direct sequence modulation characteristic of DSSS communication, and its chip rate is f_{code} . As most of the times the sine wave is used in the generation of the BOC modulation instead of the cosine one, the sine subscript is usually omitted, and it is only included when the cosine wave is used. An alternative notation for these modulations is $BOC(m, n)$, where m stands for the ratio between the subcarrier frequency and the reference frequency, $f_0 = 1.023\text{MHz}$, and n stands for the ratio between the code rate and f_0 .

The result of the BOC modulation is a symmetric split spectrum with two main lobes shifted from the carrier frequency by the amount equal to the subcarrier frequency. The power spectrum of the $BOC(1,1)$ and BPSK modulations at the E1/L1 central frequency, $f_c = 1575.42\text{MHz}$, is shown in Figure 2.19. The autocorrelation function for a $BOC(m, n)$ modulation is characterized by $2r-1$ peaks, where $r = m/n$, and the magnitude of the k^{th} peak with respect to the main one is $(-1)^k(r - |k|)/r$ [4]. In Figure 2.20, the autocorrelation for the $BOC(1,1)$ and $BOC(6,1)$ modulations are compared to the autocorrelation of the BPSK modulation.

The final modulation chosen for application in the Galileo E1 OS signal is a combination of the two BOC modulations shown in Figure 2.20, known as Multiplexed BOC (MBOC), and represented

as MBOC(6,1,1/11). This modulation results from the multiplexing of the wideband BOC(6,1) modulation with the narrow-band BOC(1,1) modulation, such that 1/11 of the power is allocated to the high frequency component [34]. This spreading modulation places a small amount of additional power at higher frequencies in order to improve tracking performance, and it does not interfere with other wideband signals in the band, such as, the GPS M- and P(Y)-code or the Galileo PRS, a requirement for this modulation. A biography of the MBOC modulation can be found in [33, 124, 125]. The spectrum of all GPS and Galileo signals sharing the E1/L1 band is shown in Figure 2.21. In Appendix A, a summary of all current and planned GPS and Galileo signals is provided.

As shown in [34], the block diagram for the generation of the Galileo E1 OS signal is as shown in Figure 2.22, corresponding to:

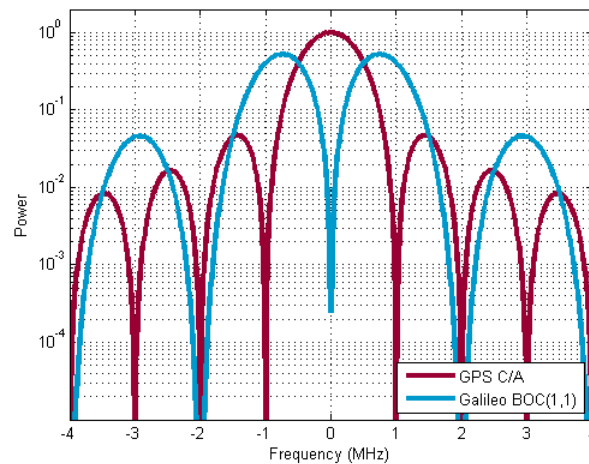


Figure 2.19 – GPS C/A and Galileo BOC(1,1) power spectral density

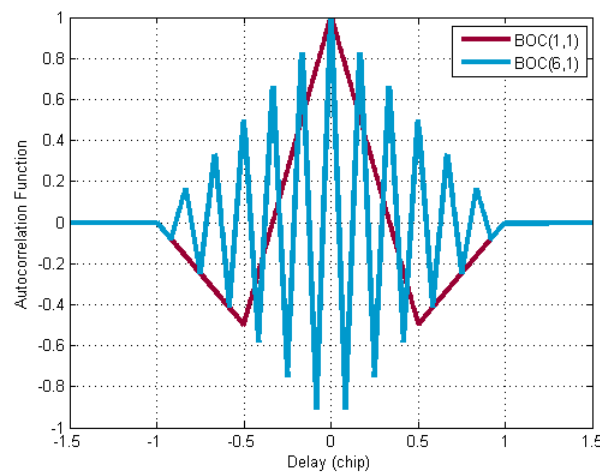


Figure 2.20 – Autocorrelation function of the BOC(1,1), and BOC(6,1) modulations

$$s_{E1}(t) = \frac{1}{\sqrt{2}} \left(e_{E1-B}(t) (\alpha s_{C_{E1-B,a}}(t) + \beta s_{C_{E1-B,b}}(t)) - e_{E1-C}(t) (\alpha s_{C_{E1-C,a}}(t) + \beta s_{C_{E1-C,b}}(t)) \right) \quad (2.47)$$

where e_{E1-B} corresponds to the product of the E1-B code, c_{E1-B} , with the navigation data, d_{E1-B} , and e_{E1-C} is directly obtained as the E1-C code, c_{E1-C} . This sub-division of the signal into two separate components, known as *data* and *pilot*, is common in modern signals, and its impact in acquisition is analyzed in the next section. Furthermore, the E1-C code is also the product of two components, known as *primary* and *secondary* codes, and is therefore referred to as a *tiered* code. The role of secondary codes and its impact in acquisition is discussed in section 2.5.3.

The two subcarriers, $s_{C_{E1-B/C,a}}$, and $s_{C_{E1-B/C,b}}$, correspond, respectively to the BOC(1,1) and BOC(6,1) modulations, and $\alpha = \sqrt{10/11}$ and $\beta = \sqrt{1/11}$ define the power partitioning between the two sub-carriers. This way of implementing the MBOC modulation is known as Composite BOC (CBOC). One other implementation, known as Time-Multiplexed BOC (TMBOC), can also be

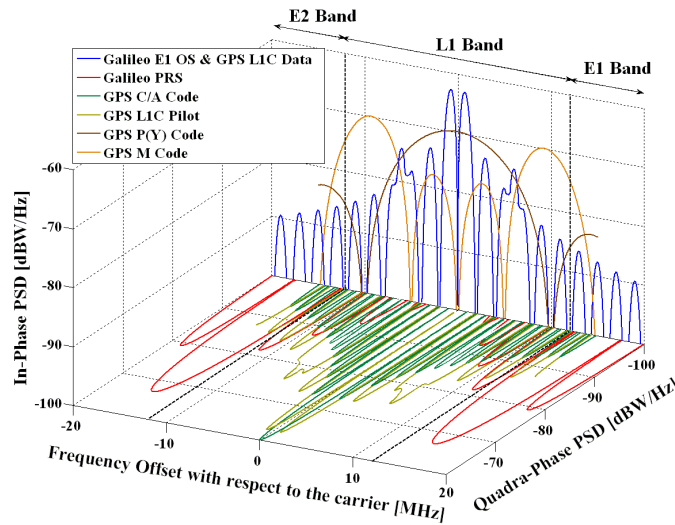


Figure 2.21 – Spectrum of GPS and Galileo signals transmitted in the L1 band [33]

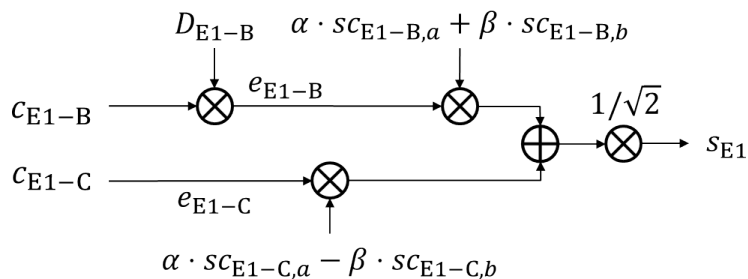


Figure 2.22 – Galileo E1 OS signal generation block diagram

used, through which the two modulations are time-multiplexed according to a predefined pattern optimized to improve the correlation properties of the signal when the effect of the PRN code is taken into account [33]. Examples of acquisition of BOC and MBOC signals are shown in [126–136]

Besides MBOC, other spreading modulations having per basis the BOC structure were also developed and will be applied in other Galileo signals. One example is the Alternative BOC (AltBOC) modulation that is applied in the Galileo E5 signal [34]. For this modulation a complex sub-carrier is used so that the signal spectrum is not split but simply shifted to higher or lower frequencies [33]. Examples of acquisition of the Galileo E5 signal can be found in [137–141].

2.5.2 Composite Signals Acquisition

As mentioned in the previous section, modern signals often have a data and a pilot (dataless) component. The introduction of a pilot component in modernized signals has per objective allowing GNSS receivers to achieve higher-sensitivity, by longer coherent integrations of this signal component [33]. Nevertheless, as can be seen in the tables present in Appendix A, the power split between the two components is often 50-50, which means that, if only the pilot component is used in acquisition, half of the signal power is not being accounted for in signal detection. In the case of weak signal acquisition, not making use of the total signal power available can be a determining factor in the success or failure of acquisition. This way, a considerable number of studies have been undertaken which study the optimal way of composite signals acquisition [142–152].

In [142], five different acquisition strategies to combine the data and pilot components in the acquisition of the Galileo E1 OS signal, E1-B and E1-C respectively, are presented and compared. These strategies are shown in Figure 2.23. The most straightforward approach is the Dual Channel approach (Figure 2.23a), in which each signal component is treated separately and the individual detection metrics are noncoherently summed prior to the detection test. The $(B \times C)$ approach (Figure 2.23b) is a modification of the differential technique, where instead of correlating each output with its previous conjugate, this correlation is done with the other component. The Assisted $(B - C)$ approach requires an assistance channel in order to assure that the navigation data bit and the pilot secondary code bit can always be considered to be in opposition. If their relative sign is known to be fixed, the structure presented in Figure 2.23c can be employed. The following approach, Summing Combination (Figure 2.23d), is an extension of the concept of the $(B - C)$ approach, but no information about the relative data/secondary code bit value is required. The final approach, Comparing Combination (Figure 2.23e), is similar to the previous one, but uses a comparator instead of a summer.

The evaluation of the performance of the different approaches is also carried in [142], and the conclusions of this study are that, in A-GNSS receivers the $(B - C)$ strategy is the one which offers better performance, while in standalone receivers, the Comparing Combination works best for

signals until 24dB-Hz, and the Dual Channel approach should be employed for signals at lower powers.

2.5.3 Handling Secondary Codes

Secondary codes have been introduced in modern GNSS signals as a way to improve the cross-correlation properties between pilot signals from different satellites [138, 145, 153–155]. The effect of the secondary code, whose data bit may span over one or more primary code periods, is very similar to that of the modulation by navigation data in data signals. Thus, one of the main consequences for the acquisition of signals containing secondary codes is that these may limit the extent to which the coherent integration time can be extended, if no consideration of the secondary code presence is taken. Several approaches for handling secondary codes in acquisition can be found in literature [15, 156–162].

The most straightforward techniques perform an extensive analysis of the different secondary codes employed, in order to be able to detect the secondary code phase prior to further increase the coherent integration time employing multi-hypothesis trial over several code periods [156, 157], and possibly applying branch elimination for reduced complexity [158]. In [15], the adaptation of the BPS correlation method for the acquisition of pilot signals in the presence of secondary codes is also shown.

Other approaches consider acquisition over a full period of the secondary code, such as [159–

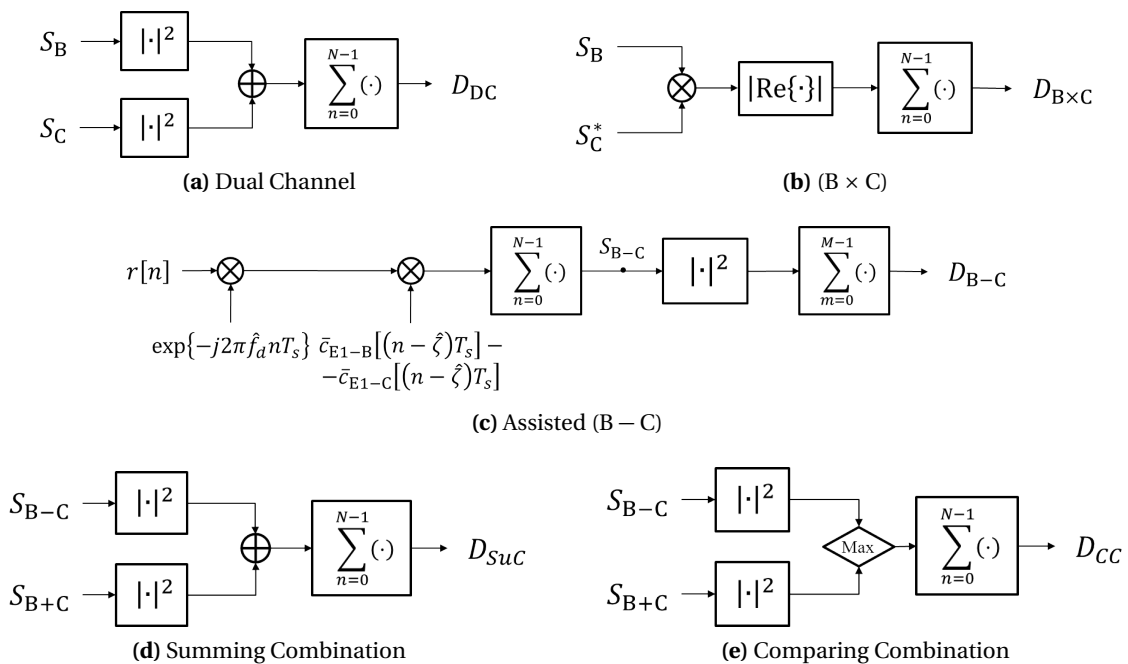


Figure 2.23 – Galileo E1 OS acquisition methods [142]

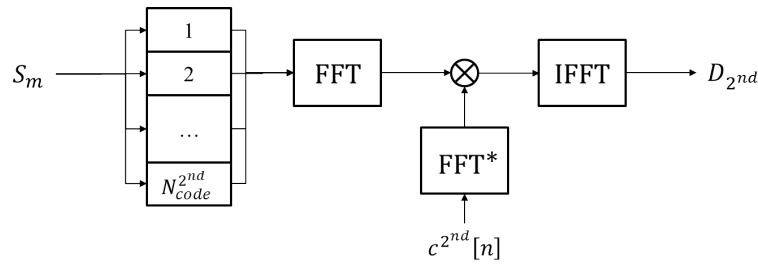


Figure 2.24 – Secondary code acquisition example

162], which consists of generating N_{code}^{2nd} correlation outputs, corresponding to the number of chips of the secondary code, and then correlating the results obtained with the secondary code itself. The method proposed in [159] for the acquisition of such signals is shown in Figure 2.24. The structure shown in this figure allows full exploitation of the secondary code, while also determining its current code phase offset.

Naturally, secondary codes can also be handled simply by treating the pilot signals as data ones, transitioning to noncoherent integration in standalone receivers or canceling the secondary code if its phase can be supplied to the user in A-GNSS receivers.

2.6 Combined Acquisition Approaches

In the new wave of GNSS developments, the multitude of available signals and constellations led to the widespread of techniques that exploit the power from several signals present, in the attempt to improve GNSS working performance in challenging environments. These techniques are given the name of *combined* acquisition approaches, and are categorized under three groups in [119]:

Channels Combining This approach refers both to the combination of data/pilot components, as shown in section 2.5.2, as well as to the acquisition of signals from the same satellite at the same frequency band.

Since the beginning of GPS, two signals in different spectral bands have been transmitted, the C/A signal in the L1 band and the P(Y)-code in both L1 and L2 bands. Even if the P(Y)-code signal is restricted to military use, authorized users can make use of both signals to improve signal detection performance at the L1 band. More recently, other studies based on publicly available signals have been published, such as [148, 163, 164]. In [163, 164] the combined GPS L1 C/A and L1C acquisition scheme shown in Figure 2.25 is proposed and evaluated, showing its merits in weak signal acquisition.

Frequencies Combining Given the significant number of transmission frequencies in which open access GNSS signals are nowadays available, a natural approach to achieve enhanced sensitivity is

by combining the energy from all signals originating from the same satellite. Several studies dealing with the acquisition of multi-frequency GNSS signals can be found in literature [165–171].

In [166], noncoherent and differential combining approaches to better exploit the availability of multi-frequency signals are analyzed, focusing on the GPS L1/L2C signals. In [168], the combined acquisition of these two signals is also analyzed, by employing a generalized differential combination technique, achieved through variable relative delay between the available correlation outputs. In [170], the best candidates of the Galileo signals for multi-frequency acquisition are investigated, concluding that a combined E1/E5a scenario is the one which provides more advantages.

Satellites Combining Satellites combining at acquisition level can take the form of Collective Detection, as presented in section 2.4.2 and further discussed in Chapter 5, or by combining satellite replicas in order to speed-up the acquisition process, in an approach known as *sum of replicas* [172–175]. The sum of replicas proposal is shown in Figure 2.26 and the result of this combined acquisition approach is seen in Figure 2.27. While Collective Detection can be seen as a high-sensitivity acquisition method as it combines all satellites into a single detection metric, thus increasing detection performance of weak signals, the approach of sum of replicas fails at achieving this objective, as signal detection is still performed relatively independent and the multiple replicas actually degrade the signal sensitivity [172–175].

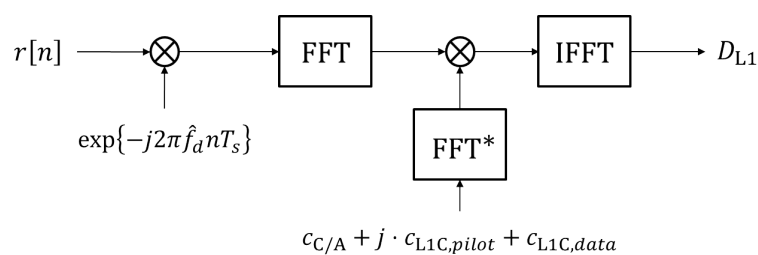


Figure 2.25 – Combined GPS L1 C/A and L1C acquisition scheme

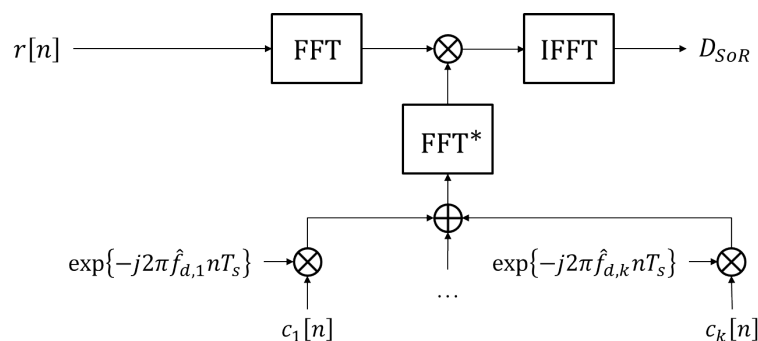


Figure 2.26 – Methodology for combined satellites acquisition through sum of replicas

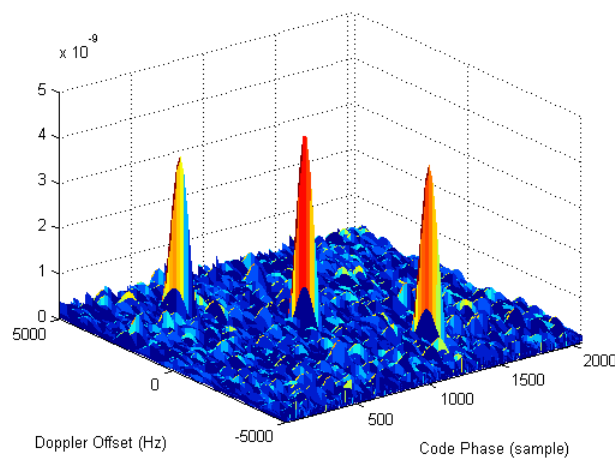


Figure 2.27 – Example of result of combined satellites acquisition through sum of replicas for the acquisition of three satellites simultaneously

2.7 Discussion

In this chapter, the principles of GNSS acquisition and the state-of-the-art of the most relevant approaches have been reviewed. For the goal of high-sensitivity acquisition, the topics approached in this subject can be summarized in a very minimal and simplified way as follows (for more details refer to all previous sections):

Frontend Signal Processing imposes minor sensitivity losses due to quantization, filtering, or other nonidealities, which could ideally be minimized but that are usually not highly significant;

Correlation and Coherent Integration incurs sensitivity losses due to the search grid employed (maximum tolerable parameter estimation error) and the extent to which it can be increased is highly dependent on the signal structure (in particular data bit or secondary codes) as well as on its parameters (in particular their rate of change during the signal integration time);

Postcoherent Integration incurs sensitivity losses with respect to coherent integration but it enables further pursuing enhanced sensitivity once coherent integration reaches its limits;

Signal Structure imposes limitations on coherent integration time and may lead to the need for transition to postcoherent integration;

Assistance Link enables the receiver to focus its computational resources in order to achieve higher sensitivities (MS-Based mode) or the calculations are performed in a base station (MS-Assisted mode); and

Combination Approaches through the combination of channels, frequencies, or even satellite signals, it is possible to increase the receiver sensitivity - this increase is dependent not only on

the signal structure but also in the different types of combinations.

Bearing in mind this simplified list, the number of interesting aspects which could have been targeted in the research of GNSS signal acquisition during this doctoral research is considerably large. As so, the choices made regarding the subjects in which to focus were object of careful consideration throughout the research period. Finally, the research angles that were defined as being relevant to the current state-of-the-art of GNSS acquisition, both from a scientific and practical engineering standpoint, and that are analyzed in detail in the remainder of this thesis are:

- Analysis and Compensation of the Doppler Effect in GNSS Acquisition - Chapter 3;
- Sensitivity Characterization of Differential GNSS Detectors - Chapter 4; and
- Systematic and Efficient Collective Acquisition of Multi-Constellation GNSS Signals - Chapter 5.

These choices were motivated by the relevance of these topics and the opportunities for meaningful contributions, achievable during the limited doctoral research period. In Chapter 3 practical solutions for adapting the design of acquisition schemes in order to obtain more Doppler-robust solutions is addressed. In Chapter 4 one of the biggest open problems in GNSS signal detection, which is the quantification of the sensitivity loss of differential detectors, is investigated, allowing for a much anticipated formal comparison between noncoherent and differential detectors. Chapter 5 is dedicated to the analysis of Collective Detection as both a high-sensitivity and direct positioning method, proposing an optimized algorithm for the systematic, robust, and efficient application of this method, also in the context of a multi-GNSS constellation receiver.

ANALYSIS AND COMPENSATION OF DOPPLER SHIFT EFFECT IN GNSS ACQUISITION

In today's world, GNSS receivers can be found in a multitude of fields and applications of human activities. Naturally, different scenarios of application also means different requirements and environments to consider, and the receiver and its algorithms must be tailored accordingly. For the acquisition module in particular, one of the main design drivers is the Doppler shift that is expected to be experienced by the user with respect to the transmitting satellites. The Doppler shift characteristic of a typical land-based GNSS user is mostly due to three major contributing sources, listed in Table 3.1 [3, 76, 77]. Apart from these, atmospheric propagation and multipath may also have an impact but on a lower scale [53, 80].

Of the three items listed in Table 3.1, a user may be able to remove to a great extent the components due to: the satellite motion, by consulting previously stored ephemeris or receiving these through an assistance link; and due to the receiver oscillator, also through calibration through an assistance link [3, 71, 76, 81]. On the other hand, the remaining component, due to the user own motion, cannot be easily modeled or removed. One option is the integration of Inertial Navigation Sensors (INS) in the acquisition module, in what is known as *aided acquisition* [53, 54, 79]. This is not, however, an easy solution to apply, raising several non-trivial challenges, such as synchroniza-

Table 3.1 – Main Doppler shift sources for GNSS receivers and typical values for land-based users

| Source | Value (Hz) |
|---------------------|--------------|
| Satellite motion | ±4880 |
| User motion | ±190 |
| Receiver oscillator | ±440 |
| Total | ±5510 |

tion between the different data sources and the reliable coupling between the two systems, as well as increasing the receiver cost.

In most existing works it is usual to assume a relatively unchanged Doppler frequency during the whole acquisition time. In these cases the impact of the Doppler offset in acquisition (in coherent integration, in particular) is managed as described in section 2.2, by imposing a limit on the product $\Delta f_d N T_s$. However, the assumption of a constant Doppler offset cannot be always considered as adequate to the study case. This is the case, for example, for the acquisition of weak signals when the observation times required in order to reliably detect their presence must be extended to tens or hundreds of code periods. According to [3], the maximum rate of change of the Doppler shift due to satellite motion for the GPS constellation is around 9Hz/s, and in average not superior to 1Hz/s. In what concerns the user motion, the frequency change rate, α , can be found through [3, 176]:

$$\alpha = a_u \cdot \frac{f_c}{c} \quad (3.1)$$

where a_u is the user acceleration projected in the user-satellite relative motion vector (the worst-case scenario can be assumed, in which the velocity vectors are parallel), f_c is the signal carrier frequency, and c is the speed of light in vacuum. Considering typical land-based user applications, in which accelerations may reach up to $1g = 9.8\text{m/s}^2$ (acceleration due to Earth's gravity), the Doppler change rate may achieve values to as much as 50Hz/s for the signals in the L1 band. This range of values may be significant when considering the tight frequency bins involved in long coherent integrations for the acquisition of weak signals. As for the receiver oscillator, it is well-known that its quality may significantly impact the acquisition sensitivity when dealing with very long coherent integration times [54, 79–81], but its effect will be considered in the upcoming analyses to be less stringent than the uncompensated user motion.

This way, three scenarios can be defined in order to assess the impact of the Doppler offset in the overall GNSS acquisition scheme design:

1. The Doppler shift remains approximately unchanged during the acquisition time - *low-dynamics*;
2. The Doppler shift changes during the acquisition time and a dynamic compensation of this change is not required to meet the user requirements - *medium-dynamics*;
3. The Doppler shift changes during the acquisition time and a dynamic compensation of this change is required to meet the user requirements - *high-dynamics*;

Each of these scenarios is analyzed in the coming sections, evaluating the effects in acquisition of the Doppler shifts respective to each scenario. For the first and third scenarios, considered as

low- and high-dynamics cases, practical solutions are proposed to improve the acquisition module design either in terms of sensitivity or complexity, and for the second scenario, named medium-dynamics, conditions for the signal integration limits that can be employed without incurring overly high decreases in sensitivity are proposed. Examples of application scenarios where the new algorithms could be useful are provided at the end of each section.

3.1 Doppler Effect Compensation in Low-Dynamics

One of the biggest challenges within acquisition is the compromise between *sensitivity* and *complexity*. Aptly defining the 2D search grid that covers the uncertainty in both code phase and Doppler frequency dimensions, in particular, is one of the main drivers of this trade-off. As the code search resolution is dictated by the PRN codes autocorrelation function and very seldom it is changed from well-known values ($1/2$ chip for BPSK modulations and $1/4$ chip for BOC(1,1)), this is particularly relevant for the resolution for the Doppler search. It was seen in section 2.2 that the correlation (or coherent processing) frequency response, $|H(\hat{f}_d)|$, in the presence of a stationary Doppler offset during the acquisition time is:

$$|H(\hat{f}_d)| = \text{sinc}(\Delta f_d N T_s) \quad (3.2)$$

where \hat{f}_d is the candidate demodulation frequency, and $\Delta f_d = f_d - \hat{f}_d$ is the offset between the true and candidate frequencies. Through this relation, the resolution of the frequency search can then be set according to the maximum desired attenuation of the correlation output. Nevertheless, as also seen in section 2.2, it is only possible to freely set the frequency resolution in correlation methods employing serial search in the frequency resolution, that is, the Serial Search (SS) and Parallel Code Search (PCS) methods. Still, it was shown that the most computationally effective correlation methods, the Bidimensional Parallel Search (BPS) and Double-Block Zero-Padding (DBZP) methods, employ Fast Fourier Transform (FFT) for frequency estimation, thus parallelizing this search. This intrinsically imposes a Doppler search resolution of $\delta f_d = 1/(N T_s)$ for these methods, and the resulting attenuation of the correlation output may reach up to 1.96dB, a loss commonly known in

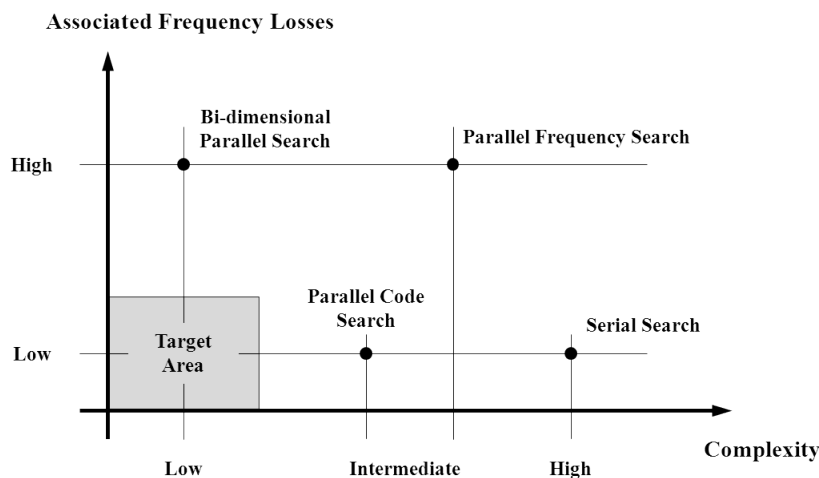


Figure 3.1 – Correlation methods qualitative comparison

digital signal processing as the FFT *scalloping loss*. Given that for the SS and PCS methods, attenuations as low as desired (for example, 0.1dB) may be achieved, the BPS and DBZP methods may be considered as unsuitable for the acquisition of weak signals, and consequently more computationally expensive methods may have to be chosen. In the case of the DBZP method, the effect of the Doppler offset on the correlation output will even be twofold as shown in section 2.2.

Therefore, the objective of the work described in this section is to achieve the target correlation methods area shown in Figure 3.1, by combining the computationally low requirements of the BPS correlation method with the level of frequency-associated losses of the SS and PCS methods. The desired objective is achieved through a fine frequency estimation stage which applies a fast and accurate FFT-based frequency estimation technique (thus compatible with FFT-base acquisition schemes) known as *Spectral Peak Location* (SPL) algorithms. This section starts with a short revision of fine frequency estimation in acquisition. Next, SPL algorithms and their advantages in fine frequency estimation are described. A methodology for their application in GNSS acquisition is then proposed, and the merits of the new approach are illustrated in the acquisition of both simulated and real data.

3.1.1 Fine Frequency Estimation in Acquisition

It may be the case that the resolution obtained from acquisition for both code phase and Doppler estimates is too coarse for the following step in the signal processing chain. An approach which can be followed in order to improve the estimation accuracy without significantly increasing the complexity, or the execution time, of the acquisition process is to employ a *fine acquisition stage*. This additional stage has per objective reducing the residual uncertainties for both parameters within the search bins (Figure 3.2). The issue of improved code phase estimation has received recent attention in order to allow more advanced GNSS receiver approaches such as open-loop [177] and snap-shot [112–116] positioning techniques, and can be achieved by applying code interpolation techniques, derived according to the spreading code auto-correlation shape [112, 113].

For fine frequency estimation, algorithms such as phase difference have been extensively used that allow precisely the refining of the frequency estimate, given a first rough estimate [3, 55, 178–181]. Fine frequency estimation, however, is often treated only once signal detection has already been achieved, which ultimately depends on the coarse search grid's suitability to detect signals. A good example of frequency offset estimation to improve signal detection is shown in [17, 52], in which this information is used to form a Frequency Offset Correction (FOC) loop, to update the local carrier frequency during the acquisition process, therefore enhancing its signal detection capabilities (see section 3.3). These are, nevertheless, computationally expensive techniques.

Another common approach to determine the frequency of a given signal, repeatedly employed in GNSS acquisition as well as in other engineering and scientific domains, is spectral analysis

by means of the Discrete Fourier Transform (DFT), or its efficient implementation, the Fast DFT (FFT) [4, 15, 182]. The main drawback of its use is the previously described scalloping loss, which may become problematic once the expected input signal powers are too low. To counteract this limitation of the FFT, techniques such as windowing [69] or zero-padding [72] of the input signal have been proposed. These, however, are computationally demanding operations for the acquisition module of a GNSS receiver. Therefore, we shall employ a lower complexity solution, as presented next.

3.1.2 Fine Frequency Estimation using Spectral Peak Location Algorithms

One approach to refine the FFT frequency estimation is the application of Spectral Peak Location (SPL) techniques (Figure 3.3) [179, 183–189]. The general concept of SPL estimators is to obtain the estimate of the spectral peak index, k_{peak} , based on three consecutive FFT samples. For a given signal $r[n]$, spectral analysis through FFT will produce:

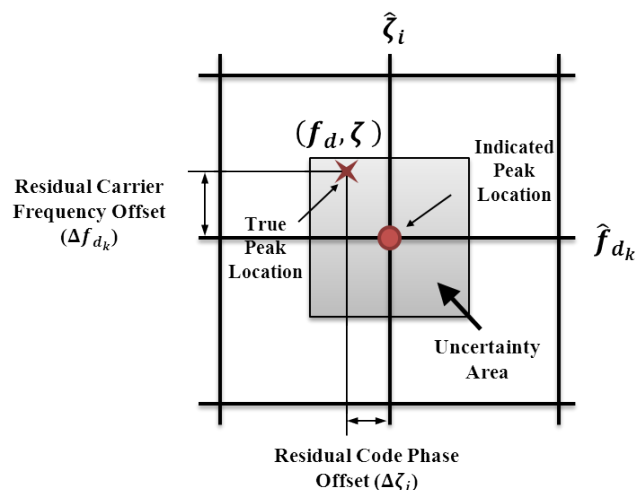


Figure 3.2 – Acquisition parameters residual uncertainty in a coarse search grid

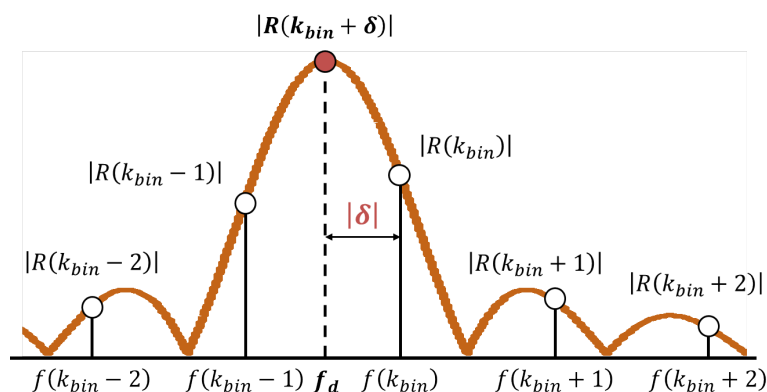


Figure 3.3 – Illustration of scalloping loss and principle of Spectral Peak Location algorithms

$$\begin{aligned}
R(k_{bin} - 1) &= \sum_{n=0}^{N-1} r[n] \cdot e^{-j2\pi(k_{bin}-1)\frac{n}{N}} \\
R(k_{bin}) &= \sum_{n=0}^{N-1} r[n] \cdot e^{-j2\pi(k_{bin})\frac{n}{N}} \\
R(k_{bin} + 1) &= \sum_{n=0}^{N-1} r[n] \cdot e^{-j2\pi(k_{bin}+1)\frac{n}{N}}
\end{aligned} \tag{3.3}$$

where $R(k)$ is the FFT output at index k , and k_{bin} corresponds to the frequency bin which produces the highest magnitude FFT output (ideally corresponding to the candidate frequency closer to the actual signal frequency). From these three FFT outputs, the SPL estimator then provides a fractional correction term, δ , which is added to the k_{bin} index to determine the fine k_{peak} estimate:

$$k_{peak} = k_{bin} + \delta \tag{3.4}$$

In [183, 184], a thorough comparison of 7 different SPL estimators is undertaken. One of the best-performing algorithms was picked for analysis in this study, through which the delta-correction term is obtained as:

$$\delta = -\Re \left\{ \frac{R(k_{bin} + 1) - R(k_{bin} - 1)}{2R(k_{bin}) - R(k_{bin} - 1) - R(k_{bin} + 1)} \right\} \tag{3.5}$$

Although (3.5) was first proposed as a heuristic formulation, it is shown in [189] that this formula is very similar to the one obtained when mathematically deriving it by expanding the DFT operation into a Taylor series and solving for δ . It should be noted that in [179], an interesting derivation of an estimator resembling the one in (3.5) is presented, and it is mentioned that the new estimator has the potential to outperform the chosen one for lower input signal powers. This improvement, nevertheless, should not be significant as both estimators are shown to approach the Cramer-Rao lower bound.

To illustrate the SPL algorithm's capacity to improve the FFT frequency estimation accuracy of a GNSS signal, a 1ms-long GPS C/A signal is generated at a 500Hz Doppler offset, which corresponds to the middle frequency between two consecutive FFT bins ($\delta f_d = 1/T_{coh} = 1\text{kHz}$). This signal is then processed by the PFS acquisition method described in section 2.2.2 and for the purposes of this illustration the signal and local codes were previously aligned ($\hat{\zeta} = \zeta$). The results of the FFT frequency estimation with and without the SPL-corrected (or delta-corrected) algorithm are shown in Figure 3.4. Three different C/N_0 values are employed in this analysis and the procedure is repeated 10000 times for each of them. The histograms presented in Figure 3.4 show that, as

expected, the simple or uncorrected FFT frequency estimation (left) consistently provides the two values corresponding to the frequency bins equidistant from the true offset value (0 and 1kHz), naturally depending on the noise influence at each simulation. Contrarily, the SPL-corrected FFT estimator (right) provides a wide range of values with fewer incidences, but it is noticeable that the estimates provided are quite more accurate than the ones obtained with the uncorrected approach.

The two approaches can be statistically compared for the possible range of different Doppler shifts within a frequency bin, ranging from zero until the middle-bin offset value (the other half segment can be considered equivalent). The plots in Figure 3.5 show the evolution of the estimation bias and standard deviation of the two estimators as function of the offset employing the same 1ms-long GPS C/A signal for two different C/N_0 values (100000 simulations are carried for each offset value).

It can be observed from the plots in Figure 3.5 that for a large portion of the frequency bin, the application of the SPL delta-correction technique significantly improves the estimation bias performance without compromising its standard deviation. This is only not verified for low offsets at high C/N_0 values, which is explained due to the accuracy of the simple FFT estimation in these cases (see Figure 3.6 for the comparison of estimation of a 0Hz offset). Furthermore, it should be noted that, even though the bias of the uncorrected approach tends to zero when the offset approaches the middle-bin value, this is due to the effect shown in Figure 3.4, where the estimation is equally divided between the two consecutive bins. This is observable on the high standard deviation observed for the uncorrected approach for the same offset values.

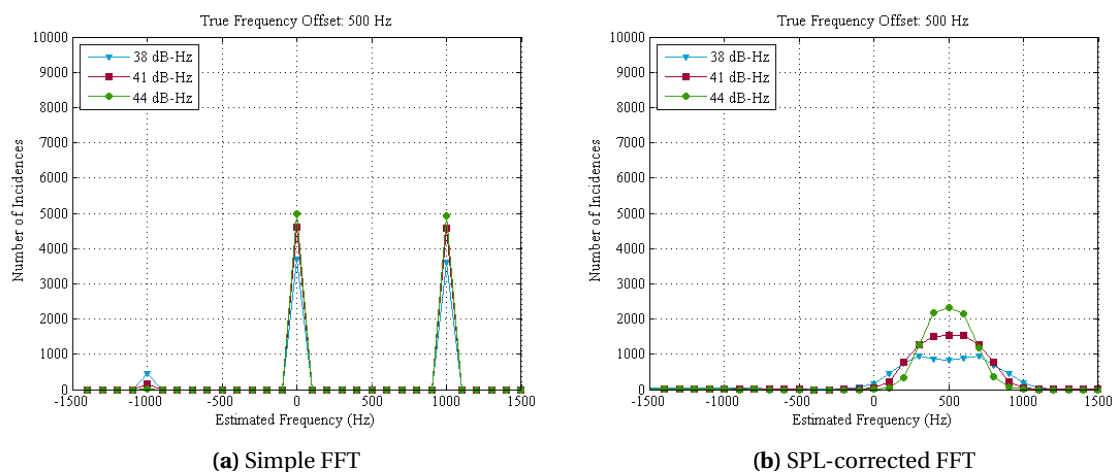


Figure 3.4 – Histograms of FFT frequency estimation applying the simple and SPL-corrected estimator for a mid-bin ($\delta = 0.5$) offset value for a 1ms GPS C/A signal

3.1.3 Application of SPL Algorithms in GNSS Acquisition

Having introduced the suitability of SPL techniques for the accurate estimation of an unknown frequency of a GNSS signal, a new methodology for GNSS signal acquisition can now be developed. The delta-corrected algorithm can be useful in any acquisition method employing parallel frequency search, as are the cases of the PFS, BPS, and DBZP correlation methods. As shown in Figure 3.7, SPL algorithms can be employed jointly with these correlation methods in two different ways:

1. Refine the frequency estimation once detection is achieved; or
2. Attempt acquisition with the fine frequency if detection has not been achieved.

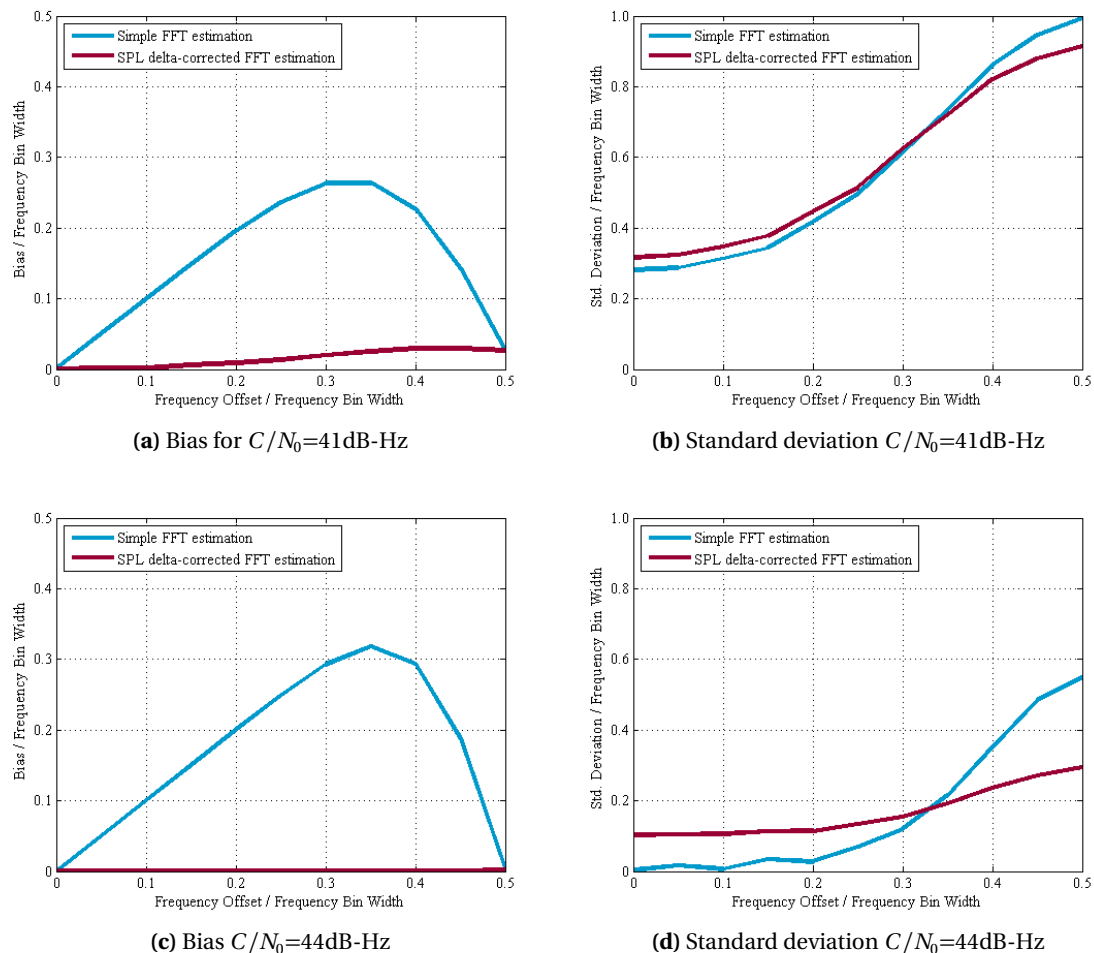


Figure 3.5 – Frequency estimation applying simple and SPL-corrected estimator for a middle-bin offset value at $C/N_0 = 41$ dB-Hz (top) and 44 dB-Hz (bottom) for a 1ms GPS C/A signal

In the case when no detection is achieved, the posterior acquisition attempt with the fine frequency is done through an execution of the serial search correlation method described in section 2.2.1, using the code phase corresponding to the peak location which produced the highest output in the initial execution, and the delta-corrected frequency, $\hat{f}_d = \hat{f}_{d_k} + \hat{f}_\delta$, where \hat{f}_δ is the frequency correction term obtained as $\hat{f}_\delta = \hat{\delta} \cdot \delta f_d$ and $\hat{\delta}$ is calculated as in (3.5). The new delta-corrected coherent output, $S_{delta}(\hat{\zeta}, \hat{f}_d)$, is then obtained as:

$$S_{delta}(\hat{\zeta}, \hat{f}_d) = S_{delta}(\hat{\zeta}, \hat{f}_{d_k} + \hat{f}_\delta) = \sum_{n=0}^{N-1} r[n] \cdot c_k[(n - \hat{\zeta})T_s] e^{-j2\pi(f_{IF} + (\hat{f}_{d_k} + \hat{f}_\delta)nT_s)} \quad (3.6)$$

which, according to (2.18) results in:

$$S_{delta}(\hat{\zeta}, \hat{f}_d) = \sqrt{\frac{P_k}{2}} R(\Delta\zeta) \text{sinc}(\Delta f_{d,\delta} N T_s) + \tilde{w}_N \quad (3.7)$$

The new offset term, $\Delta f_{d,\delta}$, is characterized by the bias and standard deviation plots shown in Figure 3.5. It should be noted that this calculation of the delta-corrected detection metric is not in fact required, as the additional gain can be simply summed to the already existing detection metrics. Nevertheless, the additional computational complexity will be seen not to be significant in any case. The performance of the new acquisition approach is assessed next.

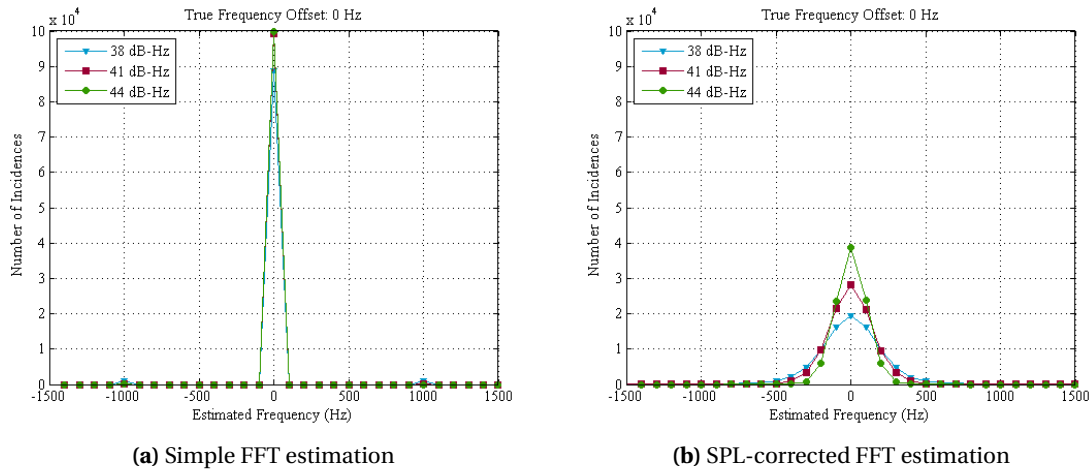


Figure 3.6 – Histograms of FFT frequency estimation applying the simple and SPL-corrected estimator for a 0Hz offset for a 1ms GPS C/A signal

3.1.4 Performance Analysis

According to the diagram in Figure 3.1, the targeted correlation approach should ideally present a computational complexity of the same order of the BPS method and, at the same time, be capable of achieving the low frequency losses of the PCS and SS methods. For this reason, in the following analysis we focus on the delta-corrected BPS implementation rather than on the PFS one. As previously mentioned, the DBZP method is not considered in this analysis due to the twofold effect of the Doppler offset in its sensitivity, which is not fully mitigated by the proposed approach.

Two types of analysis are carried to evaluate the improvements obtained with the newly-developed methodology. At first, the sensitivity gain of the delta-corrected BPS approach with respect to the simple or uncorrected BPS is assessed. Next, the computational complexity of the new approach is compared with the one of a PCS implementation that ensures an equivalent maximum correlation output attenuation.

Delta-corrected BPS Sensitivity Gain To illustrate the sensitivity gain achievable when employing the delta-corrected BPS approach with respect to the simple or uncorrected BPS, three examples

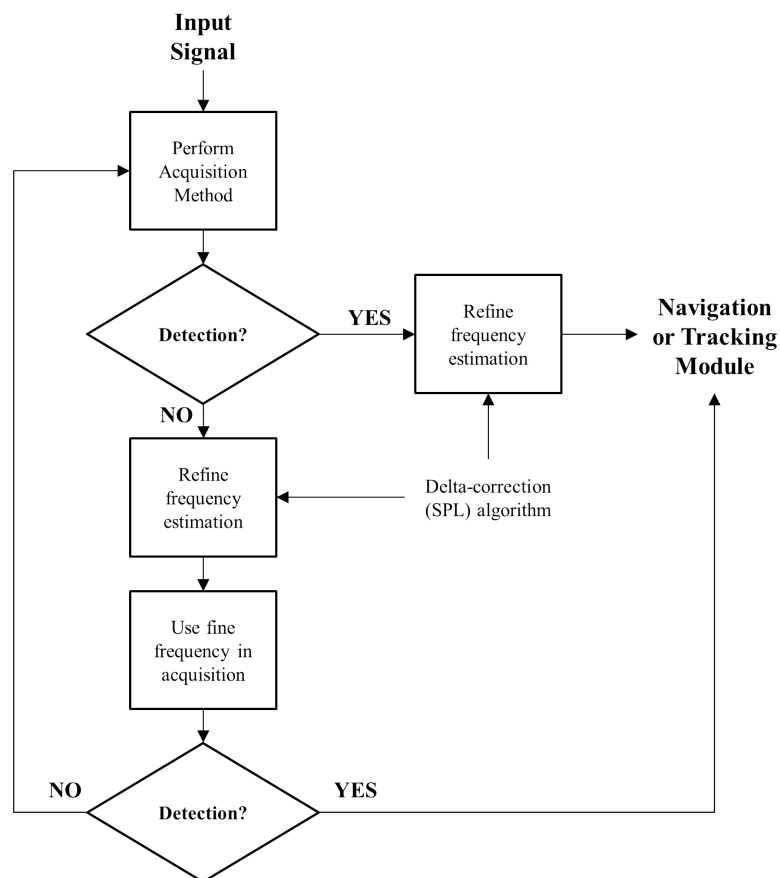


Figure 3.7 – Block diagram of the proposed delta-corrected acquisition method

applying a 1ms-long GPS C/A signal are shown in Figure 3.8. These examples consist of generating the input signal, sampled at twice the chip rate, 10000 times for a set of C/N_0 values in the range shown in the plots. The SLD detector is applied, meaning that the detection metric considered is:

$$D(\hat{\zeta}, \hat{f}_d) = |S(\hat{\zeta}, \hat{f}_d)|^2 \quad (3.8)$$

The total Doppler uncertainty considered is $\pm 5\text{kHz}$, which implies that a total of $N_{f_d} = \lceil \Delta F_d / \delta f \rceil = \lceil \Delta F_d \cdot T_{coh} \rceil = 11$ frequency search bins must be scanned, with $\lceil \cdot \rceil$ standing for the nearest integer rounded towards $+\infty$. The number of code bins to be searched is equivalent to the number of samples per code period, that is, $N_s = f_s \cdot T_{code} = 2046$, which means that for each satellite a total of approximately $2.3 \cdot 10^4$ search cells need to be considered. This way, the overall probability of false alarm is set to 10^{-6} , which assures one false alarm in approximately 50 acquisitions. The detection threshold is set according to (2.32).

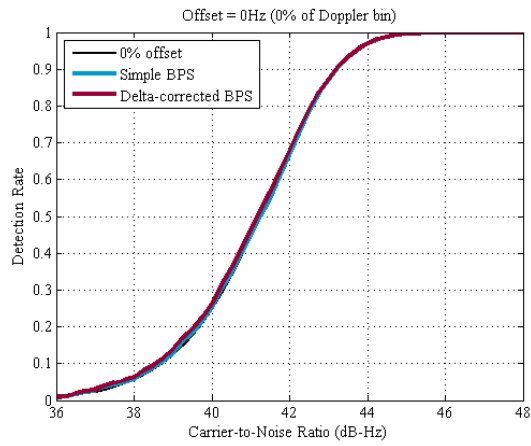
Three offset/resolution ratios ($\Delta f_d / \delta f$) are shown in the plots in Figure 3.8: 0% (no offset), 25% (middle value), and 50% (extreme value). From the analysis of these plots, it can be noted that, while the simple BPS acquisition method on its own naturally suffers the attenuations derived from the non-zero offsets, the delta-corrected one is effectively capable of mitigating this effect with minimal decrease in performance. A more in-depth analysis of simulation results shows that the delta-corrected approach is more efficient in signal detection than the uncorrected one for offsets $\Delta f_d / \delta f \geq 0.05$, which amounts to 90% of the search grid. For the worst-case situation of a middle bin offset value ($\Delta f_d / \delta f = 0.5$), the attenuation observed with respect to the ideal case ($\Delta f_d / \delta f = 0$) is only of approximately 0.3dB.

It is also interesting to note that for a mid-bin offset value (Figure 3.8c), although the peak attenuation for the simple BPS method at the expected frequency bin is of 3.92dB, an average loss of performance of only about 2.8dB is verified with this method. This is due to the fact that the true signal frequency is in the border between two consecutive frequency bins, so the central frequencies of bins k and $k + 1$ are equidistant to the true signal frequency. This way the probability of detection verified is in fact given by:

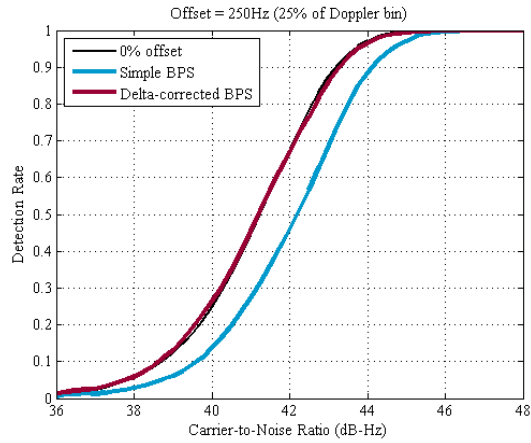
$$P_d = P\left(D(\hat{\zeta}, \hat{f}_{d_k}) > V_{th} \cup D(\hat{\zeta}, \hat{f}_{d_{k+1}}) > V_{th}\right) \quad (3.9)$$

which is then reflected in a lower sensitivity decrease than would be expectable.

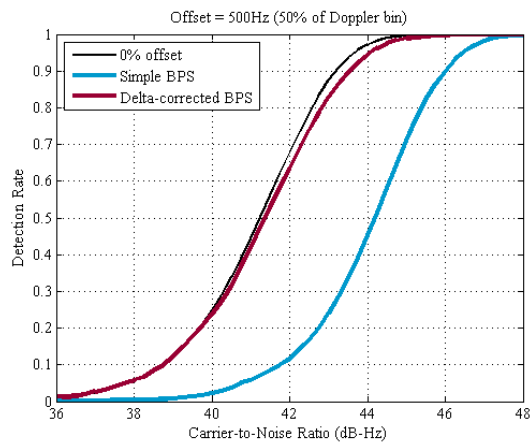
Delta-Corrected Approach Complexity Gain The maximum attenuation of the new acquisition method was seen to be of only around 0.3dB with respect to the 0% offset case. This way, the delta-corrected BPS method is equivalent in detection performance to a PCS implementation ensuring a



(a) 0% offset/resolution ratio



(b) 25% offset/resolution ratio



(c) 50% offset/resolution ratio

Figure 3.8 – Sensitivity analysis of the simple and delta-corrected BPS acquisition methods for a 1ms GPS C/A signal and $\Delta f_d / \delta f = 0\%$ (top), 25% (middle), and 50% (bottom)

similar maximum attenuation. According to (2.18), the search grid resolution required for the PCS method to ensure this maximum attenuation of the detection metric is (note that 20 is used in the conversion to dB instead of 10 due to the squaring of the correlation output to generate the SLD detection metric):

$$20 \cdot \log_{10} [\text{sinc}(\delta_f/2 \cdot T_{coh})] = 0.3 \iff \delta_f = \frac{0.288}{T_{coh}} \approx 300\text{Hz} \quad (3.10)$$

For a total Doppler uncertainty of 10kHz, this implies scanning $N_{fd} = 34$ frequency bins. The comparison of the PCS, simple and delta-corrected BPS algorithms in terms of mean execution time and correct detections is shown in Table 3.2 for the worst-case Doppler offset for each acquisition method. Two PCS implementations are shown, PCS1 employing a grid resolution of 1kHz, equivalent to that of the uncorrected BPS scheme, and PCS2 with a resolution of 300Hz, to ensure the 0.3dB maximum attenuation of the detection metric. The algorithms' execution times presented are obtained for a Matlab implementation, and correspond exclusively to the time of execution of the routine of the acquisition method. The SLD detector is applied once again and the probability of false alarm is set to 10^{-6} for all acquisition schemes.

From the results shown in Table 3.2, the computational efficiency of the delta-corrected BPS method with respect to the PCS2 is well remarked, the former being approximately 2.5 times faster while achieving the same detection performance of the latter. The difference in computational efficiency between the two methods may even be higher if efficient architectures, such as in [190], are employed. Furthermore, it can also be seen in the table that the delta-corrected BPS approach exhibits a very slight increase in computation time with respect to the simple BPS, thus fulfilling the objective previously set.

Table 3.2 – Fine and coarse-grid PCS, simple and delta-corrected BPS methods comparison

| Method | Average run time (ms) | % of detections per C/N_0 | | |
|--------------|-----------------------|-----------------------------|---------|---------|
| | | 38dB-Hz | 41dB-Hz | 44dB-Hz |
| PCS1 | 9.6 | 3.4 | 6.9 | 45.5 |
| PCS2 | 27.7 | 11.6 | 53.7 | 97.3 |
| BPS | 11.1 | 3.4 | 6.9 | 45.5 |
| δ BPS | 11.3 | 11.6 | 53.7 | 97.3 |

3.1.5 Real Signals Acquisition

To validate the merits of the newly developed acquisition method, its performance is tested in real urban conditions. Three different scenarios of application are chosen for illustration.

- Scenario S1: static data collection in “unobstructed” parking lot;
- Scenario S2: Toulouse downtown, narrow streets (Figure 3.9a);
- Scenario S3: Toulouse downtown, avenues (Figure 3.9b).

For this evaluation, 1 second of data is recorded at each scenario, from which 1000 independent blocks of data corresponding to 1ms-long GPS C/A signals are extracted. The data collection was carried with a NordNav R30 receiver working at a sampling frequency of 16.37MHz, and a NovAtel SPAN system was used to obtain reference values for the visible satellites’ Doppler offsets and C/N_0 .

The first step for the data analysis is setting the detection threshold according to the noise distribution and its variance. For this purpose, the distribution of the output of the correlation (real or imaginary part) when testing a non-present PRN is used to generate a noise-only data set. An example histogram of the noise samples obtained in this way is shown in Figure 3.10, where the Gaussian nature of the noise is well-remarked. Also here the SLD detector is applied so, once the correlation output noise variance is estimated, the threshold is set according to (2.32).

Considering again a Doppler uncertainty of $\pm 5\text{kHz}$ and the signal observation time of 1ms, the number of grid points in the frequency dimension is $N_{fd} = 11$. The number of code bins to be searched is equivalent to the number of samples per code period, that is, $N_s = f_s \cdot T_{code} = 16368$. This amounts to a total of approximately $1.8\text{E}5$ search cells for each satellite. This way, the overall probability of false alarm is set to $1\text{E}-7$ per satellite, which assures one false alarm in over 50 acquisitions.

The results of the application of the simple and delta-corrected BPS acquisition methods to the three sets of data are shown in Table 3.3. In this table, two figures are presented for each scenario.



(a) Toulouse downtown, narrow streets



(b) Toulouse downtown, avenues

Figure 3.9 – Scenarios of data collection - Toulouse downtown

Table 3.3 – Real data comparison of simple and delta-corrected BPS acquisition methods

| Scenario | Average number of satellites acquired | | Percentage of higher success rate | |
|----------|---------------------------------------|--------------|-----------------------------------|--------------|
| | Simple BPS | δ BPS | Simple BPS | δ BPS |
| S1 | 7.2 | 7.3 | 0.0 | 6.6 |
| S2 | 3.8 | 3.8 | 0.0 | 2.4 |
| S3 | 6.1 | 7.4 | 0.0 | 81.6 |

The first one concerns the average number of acquired satellites for the total 1000 data points, and the second one compares the percentage of time that one method exhibits better performance than the other in terms of the number of satellites acquired. According to the results in this table, no considerable difference between the two algorithms is visible for scenarios S1 and S2, but the percentage of times that the delta-corrected approach outperforms the simple approach for scenario S3 is very significant. These results can also be interpreted by comparing the number of detections achieved by each method for each visible satellite (as signaled by the reference system) for each scenario considered. These plots are shown in Figure 3.11.

From Figure 3.11 it becomes clear the effect of the delta-corrected approach on the improvement of the detection of some satellites. While in scenarios S1 and S2 this improvement is not substantial (also because most visible satellites are acquired nearly 100% of the time with the simple approach, leaving little room for improvement), in scenario S3 it can effectively be noticed a significant improvement in the acquisition of SVs PRN4, PRN5, PRN10 and PRN23.

In order to better understand the reasons for this significant improvement, the mean Doppler offset and C/N_0 provided by the reference system for the satellites in view for the data points of scenario S3 is shown in Table 3.4. Analyzing the values in this table, it becomes clear that the

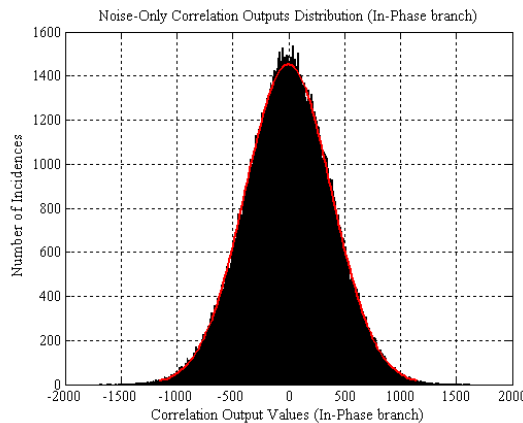


Figure 3.10 – Noise-only correlation output histogram for real data collection

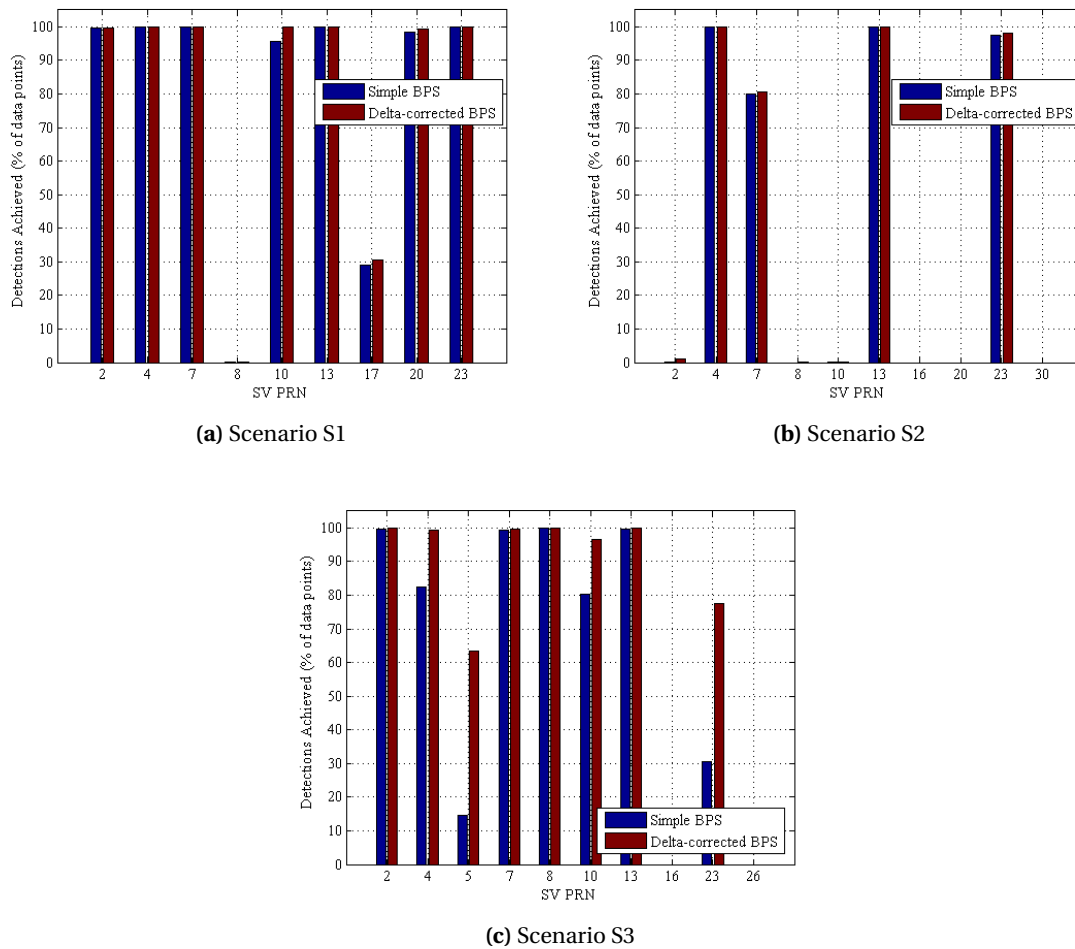


Figure 3.11 – Percentage of detections achieved with the simple and delta-corrected BPS method for each visible satellite for scenarios S1 (top left), S2 (top right), and S3 (bottom)

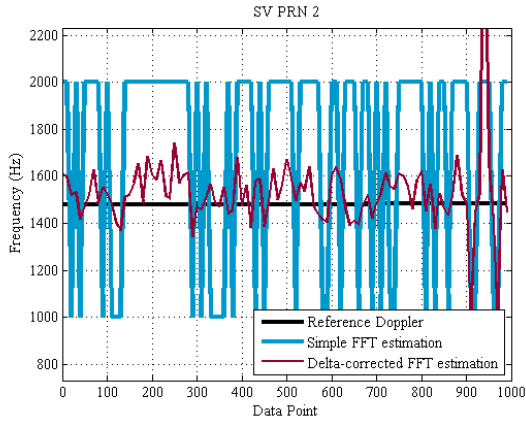
Table 3.4 – Mean Doppler offset and C/N_0 for satellites in view for scenario S3

| SV PRN | Mean Doppler offset (Hz) | Mean C/N_0 (dB-Hz) | SV PRN | Mean Doppler offset (Hz) | Mean C/N_0 (dB-Hz) |
|--------|--------------------------|----------------------|--------|--------------------------|----------------------|
| 2 | 1450 | 48.1 | 8 | 4080 | 48.9 |
| 4 | -1570 | 48.1 | 10 | 1550 | 47.1 |
| 5 | 4480 | 46.7 | 13 | -1020 | 48.6 |
| 7 | 1930 | 48.1 | 23 | -1550 | 46.4 |

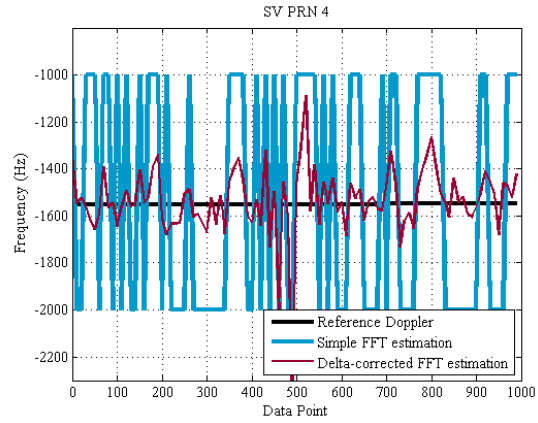
aforementioned satellites are in fact in very good conditions to profit from the application of the delta-corrected acquisition methodology, that is, their mean Doppler offset is close to a mid-bin frequency value, and in the cases of the SVs PRN5 and PRN23 their mean C/N_0 values are slightly lower than that of other satellites, but still strong enough to be acquired employing just 1ms of data. Figure 3.12 shows the simple and delta-corrected FFT frequency estimation for six satellites in this scenario. As also seen in this figure, an improved frequency estimation can also be provided by the fine acquisition stage for strong satellites such as SVs PRN2 and PRN10.

3.1.6 Scenario of Application: Mass-market receivers

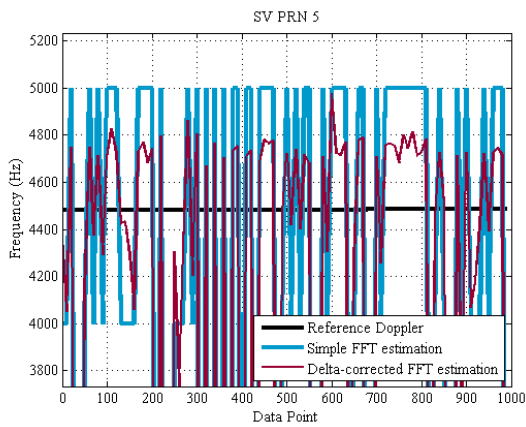
As stated in the introduction to this section, the goal of the proposed methodology is to reduce the Doppler-induced losses in the coherent processing output of the acquisition methods employing parallelization of the frequency search through FFT. By alleviating these losses for these acquisition methods, without significantly increasing their complexity of execution, the decision of the most adequate acquisition method according to the sensitivity-complexity trade-off characteristic of acquisition can be questioned. This is particularly relevant for mass-market receivers, in which the receiver power constraints and the user time-to-first-fix requirements can become troublesome to achieve. The proposed methodology may thus find usefulness in this kind of receiver design.



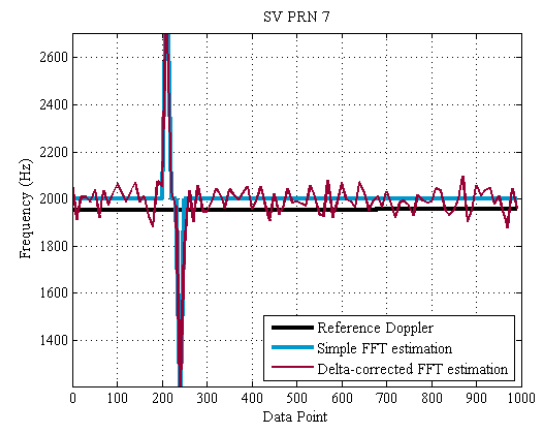
(a) Frequency estimation SV PRN2



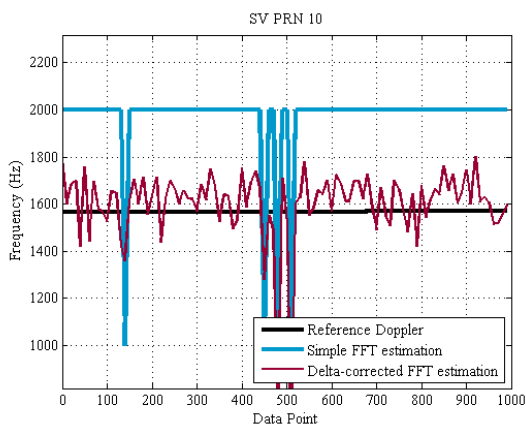
(b) Frequency estimation SV PRN4



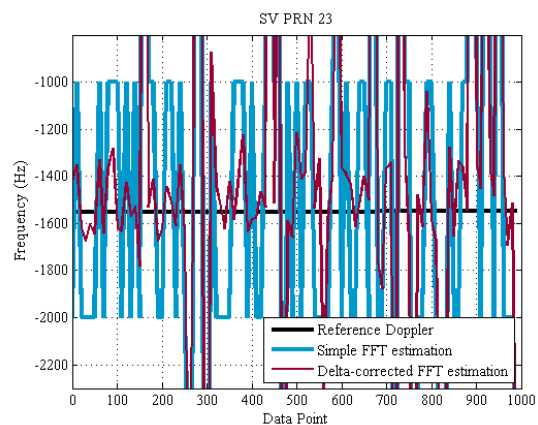
(c) Frequency estimation SV PRN5



(d) Frequency estimation SV PRN7



(e) Frequency estimation SV PRN10



(f) Frequency estimation SV PRN23

Figure 3.12 – Reference and estimated (simple and delta-corrected) frequency value for different SVs for scenario S3

3.2 Doppler Effect Analysis in Medium-Dynamics

In the previous section, the analysis of an unchanged Doppler shift during the acquisition time was carried. This assumption, however, cannot be considered as valid in every scenario of acquisition. For example, for the acquisition of weak signals, observation times equivalent to tens or hundreds of code periods may be required, and the user-satellite dynamics involved need to be considered. Likewise, for acquisition in satellite-based receivers, the signal powers involved and the satellite-to-satellite dynamics also require prior consideration [191, 192]. It may happen, nevertheless, that even if it is known that there will be a variation of the input signal frequency during the acquisition time, the impact of this change on the acquisition performance may still be considered as tolerable. This way, the Doppler change can be dealt with simply by adapting the signal integration times to the expected level of dynamics. For this, however, it is essential to analyze the effect of a changing Doppler on the different acquisition schemes' behavior.

Assuming that the Doppler shift experienced by a given user will change at a rate α , a simple 1st order model can be established for the input signal frequency:

$$f_d[n] = f_{IF} + f_{d_0} + \alpha \cdot n T_s \quad (3.11)$$

where f_{d_0} is the Doppler shift perceived by the receiver at the start of the signal observation. Such a signal, characterized by a linearly changing frequency, is known as a *chirp*. The analysis of the effect of this signal model in acquisition is split here into three different cases. First, the SLD detector is considered, meaning that only coherent integration is performed (single coherent output). In the second and third cases, other detector types are considered, in which both coherent (multiple coherent outputs) and postcoherent integrations are performed, and the effect of the chirp signal on both types of integration is assessed separately.

3.2.1 Coherent Integration - Single Output

In presence of a changing Doppler and keeping a constant candidate demodulation frequency, \hat{f}_d , the frequency response of the coherent signal processing, $|H(\hat{f}_d)|$, is given by (note that f_{IF} is omitted for readability):

$$\begin{aligned} |H(\hat{f}_d)| &= \left| \sum_{n=0}^{N-1} e^{j2\pi f_d n T_s} \cdot e^{-j2\pi \hat{f}_d n T_s} \right| = \left| \sum_{n=0}^{N-1} e^{j2\pi (f_d - \hat{f}_d) n T_s} \right| \\ &= \left| \sum_{n=0}^{N-1} e^{j2\pi (f_{d_0} - \hat{f}_d) n T_s} \cdot e^{j2\pi \alpha (n T_s)^2} \right| = \left| \sum_{n=0}^{N-1} e^{j2\pi \Delta f_{d_0} n T_s} \cdot e^{j2\pi \alpha (n T_s)^2} \right| \end{aligned} \quad (3.12)$$

where Δf_{d_0} represents the offset between \hat{f}_d and f_{d_0} . From (3.12), we can define two parameters:

$$\begin{cases} \gamma = \alpha \cdot (NT_s)^2 = \alpha \cdot T_{coh}^2 \\ \mu_0 = \Delta f_{d_0} \cdot NT_s = \Delta f_{d_0} \cdot T_{coh} \end{cases} \quad (3.13)$$

The first parameter, γ , is named as the *sweep factor* in [45]. This naming comes from the fact that γ relates the total Doppler change during the coherent integration time, $\Delta(f_d) = f_d[T_{coh} = NT_s] - f_d[0] = \alpha \cdot T_{coh}$, with a Doppler bin of width $\delta f_d = 1/T_{coh}$, that is:

$$\gamma = \frac{\Delta(f_d)}{\delta f_d} = \alpha \cdot T_{coh}^2 \quad (3.14)$$

Likewise, the second parameter, μ_0 , can also be interpreted as a ratio, in this case between Δf_{d_0} and the same Doppler bin width. The graphical definition of both parameters is shown in Figure 3.13. This way, the frequency response of coherent integration for a chirp signal can be rewritten as:

$$|H(\hat{f}_d)| = \left| \sum_{n=0}^{N-1} e^{j2\pi\mu_0(\frac{n}{N})} \cdot e^{j2\pi\gamma(\frac{n}{N})^2} \right| \quad (3.15)$$

Although no closed-form expression for (3.15) could be obtained, it can be observed from simulations that the parameters μ_0 and γ completely characterize the behavior of $|H(\hat{f}_d)|$. A plot of the normalized $|H(\hat{f}_d)|$ as function of μ_0 and γ is shown in Figure 3.14. In this figure, three Doppler bins of width $1/T_{coh}$ are shown: the one for which the central frequency is \hat{f}_d and containing f_{d_0} , marked as Doppler bin k (Doppler bin under analysis), and its two adjacent bins, $k-1$ and $k+1$. The values of μ_0 are obtained with respect to the center frequency of Doppler bin k .

From the analysis of Figure 3.14 two main conclusions can be drawn. The first one is that, somewhat surprisingly, the presence of a Doppler change *may effectively be helpful* in acquisition in some particular cases. For example, let us consider the case when $\gamma = 0$ (zone marked with the red rectangle in the figure), corresponding to the well-known sinc profile. It can be seen in the figure that

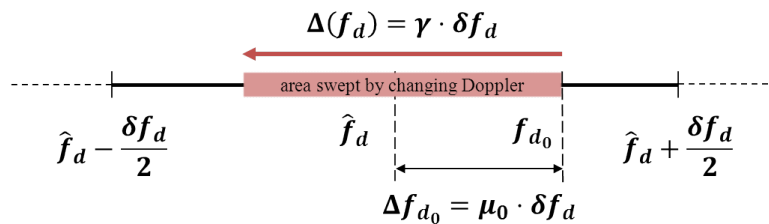


Figure 3.13 – Graphical definition of γ and μ_0

for values of Δf_{d_0} close to the limit of the frequency bin ($\mu_0 \approx 0.5$) it may be preferable to experience a Doppler change that brings the incoming frequency closer to the center of the bin, rather than remain at the initial value (compare, for example, $(\mu_0, \gamma) = (0.5, 0)$ and $(0.5, -0.5)$ or $(-0.5, 0)$ and $(-0.5, 0.5)$). Furthermore, if the adjacent bins are also considered, it can be concluded that for these particular cases and the range of γ shown in the figure, the presence of a Doppler change seems to be favorable to acquisition, as it will either approach the Doppler offset to the center of the k^{th} bin or one of its adjacent ones.

This leads to the second conclusion, which is that, under these assumptions, the Doppler bin which will contain most of the signal energy is not necessarily the one containing f_{d_0} . Comparing the two points A and B marked in the figure, corresponding to $(\mu_0, \gamma) = (-0.25, -0.75)$ and $(0.75, -0.75)$ respectively, it is clear that for the k^{th} Doppler bin the energy accumulated for point B is higher than for point A, even if point B implies that f_{d_0} is located outside the Doppler bin under analysis ($|\mu_0| > 0.5$).

This observation gains a considerable significance if the adjacent Doppler bins are also taken into account. For example, let us consider the points $(\mu_0, \gamma) = (0, -1)$ and $(1.5, -1)$. According to the plot, the energy accumulated for the Doppler bin k is clearly seen to be higher for the second point than for the first one, even if for the second case *the Doppler frequency will not even enter the Doppler bin k* . In Figure 3.15 the Doppler bins which will effectively accumulate more signal energy as function of γ when the initial signal frequency is within bin k are shown, as well as the corresponding values of $|H(\hat{f}_d)|$ (normalized). Three distinct regions can be clearly seen in this figure, highlighting the areas in which each of the bins will accumulate more energy.

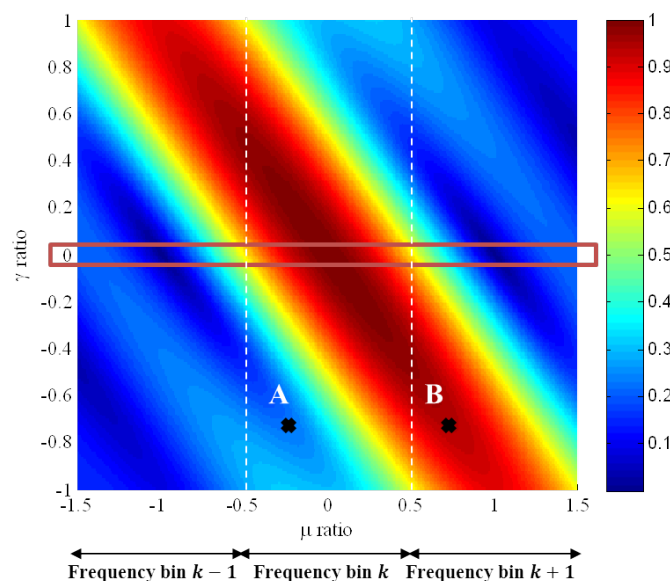


Figure 3.14 – Normalized $|H(\hat{f}_d)|$ as function of μ_0 and γ for Doppler bin k

To reinforce these observations, three sensitivity plots are shown in Figure 3.16, where for each value of μ_0 (0% in Figure 3.16a, 25% in Figure 3.16b, and 50% in Figure 3.16c), three values of γ (25%, 50%, and 100%) are compared with the case of a static Doppler offset for the same μ_0 . One code period of the GPS L1 C/A signal is used in simulations and the probability of false alarm is set to 10^{-5} . A perfect code alignment and no data bit transition are also assumed for simplification. The final detection metric is obtained as:

$$D(\hat{\zeta}, \hat{f}_{d_k}) = \max \left\{ D_{SLD}(\hat{\zeta}, \hat{f}_{d_{k-1}}), D_{SLD}(\hat{\zeta}, \hat{f}_{d_k}), D_{SLD}(\hat{\zeta}, \hat{f}_{d_{k+1}}) \right\} \quad (3.16)$$

It should be noted that this combined detection metric will induce a slightly higher probability of false alarm, but the effect is minimal. Observing the plots in Figure 3.16, the conclusions drawn from Figure 3.15 are confirmed, that is, when considering three adjacent bins, the attenuation of the correlation output for $|\gamma| < 1$ is not overly significant. In fact, from the observation of Figure 3.15, it can be noted that the maximum correlation output attenuation for $|\gamma| < 1$ is nearly the same as the attenuation for $\gamma = 0, \mu_0 = \pm 0.5$, that is $10 \cdot \log_{10}(\text{sinc}(\mu_0)) = 1.96\text{dB}$. This way, the simple conclusion can be arrived at that, according to (3.13), the maximum coherent integration time that can be employed for the SLD detector so that the coherent output attenuation does not exceed the one which would be experienced by a constant Doppler is given by:

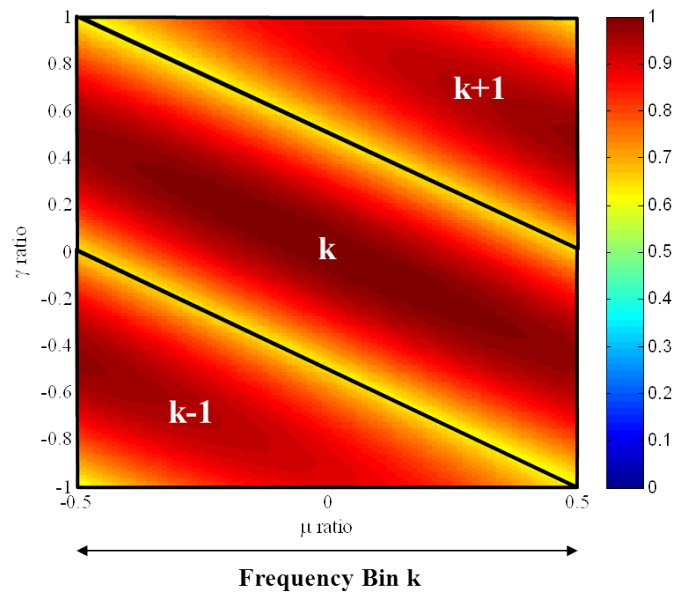
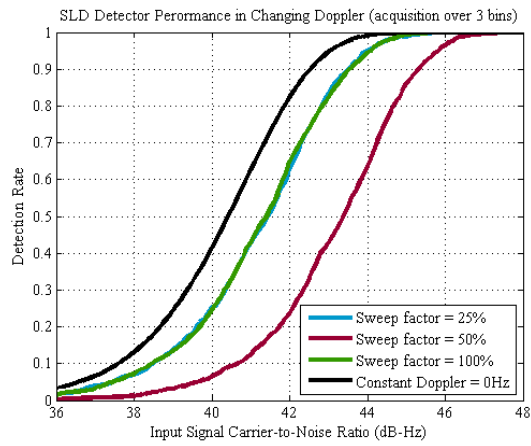
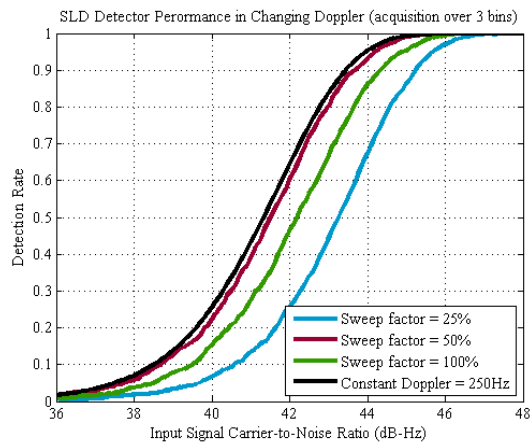


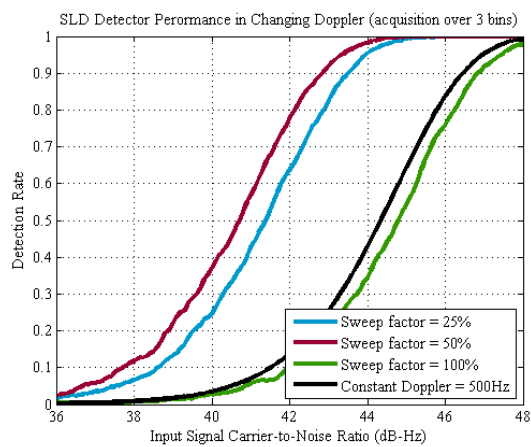
Figure 3.15 – Doppler bin containing most signal energy for $f_{d_0} \in \text{bin } k$ and $|\gamma| < 1$



(a) $\mu_0 = 0\%$



(b) $\mu_0 = 25\%$



(c) $\mu_0 = 50\%$

Figure 3.16 – Sensitivity analysis of SLD detector in changing Doppler (acquisition over 3 bins)

$$|\gamma| < 1 \iff T_{coh} < \sqrt{\frac{1}{|\alpha|}} \quad (3.17)$$

According to this simple relation, it can be concluded that, for example, for an expected $\alpha = 50\text{Hz/s}$, the coherent integration time should not exceed 140ms in order not to incur attenuations over 1.96dB of the correlation output, and 3.92dB of the final detection metric. This same analysis can also be extended to other desired attenuations.

3.2.2 Coherent Integration - Multiple Outputs

Having analyzed the effect of a chirp signal on the SLD detector, the analysis can now be extended to detectors employing both coherent and postcoherent integrations. When several successive coherent outputs are considered, the frequency response of the m^{th} coherent output is obtained as:

$$|H_m(\hat{f}_d)| = \left| \sum_{n=(m-1)N}^{mN-1} e^{j2\pi\mu_0(\frac{n}{N})} \cdot e^{j2\pi\gamma(\frac{n}{N})^2} \right| \quad (3.18)$$

We shall focus exclusively on the term related to the Doppler change rate, that is considering $\mu_0 = 0$. Once again no closed-form expression was found for $|H_m(\hat{f}_d)|$, so the analysis of (3.18) must also be carried recurring to simulation results. In Figure 3.17, the normalized $|H_m(\hat{f}_d)|$ as function of γ is shown for three different values of m .

From Figure 3.17 it becomes clear the increasingly higher effect of the Doppler change on the magnitude of the consecutive correlation outputs, even for low values of γ . This is a natural consequence of the input signal frequency being continuously drifting away from the local carrier fre-

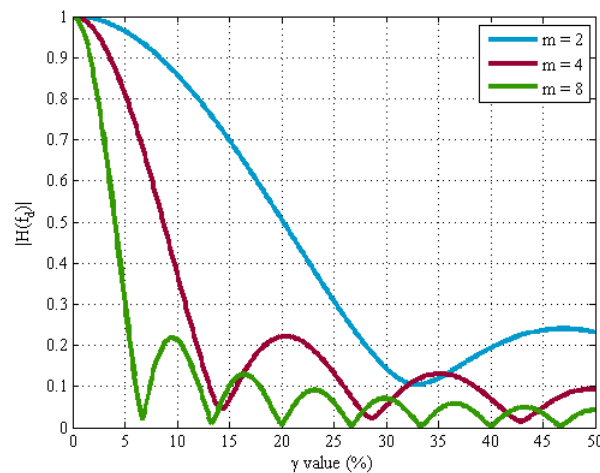


Figure 3.17 – Normalized $|H_m(\hat{f}_d)|$ for different correlation outputs as function of γ

quency, according to the signal model chosen and the assumption that $\Delta f_{d_0} = \mu_0 = 0$. Let us consider a frequency change rate of $\alpha = 50\text{Hz/s}$. For a coherent integration time of 20ms, we get:

$$\gamma = \alpha \cdot T_{coh}^2 = 2\% \quad (3.19)$$

If a total signal observation time of 200ms is desired, then a total of 10 coherent outputs will be available. In Figure 3.18, the attenuation of each correlation output with respect to the first one is shown, according to (3.18). From the example shown in this figure, it can be seen that, if no measures are taken to try to compensate this frequency change, the 10th coherent output will be attenuated roughly by 1.1dB with respect to the first one. If an even longer signal observation time is employed, higher frequency-derived attenuations will be observed in the following correlation outputs. Thus, if the coherent output attenuation is bounded, the maximum number of coherent outputs achievable can be defined as a function of γ and vice-versa. Unfortunately the proposal of an analytical formula would require obtaining a closed-form expression for (3.18), which was not achieved. This way, the results from simulation are interpolated in order to obtain a model for the value of γ which leads to a given attenuation as function of m . This analysis is shown in Figure 3.19.

From the results shown in Figure 3.19, a general approximation to the curves shown is proposed:

$$\gamma_{max} = \frac{x}{m^{1.15}} \quad (3.20)$$

where x is a coefficient depending on the maximum tolerable attenuation. Some values of x ob-

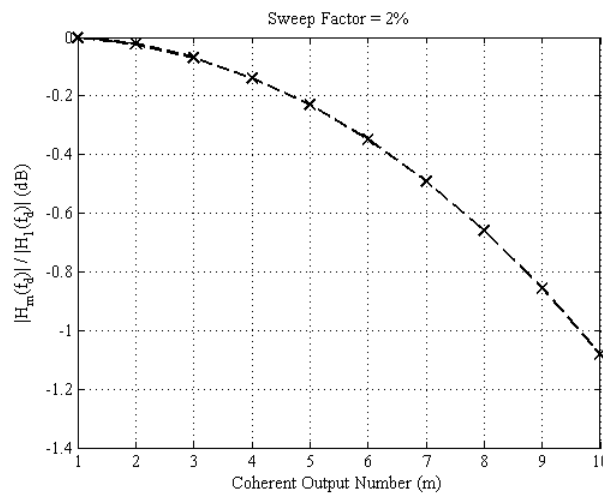


Figure 3.18 – $|H_m(\hat{f}_d)|/|H_1(\hat{f}_d)|$ as function of m for $\gamma = 2\%$

tained from curve-fitting to the simulation results are shown in Table 3.5. Finally, recurring to (3.20) it is possible to set the maximum signal observation time, $M T_{coh}$, which will not result in an attenuation of the coherent integration output above a certain value for a given γ . An inverse analysis can also be carried taking into account the definition of γ :

$$\gamma = \alpha T_{coh}^2 \leq \frac{x}{m^{1.15}} \iff \alpha \leq \frac{x}{T_{coh}^2 \cdot m^{1.15}} \quad (3.21)$$

According to this relation, it is now possible to define the maximum coherent and total signal integration time that will not lead to a coherent output attenuation higher than a given desired value. This is shown in Figure 3.20 assuming a maximum Doppler rate of 50Hz/s. According to the plot shown in this figure, if a coherent output attenuation not exceeding, for example, 1dB, is desired, we may choose $T_{coh} = 10$ ms and $M = 27$ (for a total of 270ms of signal observation) or otherwise $T_{coh} = 20$ ms and $M = 9$ (for a total of 180ms of signal observation). The total frequency change would be 13.5Hz in the first case and 9Hz in the second. This result also comes as logical as it is well-known that longer coherent integrations are more affected by smaller frequency errors than

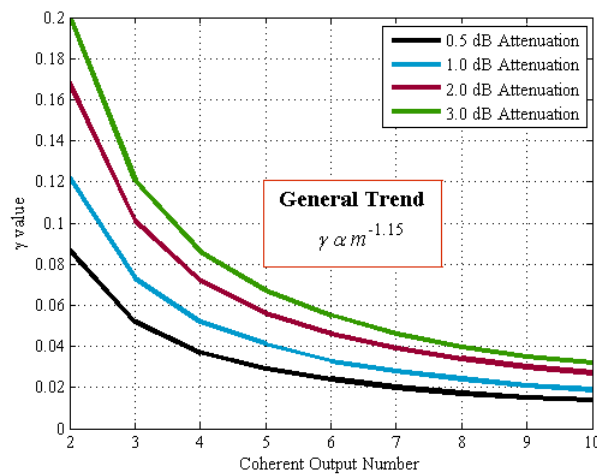


Figure 3.19 – Values of γ as function of m for a fixed coherent output attenuation

Table 3.5 – Coefficient x for application in (3.21)

| Attenuation (dB) | x |
|------------------|------|
| 0.5 | 0.19 |
| 1.0 | 0.26 |
| 2.0 | 0.35 |
| 3.0 | 0.43 |

shorter coherent integrations. The preferable solution depends on the sensitivity gain achievable with the postcoherent integration strategy adopted and other factors, such as the presence or absence of navigation data. Finally, it should be reminded that these values are only applicable for $\mu_0 \approx 0$, which can only be achieved with a sufficiently fine search grid or through the usage of an assistance link.

3.2.3 Postcoherent Integration

Having assessed the effect of a chirp signal on coherent integration, both over a single and multiple coherent outputs, its impact on the two postcoherent integration strategies, noncoherent and differential, is now evaluated. The assumption of $\mu_0 \approx 0$ will also be made, for simplification. Under this assumption, it was seen in the previous section that the frequency-derived attenuation of the consecutive coherent outputs is increasingly higher, that is:

$$|H_m(\hat{f}_d)| = \left| \sum_{n=(m-1)N}^{mN-1} e^{j2\pi\gamma\left(\frac{n}{N}\right)^2} \right| \geq \left| \sum_{n=mN}^{(m+1)N-1} e^{j2\pi\gamma\left(\frac{n}{N}\right)^2} \right| = |H_{m+1}(\hat{f}_d)| \quad (3.22)$$

where the equality is verified for $\gamma = 0$. Therefore:

$$|H_m(\hat{f}_d)|^2 \geq |H_m(\hat{f}_d)| \cdot |H_{m+1}(\hat{f}_d)| \quad (3.23)$$

where the left-hand operation corresponds to the squaring operation and the right-hand operation to the differential one. This way, due to the effect on the magnitude of the consecutive coherent out-

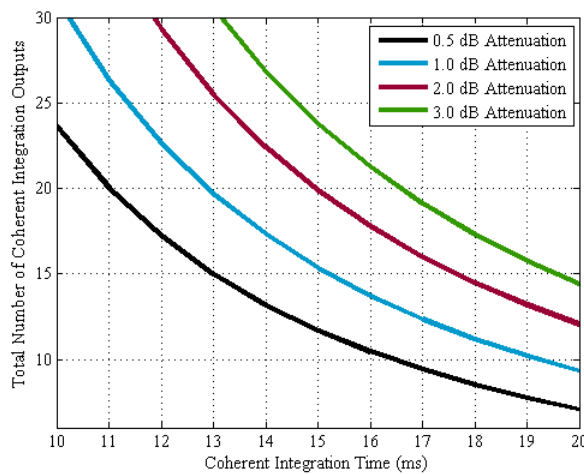


Figure 3.20 – Total number of coherent outputs achievable as function of coherent integration time for 4 different maximum coherent output attenuations and $\alpha = 50\text{Hz/s}$

puts, the differential operation will incur higher attenuations than the squaring one in the presence of a Doppler change.

Furthermore, through analysis of the simulation results it can be seen that the phase of the coherent output in presence of a changing Doppler offset can be well approximated by:

$$\arg\{S_m(\zeta, \hat{f}_d)\} \approx 2\pi\gamma(m^2 - m) + \mathcal{O}(0) \quad (3.24)$$

where $\mathcal{O}(0)$ stands for 0-order terms (independent of m). While this phase change will not have any particular impact on the noncoherent integration scheme, as it is promptly discarded by the squaring operation, it will however affect differential integration. The phase difference between two consecutive coherent outputs will then be:

$$\phi_{diff} = \arg\{S_m(\zeta, \hat{f}_d)\} - \arg\{S_{m-1}(\zeta, \hat{f}_d)\} \approx 2\pi\gamma(2m - 2) \quad (3.25)$$

Thus, the frequency response of differential integration due to the changing Doppler is given by:

$$|H_{diff}(\gamma)| = \left| \sum_{m=1}^{N_{DC}-1} e^{j2\pi\gamma(2m-2)} \right| = (N_{DC} + 1) \cdot \text{sinc}(2\gamma(N_{DC} + 1)) \quad (3.26)$$

meaning that the presence of a Doppler change rate results in the appearance of a new attenuation term for differential detectors in the form of a sinc function. This way we can conclude that, while both postcoherent integration forms are adversely affected by the presence of a changing Doppler, this effect is more harsh for differential detectors than for the noncoherent one.

It will be shown in Chapter 4 that differential detectors, in particular the Noncoherent Differential Detector (NCDD), have the capacity to outperform the Noncoherent Detector (NCD) in the acquisition of weak signals. The important question that should then be asked is: in the range where the NCDD detector is more effective than the NCD, what is the required level of dynamics that leads to an inversion of the preferable detector choice? Unfortunately, due to the impossibility of finding a closed-form expression for 3.18 at the start of this analysis, no analytical formula for the values of γ of interest could be obtained, and this analysis is once again performed through simulations. The results obtained for the acquisition of a GPS C/A signal at a working point $(P_d, P_{fa}) = (0.9, 10^{-5})$ are shown in Figure 3.21. According to the values of γ shown in the figure, it can be considered that the NCD detector will be a preferable choice in most scenarios where dynamics are significant.

3.2.4 Scenarios of Application: Low Earth Orbit and Geostationary Satellites & Urban environments

The usefulness of GNSS receivers as navigation tool goes well beyond mass-market applications. One particular scenario that stands out due to its unique requirements is *space applications*. Recent interest has been shown in the application of GNSS receivers in Low Earth Orbit (LEO) and Geostationary (GEO) satellites. Within these two cases, each one also has its own specific requirements.

LEO Satellites A satellite is generally considered to be in LEO if its orbit height does not exceed 1000km from the Earth surface. A GNSS receiver in a LEO satellite would have a good visibility of the GNSS constellation, and most of the error sources commonly affecting terrestrial receivers are either not present (multipath) or reduced to a great extent (ionospheric delay, internal receiver noise).

The main constraint to be considered for such a receiver is the very high speed of the satellite itself, on the order of several km/s, which induces not only large Doppler offset uncertainties of $\pm 40\text{kHz}$ but also Doppler rates of up to $\pm 75\text{Hz/s}$. This Doppler rate in particular could easily become very harsh for the acquisition of highly attenuated signals, however, fortunately the large number of signals visible to these satellites can dictate an acquisition threshold of 40dB-Hz or higher [191, 192], so that the acquisition times employed can be relatively small. If a coherent integration time of 2ms for a GPS C/A signal is chosen, a value of γ of around 0.03% is obtained, which can be fairly well accommodated, according to the analysis carried in this section.

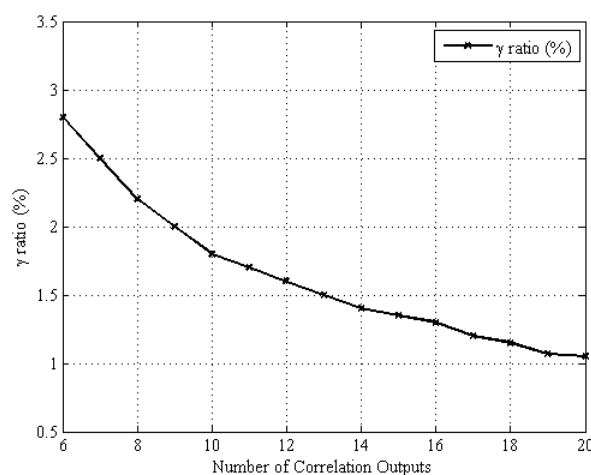


Figure 3.21 – γ value leading to equal detection performance of the NCD and NCDD detectors as function of number of coherent outputs and a working point $(P_d, P_{fa}) = (0.9, 10^{-5})$

GEO Satellites The geostationary belt, where GEO satellites are located, is at a distance of 35.786km above the Earth's equator. Given that the GEO belt is above GNSS orbits, the signals available for the receivers in GEO originate from satellites on the opposite side of the Earth. This way, an acquisition threshold of 30dB-Hz is required in order to ensure that the minimum number of 4 satellites are visible for most of the time [191, 192]. However, the Doppler rates expected for these receivers are within $\pm 1\text{Hz/s}$ and the total Doppler uncertainty is of $\pm 18\text{kHz}$. As so, if a coherent integration time not exceeding 10ms for the GPS C/A signal is set, in order to avoid having to deal with data bit transition issues, the resulting sweep factor is of 0.01%, which once again can be fairly well accommodated, according to the previous analysis.

Also in some well-known Earth-based scenarios, such as urban environments, it is fairly common to have to deal with signals attenuated at around 30dB-Hz. According to the discussion at the beginning of this chapter, the maximum Doppler rate expected for a terrestrial user may reach up to 50Hz/s. In this case values of $\gamma = 2\%$ may be expected for a coherent integration time of 20ms, as the example shown in section 3.2.2. In these cases, the previous methodology can be followed in order to set the most appropriate signal integration time.

3.3 Doppler Effect Compensation in High-Dynamics

In the previous section, the conditions for establishing the range of Doppler change rates that can be considered as tolerable during acquisition were presented. Once the expected Doppler change rates are above those limit values or longer coherent integration times are desired, a dynamic compensation of the Doppler change must be put in place. This dynamic frequency compensation can be achieved through the application of a Frequency Offset Correction (FOC) loop (Figure 3.22). Acquisition schemes employing a FOC loop generate an estimate of the Doppler offset through an intermediate result of the acquisition processing and update the candidate downconversion frequency accordingly, such that the coherent processing losses of the following blocks of data can be reduced [17, 52].

An example of an acquisition scheme including a FOC loop is introduced in [17], applied to the NCDD detector and considering a static Doppler offset. The block diagram of this acquisition scheme is shown in Figure 3.23. The frequency offset estimation in this structure is made through the argument of the differential operation. Given the assumption of a stationary Doppler offset, the coherent output phase is a linear function of the Doppler offset ($\phi_m = 2\pi m \Delta f_d N T_s + \phi_0$) and the phase of the differential output results as:

$$\arg\{S_{m+1}(\zeta, \hat{f}_d) \cdot S_m^*(\zeta, \hat{f}_d)\} = \phi_{m+1} - \phi_m = 2\pi \Delta f_d N T_s \quad (3.27)$$

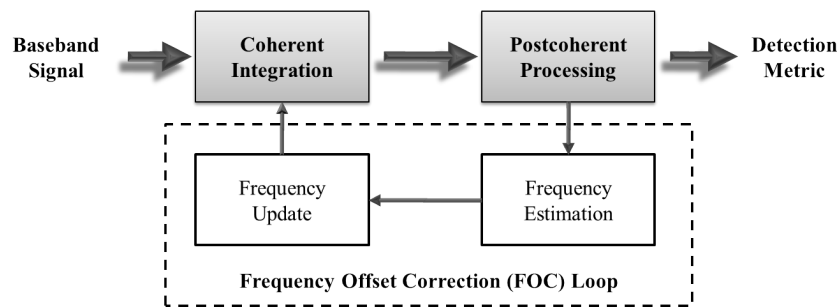


Figure 3.22 – General structure of an acquisition scheme employing a FOC loop

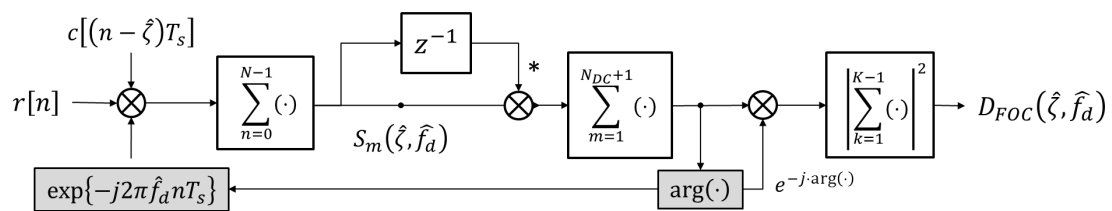


Figure 3.23 – Acquisition scheme employing a FOC loop [17]

This way, the frequency offset estimation can be simply obtained through:

$$\Delta \hat{f}_d = \frac{\arg\{S_{m+1}(\zeta, \hat{f}_d) \cdot S_m^*(\zeta, \hat{f}_d)\}}{2\pi N T_s} \quad (3.28)$$

While this structure may be well adapted to a stationary Doppler offset, it may not be the preferable choice under high-dynamics, as it was observed in the previous section that differential detectors are more adversely affected by a chirp signal than the noncoherent detector. As so, the NCD detector is the natural choice for application under high-dynamics scenarios, and an alternative FOC loop structure adapted to the NCD detector must be employed. The most straightforward option is *phase differentiation* of the consecutive coherent outputs [3, 181]. The resulting acquisition scheme is shown in Figure 3.24.

Frequency offset estimation through phase differentiation is very similar to estimation through the argument of differential integration, as essentially the same operation is performed. There is, nevertheless, the difference that recurring to the structure of Figure 3.23, several differential integrations may take place prior to the offset estimation, thus tentatively increasing the SNR prior to the estimation. At the same time it should also be noted that the more integrations are performed prior to the estimation, the lower the rate update of the downconversion frequency, so higher coherent integration losses may be experienced.

The frequency update can be done in one of two ways. Either the update is done at specific time instants, referred to as a *staircase* approach [17], or the compensation is attempted at each signal sample, in a *ramp* fashion [98, 176, 193]. The two cases are analyzed next.

3.3.1 Staircase Frequency Update

The staircase frequency update occurs at specific time instants, not attempting to estimate the chirp rate, that is:

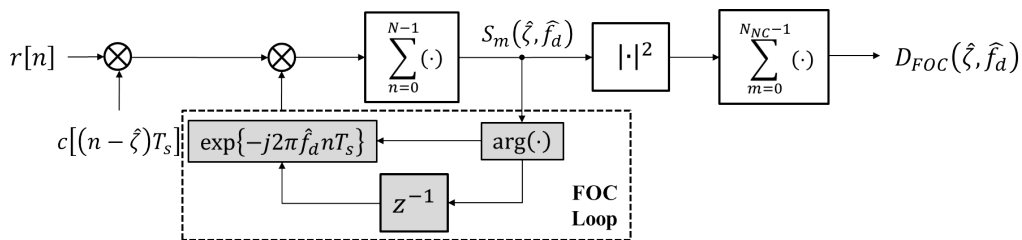


Figure 3.24 – Noncoherent detector employing a phase difference-based FOC loop

$$\hat{f}_d = \hat{f}_{d_0} + \Delta(f_d)_{comp} \quad (3.29)$$

where $\Delta(f_d)_{comp}$ represents the Doppler change compensation. According to the FOC loop structure adopted in this analysis (Figure 3.24), compensation can be achieved every two coherent outputs. In this case, the accurate value for $\Delta(f_d)_{comp}$ for each update step will be $2i \cdot \Delta(f_d) = 2i \cdot \alpha T_{coh}$, where i is the update number. The estimated frequency profile will resemble the one shown in Figure 3.25. The frequency response of the m^{th} coherent output for the staircase compensation approach is given by:

$$\begin{aligned} |H_m(\hat{f}_d)| &= \left| \sum_{n=(m-1)N}^{mN-1} e^{j2\pi(f_d - \hat{f}_d)nT_s} \right| = \left| \sum_{n=(m-1)N}^{mN-1} e^{j2\pi(\Delta f_{d_0} + \alpha n T_s - 2i \cdot \alpha T_{coh})nT_s} \right| \\ &= \left| \sum_{n=(m-1)N}^{mN-1} e^{j2\pi\Delta f_{d_0} n T_s} \cdot e^{j2\pi\alpha(n-2iN)nT_s^2} \right| \\ &= \left| \sum_{n=(m-1)N}^{mN-1} e^{j2\pi\mu_0(\frac{n}{N})} \cdot e^{j2\pi\gamma[(\frac{n}{N})^2 - 2i(\frac{n}{N})]} \right| \end{aligned} \quad (3.30)$$

Comparing this expression with (3.18), it becomes clear the effect of the compensation in reducing the impact of the Doppler change rate on the coherent output attenuation. Nevertheless, it can also be seen that the compensation will offer limited reliability, given that for large values of n , the difference between the two terms (quadratic and linear) will tend to values close to the quadratic term. Furthermore, in order to design a frequency estimator from (3.30), an expression for $\arg\{H_m(\hat{f}_d)\}$ is required but, looking at the above expression it is clear that such an estimator is not easy to be

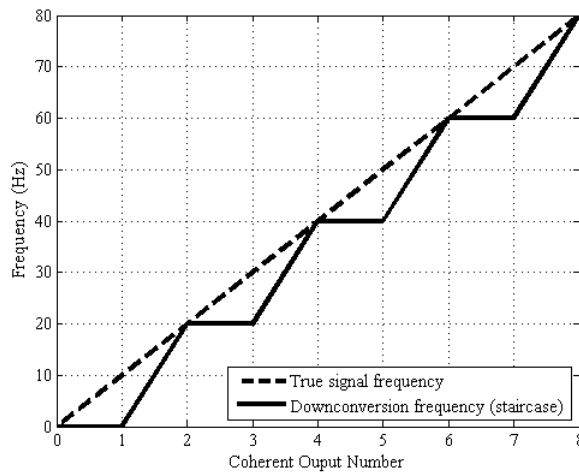


Figure 3.25 – Staircase frequency update profile

derived.

3.3.2 Chirp Frequency Update

The other option at hand is to model the demodulation frequency as a ramp, by estimating the Doppler change rate being incurred, that is:

$$\hat{f}_d = \hat{f}_{d_0} + \hat{\alpha} n T_s \quad (3.31)$$

where $\hat{\alpha}$ is the estimate of the chirp rate. The frequency profile would be the one in Figure 3.26. In this case, the frequency response of the m^{th} coherent output becomes:

$$\begin{aligned} |H_m(\hat{f}_d)| &= \left| \sum_{n=(m-1)N}^{mN-1} e^{j2\pi(f_d - \hat{f}_d)nT_s} \right| = \left| \sum_{n=(m-1)N}^{mN-1} e^{j2\pi(\Delta f_{d_0} + \alpha n T_s - \hat{\alpha} n T_s)nT_s} \right| \\ &= \left| \sum_{n=(m-1)N}^{mN-1} e^{j2\pi\Delta f_{d_0} n T_s} \cdot e^{j2\pi\Delta\alpha(nT_s)^2} \right| \\ &= \left| \sum_{n=(m-1)N}^{mN-1} e^{j2\pi\mu_0(\frac{n}{N})} \cdot e^{j2\pi\gamma'(\frac{n}{N})^2} \right| \end{aligned} \quad (3.32)$$

where $\Delta\alpha$ is the chirp rate estimation error and $\gamma' = \Delta\alpha \cdot T_{coh}^2$. Comparing (3.30) and (3.32), the advantages of the ramp approach with respect to the staircase one are notorious. In this approach, the estimation can be performed employing the two first coherent outputs and a refinement can be attempted during the following steps of execution. According to (3.25), the phase difference for

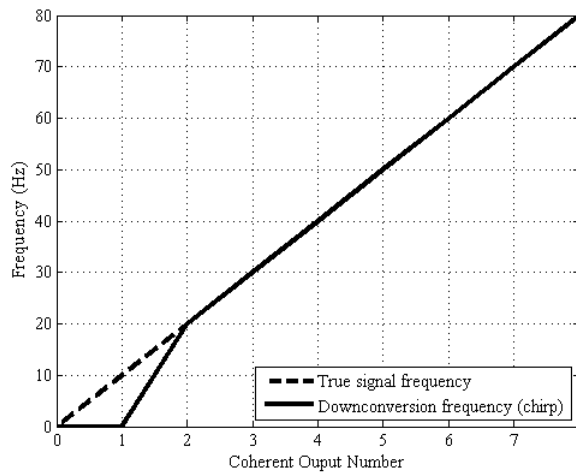


Figure 3.26 – Chirp frequency update profile

two consecutive coherent outputs, m and $m - 1$, for $\Delta f_{d_0} \approx 0$ is approximately $2\pi\gamma(2m - 2)$. This way, $\hat{\alpha}$ can be obtained from the two first coherent outputs as:

$$\hat{\alpha} = \frac{\arg\{S_2(\zeta, \hat{f}_d)\} - \arg\{S_1(\zeta, \hat{f}_d)\} + \kappa \cdot 2\pi}{4\pi T_{coh}^2} \quad (3.33)$$

where the term $\kappa \cdot 2\pi$ is introduced in order to ensure that the denominator in (3.33) is contained in the interval $[-\pi, \pi]$ so that the Doppler rate estimation is unambiguous. It should be noted however, that this introduces a limit to the maximum values of γ which can be supported by (3.33). The condition for the first estimation is:

$$4\pi\gamma < \pi \iff \gamma < 25\% \quad (3.34)$$

and the value of κ is simply determined as:

$$\kappa = \begin{cases} -1 & \text{if } \Delta\phi > \pi \\ 1 & \text{if } \Delta\phi < \pi \\ 0 & \text{otherwise} \end{cases} \quad (3.35)$$

with $\Delta\phi = \arg\{S_2(\zeta, \hat{f}_d)\} - \arg\{S_1(\zeta, \hat{f}_d)\}$.

Doing the parallel between (3.32) and (3.18), it can be easily seen that the phase of the coherent outputs right after the frequency update will be given by $2\pi\gamma'(2m - 2)$. This way, the Doppler error estimation can be obtained from the following correlation outputs as:

$$\hat{\Delta\alpha} = \frac{\arg\{S_m(\zeta, \hat{f}_d)\} - \arg\{S_{m-1}(\zeta, \hat{f}_d)\}}{2\pi(2m - 2)T_{coh}^2} \quad (3.36)$$

and the Doppler rate estimation can be simply updated as $\hat{\alpha}_m = \hat{\alpha}_{m-2} + \hat{\Delta\alpha}$, with $\hat{\alpha}_2$ given by (3.33). Although this estimator provides the correct estimation for noiseless conditions, its performance in the presence of noise naturally depends on the coherent output SNR. The plots in Figure 3.27 show the evolution of the estimation bias and standard deviation for different values of γ and $T_{coh} = 1\text{ms}$.

3.3.3 Approaches Comparison

In order to assess the performance of the two FOC-corrected NCD approaches with respect to their uncorrected counterpart, that is, the NCD detector on its own, simulations were run at different values of γ . These can be seen in Figure 3.28. The results presented were obtained for the acquisition of a 10ms-long GPS C/A signal, employing 1ms coherent integration and subsequently doing

10 noncoherent integrations. It should be noted that even if this short coherent integration time is applied, the relative results between the detectors would remain unchanged if longer coherent integrations were applied, while keeping the same value of γ . It should be noted as well that, as the derivation of a frequency offset estimator was not attempted for the staircase loop, the correct values of $\Delta(f_d)_{comp}$ are always used in the algorithm, as it has been previously shown that this solution will be ultimately worse than the chirp-compensated one.

Several conclusions can be drawn from the plots in Figure 3.28. First of all, the effect on the three detectors of an increasingly higher value of γ is well remarked in these figures. With respect to the static case ($\gamma = 0\%$), the uncorrected NCD detector shows roughly 9dB-Hz sensitivity loss for $\gamma = 20\%$.

Secondly, as expected, the chirp-compensated FOC approach appears to be more effective than the staircase one, even when the accurate values for $\Delta(f_d)_{comp}$ are provided to the staircase FOC loop (zero estimation error). From these plots, it can be seen how the chirp-compensated detector is capable of providing reliable performance for values of γ until 15%. For higher values of γ , the Doppler frequency after two coherent integrations will approach the limit of the range of unambiguous estimation according to phase relation, and the FOC-corrected structure loses its ability to correctly compensate the Doppler change. Also, for low values of γ ($\leq 5\%$), it seems that the application of the FOC loop can be slightly damaging to the acquisition process, so the expected dynamics should be carefully considered before its application. This is a natural consequence of the estimator's incapacity to perform well at low coherent output SNRs.

This way, from the analysis of the plots in Figure 3.28, it seems that the chirp-compensated approach attains its best performance for values of γ around 15%, where an added robustness of over 5dB-Hz with respect to the uncorrected detector is verified. In order to reinforce this conclu-

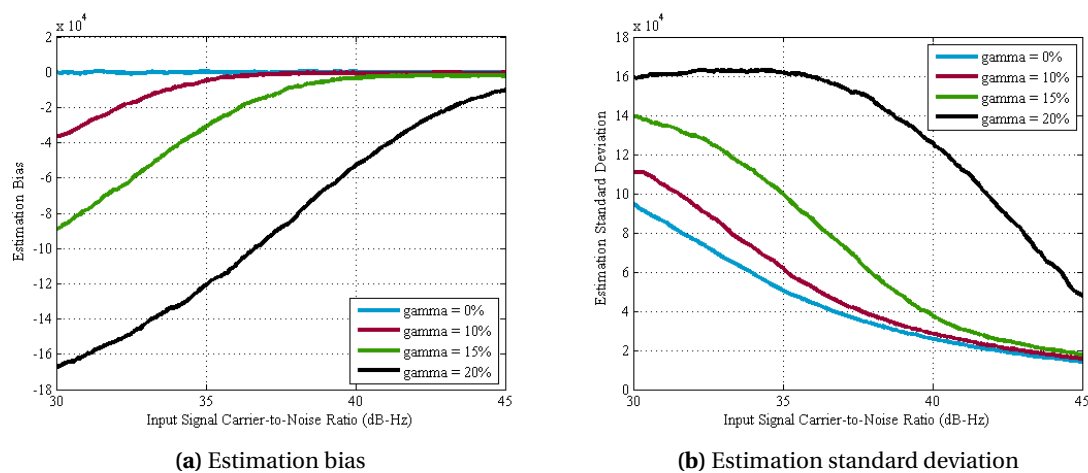


Figure 3.27 – Bias and standard deviation of the first Doppler rate estimator for $\gamma = 0\%$, 10% and 20%

sion, the performance of the three detection schemes is compared for this value of γ for different numbers of noncoherent integrations. The resulting plots are shown in Figure 3.29.

From these plots two main conclusions can be drawn. The first one is that the good performance of the FOC loop structure at this value of γ seems to be verified in the three cases in which the frequency compensation algorithm is put into practice (more than 2 noncoherent integrations). Second, it is also clear the limit of the sensitivity enhancement drawn from this approach, once again, essentially due to the low performance of the estimator employed at low coherent output SNRs.

3.3.4 Comparison with Medium-Dynamics Assumption

In the analyses carried previously it was seen that the γ limit for the applicability of the chirp-compensated FOC loop approach is 25% and that this technique works best at values of γ between

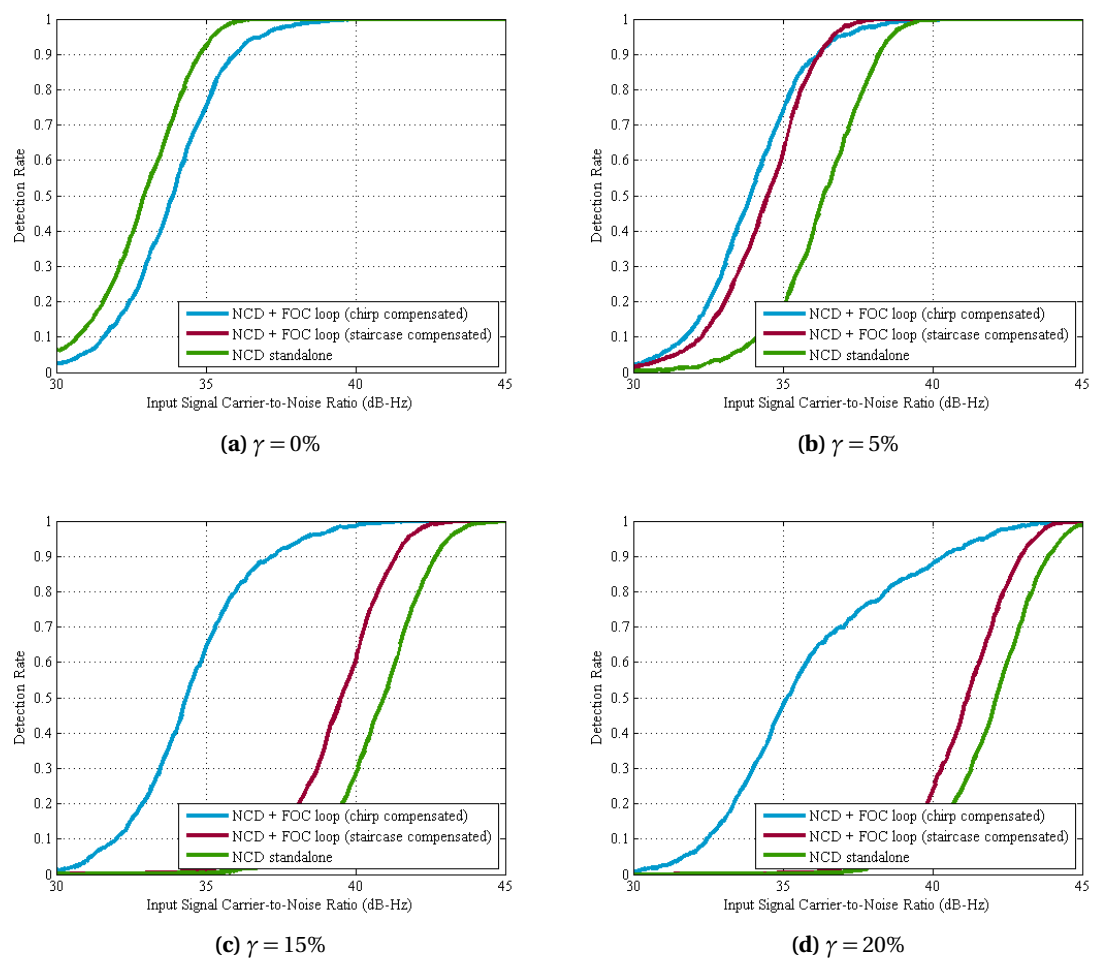
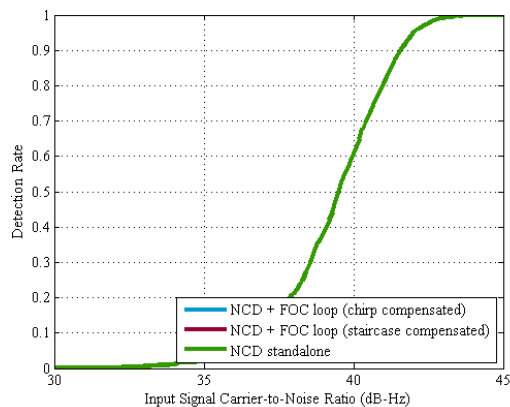


Figure 3.28 – Sensitivity analysis of NCD detector with staircase and chirp frequency compensation

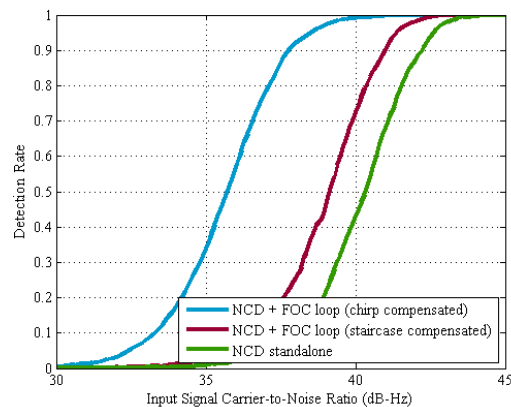
5-15%. Nevertheless, in section 3.2, dealing with the medium-dynamics assumption, it was seen that for values of $\gamma < 100\%$, the Doppler change impact on the SLD detector can be fairly well accommodated. Furthermore, it was also seen that there is an actual limitation of the FOC structure proposed, that after a certain number of noncoherent integrations, the FOC-compensated NCD detector seems to be unable to continue improving its sensitivity. This way, it must be assessed if the high-dynamics solution proposed is effectively useful.

For a given value of α , the relation between the coherent integration time for the medium-dynamics case (where we can consider $\gamma = 100\%$) and for the high-dynamics one (which achieves best performance at $\gamma = 15\%$) is:

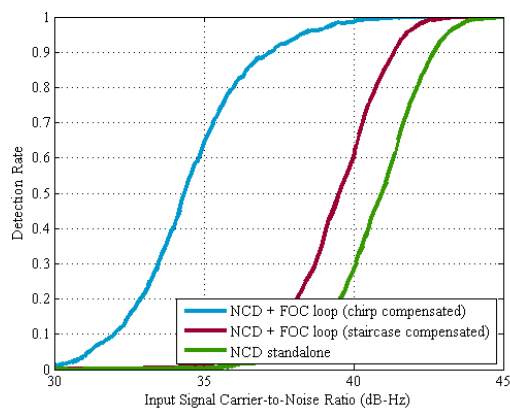
$$\alpha = \frac{\gamma}{T_{coh}^2} \iff \frac{T_{coh,high}}{T_{coh,medium}} = \sqrt{\frac{\gamma_{high}}{\gamma_{medium}}} = 2.58 \quad (3.37)$$



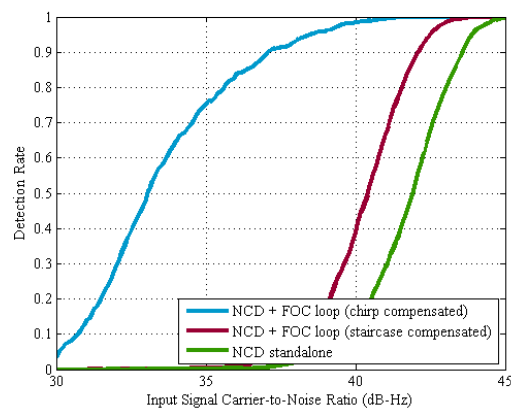
(a) 2 noncoherent integrations



(b) 6 noncoherent integrations



(c) 10 noncoherent integrations



(d) 20 noncoherent integrations

Figure 3.29 – Sensitivity analysis of NCD detector with staircase and chirp frequency compensation for $\gamma = 15\%$ and 2, 6, 10, and 20 noncoherent integrations

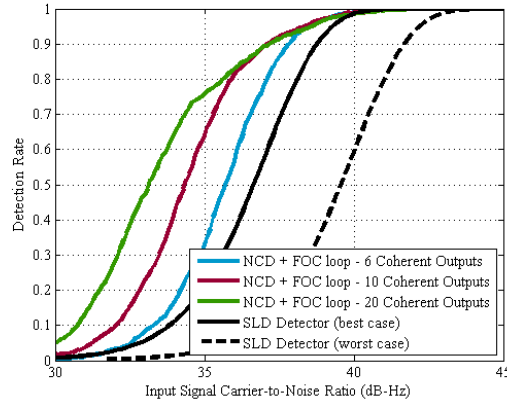


Figure 3.30 – Comparison between medium- and high-dynamics solutions proposed

Rounding up this ratio to 3, in order to avoid partial correlations, it then results that the coherent integration time for the medium-dynamics assumption can be extended to the triple of that for the high-dynamics case. Note however that, while for the SLD detector a fixed total signal integration time must be respected (equal to the coherent integration time), there is no specific limitation for the FOC-corrected NCD detector, except the receiver's processing capabilities. Nevertheless, according to the plots in Figure 3.29, extension to more than 20 noncoherent integrations will result in very little sensitivity improvements, if any. Furthermore, it should also be taken into account that, from the plot in Figure 3.15, the attenuation of the SLD detection metric for $\gamma = 100\%$ varies from 1 (best case) to 3.92dB (worst case). Both cases are considered in this comparison.

The assessment of the usefulness of the high-dynamics solution proposed can now take place. In Figure 3.30, the two detectors in the presence of the same Doppler change rate are compared. In order to speed-up the simulations, $T_{coh,medium}$ is set to 1ms and the value of α is determined from it, but the same analysis could be carried for longer values of $T_{coh,medium}$ and the detectors' relative performance would remain the same.

From the analysis of the plot in Figure 3.30, it becomes clear that the high-dynamics solution proposed is capable of providing enhanced reliability in achieving higher sensitivity than the medium-dynamics assumption. Further simulation analysis shows that this superior performance is verified for the values of γ previously identified as the ones in which the FOC loop is effective (between 5% and 15%).

3.3.5 Scenario of Application: Deep urban & Indoor environments

The application of GNSS techniques in indoor positioning has brought unmatched challenges with respect to other scenarios of application. In order to detect the signals' weak power which can be well below 30dB-Hz, signal integration times of hundreds of milliseconds and even a few seconds may be required. With the help of an assistance link, or recurring exclusively to pilot signals, the

effect of the navigation data bit may be removed from coherent integration, and the coherent integration time can be significantly increased (within the receiver's processing capabilities and local oscillator stability). In these cases, the main element affecting acquisition sensitivity is the Doppler change which is experienced during the acquisition time. Even if counter-intuitive, such indoor scenarios may need to be considered as *high-dynamics*.

In the previous analysis it was seen that, if the coherent integration time is set according to the expected level of dynamics, such that the sweep factor falls in the range 5-15%, the application of the chirp-compensated NCD detection scheme can provide up to 5dB-Hz added robustness with respect to its uncorrected counterpart. For coherent integration times around 100ms, the level of dynamics that can be tolerated so that γ falls in the expected range is 5 to 15Hz/s. Considering the expected Doppler change rates discussed at the beginning of this chapter, the proposed solution may find application in some indoor applications requiring coherent integration times of a few hundreds of milliseconds. For even longer coherent integration times, higher-end technological solutions involving fusion with INS systems or other information sources are required.

3.4 Conclusion

In this chapter the assessment of the impact of the Doppler shift in acquisition for low-, medium-, and high-dynamics scenarios has been presented. The resulting conclusions for each scenario are described below.

Low-Dynamics When the Doppler offset can be considered to be constant during the acquisition time, the search grid resolution for the Doppler search has to be weighted with the computational efficiency of the correlation method to be applied. It was seen that the most computationally efficient correlation methods are subject to Doppler-derived attenuations higher than those for less efficient methods, and a methodology to alleviate these losses was proposed. By applying Spectral Peak Location (SPL) algorithms, the offset between the true and the closest FFT candidate frequencies can be estimated, and a fine search grid can be emulated with the otherwise less Doppler-robust methods. A new acquisition methodology was developed for the application of SPL algorithms in acquisition, and its merits were proven in the acquisition of both simulated and real GNSS signals, showing that this can be a promising solution for receivers where the sensitivity-complexity trade-off is an important design driver.

Medium-Dynamics For the medium-dynamics hypothesis, defined as the case when the Doppler change rate is not high enough to justify higher complexity solutions to attempt compensation, the analysis of this change rate on the SLD, NCD, and NCCD detectors was assessed.

For the case of the SLD detector, it was established a limit for the coherent integration time, which ensures that the attenuations of the final detection metric are not higher than those which would be expected for a stationary Doppler. According to (3.17), this limit is $T_{coh} = \sqrt{\alpha^{-1}}$.

For the NCD and NCCD detectors, a formula relating the maximum coherent integration time with the number of coherent outputs, depending on the expected dynamics and the maximum allowable attenuation for the coherent outputs, was obtained (equation (3.21)). It was equally seen that under the assumption of a chirp signal and initial offset frequency close to 0, the NCD detector is a more reliable choice than the NCCD in these scenarios. The second solution is more indicated for relatively low coherent integration times (10-20ms), so it can be applicable in standalone receivers, while the first one aims at very long coherent integration times (>100ms).

High-Dynamics Finally, when the Doppler change rate is considered to be significant with respect to the coherent integration time, it was shown that the inclusion of a chirp-compensated FOC-loop in the NCD detector is capable of providing several dB additional sensitivity with respect to the uncorrected NCD detector (Figure 3.28 and Figure 3.29). The sensitivity enhancement of the proposed solution, however, is limited by the capability of the applied estimator to perform well at

Table 3.6 – Preferable detection scheme selection for $\gamma \leq 100\%$

| γ | Preferred Assumption / Detector | Coherent Integration Time Determination | Coherent Integration Time for $\alpha = 50\text{Hz/s}$ (ms) |
|----------|---------------------------------|---|---|
| 0-5% | Medium-Dynamics / SLD or NCD | $\sqrt{\alpha^{-1}}$ (SLD) $\sqrt{xM^{-1.15} \cdot \alpha^{-1}}$ (NCD) | 140 (SLD) Variable (NCD) |
| 5-15% | High-Dynamics / NCD | $\sqrt{\gamma \cdot \alpha^{-1}}$ | 45-63 |
| 15-100% | Medium-Dynamics / SLD | $\sqrt{\alpha^{-1}}$ | 140 |

low coherent output SNRs. It was seen that for values of γ between 5 and 15%, the proposed solution can offer enhanced reliability with respect to the medium-dynamics assumption. Table 3.6 shows the preferable solution and detector to be applied as function of γ .

SENSITIVITY CHARACTERIZATION OF DIFFERENTIAL GNSS DETECTORS

In many of today's scenarios where GNSS signals are sought by their users, several phenomena come into play as attenuation sources, reducing the available signals' power and making it considerably more difficult for the receivers to detect them. As already mentioned in the previous chapters, in order to reliably detect these weak signals, signal observation or *integration* over several code periods is needed.

Also in the previous chapters, coherent integration was highlighted as the most efficient signal integration strategy, maximizing the sensitivity gain obtainable in the processing of a given data set. Nevertheless, several obstacles to the extension of the coherent integration time were also pointed out, including Doppler offset, data bit transition, and the receiver's processing capabilities. Therefore, after a certain number of coherent accumulations, transition to postcoherent integration strategies is usually employed to keep on increasing acquisition sensitivity. The most well-known, and generally applied, postcoherent integration strategy is *noncoherent* integration, in which the coherent outputs' phase is discarded prior to further accumulation [2–4, 6, 7]. It is equally well-known, however, that noncoherent integration is less effective than coherent integration, as the phase removal operation by squaring the In-phase and Quadrature (I&Q) branches of the coherent output incurs a loss, known as *squaring loss*, which reduces the signal's Signal-to-Noise ratio (SNR) [20, 86].

An alternative postcoherent integration approach is *differential*, or *semicoherent*, integration [6, 7, 17, 45, 89, 90, 97, 101, 104, 194]. In this approach, the coherent outputs are not squared, but rather correlated with a previous output. The product of the two uncorrelated outputs is statistically less detrimental to SNR than the squaring operation, given the independence of the noise terms. Different forms of detection schemes employing postcorrelation differential integration can be found in literature [6, 89, 90, 104]. In this chapter, the analysis of different forms of differential

detectors is carried. The significance of this work and the chapter organization are discussed in the following section.

4.1 Background

It was previously mentioned that different forms of detection schemes employing postcorrelation differential integration can be found in literature. One of the two main factors that distinguish these detectors is the generation of the differential outputs. Given the nature of the differential operation, each coherent output, except the first and last, may be used more than once. This results in a dependency between consecutive differential outputs which is remarkably difficult to characterize statistically. One approach to avoid this dependency is studied in [104], where each coherent integration output is used only once, in an approach termed as *pair-wise integration*. The drawback of this approach is that a reduced number of accumulations naturally leads to a smaller sensitivity increase than if all differential outputs were exploited [6].

The second main factor that distinguishes differential detectors is the formulation of the detection metric from the differential integration outputs. In [89], only the in-phase branch of the differential integration output is considered in the detection test. A posterior evaluation of this detection metric in [90] notes that a residual Doppler offset leads to a partition of the useful signal power between the I&Q branches of the differential integration output, and a Doppler-robust *noncoherent differential* form is instead adopted, in which the detection metric is obtained as the squared magnitude of the differential integration output (Figure 4.1). Although this form significantly improves the differential detection scheme performance in the presence of an unknown Doppler offset, its detection metric is obtained as the sum of two dependent random variables. This dependency once again complicates the statistical analysis of the detector.

In [6], a complex mathematical approach is followed that enables the author to derive expressions for characterizing the pair-wise detector (PWD) from [104] as well as the noncoherent differential detector (NCDD) from [90]. The author also notes however that, while exact, the expressions derived are of limited application due to the presence of functions which easily become both burdensome and inaccurate for a high number of differential accumulations. An equally complex analysis of differential detectors with similar results is also found in [101]. The approach which is frequently followed in the analysis of differential detectors is to resort to the Central Limit Theorem, through which the noise terms resulting from differential integration can be approximated by a Gaussian distribution for a sufficiently high enough number of integrations [17, 97]. In [6], the author also develops a Gaussian approximation for each detector and points out the risk of employing this approximation for a low number of accumulations, given that the actual distributions of the I&Q components of the differential operation are heavier at the tails than the Gaussian distribution, leading to large inaccuracies in the threshold setting process.

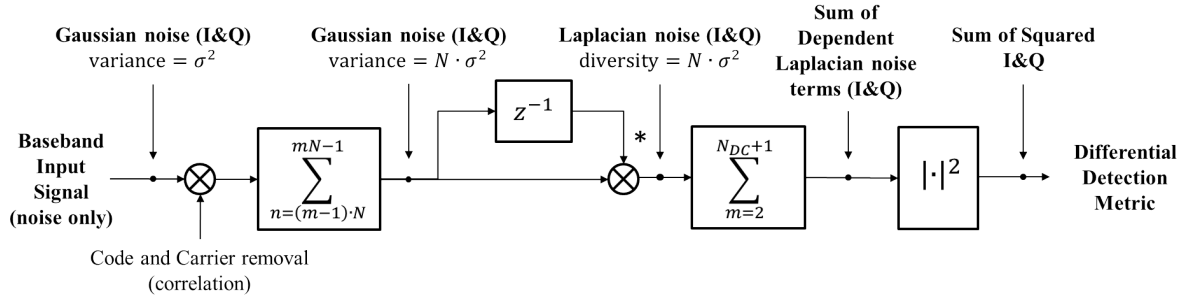


Figure 4.1 – Noncoherent differential detector block diagram and resulting noise distribution under no signal present case

Both the multitude of existing differential detector forms and the complexity of their statistical characterization have been obstacles to the comparison of the two postcoherent integration approaches, noncoherent and differential. Although in several publications it has been found that differential detectors are a preferable choice for weak signals acquisition, it was not until [106] and [107] (both co-authored by the thesis author) that a formal comparison between the sensitivity losses of the squaring and differential operations was encountered. The approach presented in these two publications is described in this chapter.

This chapter is organized as follows. In section 4.2, we characterize statistically the differential operation, applied in the context of the PWD detector. Next, given the difficulty of following a similar analysis for other differential detectors, in particular the NCDD, the methodology for characterizing a detector through its sensitivity loss with respect to coherent integration is described. This methodology is then applied to the differential operation and the NCDD detector, to produce a sensitivity loss formula for this detector. Recurring to this formula, a comparison between the NCDD and the Noncoherent Detector (NCD) is carried in section 4.5 and this comparison is extended to the acquisition of real signals in section 4.6.

4.2 Statistical Characterization of the PWD Detector

Given that coherent integration is limited by several factors, transition to postcoherent integration is required in order to efficiently detect the presence of weak signals. While the statistical characterization of noncoherent integration poses no significant challenge, the same is not verified for differential integration. As mentioned in the introduction, the attempts to characterize detectors employing postcoherent differential integration found in literature have repeatedly resulted in either highly complex closed-form expressions or simplifications through Gaussian approximations. This fact becomes even more significant considering the variety of such detectors that can be envisaged. Three different differential detection schemes are considered in the course of this work:

-
- Pair-wise differential detector (PWD) [104]:

$$S_{PWD}(\hat{\zeta}, \hat{f}_d) = \Re \left\{ \sum_{m=1}^{\lfloor N_c/2 \rfloor} S_{2m}(\hat{\zeta}, \hat{f}_d) \cdot S_{2m-1}^*(\hat{\zeta}, \hat{f}_d) \right\} \quad (4.1)$$

- Coherent differential detector (CDD) [89]:

$$S_{CDD}(\hat{\zeta}, \hat{f}_d) = \Re \left\{ \sum_{m=2}^{N_c} S_m(\hat{\zeta}, \hat{f}_d) \cdot S_{m-1}^*(\hat{\zeta}, \hat{f}_d) \right\} \quad (4.2)$$

- Noncoherent differential detector (NCDD) [90]:

$$S_{NCDD}(\hat{\zeta}, \hat{f}_d) = \left| \sum_{m=2}^{N_c} S_m(\hat{\zeta}, \hat{f}_d) \cdot S_{m-1}^*(\hat{\zeta}, \hat{f}_d) \right|^2 \quad (4.3)$$

where N_c represents the number of available coherent outputs. The differences between these three detectors are firstly on the accumulation of the differential outputs (note the $2m$ index for each coherent integration output for the PWD detector) and secondly on the generation of the final detection metric (coherent or noncoherent). The PWD form is the simplest to analyze due to the absence of dependency terms either in the differential outputs accumulation as in the generation of the detection metric. On the contrary, the most difficult one to characterize statistically is the NCDD detector. In this section, we analyze statistically the PWD detector which will afterwards allow advancing to the characterization of the NCDD detector.

In both its original publication as in [6, 7], the PWD detection metric has been characterized as the difference of two χ^2 random variables (central under H_0 and noncentral under H_1). In this work we follow a different approach for this characterization, making use of the Laplace nature of the differential operation output under H_0 , and employing the Gaussian approximation under H_1 , not without first justifying its suitable usage under this condition.

4.2.1 Characterization under Noise-only Hypothesis (H_0)

Modeling the output of a detector under no signal present, only noise, allows establishing a threshold for deciding if a candidate signal is present or not with a certain degree of confidence, established by the acceptable probability of false alarm, P_{fa} . In this case, the coherent integration outputs consist solely of the accumulation of Gaussian noise terms, and the output of the PWD detector is:

$$\begin{aligned} S_{PWD}^{H_0}(\hat{\zeta}, \hat{f}_d) &= \Re \left\{ \sum_{m=1}^{N_{DC}^{PW}} S_{2m}(\hat{\zeta}, \hat{f}_d) \cdot S_{2m-1}^*(\hat{\zeta}, \hat{f}_d) \right\} = \sum_{m=1}^{N_{DC}^{PW}} \Re \{ w_{2m} \cdot w_{2m-1}^* \} \\ &= \sum_{m=1}^{N_{DC}^{PW}} \Re \{ Y_{H_0, m} \} = \sum_{m=1}^{N_{DC}^{PW}} w_{2m}^I \cdot w_{2m-1}^I + w_{2m}^Q \cdot w_{2m-1}^Q = \sum_{m=1}^{N_{DC}^{PW}} Y_{H_0, m}^I \end{aligned} \quad (4.4)$$

where $N_{DC}^{PW} = \lfloor N_c/2 \rfloor$ is the number of differential integrations that can be performed for this detector having N_c coherent outputs available. The $Y_{H0,m}^I$ term can be rewritten as:

$$Y_{H0,m}^I = w_{2m}^I \cdot w_{2m-1}^I + w_{2m}^Q \cdot w_{2m-1}^Q = \frac{\sigma_w^2}{2} \cdot [(U_1^2 + U_3^2) - (U_2^2 + U_4^2)] = \frac{\sigma_w^2}{2} \cdot [x_1 - x_2] \quad (4.5)$$

where all the U_n terms are Normal-distributed with zero mean and variance 1:

$$\begin{aligned} U_1 &= \frac{w_{2m}^I + w_{2m-1}^I}{\sqrt{2}\sigma_w}, & U_2 &= \frac{w_{2m}^I - w_{2m-1}^I}{\sqrt{2}\sigma_w} \\ U_3 &= \frac{w_{2m}^Q + w_{2m-1}^Q}{\sqrt{2}\sigma_w}, & U_4 &= \frac{w_{2m}^Q - w_{2m-1}^Q}{\sqrt{2}\sigma_w} \end{aligned} \quad (4.6)$$

and, as so, both x_1 and x_2 are independent χ^2 random variables with two degrees of freedom [195]. From [196], the distribution of the subtraction of two independent random variables is given by:

$$f_Z(z) = \begin{cases} \int_0^\infty f_{X_1}(z+x_2) f_{X_2}(x_2) dy, & \text{if } z \geq 0 \\ \int_{-z}^\infty f_{X_1}(z+x_2) f_{X_2}(x_2) dy, & \text{if } z < 0 \end{cases} \quad (4.7)$$

where $z = x_1 - x_2$, and $f_{X_1}(x_1)$ and $f_{X_2}(x_2)$ are the PDFs of x_1 and x_2 , that is [196]:

$$f_X(x) = \frac{x^{n/2-1}}{2^{n/2} \cdot \Gamma(n/2)} \cdot e^{-x/2} = \frac{e^{-x/2}}{2}, \quad x \geq 0 \quad (4.8)$$

with $n = 2$ the number of degrees of freedom of the χ^2 distribution for both x_1 and x_2 . This way, $f_Z(z)$ can be easily rewritten as:

$$f_Z(z) = \begin{cases} 1/4 \cdot e^{-z/2} & \text{if } z \geq 0 \\ 1/4 \cdot e^{z/2} & \text{if } z < 0 \end{cases} = \frac{1}{4} \cdot e^{-|z|/2} \quad (4.9)$$

which corresponds to a Laplace distribution of zero mean and diversity or scale parameter, λ , equal to 2 [195]. From this same reference it comes that the variance of the Laplace distribution is $2\lambda^2$, which results in the variance of $c \cdot \text{Laplace}(\lambda)$ being $c^2 \cdot 2\lambda^2 = 2\lambda'^2$, implying that:

$$\frac{\sigma_w^2}{2} \cdot \text{Laplace}(\lambda) = \text{Laplace}\left(\frac{\sigma_w^2}{2} \cdot \lambda\right) \quad (4.10)$$

It finally results that $Y_{H_0}^I \sim \text{Laplace}(\sigma_w^2)$. The same reasoning can also be followed to demonstrate that $Y_{H_0}^Q \sim \text{Laplace}(\sigma_w^2)$ by simply defining a normal random variable $x = -w_{2m}^Q$ and analyzing the distribution of $w_{2m}^Q w_{2m-1}^I + x w_{2m-1}^I$. The corresponding Cumulative Density Function (CDF) of $Y_{H_0,m}^I$ is given by [195]:

$$F_{Y_{H_0,m}^I}(y) = \frac{1}{2} \left[1 + \text{sgn}(y) \left(1 - e^{-\frac{|y|}{\lambda}} \right) \right] \quad (4.11)$$

This way, the PWD detection metric under H_0 is obtained as the sum of N_{DC}^{PW} such $Y_{H_0,m}^I$ terms. Given the independency between the consecutive differential outputs characteristic of the PWD detector, the PDF of $S_{PWD}^{H_0}$ is that of the sum of independent Laplacian random variables. This PDF is known from [197] as:

$$f_{S_{PWD}^{H_0}}(y) = \sum_{k=0}^{N_{DC}^{PW}-1} \binom{N_{DC}^{PW} + k - 1}{k} \frac{e^{-\frac{|y|}{\lambda}} \left(\frac{|y|}{\lambda} \right)^{N_{DC}^{PW} - k - 1}}{2^{N_{DC}^{PW} + k} \cdot (N_{DC}^{PW} - k - 1)! \cdot \lambda} \quad (4.12)$$

and the respective CDF is found by integrating (4.12) with respect to y :

$$F_{S_{PWD}^{H_0}}(y) = \frac{1}{2} + \text{sgn}(y) \sum_{k=0}^{N_{DC}^{PW}-1} \binom{N_{DC}^{PW} + k - 1}{k} \frac{\Gamma_{N_{DC}^{PW} - k} \left(\frac{|y|}{\lambda} \right)}{2^{N_{DC}^{PW} - k}} \quad (4.13)$$

where $\Gamma_a(b)$ is the lower incomplete Gamma function of order a . The accuracy of this formulation can be asserted by comparing the histogram of simulation results with the theoretical distribution given by (4.12). This comparison is shown in Figure 4.2 for $N_{DC}^{PW} = 10$. As can be seen in this figure, the PDF corresponding to the sum of Laplace random variables accurately matches the simulation results. It is now possible to set the detection threshold, V_{th} , for the PWD detector according to the specified P_{fa} by using (4.13) and solving:

$$P_{fa} = 1 - F_{S_{PWD}^{H_0}}(V_{th}) \quad (4.14)$$

This characterization of the PWD detector under H_0 can be used as an alternative to the equivalent formulas in [6, 104].

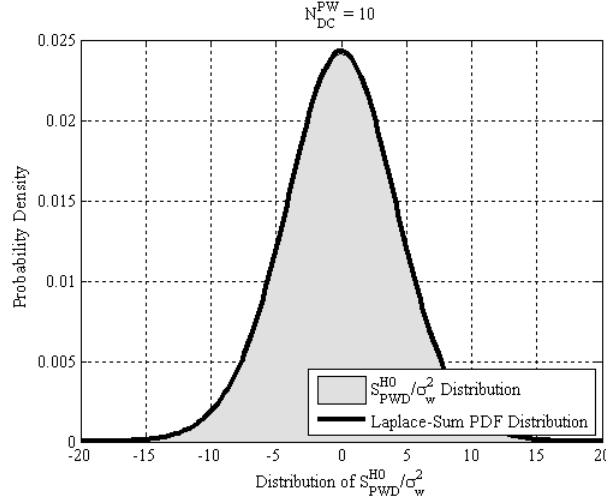


Figure 4.2 – Distribution of S_{PWD}^{H0} for $N_{DC}^{PW} = 10$ and PDF of sum of 10 independent Laplace random variables with $\lambda = \sigma_w^2$

4.2.2 Characterization under Signal and Noise Hypothesis (H_1)

Under H_1 , the signal under test is considered to be present and the detection performance of the detector as function of the input signal power, and the threshold set via the H_0 analysis, is assessed. In the presence of signal the PWD detection metric results as:

$$\begin{aligned}
 S_{PWD}^{H1}(\hat{\zeta}, \hat{f}_d) &= \Re \left\{ \sum_{m=1}^{N_{DC}^{PW}} S_{2m}(\hat{\zeta}, \hat{f}_d) \cdot S_{2m-1}^*(\hat{\zeta}, \hat{f}_d) \right\} \\
 &= \sum_{m=1}^{N_{DC}^{PW}} \Re \{ s_{2m} \cdot s_{2m-1}^* + s_{2m} \cdot w_{2m-1}^* + w_{2m} \cdot s_{2m-1}^* + w_{2m} \cdot w_{2m-1}^* \} \\
 &= \sum_{m=1}^{N_{DC}^{PW}} \Re \{ \mu_m + w_{Y,m} + Y_{H0,m} \} = \sum_{m=1}^{N_{DC}^{PW}} \Re \{ Y_{H1,m} \}
 \end{aligned} \tag{4.15}$$

The first term, μ_m , is the deterministic component originating from the product of the two signal components and the third term, $Y_{H0,m}$, was analyzed in the previous section. The remaining term, $w_{Y,m}$, is obtained as the sum of the products of the deterministic signal with Gaussian noise, and is therefore a Gaussian random variable. Thus, the statistical analysis of the differential integration output under H_1 involves analyzing the sum of a Laplace and a Gaussian random variable, dependent between them. If these two terms were independent, their distribution could be directly expressed as a Normal-Laplace random variable [198], however, this is not the case. In [104] as in [6], it is suggested to rewrite $\Re \{ Y_{H1,m} \}$ as the subtraction of two Chi-square random variables, but this approach does not seem to lead to a closed-form expression, having to resort to numerical methods in order to be able to obtain the final result.

Instead in [17] it is proposed to approximate $\Re\{Y_{H_0,m}\}$ by a Gaussian random variable, under the claim of the Central Limit Theorem (CLT) through which the summation of several such terms will tend to a normal distribution with variance equal to that of the individual terms. While this is not a recommended approach to follow under H_0 given the low precision at the tails of the Gaussian approximation vis-a-vis the requirement for the accurate threshold determination, it can be considered an acceptable approach under H_1 . Furthermore, in [97] four different PDFs are fitted to the actual distribution of the differential integration outputs under H_1 , concluding that the Gaussian distribution is the one that most accurately matches the true detector output distribution in these conditions. This will be especially true when the input signal power is high, and the Gaussian noise term becomes much more significant than the Laplacian one.

From [195] the variance of a Laplace-distributed random variable is $2\lambda^2$, which leads to:

$$\text{var}\{\Re\{Y_{H_0,m}\}\} = 2\sigma_w^4 \quad (4.16)$$

Assuming stationarity of all parameters during the signal integration time, the variance of $\Re\{w_{Y,m}\}$ can be easily seen to be given by:

$$\text{var}\{\Re\{w_{Y,m}\}\} = 2 \cdot \text{var}\{\Re\{s_m w_m\}\} = 2 \cdot |s_m|^2 \cdot \sigma_w^2 \quad (4.17)$$

This way, $S_{P_{WD}}^{H_1}(\hat{\zeta}, \hat{f}_d)$ can be modeled as a noncentral Gaussian random variable with mean $\mu_{S_{P_{WD}}^{H_1}}$ and variance $\sigma_{S_{P_{WD}}^{H_1}}^2$ given by:

$$\mu_{S_{P_{WD}}^{H_1}} \approx N_{DC}^{PW} \cdot \Re\{\mu_m\} = N_{DC}^{PW} \cdot |s_m|^2 \cdot \cos(2\pi\Delta f_d N T_s) \quad (4.18)$$

$$\sigma_{S_{P_{WD}}^{H_1}}^2 \approx N_{DC}^{PW} \cdot (\Re\{w_{Y,m}\} + \Re\{Y_{H_0,m}\}) = N_{DC}^{PW} \cdot 2\sigma_w^2 \cdot (|s_m|^2 + \sigma_w^2) \quad (4.19)$$

where once again the approximate equalities are obtained assuming stationarity of all parameters during the signal integration time. Evidently this is not the case when dealing with real signals, but it is an essential assumption for the characterization of the detectors' performance.

The drawbacks of the PWD detection metric are now well remarked in (4.18), as not only N_{DC}^{PW} is approximately only half of the number of differential integration outputs that can be generated, but also given $\Delta f_d \neq 0$ a portion of the signal power is allocated to the imaginary part of $Y_{H_1,m}$, and is therefore not useful. The expression for the probability of detection, P_d , for the PWD detector is finally obtained as:

$$P_{d,PWD} = \frac{1}{\sqrt{2\pi\sigma_{SPWD}^{H_1}}} \cdot \int_{V_{th}}^{\infty} \exp\left\{-\frac{(t - \mu_{SPWD}^{H_1})^2}{2\sigma_{SPWD}^{H_1}}\right\} \cdot dt = \frac{1}{2} \operatorname{erfc}\left(\frac{V_{th} - \mu_{SPWD}^{H_1}}{\sqrt{2\sigma_{SPWD}^{H_1}}}\right) \quad (4.20)$$

where $\operatorname{erfc}(\cdot)$ is the complementary error function, representing the tail probability of the standard normal distribution. To assess the accuracy of the fit provided by this expression, a comparison between the predicted and simulated detection rate for a GPS L1 C/A signal sampled at twice the chip rate is shown in Figure 4.3 for $N_{DC}^{PW}=1, 5$, and 10, employing 1ms coherent integration ($N = 2046$) and $\Delta f_d = \Delta \zeta = 0$. The theoretical analysis is carried by first calculating the threshold using (4.14) and then employing (4.20) to predict the detection probability, while the simulation analysis calculates the threshold based on the simulated noise distribution and then measures the detection rate as the percentage of threshold crossings for each Carrier-to-Noise (C/N_0) value.

As shown in Figure 4.3, the predicted pair-wise detector performance according to (4.20) is very close to the one observed in the simulations, what validates the Gaussian approximation under H_1 . The accuracy of this approximation can also be observed by comparing the normal PDF and the histogram of the detector outputs. Two examples are shown in Figure 4.4. From the plots in this figure it is clear that the Gaussian approximation is very accurate for high input C/N_0 values even for a low number of accumulations. This is due to the higher influence of the cross noise-signal multiplication, $w_{Y,m}$ in (4.15), with respect to the noise-only Laplacian term. Contrarily, for weak signals and a low number of accumulations, the Gaussian fit is not an accurate representation of the detector output distribution, but the closeness between the two distributions is still high. In fact, the area matched in the left plot of Figure 4.4 is close to 90%. This also explains why the

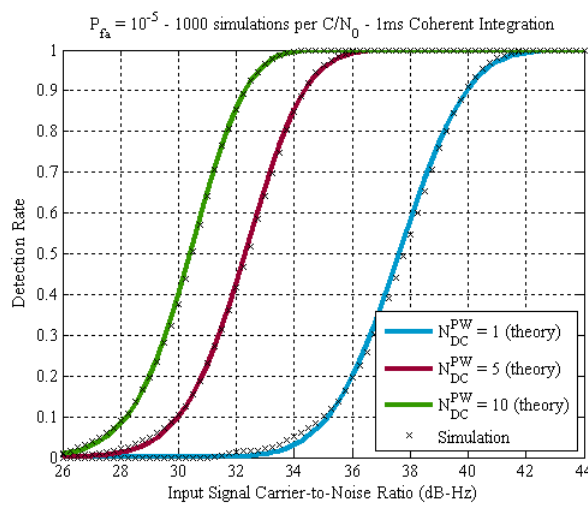


Figure 4.3 – Comparison between theoretical and simulated detection probability for $N_{DC}^{PW}=1, 5$, and 10 (1ms coherent integration, $\Delta f_d = \Delta \zeta = 0$)

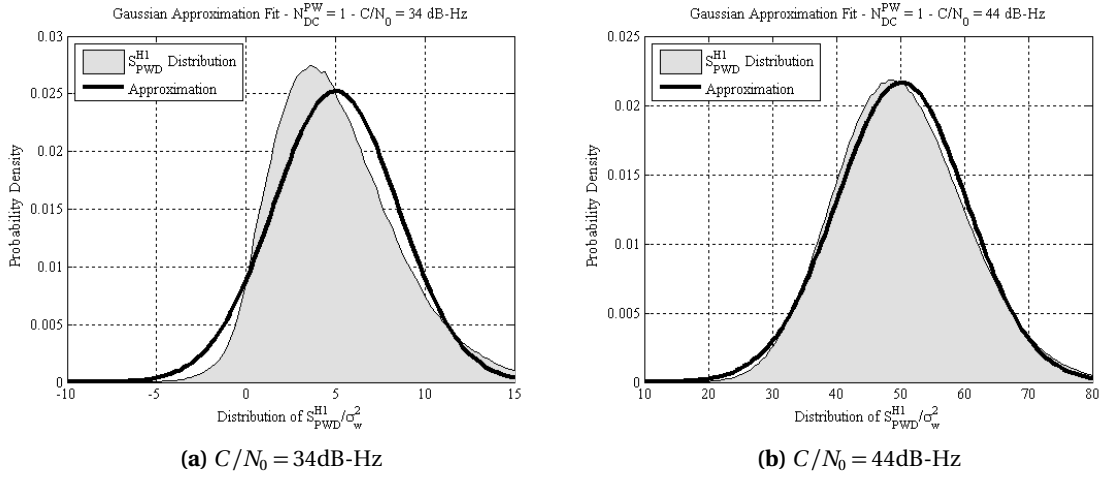


Figure 4.4 – Accuracy of Gaussian approximation of differential integration output under H_1 for $N_{DC}^{PW}=1$

difference between the predicted and simulated results in Figure 4.3 is not substantial even for low C/N_0 values. Additional simulations confirm that the Gaussian approximation becomes gradually more accurate for a higher number of accumulations, being the area match in these cases even greater than for the two presented here.

The expressions of the probability of false alarm and probability of detection derived in this section completely characterize the pair-wise differential detector. The derivation of similar expressions for the CDD and NCDD detectors is significantly more complex due to the rise of dependency between terms. Therefore, we follow a different approach in the next section to assess the performance of these two detectors.

4.2.3 Limitations of the PWD Detector

In the previous section, the pair-wise differential detector has been studied, highlighting its drawbacks for GNSS signals acquisition, particularly in the presence of a nonzero Doppler offset. A more suitable detector form when this condition cannot be ensured is the noncoherent differential detector (NCDD) whose detection metric is expressed as [90]:

$$S_{NCDD}(\hat{\zeta}, \hat{f}_d) = \left| \sum_{m=2}^{N_{DC}+1} S_m(\hat{\zeta}, \hat{f}_d) \cdot S_{m-1}^*(\hat{\zeta}, \hat{f}_d) \right|^2 \quad (4.21)$$

where $N_{DC} = N_C - 1$ is the number of differential integrations achievable with this detector form having N_C correlation outputs available. The advantage of this detector form with respect to the pair-wise one can be directly observed in simulations. In Figure 4.5, the two detectors' detection performance is compared for three different simulation scenarios whose details are shown in Ta-

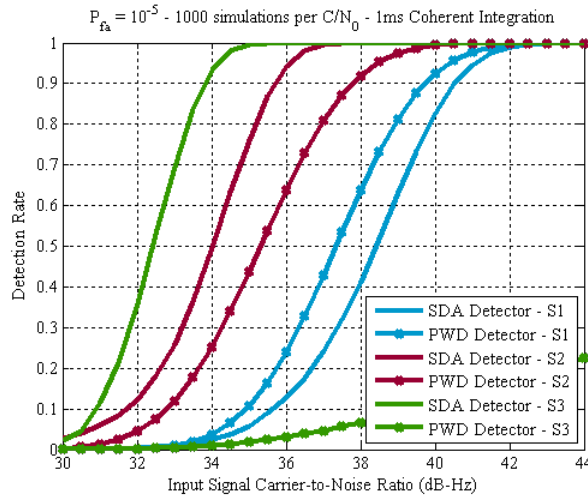


Figure 4.5 – Comparison of pair-wise and noncoherent differential detectors for simulation scenarios described in Table 4.1

Table 4.1 – Simulation scenarios for detectors comparison in Figure 4.5

| Simulation Parameters | Simulation Scenario | | |
|---------------------------|----------------------------------|-----------------|------------------|
| | S1 | S2 | S3 |
| Signal | GPS L1 C/A | | |
| Sampling Frequency | 2.046MHz | | |
| Coherent Integration Time | 1 code period - 1ms/2046 samples | | |
| Number of Code Periods | 2 | 6 | 11 |
| Differential Integrations | NCDD 1 PWD 1 | NCDD 5 PWD 3 | NCDD 10 PWD 5 |
| Doppler Offset | 0Hz | 125Hz | 250Hz |

ble 4.1. While for the case where the Doppler offset is null, or very small, the PWD detector outperforms the NCDD, due to the absence of the squaring loss and all the signal power being in the inphase branch according to (4.18), as this offset grows the limitations of the PWD detector with respect to the NCDD are well remarked. For scenario S3, for example, the nonzero detection rate for the PWD detector at high input signal power is achieved merely due to the influence of the cross signal-noise Gaussian terms $w_{Y,m}$ in (4.15).

4.3 Evaluation of the Sensitivity Loss of a Nonoptimal Detector

As the statistical characterization of the NCDD detector is not easy to accomplish, works in literature commonly use the Gaussian approximation under both H_0 and H_1 hypotheses. However, as previously noted, this cannot be considered a reasonable option under H_0 for a low number of differential accumulations given the required precision at the tails of the distribution. Instead we propose to follow an alternative to the formal statistical analysis of this detector, establishing a comparison with a reference scheme whose analysis is mathematically viable. This approach is followed in [18] for the characterization of the noncoherent detector applied to radar systems. In [18], a sensitivity loss term is defined that allows predicting the detection performance of a noncoherent detection scheme operating at a target receiver working point (P_d, P_{fa}) , with respect to the one which would be obtained if a coherent solution was instead applied. The formula provided in [18] is usually adopted in GNSS literature for analysis of the squaring loss of noncoherent integration [3, 71, 80]. The same procedure is followed in this section to propose a loss formula for the noncoherent differential detector, L_{NCDD} .

This section starts by reviewing the optimal GNSS detector as well as the procedure to derive a sensitivity loss formula with respect to this detector. The procedure followed in [18] for the derivation of the squaring loss is then described as an example of application of this approach. Next, a formula for the differential integration loss is proposed, and the sensitivity loss of the NCDD detector is finally obtained as a combination of the differential and squaring losses.

4.3.1 Optimal Detector and Sensitivity Loss Definition

The optimal detector in the presence of a stationary signal and known signal phase is the purely coherent detector (CD) [45]. The detection metric for the coherent detector is defined as:

$$S_{CD}(\hat{\zeta}, \hat{f}_d) = \Re \left\{ \sum_{m=1}^{N_c} S_m(\hat{\zeta}, \hat{f}_d) \right\} \quad (4.22)$$

It should be noted that this detector is only possible to apply in theory given the assumption of knowledge of the input signal phase. However it serves as a reference for the evaluation of the detection loss of nonoptimal, but practical, detectors. The equation that characterizes this detector's performance is [18]:

$$P_{d,CD} = \frac{1}{2} \operatorname{erfc} \left[\operatorname{erfc}^{-1}(2P_{fa}) - \sqrt{N_c N_s \operatorname{snr}_{in}} \right] = \frac{1}{2} \operatorname{erfc} \left[\operatorname{erfc}^{-1}(2P_{fa}) - \sqrt{\operatorname{snr}_{coh}} \right] \quad (4.23)$$

where snr_{in} and snr_{coh} are, respectively, the Signal-to-Noise Ratio (SNR, expressed in linear dimen-

sions) at the detector input and after coherent integration (in this case coincident with the detector output). Inverting (4.23), the SNR at the coherent integration output can be expressed as function of the target working point:

$$\text{snr}_{\text{coh}} = [\text{erfc}^{-1}(2P_{fa}) - \text{erfc}^{-1}(2P_d)]^2 = D_c(P_d, P_{fa}) \quad (4.24)$$

This SNR is also known as ideal detectability factor, D_c , and represents the minimum SNR at the coherent integration output that allows detection of signal at the target receiver working point (P_d, P_{fa}) . The minimum input precorrelation SNR is then expressed as a function of D_c as:

$$\text{snr}_{\text{in,min}} = \frac{D_c(P_d, P_{fa})}{N_c N_s} \quad (4.25)$$

The product $N_c N_s$ in (4.25) corresponds to the gain of coherently integrating the $N_c N_s$ signal samples, N_s being the number of samples per code period, and is the maximum achievable signal integration gain [18]. Consequently, the required input SNR, $\text{snr}_{\text{in,req}}$, for achieving a similar working point with detectors employing other integration approaches (such as noncoherent or differential integration), must always be higher than $\text{snr}_{\text{in,min}}$, given the nonideality of the operations involved. A sensitivity loss characteristic of the nonideal detector, L_{detector} , with respect to the ideal coherent one may then be expressed as [18]:

$$L_{\text{detector}} = \frac{\text{snr}_{\text{in,req}}}{\text{snr}_{\text{in,min}}} = \frac{\text{snr}_{\text{in,req}} \cdot N_s}{D_c(P_d, P_{fa})/N_c} \quad (4.26)$$

Given the linearity of the correlation operation, L_{detector} can also be interpreted as the ratio of the two correlation output SNRs (Figure 4.6). This can also be noted from (4.26) as the product $\text{snr}_{\text{in,req}} \cdot N_s$ corresponds to the SNR at the correlation output of the nonoptimal detector, and $D_c(P_d, P_{fa})/N_c$ corresponds to the SNR at the correlation output of the coherent detector. Finally, the required SNR to acquire a signal at a given working point with the nonoptimal detector can be expressed as:

$$\begin{aligned} \text{SNR}_{\text{in,req,dB}} &= \text{SNR}_{\text{in,min,dB}} + L_{\text{detector,dB}} \\ &= 10 \cdot \log_{10} \left(\frac{D_c(P_d, P_{fa})}{N_c N_s} \right) + L_{\text{detector,dB}} \end{aligned} \quad (4.27)$$

The ratio D_c/N_s corresponds to the input SNR that would be required by the CD detector if only 1 code period would be available and can be denoted as $\text{snr}_{\text{in,min},N_c=1}$. Equation (4.27) can then be rewritten as:

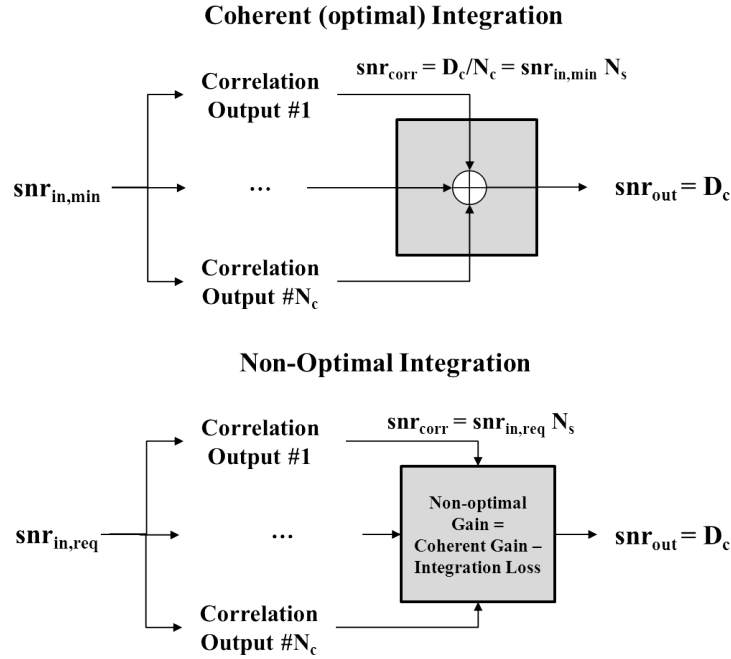


Figure 4.6 – Coherent (optimal) and nonoptimal integration strategies diagram and SNR measuring points

$$\begin{aligned}
 \text{SNR}_{\text{in,req,dB}} &= \text{SNR}_{\text{in,min},N_c=1,\text{dB}} - (10 \cdot \log_{10}(N_c) - L_{\text{detector,dB}}) \\
 &= \text{SNR}_{\text{in,min},N_c=1,\text{dB}} - G_{\text{detector,dB}}(N_c)
 \end{aligned}
 \tag{4.28}$$

where G_{detector} corresponds to the detector sensitivity gain of integrating a number N_c of code periods and is defined as the difference between the ideal gain of coherent integration and the loss of the nonoptimal operations performed with respect to the ideal detector.

4.3.2 Sensitivity Loss of the Squaring Operation

These expressions can be used in the quantification of the squaring loss, L_{sq} , that is incurred by the phase removal operation, representing the price to pay in terms of additional input SNR for not knowing the input signal phase. In this case, the optimal detector is the square-law detector (SLD), whose detection metric is expressed as [45]:

$$S_{\text{SLD}}(\hat{\zeta}, \hat{f}_d) = \left| \sum_{m=1}^{N_c} S_m(\hat{\zeta}, \hat{f}_d) \right|^2
 \tag{4.29}$$

The equation that characterizes the detection performance of the SLD detector is [6]:

$$P_{d,SLD}(\hat{\zeta}, \hat{f}_d) = Q_1\left(\sqrt{2N_c N_s \text{snr}_{in}}, \sqrt{-2 \cdot \ln(P_{fa})}\right) = Q_1\left(\sqrt{2\text{snr}_{coh}}, \sqrt{-2 \cdot \ln(P_{fa})}\right) \quad (4.30)$$

where $Q_K(a, b)$ is the K^{th} order Marcum Q-function. The effect of the squaring loss can be observed through the comparison of the performance of the CD and SLD detectors, through (4.23) and (4.30), respectively. This is shown in Figure 4.7. According to the methodology described in the previous section, the squaring loss can be expressed as the ratio between the input SNRs required by the two detectors in order to achieve similar detection performance:

$$L_{sq} = \frac{\text{snr}_{in,SLD}}{\text{snr}_{in,CD}} = \frac{\text{snr}_{coh,SLD}}{\text{snr}_{coh,CD}} = \frac{\text{snr}_{coh,SLD}}{D_c(P_d, P_{fa})} \quad (4.31)$$

This loss can be promptly obtained by solving (4.23) and (4.30) for any pair (P_d, P_{fa}) and using the results in (4.31). Nevertheless, solving these equations is a nontrivial mathematical process, and in [18] a simple approximation for L_{sq} is suggested:

$$L_{sq} = \frac{\text{snr}_{coh,SLD}}{D_c(P_d, P_{fa})} \approx 1 + \frac{2.3}{\text{snr}_{coh,SLD}} \approx \frac{1 + \sqrt{1 + 9.2/D_c(P_d, P_{fa})}}{2} \quad (4.32)$$

The values for L_{sq} obtained through (4.31) and the approximation of (4.32) are shown in Figure 4.8. This way, the sensitivity gain of the SLD detector in the presence of N_c code periods is then given by:

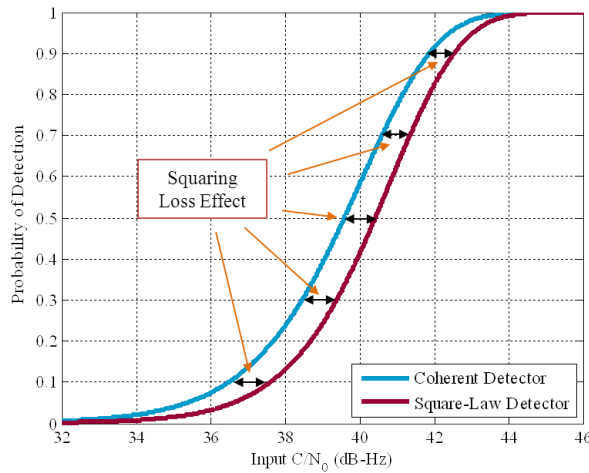


Figure 4.7 – Comparison of the CD and SLD detectors for the acquisition of a 1ms GPS C/A signal sampled at twice the chip rate and $P_{fa} = 10^{-5}$

$$G_{SLD,dB}(N_c) = G_{coh,dB}(N_c) - L_{sq,dB} \quad (4.33)$$

where $G_{coh}(N_c) = N_c$. As an example, the input signal power required by the SLD detector for the acquisition of a single GPS C/A code period, sampled at 2 times the chip rate ($N_s = 2046$), and for a working point $(P_d, P_{fa}) = (0.9, 10^{-5})$ can be found through:

$$D_{c,dB}(0.9, 10^{-5}) = [\text{erfc}^{-1}(2 \cdot 10^{-5}) - \text{erfc}^{-1}(2 \cdot 0.9)]^2 = 11.9 \text{ dB}$$

$$L_{sq,dB} = 10 \cdot \log_{10} \left(\frac{1 + \sqrt{1 + 9.2/D_c(P_d, P_{fa})}}{2} \right) = 0.6 \text{ dB}$$

$$G_{SLD,dB}(1) = G_{coh,dB}(0) - L_{sq,dB} = -0.6 \text{ dB}$$

$$\text{SNR}_{in,SLD,dB} = \text{SNR}_{in,min,N_c=1,dB} - G_{SLD,dB}(1) \approx -20.6 \text{ dB}$$

Naturally, a very similar result is obtained by solving (4.30):

$$0.9 = Q_1 \left(\sqrt{2 \cdot 1 \cdot 2046 \cdot \text{snr}_{in}}, \sqrt{-2 \ln(10^{-5})} \right) \iff \text{SNR}_{in,dB} \approx -20.6 \text{ dB}$$

This approach can be generalized to any number of squaring operations, and is the basis to obtain the loss of the noncoherent integration scheme in [18]. This method of evaluating the nonoptimal detectors' sensitivity loss differs from the traditional approach of calculation of a deflection coef-

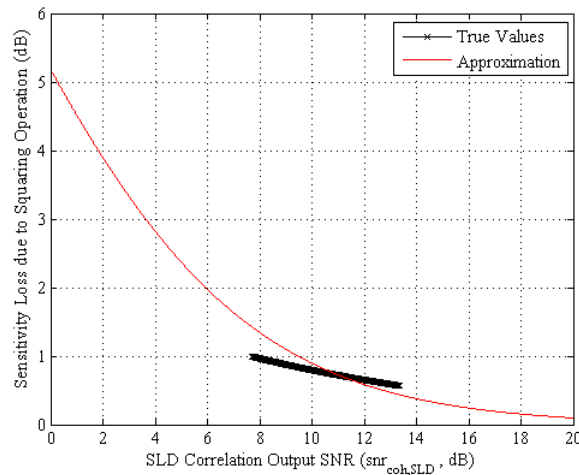


Figure 4.8 – Comparison of the squaring loss values obtained for the curves shown in Figure 4.7 and the approximation of (4.32) for $P_d \in [0.1; 0.9]$ (leftmost point corresponding to $P_d = 0.1$ and rightmost to $P_d = 0.9$)

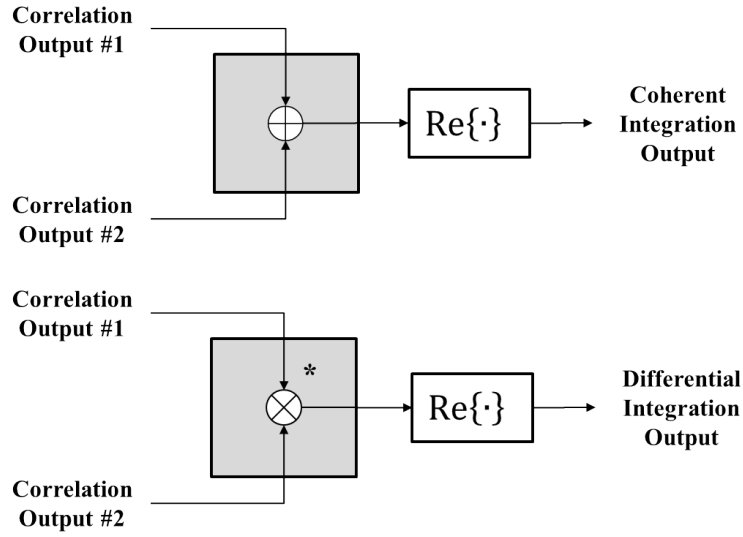


Figure 4.9 – Comparison for determination of differential operation sensitivity loss

ficient, as a measure of the output SNR. This approach has been followed for both the differential and noncoherent detection schemes in several publications such as [20, 97], but its inapplicability in these cases is explicitly illustrated in [19] and, therefore, it is not considered here.

4.3.3 Sensitivity Loss of the Differential Operation

In order to be able to quantify exclusively the loss of the differential operation with respect to coherent summing, the detection scheme employed in this analysis must avoid any other operations, in particular the squaring of the signal for phase removal. This can be achieved by concentrating all the signal power on the in-phase branch of the differential integration output (zero Doppler offset) and then taking just its real part as the detection metric (Figure 4.9). By comparing the required input SNRs for the two schemes in Figure 4.9, it is guaranteed that the difference in performance between both is exclusively due to the nonoptimality of differential operation with respect to coherent summing. The differential detector employed in this case corresponds to the CDD detector:

$$S_{CDD}(\hat{\zeta}, \hat{f}_d) = \Re \left\{ \sum_{m=2}^{N_{DC}+1} S_m(\hat{\zeta}, \hat{f}_d) \cdot S_{m-1}^*(\hat{\zeta}, \hat{f}_d) \right\} \quad (4.34)$$

As for the moment we are focusing in the assessment of the sensitivity loss of a single differential operation, the detection metric of interest is:

$$S_{CDD}(\hat{\zeta}, \hat{f}_d) = \Re \left\{ S_2(\hat{\zeta}, \hat{f}_d) \cdot S_1^*(\hat{\zeta}, \hat{f}_d) \right\} \quad (4.35)$$

To characterize the sensitivity of this detector using its probability of detection, we need the PDF of the detection metric in (4.35) under H_1 . As this detection metric is equivalent to the pair-wise detector one for $N_{DC}^{PW} = 1$, the results from the previous section can be directly applied. Making use of (4.11), (4.14), and (4.18)-(4.20), the equation that characterizes this detector for $N_{DC}^{PW} = 1$ is:

$$\begin{aligned}
P_{d,CDD} &= \frac{1}{2} \operatorname{erfc} \left(\frac{V_{th} - \mu_{S_{P_{WD}}^{H_1}}}{\sqrt{2\sigma_{S_{P_{WD}}^{H_1}}^2}} \right) = \frac{1}{2} \operatorname{erfc} \left(-\frac{\sigma_w^2 \cdot \ln(P_{fa}) + |s_m|^2}{\sqrt{4\sigma_w^2 \cdot (|s_m|^2 + \sigma_w^2)}} \right) \\
&= \frac{1}{2} \operatorname{erfc} \left(-\frac{\ln(P_{fa}) + 2\sigma_w^2 \cdot N_s \cdot \operatorname{snr}_{in}}{\sqrt{8N_s \cdot \operatorname{snr}_{in} + 4}} \right)
\end{aligned} \tag{4.36}$$

According to (4.26), the sensitivity loss of a single differential operation as function of D_c , $L_{diff}(1, D_c)$, can be expressed as:

$$L_{diff}(1, D_c) = \frac{\operatorname{snr}_{in,req}}{\operatorname{snr}_{in,min}} = \frac{\operatorname{snr}_{in,req} \cdot N_s}{D_c (P_d, P_{fa})/2} \tag{4.37}$$

where $\operatorname{snr}_{in,req}$ in this case is the input SNR required by the CDD detection scheme to achieve the working point specified by D_c . This required input SNR can be directly obtained by solving (4.36) for any pair (P_d, P_{fa}) , but it should be noted that this expression is based on the Gaussian approximation under H_1 , which was seen not to be entirely accurate. Another option is simply to consider the Gaussian and Laplace terms independent, in which case a Normal-Laplace random variable is obtained [198]. The expression that characterizes this detector under this assumption is shown in Appendix B. The accuracy of these two approximations of $P_{d,CDD}$ can be assessed by comparing the predicted P_d from (4.36) and (B.4) with the results obtained from simulation. This comparison is shown in Figure 4.10 for the acquisition of a GPS C/A signal, sampled at 2 times the chip rate ($N_s=2046$), $P_{fa} = 10^{-5}$ and $\Delta f_d = \Delta \zeta = 0$. As expected, none of the approximations represents an entirely accurate prediction of the detector performance. In fact, the predicted performances according to both approximations are almost coincident, from which it can be concluded that the oddity of the differential detector behavior is mostly due to the dependence between the two stochastic terms under analysis.

Figure 4.11 shows $L_{diff}(1, D_c)$ calculated through (4.37) using the $\operatorname{snr}_{in,req}$ values for the approximations and simulation values shown in Figure 4.10. All curves are expressed as function of $D_c/2$. Although the difference between the approximations and simulation loss values is not considerable, the profile exhibited is significantly different. This fact complicates the proposal of an expression to $L_{diff}(1, D_c)$ based on the theoretical loss curves which is consistent at both high and low SNR values. Therefore, in order not to propagate the errors of the approximations in the exten-

sion to $L_{diff}(N_{DC}, D_c)$, the simulation-derived loss curve is considered. The theoretical analysis, nevertheless, is useful to validate the simulation results. Several different models can be employed in the attempt to approximate the simulation points of $L_{diff}(1, D_c)$ shown in Figure 4.11. Although various approximations of different orders of $1/(D_c/2)$ offer a good fit in the SNR area under consideration in the figure, their behavior at high and, especially, low SNR values makes them unsuitable for the approximation sought. One approximation that closely matches the simulation results in the SNR range under consideration and that is consistent for both low and high SNR values is:

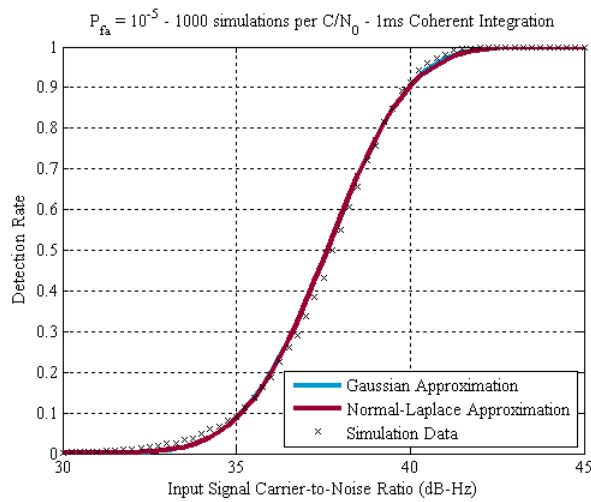


Figure 4.10 – Comparison of Gaussian and Normal-Laplace approximations for the CDD detector for $N_{DC} = 1$

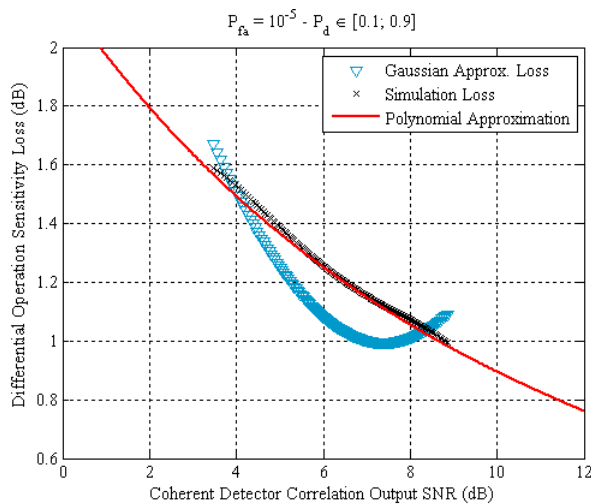


Figure 4.11 – Sensitivity loss due to the differential operation – theory, simulation and approximation for $P_{fa} = 10^{-5}$ and $P_d \in [0.1; 0.9]$ (leftmost point corresponding to $P_d = 0.1$ and rightmost to $P_d = 0.9$)

$$L_{diff}(1, D_c) \approx 1 + \frac{0.2}{D_c/2} + \frac{0.45}{\sqrt[3]{D_c/2}} \quad (4.38)$$

This curve is also shown in Figure 4.11, where its accuracy in predicting the sensitivity loss induced by one differential operation is verified. In order to generalize this loss formula to any number of differential operations, $L_{diff}(N_{DC}, D_c)$, it suffices to note that the SNR at the correlation output of the coherent detector is written as D_c/N_c or, for the case of the NCDD detector, $D_c/(N_{DC} + 1)$. Equation (4.37) can then be rewritten as:

$$L_{diff}(1, D_c) \approx 1 + \frac{0.2 \cdot (N_{DC} + 1)}{D_c} + \frac{0.45 \cdot \sqrt[3]{(N_{DC} + 1)}}{\sqrt[3]{D_c}} \quad (4.39)$$

This formula expresses the sensitivity loss incurred by a number N_{DC} of differential integrations (employing $N_{DC} + 1$ coherent outputs) and a receiver working point specified by $D_c(P_d, P_{fa})$, with respect to the coherent operation. It should be noted that this simple passage from (4.38) to (4.39) does not actually take into account the dependence between the consecutive differential outputs. Nevertheless, as it will be seen further, it still seems to be a good approximation of the actual loss experienced by the NCDD detector. If this formula would be to be applied in a detector which employs the pair-wise integration approach, then $N_c = 2N_{DC}$ should instead be used in (4.39). Making use of this loss formula, the loss of the NCDD detector can finally be determined.

4.3.4 Sensitivity Loss of the NCDD Detector

After characterizing the loss of differential integration, we now extend the analysis to the NCDD detector loss, L_{NCDD} , which, according to the block diagram shown in Figure 4.12, is a combination of both differential integration and squaring loss. According to the procedure previously described, the NCDD detector sensitivity loss is defined as the additional input SNR that is required by this detector with respect to the input SNR that is required by the coherent detection scheme to achieve a similar target working point. The sensitivity gain of the NCDD scheme having N_c coherent outputs available is then expressed as follows (D_c is omitted in the loss formulas for simplicity of notation and all the terms are in dB):

$$\begin{aligned} G_{NCDD}(N_c) &= G_{coh}(N_c) - L_{NCDD}(N_c) \\ &= G_{coh}(N_c) - (L_{diff}(N_{DC}) + L_{sq}) \\ &= G_{SLD} - L_{diff}(N_{DC}) \end{aligned} \quad (4.40)$$

This way we can directly relate the sensitivity gain of the NCDD detector with that of the SLD de-

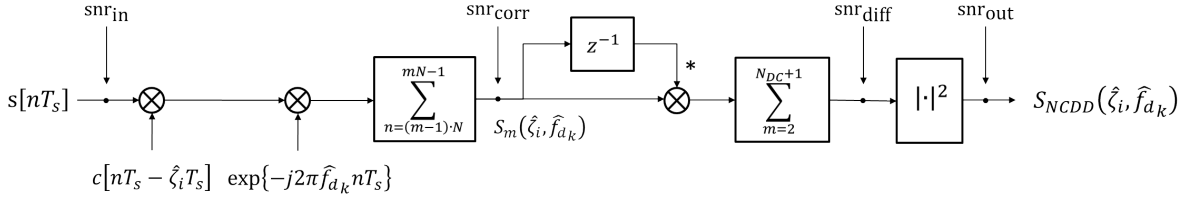


Figure 4.12 – Noncoherent differential detector block diagram and SNR measuring points

detector by $L_{diff}(N_{DC})$. This will be particularly useful in the comparison of the NCDD and NCD detectors, as the sensitivity loss formula proposed in [18] for the latter is also related to the SLD detector. It should be noted that, even if $L_{diff}(N_{DC})$ was obtained for the CDD scheme by concentrating all the signal power in the real branch of the correlation output, it expresses the sensitivity loss of the differential operation as function of the SNR of the coherent output and it is independent of its phase. This way, it can be directly applied in (4.40).

It then suffices to express the differential operation loss as function of the SNR prior to the phase removal operation, snr_{diff} in Figure 4.12. This can be done by recurring to the squaring loss formula:

$$L_{sq} = \frac{\text{snr}_{diff}}{\text{snr}_{out}} \approx \frac{1 + \sqrt{1 + 9.2/\text{snr}_{out}}}{2} \quad (4.41)$$

where snr_{out} is the SNR at the output of the NCDD detector as shown in Figure 4.12. Given that all the loss formulas have been developed with respect to the coherent detector, it then follows that $\text{snr}_{out} = D_c$ and therefore:

$$L_{sq} = \frac{\text{snr}_{diff}}{\text{snr}_{out}} = \frac{\text{snr}_{diff}}{D_c} \approx \frac{1 + \sqrt{1 + 9.2/D_c}}{2} \iff \text{snr}_{diff} \approx D_c \cdot \frac{1 + \sqrt{1 + 9.2/D_c}}{2} \quad (4.42)$$

The sensitivity loss of the NCDD detector with respect to SLD is finally given by:

$$L_{diff}(N_{DC}) \approx 1 + \frac{0.2 \cdot (N_{DC} + 1)}{\text{snr}_{diff}} + \frac{0.45 \cdot \sqrt[3]{(N_{DC} + 1)}}{\sqrt[3]{\text{snr}_{diff}}} \quad (4.43)$$

The accuracy of this formula can be assessed by comparing the predicted and observed sensitivity losses obtained through simulations. Defining a target $P_d = 0.9$, the predicted and observed sensitivity loss of the NCDD detection scheme with respect to the SLD detector in the acquisition of a GPS L1 C/A signal ($N_s = 2046$) is shown in Figure 4.13 for three different values of P_{fa} . From this figure it can be seen that there is a very close match between the observed and expected loss profiles for this detector. In fact, the prediction is accurate to within ± 0.3 dB in the interval presented for each of the three P_{fa} values considered. For N_{DC} between 50 and 100 the maximum error is still

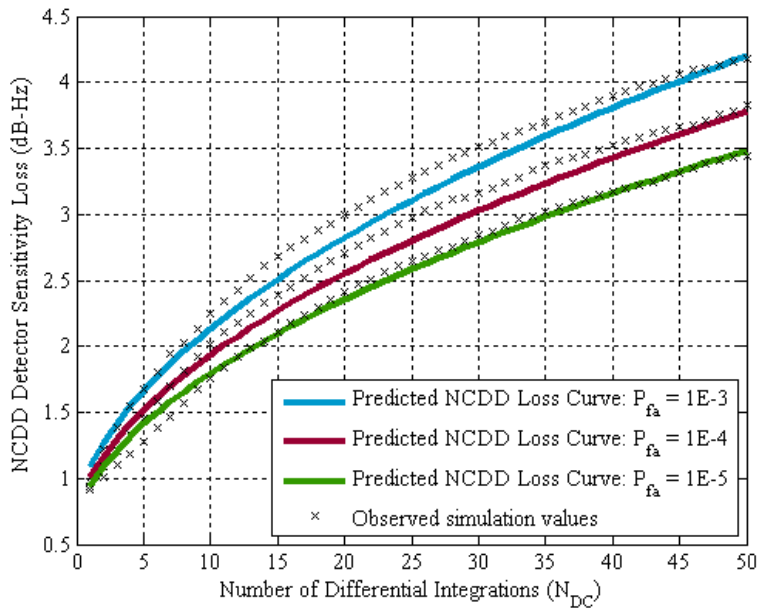


Figure 4.13 – Predicted and observed losses for the NCDD detection scheme with respect to the SLD detector as function of N_{DC} and P_{fa} for $P_d = 0.9$

within ± 0.5 dB.

4.4 Applications of the NCDD Detector Sensitivity Loss Formula

One of the applications of the proposed formula is for characterizing the detection performance of the NCDD detector. We can use this formula to construct the sensitivity curve of the detector using as reference the curve of the SLD detector given by (4.23). The comparison between the simulated and predicted detector performance for $N_{DC} = 20$ is shown in Figure 4.14. It can be noticed from this figure that the predicted NCDD sensitivity loss at $(P_d, P_{fa}) = (0.9, 10^{-5})$ with respect to SLD is very close to the actual value.

Another application of this formula is in the estimation of the number of differential integrations required for the acquisition of a GPS L1 C/A signal at a given input C/N_0 . Figure 4.15 shows this estimation for three different values of coherent integrations. One more interesting application of this loss formula is in the comparison of the NCDD detector with the NCD one. This analysis is carried in the next section.

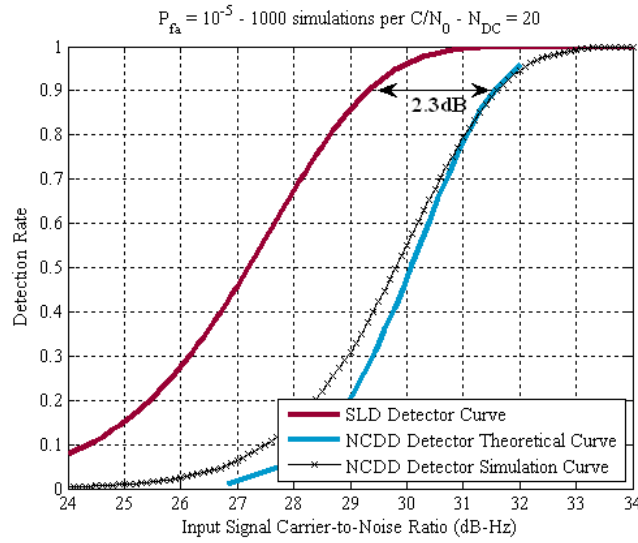


Figure 4.14 – Illustration of NCDD detector sensitivity loss with respect to SLD detector for $N_{DC} = 20$ and accuracy of loss formula

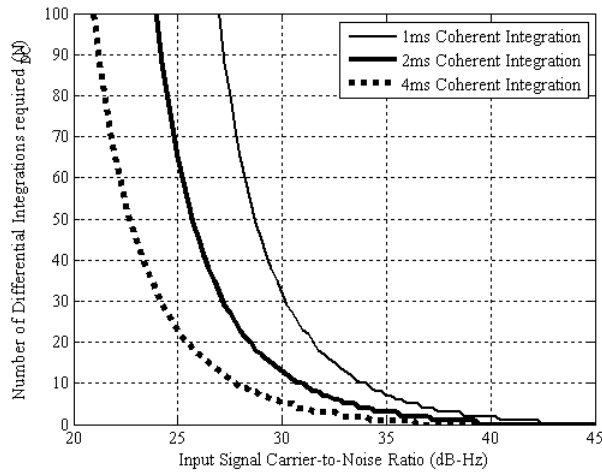


Figure 4.15 – Number of differential integrations required for the NCDD detector to achieve detection at $(P_d, P_{fa}) = (0.9, 10^{-5})$ as function of coherent integration time and input C/N_0

4.5 Differential and Noncoherent Detection Schemes Theoretical Comparison

The comparison of differential and noncoherent detection schemes has been the subject of several publications in recent years [6, 17, 45, 97, 101]. To the author's best knowledge, the first formal comparisons between the sensitivity losses of the NCDD and the noncoherent detector (NCD) are found in [106, 107], recurring to (4.43). These comparisons are revisited in this section.

The detection metric for the NCD detector is defined as:

$$S_{NCD}(\hat{\zeta}, \hat{f}_d) = \sum_{m=1}^{N_{NC}} |S_m(\hat{\zeta}, \hat{f}_d)|^2 \quad (4.44)$$

where $N_{NC} = N_c$ is the number of noncoherently accumulated correlation outputs. The sensitivity loss of the NCD detector, L_{NCD} , with respect to the SLD detector is given in [3, 18] as an extension of the squaring loss formula in (4.31):

$$L_{NCD}(N_{NC}) = \frac{1 + \sqrt{1 + 9.2 \cdot N_{NC}/D_c}}{1 + \sqrt{1 + 9.2/D_c}} \quad (4.45)$$

Two analyses are carried next, comparing the sensitivity of the two detectors in the presence or absence of Doppler estimation errors in correlation.

4.5.1 Comparison in Absence of Doppler Sensitivity Losses

If the Doppler offset is small enough for its effect on the coherent integration output to be disregarded, a direct comparison between the two loss formulas, (4.43) and (4.45), can be used to compare the relative performance of the detectors. In Figure 4.16, the losses that would be observed by each scheme with respect to the SLD detector for three different working points are presented. The number of available code periods is varied from 2 to 50 to obtain the curves shown. According to Figure 4.16, for a low number of differential integrations the combined effect of the differential and squaring loss leads to an inferior performance of the NCDD detector with respect to the NCD. This can also be seen in Figure 4.17 where the curves for the sensitivity loss of each detector are shown for $(P_d, P_{fa}) = (0.9, 10^{-5})$. As the predictions from both loss formulas are not exact, conclusions about the precise crossing point should not be taken from these plots. In any case, it is safe to state that for the acquisition of weak signals, requiring a high number of postcoherent accumulations, the differential detector is a preferable choice.

The effect of the inferior sensitivity loss of the NCDD detector with respect to the NCD for the acquisition of weak signals is reflected on the acquisition time that each detector needs to achieve the required degree of confidence in the detection of a given signal with a certain power. In the detection of the presence of signal, the allocation of the signal integration time between the coherent and postcoherent strategy involves a trade-off between sensitivity and complexity. The ultimate practical restriction to the increase of the coherent integration time (considering no navigation data bit influence or dynamics and clock instability effects) is the number of frequency grid points, N_{f_d} , to be evaluated in the acquisition process. The usual practice is to define a maximum allowable frequency attenuation for the coherent output which should not be exceeded, resulting in a rule such as [1]:

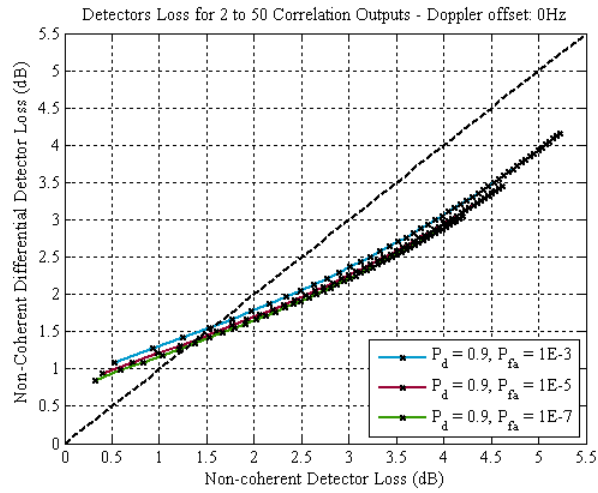


Figure 4.16 – Sensitivity loss of NCDD and NCD with respect to SLD for $\Delta f_d = 0$ and $N_{NC} = N_{DC+1} \in [2,50]$ (leftmost point corresponding to $N_{NC} = 2$ and rightmost one to $N_{NC} = 50$)

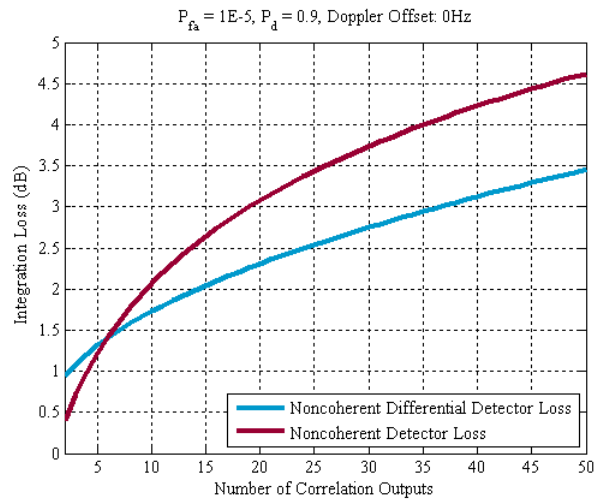


Figure 4.17 – Sensitivity loss of NCDD and NCD with respect to SLD as function of number of correlation outputs for $\Delta f_d = 0$ and $(P_d, P_{fa}) = (0.9, 10^{-5})$

$$N_{f_d} = \frac{\Delta F_d}{\delta f_d} = \frac{\Delta F_d}{x/T_{coh}}$$

where ΔF_d is the width of the Doppler frequency search space (typically around 10kHz), δf_d is the frequency grid resolution, and x is the coefficient resulting from the maximum desired amplitude attenuation [1]:

$$L_{\delta f, \max} = \text{sinc}(T_{coh} \cdot \delta f_d / 2) \iff \delta f_d = \frac{x}{T_{coh}}$$

- $L_{\delta f, \max, dB} = 0.5 \text{dB} \implies x = 1/2$
- $L_{\delta f, \max, dB} = 1.9 \text{dB} \implies x = 1$

This way, even if the maximum integration gain is obtained through the increase of the coherent integration time, it directly impacts the acquisition process complexity (number of operations required). As an example, we consider a total signal observation time of 20ms. The highest sensitivity gain possible corresponds to coherently integrating throughout the 20 code periods, that is:

$$G_{coh, dB}(20) = 10 \cdot \log_{10}(20) = 13 \text{dB}$$

The other alternatives imply trading-off the coherent and postcoherent integration gains according to the equations (values in dB):

$$G_{NCD}(N_{NC}) = G_{coh}(N_C) - L_{NCD}(N_{NC}) \quad (4.46)$$

$$G_{NCDD}(N_{DC}) = G_{coh}(N_C) - L_{NCDD}(N_{DC}) \quad (4.47)$$

In Table 4.2, the number of coherent outputs required for each different postcoherent integration strategy to achieve the 13dB gain for a working point of $(P_d, P_{f_a}) = (0.9, 10^{-5})$ and for different number of coherent integrations is shown. The number of frequency grid points is calculated for a grid employing $\delta f_d = 1/T_{coh}$. Naturally, the strategy requiring the shortest observation time is the one employing the longest coherent integration time. It can also be seen that the performance of the NCDD and NCD schemes become very similar when low postcoherent integration gains are sought. The preferable solution from the ones presented in the table should be found as a compromise between integration time and complexity.

The inverse analysis can also be conducted, which is to determine the preferable integration strategy given an input signal C/N_0 . Take, for example, a GPS C/A signal at 35dB-Hz which is coherently integrated during 1 code period, and that is intended to be detected at $(P_d, P_{f_a}) = (0.9, 10^{-5})$.

The SNR at the correlation output will be:

$$\text{SNR}_{\text{coh}} = C/N_0 - 10 \cdot \log_{10}(B) + 10 \cdot \log_{10}(N_s) = 5\text{dB}$$

where the bandwidth, B , is approximately equal to the sampling frequency. According to (4.24), the required SNR to achieve this working point for coherent detection would be:

$$D_c = 10 \cdot \log_{10} \left(\left[\text{erfc}^{-1}(2P_{fa}) - \text{erfc}^{-1}(2P_d) \right]^2 \right) = 11.9\text{dB}$$

and for the SLD detector, to which both L_{NCD} and L_{NCDD} formulas are related:

$$\text{SNR}_{\text{SLD}} = D_c + 10 \cdot \log_{10} \left(\frac{1 + \sqrt{1 + 9.2/D_c(P_d, P_{fa})}}{2} \right) = 11.9\text{dB}$$

which implies that an additional of 7.4dB must be obtained from the post-coherent integration strategies. Solving (4.46) and (4.47) for the desired gain, the number of integrations required by each integration strategy can be obtained:

$$N_{NC} = 9 \implies G_{NCD}(N_{NC}) \approx 7.6\text{dB (using 9ms of data)}$$

$$N_{DC} = 7 \implies G_{NCDD}(N_{DC}) \approx 7.6\text{dB (using 8ms of data)}$$

The sensitivity curves for both detectors performing the number of operations determined above are shown in Figure 4.18.

Table 4.2 – Integration strategies comparison

| Coherent Time (ms) | Frequency Grid Points | Coherent Outputs Required | |
|--------------------|-----------------------|---------------------------|------|
| | | NCD | NCDD |
| 1 | 10 | 64 | 40 |
| 2 | 20 | 21 | 16 |
| 4 | 40 | 8 | 7 |
| 5 | 50 | 6 | 6 |
| 10 | 100 | 3 | 3 |
| 20 | 200 | - | - |

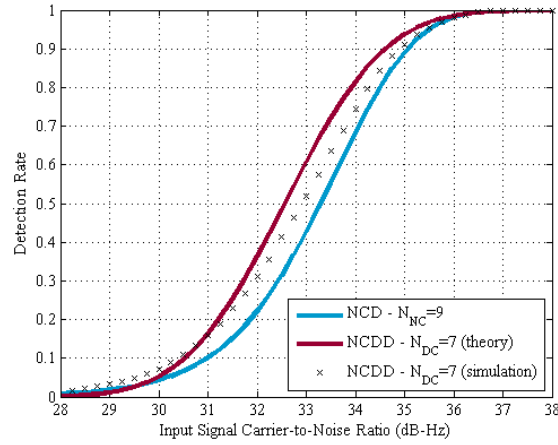


Figure 4.18 – Sensitivity comparison of the NCD and NCDD detectors in the acquisition of a GPS C/A signal for $N_{DC} = 7$ and $N_{NC} = 9$ and $P_{fa} = 10^{-5}$

4.5.2 Comparison in Presence of Doppler Sensitivity Losses

In the presence of a nonzero and stationary Doppler offset, the coherent processing output is affected by the sinc function (see section 2.2). This means that the SNR at the coherent processing output will be less than what would be expected for a zero Doppler offset [3], [34]. This way, the effective coherent output SNR, $\text{snr}_{\text{coh,eff}}$, is given by:

$$\text{snr}_{\text{coh,eff}} = \text{snr}_{\text{coh}} \cdot \text{sinc}^2(\Delta f_d \cdot N T_s) < \text{snr}_{\text{coh}, \Delta f_d=0} \quad (4.48)$$

This extra attenuation in the coherent processing is translated into (4.42) and (4.45) as an increase of D_c by $1/\text{sinc}^2(\Delta f_d N T_s)$. In this case, it is expected that the gap between the performance of the two detectors for a low number of accumulations becomes narrower, favoring the NCDD detector, over the NCD one. The comparison for a Doppler offset of 500Hz (typically middle of a frequency bin for one coherent integration) is shown in Figure 4.19. Although in this figure it can be seen that the crossing point between the NCD and NCDD sensitivity losses occurs at a higher loss value, this crossing occurs in fact for a lower number of accumulations, comparing Figure 4.17 and Figure 4.20. According to these plots it can be seen that the NCDD detector remains as the most suitable detector for the acquisition of weak signals.

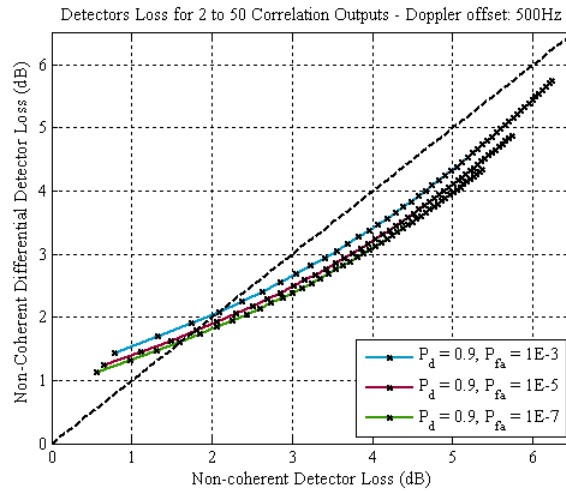


Figure 4.19 – Sensitivity loss of NCDD and NCD with respect to SLD for $\Delta f_d = 0$ and $N_{NC} = N_{DC+1} \in [2,50]$ (leftmost point corresponding to $N_{NC} = 2$ and rightmost one to $N_{NC} = 50$)

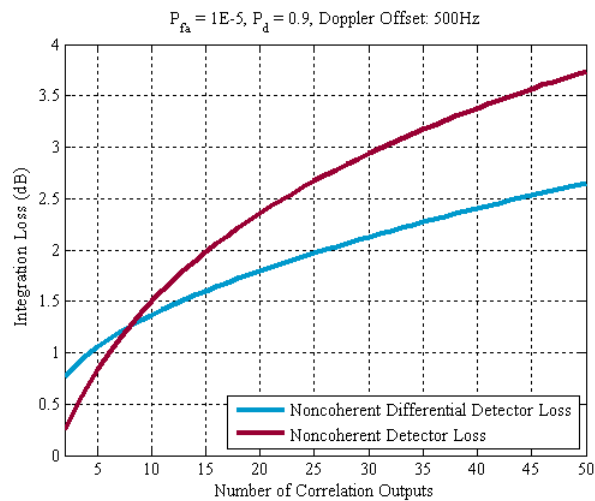


Figure 4.20 – Sensitivity loss of NCDD and NCD with respect to SLD as function of number of correlation outputs for $\Delta f_d = 0$ and $(P_d, P_{fa}) = (0.9, 10^{-5})$

4.6 Differential and Noncoherent Detection Schemes Comparison in Real Data Acquisition

The validation of the theoretical analysis described in the previous sections, as well as the comparison between the differential and noncoherent detectors, have been carried using simulated data. In this section, the NCDD and NCD detectors' performance is assessed with real GPS L1 C/A signals. The data acquisition was carried with a NordNav R30 receiver operating at a sampling frequency of 16.4MHz.

The focus of this work is in the acquisition of weak signals, however the reception of such signals is always unpredictable and their actual signal power difficult to assess. This way, an alternative approach is followed in which a strong signal is identified and then corrupted with an extra Gaussian noise component. For this purpose, it is essential to demonstrate that the noise environment is effectively Gaussian. As the signal provided by the NordNav R30 receiver is already digitized, this can be achieved by analyzing the noise distribution at the output of correlation when testing the presence of an absent PRN code, which enables us to estimate the input signal variance. The result of this analysis is shown in Fig. 20. From the histogram shown in this figure, the Gaussian nature of the environment noise is well-remarked. It should be noted that this Gaussian feature was verified in data collections also in deep urban scenarios, as in the city center of Toulouse. This validates the methodology employed for the emulation of weak signals and allows testing the algorithms under a wide range of signal strengths.

Two types of analysis are carried. First the detectors are compared employing data blocks of fixed size, and their sensitivity curve is drawn, and in the second analysis a fixed attenuation is imposed and the detectors' detection rate is plotted as function of the number of available code periods. The Doppler search grid considered in the following examples spans from -5 to 5 kHz and the frequency resolution in every case is $1/T_{coh}$. For each analysis a mean of 1 false alarm per 100 detections is fixed, so the detection thresholds are set by running the detectors for 100 independent data blocks extracted from the short collection time while testing a nonpresent PRN code. The detectors are then run for these same 100 blocks using the PRN code of the strong signal previously identified. This procedure is repeated for each C/N_0 point shown in the plots.

4.6.1 Sensitivity Comparison

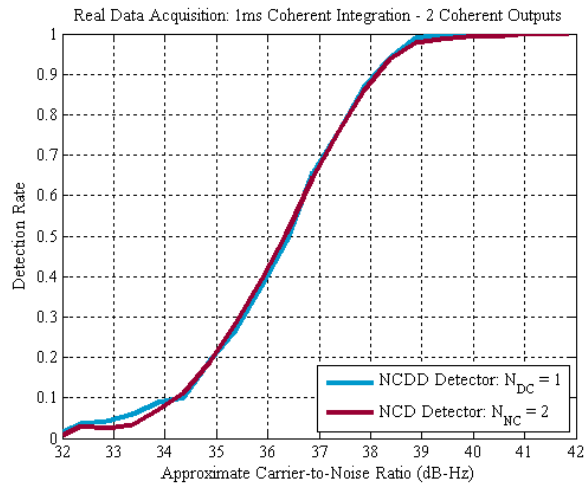
The first comparison of the performance of the NCDD and NCD detectors in real data acquisition is performed employing a coherent integration time of 1ms and 2, 5, and 10 correlation outputs. The signal C/N_0 is varied as shown in the plots of Figure 4.21. The first feature that can be observed in these plots is that the detectors appear to be overperformant, as the detection rate verified for each is superior to what could be theoretically expected. This is due to the high sampling frequency

of the NordNav R30 receiver, which produces approximately 16 samples per code chip. This way the peak observed in the analysis is not narrow but a rather large one, leading to a higher overall probability of detecting the signal. This, nevertheless, is representative of the actual receiver functioning so the results observed are compliant with what would be expected if the algorithms had been implemented in the receiver itself.

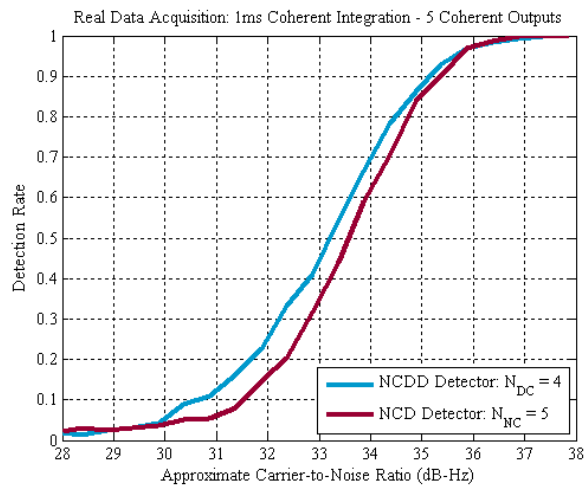
In these plots, it is clear that the NCDD detector becomes more effective than NCD as the input signal C/N_0 decreases and, consequently, a longer signal observation time is required for reliable signal detection. It should be noted that in this analysis no methods for attempting compensation of data bit transition were applied, so in several data blocks the change in data bit value is encountered. Given the long data bit duration for the GPS L1 C/A signal with respect to its code period, the data bit transition affects both detectors nearly in the same way, even if non-coherent integration is naturally more robust. Nevertheless, the data bit transition issue requires further attention in modern GNSS signals, as Galileo E1, in which the navigation data period is similar to the spreading code period.

4.6.2 Performance in Weak Signal Acquisition

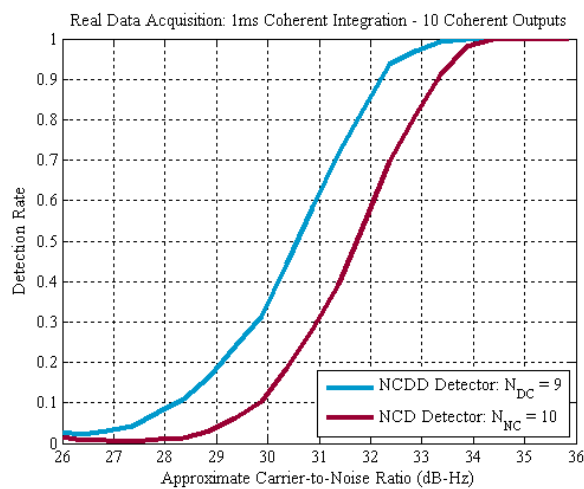
To show how detection of weak signals is achieved with different detectors, a signal at an average C/N_0 of 33dB-Hz is emulated by adding controlled simulated noise to the real signal. The attenuated signal is then attempted to be acquired with the SLD, NCD and NCDD detectors. The detection rate verified for each detector is shown in Figure 4.22 as function of the number of code periods integrated. From this plot, it can be seen that this signal can be reliably acquired with any of the three detectors, provided the number of code periods to be integrated is sufficiently high. While the SLD detector is the best performing one, its complexity of execution is considerably higher than the other two detectors, employing only 1ms coherent integration, and consequently presenting a less stringent requirement on the frequency grid resolution. Also here the superior performance of the NCDD detector with respect to the NCD is observed.



(a) 2 correlation outputs



(b) 5 correlation outputs



(c) 10 correlation outputs

Figure 4.21 – NCDD and NCD sensitivity comparison in acquisition of real signals using 2, 5 and 10 correlation outputs and 1ms coherent integration

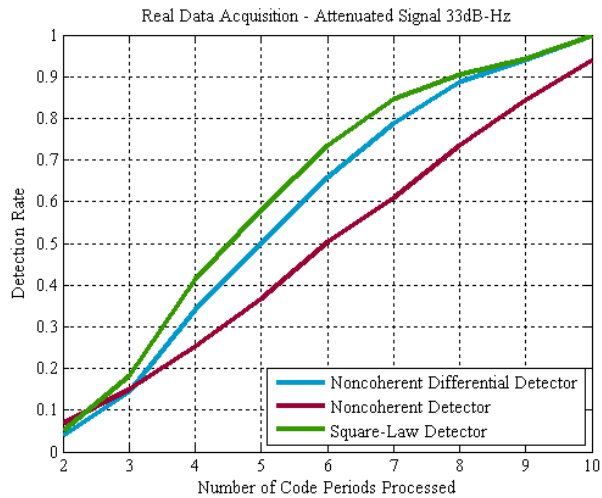


Figure 4.22 – NCDD, NCD and SLD sensitivity comparison in acquisition of real signal at 33dB-Hz using 2 to 10 correlation outputs

4.7 Conclusion

In this chapter, the performance of postcoherent differential detectors in the acquisition of weak GNSS signals was studied. First, we characterized statistically the PWD detector. Under the noise-only hypothesis, we made use of the fact that the output of pair-wise differential integration corresponds to a sum of independent Laplace random variables to propose a new expression for its characterization. Under the assumption that both signal and noise are present, it was shown that the approximation of the output of this detector by a Gaussian random variable matches closely its true distribution, and an expression for its probability of detection was derived.

Given the complexity of following the similar procedure for the NCDD detector, we instead characterized this detector through its sensitivity loss with respect to the SLD detector. Firstly, the methodology to characterize a detector in this way was described, and subsequently a formula for assessing the sensitivity loss of the NCDD detector (combining both differential and squaring losses) with respect to the SLD detector was proposed. The theoretical results were validated by simulations, showing that this is a valid approach to follow in such cases when the statistical analysis of the detectors is overly complex.

The results obtained enabled the comparison of the NCDD and NCD detectors, allowing deciding on the most adequate integration strategy for achieving a predefined sensitivity level. It was confirmed that differential integration is in fact preferable to noncoherent integration in the acquisition of weak signals. The theoretical conclusions were confirmed with the acquisition of real GPS L1 C/A signals, highlighting the potential of the NCDD detector in weak signal acquisition.

SYSTEMATIC AND EFFICIENT COLLECTIVE ACQUISITION OF MULTI-CONSTELLATION GNSS SIGNALS

It has been constantly mentioned throughout this thesis that acquisition of GNSS signals in harsh environments is a challenging task, given the low signal powers involved. This is, in fact, the main motivation for the thesis itself. In the previous chapters, several techniques for increasing sensitivity of GNSS receivers have been proposed and analyzed. Nevertheless, the algorithms proposed have always focused on the individual satellite signals, even if more signals are (hopefully) available to the receiver. This is the case in most research for GNSS signal acquisition, that signals from different satellites are treated *independently* at the acquisition level.

A different approach has been recently introduced in which instead of sequentially detecting the signals visible to the receiver, all are processed *simultaneously* or *collectively*. This approach, commonly referred to as *Collective Detection*, processes all the available signals by converting the usual code phase/Doppler shift search to a position/clock bias domain (Figure 5.1). By processing all signals collectively, it is expected that the detection of weak signals be facilitated by the presence of stronger ones as well. Furthermore, Collective Detection also provides a coarse estimation of the user position as a byproduct, so it can be seen both as a high-sensitivity and a direct positioning method. A background of Collective Detection, the objectives of this work, and the chapter organization are provided in the following section.

5.1 Background on Prior Works

An approach that is recurrently employed in tracking of weak signals is to handle all signals collectively, in what is known as vector tracking [24, 117, 118]. The main rationale behind this approach is that the processing of weaker signals is facilitated by the presence of stronger ones, due to the spatial correlation between different channels. The application of the vectorial concept to acquisi-

tion has been envisaged in [24] but it was not until [21], that an approach to do so was introduced. The proposal in [21] is to coherently combine the detection metrics from all satellites in view in order to improve the overall acquisition sensitivity. This concept relies on assistance information, for the user to define a position and clock bias uncertainty range from which a search grid is established. Using the assistance information, each position and clock bias combination (4D point) is then mapped to the pseudorange and code phase for each satellite and a single detection metric is generated as function of the expected user position and clock bias (Figure 5.2). This approach was the subject of other recent studies, in particular [22,23,119–122], where it got the name of Collective Detection. These studies refined the concept introduced in [21] and further improved upon it in several ways. In [22,119], a thorough analysis of Collective Detection is carried, demonstrating the performance improvement over traditional sequential acquisition techniques, also with real signals. These publications were also the first to propose a multi-iteration Collective Detection process, starting with a rough search grid that covers the whole user position and timing uncertainty, and that is refined in two more executions of the algorithm, as the uncertainty in both domains is also successively reduced. This enables obtaining a final search grid resolution which is quite fine, without the need to apply it to the whole uncertainty ranges.

More recently, a second set of articles on Collective Detection has been published [23,120–122]. Several issues are addressed in these papers, including different implementations of the algorithm, the impact of the resolution of the search grid on the computational cost of the Collective Detection methodology, and the effect on the positioning error of the timing accuracy supplied to the

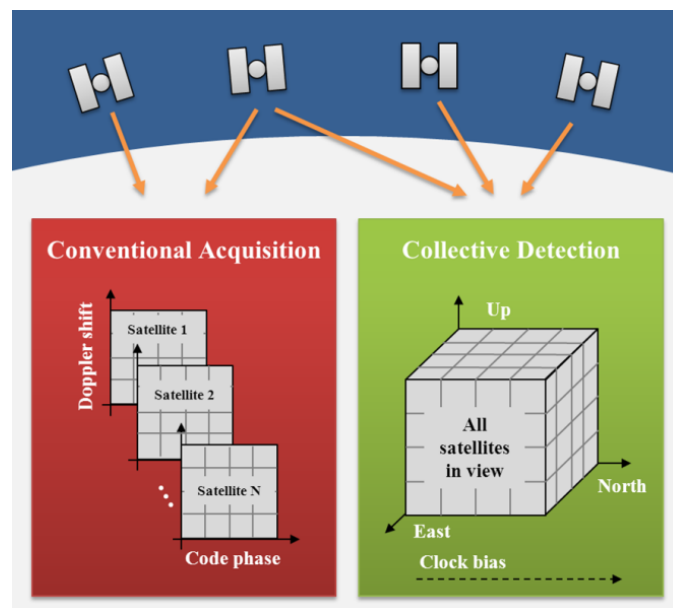


Figure 5.1 – GNSS signal acquisition employing conventional (sequential) and vector (collective) detection for the set of satellites in view

user. Furthermore, two significant advancements are also achieved in this set of papers, the first one on the assessment of the performance of a combined GPS+Locata Collective Detection implementation, paving the way for multi-constellation Collective Detection, and the second one on the hybridization of Collective Detection with traditional sequential detection.

As shown in these publications, Collective Detection is simultaneously a High-Sensitivity (HS) acquisition method, by application of vector acquisition, and a Direct Positioning (DP) method, providing a position-clock bias solution directly from the acquisition stage. As a HS acquisition method, Collective Detection is characterized by 1) sensitivity, and 2) complexity, and as a DP method, it is characterized by 1) position error, 2) Time to First Fix (TTFF) and also, to a certain extent, complexity, which may become an issue if it is excessively high. As shown in Table 5.1, all of these metrics of performance can be somehow traced to the search grid resolution.

This way, one of the biggest challenges in Collective Detection is the trade-off between the search grid resolution, which must be fine enough to allow good sensitivity and position error performance, and the total number of points to be analyzed, which has direct repercussions on the algorithm's complexity and TTFF. The ideal search grid resolution, nevertheless, has not been fully addressed in the previous studies. The main requirement for the search grids in these publications has naturally been that the resolution employed must assure that the maximum code phase estimation errors are bound to an acceptable range, but no algorithms for grid optimizations were developed.

In this chapter, we start by addressing the definition of the search grid to be employed in the

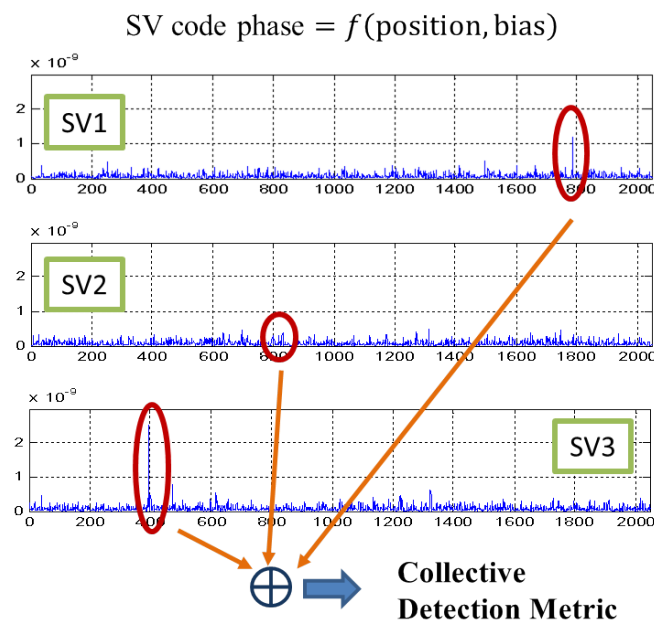


Figure 5.2 – Collective Detection metric generation by combining signals from multiple satellites

Table 5.1 – Collective Detection metrics of performance

| Metric of Performance | Depends on | Related to |
|-----------------------|---------------------------------|------------------------|
| Sensitivity | Resolution in code delay search | |
| Complexity | Number of points to search | <u>Grid resolution</u> |
| Position error | Resolution in code delay search | |
| TTFF | Number of points to search | |

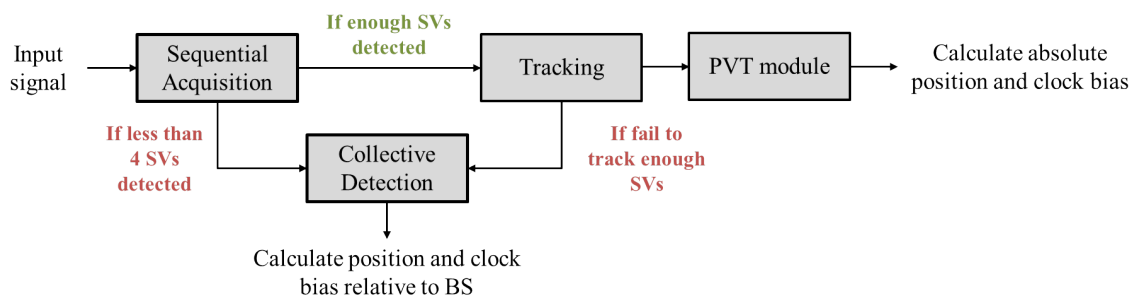


Figure 5.3 – Sequential and Collective Detection integration in a GNSS receiver

Collective Detection search process. The main goal of this part of the study is the proposal of a methodology for the application of the Collective Detection principle fulfilling two main requirements:

- Systematic: the resolution to be employed in the clock bias-position searches is determined according to a set of input parameters;
- Efficient: the search steps assure that the true signal code phase is not missed while avoiding excessively fine and computationally heavy search grids.

The new approach is then given the name of Systematic and Efficient Collective Acquisition (SECA). This is achieved through the analysis of the impact of the search grid resolution in the maximum code phase estimation error, also taking into account the geometry of the constellation of satellites in visibility. Next, we address the issue of hybridized vectorial-sequential acquisition, by adapting the proposed method to the case when one or more signals can be detected by traditional acquisition methods. The code phase information from the strong signals will allow imposing limits on the user 4D coordinates uncertainty, which can result in both an acceleration of the Collective Detection search process as well as reaching higher sensitivity. Finally, in the last section, we present a proposal for the application of Collective Detection in a combined GPS+Galileo receiver, validated with the acquisition of real signals.

5.2 Collective Detection Overview

In this section we provide a detailed description of the Collective Detection working principle and its methodology of application are provided, according to the key references found in literature [22,23,119–122]. Then, we describe the two facets of Collective Detection both as a High-Sensitivity and Direct Positioning method and the influence of the search grid definition is assessed.

5.2.1 Working Principle

The principle of Collective Detection has been introduced in [21], and has been further studied and refined since then, in particular in [22, 23, 119–122]. The main idea behind Collective Detection is that the code phase search for all visible satellites is mapped into a receiver position-clock bias grid, implying that signals are not acquired individually, but rather all at once, i.e., collectively. Depending on the expected incoming signal powers, an exhaustive Doppler search may not be necessary due to the fact that the two major Doppler sources can be eliminated with assistance information as described in section 2.4. The mapping of the signals' code phase to the position-clock bias domain is done differentially with respect to the Base Station (BS) pseudorange measurements, as shown in the scheme shown in Figure 5.4.

The difference in pseudorange from the Mobile Station (MS) with respect to the one measured by the BS for satellite k , $\Delta\rho_k$, is given by:

$$\begin{aligned} \Delta\rho_k(\Delta N, \Delta E, \Delta D, \Delta B) = & -\cos(az_k)\cos(el_k)\Delta N \\ & -\sin(az_k)\cos(el_k)\Delta E \\ & +\sin(el_k)\Delta D + c \cdot \Delta B \end{aligned} \quad (5.1)$$

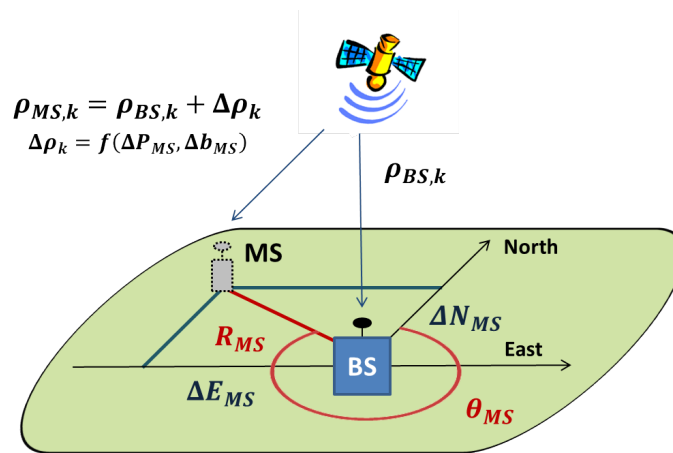


Figure 5.4 – Mapping of the code phase search to position-clock and pseudorange domains in Collective Detection

where az_k and el_k are, respectively, the azimuth and elevation angles of satellite k as seen by the BS (essentially the same as for the MS) ΔN , ΔE , and ΔD represent the 3D position displacement of the MS with respect to the BS in a North-East-Down (NED) local coordinate frame, and $c \cdot \Delta B$ is the pseudorange variation due to the clock bias of the MS, c being the speed of light. For a hypothetical location ΔN_i , ΔE_j , ΔD and clock bias ΔB_n , the estimated code phase for the k^{th} satellite, ζ_k , as would be seen by the MS at these coordinates is given by:

$$\zeta_k = \frac{[\rho_{BS,k} + \Delta\rho_k(\Delta N_i, \Delta E_j, \Delta D, \Delta B_n)]_{c \cdot T_{code}} \cdot N_{code}}{c \cdot T_{code}} \quad (5.2)$$

where T_{code} stands for the signal spreading code period, N_{code} is the number of code chips per period, and $[\]_{c \cdot T_{code}}$ represents the modulo $c \cdot T_{code}$ operation such that ζ_k can take any value (integer or float) in the interval $[0, N_{code} - 1]$. The individual detection metric for this satellite for these 4D coordinates is then calculated, for example, as:

$$D_{individual}(\zeta_k) = |S(\zeta_k)|^2 \quad (5.3)$$

where $S(\zeta_k)$ corresponds to the correlation output of this satellite at the code phase ζ_k . It should be noted that this detection metric is simply used as an example, as there is no impediment to the usage of other detection metrics, employing either non-coherent or differential integrations. The individual detection metrics for all satellites obtained for this 4D point are then summed in order to obtain one single collective detection metric for these hypothetical coordinates:

$$D_{collective}(\Delta N_i, \Delta E_j, \Delta D, \Delta B_n) = \sum_k D_{individual}(\zeta_k) \quad (5.4)$$

From this equation, it can be seen how Collective Detection profits from satellite redundancy. While the weak satellites may go undetected individually in (5.3), collectively they may be detectable.

Once all possible combinations of the unknown parameters within their search space have been tested according to the Collective Detection principle, different approaches can be followed to decide which set of values represents the best estimation of the true MS position coordinates and clock bias, as described in [22, 23, 119]. The comparison of different decision techniques, nevertheless, was not carried in this study, so the typical maximum likelihood estimation is applied in the examples shown. It should also be noted that for the application of the CD principle, a new assistance parameter is required, which is the pseudoranges for each satellite as seen by the BS. A summary of the inputs and outputs of Collective Detection is shown in Figure 5.5.

5.2.2 Methodology of Application

The application of the Collective Detection principle typically involves four steps:

1. Establish a spatial and timing uncertainty range for the MS with respect to the BS and define a grid to cover this uncertainty;
2. For each of the 4D points in the position-time search grid employ the Collective Detection principle described previously;
3. Perform an iterative refinement of the search grids resolution as the uncertainty in both domains is also successively reduced with each execution of the algorithm;
4. Determine the position-clock estimates based on the results obtained in step 2.

Examples of this 4-step methodology can be found in [22, 23, 119–122]. For step 1, in both publications a search grid is defined according to an initial position uncertainty in the NED frame and taking 1ms (GPS C/A code period) as the clock bias uncertainty. This grid involves fix steps in any of the four dimensions, and the resolutions employed are chosen keeping in mind that a too coarse resolution will directly affect the code phase resolution. The definition of the Collective Detection search grid is discussed in more detail in section 5.2.5.

For step 2, it is seen that both publications employ a multi-iteration process (3 in [22, 119] and 4 in [23, 120–122]) where the search grid uncertainty is successively reduced, and the resolution successively increased, in each execution of the algorithm. This way, a fine resolution can be achieved in the last execution of the algorithm which would be computationally costly to employ with the initial large uncertainty.

The final step, which consists of the estimation of the MS coordinates from the results of step 2, can be achieved in several ways. The most obvious and straightforward is simply to establish that the 4D point which maximizes the Collective Detection metric is the most likely location-clock bias.

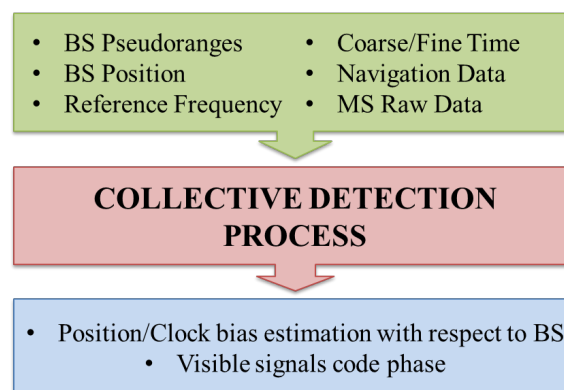


Figure 5.5 – Collective Detection inputs and outputs

This however is not necessarily the most appropriate method, as the final search grid resolution may imply a very small step in code phase search from one point to the other, and a large area can be seen which is sure to contain the most likely coordinates, as in Figure 5.6a. In [22, 23, 119–122] different threshold and position averaging techniques to estimate the true MS coordinates are presented, but these are not applied in this study. Considerations about the ambiguity in the solutions achievable with Collective Detection are presented in the next section.

5.2.3 Collective Detection as a Direct Positioning Method

Collective Detection is capable of providing the user (the MS receiver) with a first, quick estimate of its position and clock bias. The accuracy of the position estimate, however, is highly dependent on the visible satellite geometry, as any other GNSS positioning algorithm. In Figure 5.6b, the same data set as processed for Figure 5.6a is shown, but increasing the mask angle to 40 degrees, which lowers the number of visible satellites to 4 and significantly increases the GDOP value. In the examples shown, the signal strength is uneven, so the collective detection metric is still driven by the stronger signals. If one of these signals is from a satellite at a very high elevation, its code phase variation across the horizontal plane will be low, and a high ambiguity in the positioning can be obtained if this signal is much stronger than others. The analysis of real scenarios carried in [22, 23, 119–122] shows that the positioning error of the Collective Detection approach depends, naturally, on the number of satellites visible, their geometry and signal power. From these publications it seems clear that, at best, the mean horizontal positioning error expected will be within a few tens of meters.

It should be noted however, that this magnitude of positioning errors does not mean that the individual signals code phase is not being accurately estimated (within ± 0.5 chips of the correct

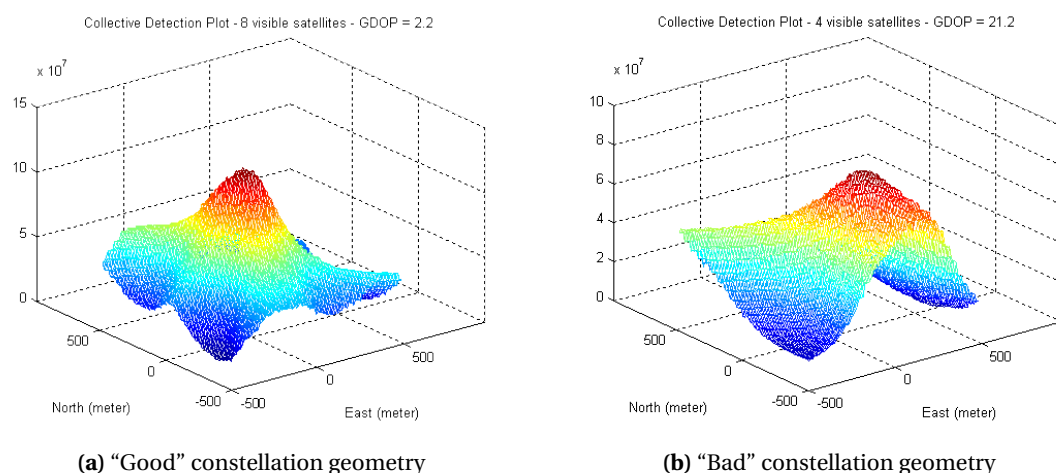


Figure 5.6 – Collective Detection positioning ambiguity in different constellation geometry

code phase), given that an error of 0.5 chips in the code phase estimation is equivalent to 150m in pseudorange. Therefore, a position error of 30 meters, for example, may still be within the correct code phase estimation region. This is analyzed next.

5.2.4 Collective Detection as a High-Sensitivity Acquisition Method

As a vector acquisition approach, Collective Detection exploits the stronger signals to facilitate the acquisition of the weaker ones. This is expected to be achieved by adding up the energy from each individual satellite in the collective metric, as seen in section 5.2.1. The complete characterization of Collective Detection as a High-Sensitivity acquisition method, however, is not easy, as its performance is dependent of several factors, including the number of signals present and their powers, and, as such, it must be examined case by case.

As an example of its effectiveness, though, let us consider the hypothetical case that several signals are present at the same carrier-to-noise ratio, C/N_0 , as done in [22]. The probability of detection of a signal within Collective Detection in this case, is roughly the same as the probability of acquiring a single signal by doing a number on noncoherent integrations equal to the number of signals present. On the contrary, the probability of detection of the sequential approach is equal to the probability of correct acquisition of all signals individually. This is equivalent to raising the probability of detection of a single satellite to the power of the number of satellites in view, that is, $P_{d,1SV}^{N_{sats}}$. The comparison results for 1ms and 100ms coherent integration of a GPS L1 C/A signal are shown in Figure 5.7, where the full colored lines refer to the Collective Detection approach, the dotted colored lines respect sequential approach, and the full black line is the reference for one satellite signal. As seen in this figure, vectorial acquisition can be very beneficial when a large number of

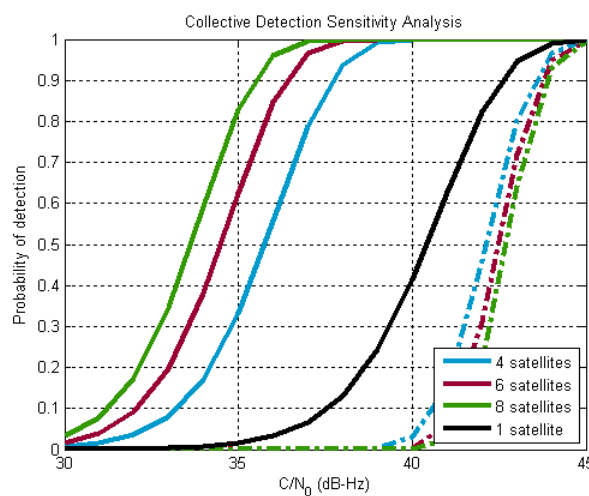


Figure 5.7 – Illustration of sensitivity enhancement drawn from vectorial (full lines) with respect to sequential (dotted lines) acquisition

satellites are in view. A more in-depth evaluation of the sensitivity of Collective Detection will be made in section 5.4, taking also into account the search grid influence, which is discussed next.

5.2.5 Search Grid Influence

The biggest drawback of Collective Detection highlighted in literature is the potentially very high number of points that needs to be evaluated in order to have an acceptable resolution in the code search. The clock bias dimension, in particular, can become very burdensome to search, given its large uncertainty and its direct 1 to 1 impact in the pseudorange and code phase. This way, if a very fine resolution is directly employed in the search over the whole uncertainty range, the number of points to be analyzed becomes massive, and this approach will be impractical. Therefore, a compromise between sensitivity and complexity must be made also in Collective Detection.

The approach followed in [22, 23, 119–122] is to define an initial “rough” grid that covers the whole 4D uncertainty search space with a coarse resolution, and then iteratively refine it until the desired resolution is achieved, while the uncertainty in all dimensions keeps being reduced. The initial coarse grid resolution however, needs to be carefully chosen, in order not to incur the risk of wrongly estimating the uncertainty region to be analyzed in the following iteration. For this, two options can be employed:

1. Either the search resolution is fine enough to assure that the maximum estimation error in the code phase is under half chip for every satellite; or
2. An averaging approach is chosen, in which the grid allows an estimation error higher than half chip, and the individual detection metric for each satellite is chosen as the average of the detection metrics within a certain range.

Both approaches have pros and cons, in particular, in the trade-off between complexity and sensitivity. It is clear that the first approach involving a finer grid offers enhanced robustness in signal detection with respect to the second one, but it may also be much more computationally demanding. This trade-off and the sensitivity loss due to the averaging of detection metrics will be analyzed in the coming sections.

5.3 Systematic and Efficient Collective Acquisition (SECA)

In the previous section the principle and the features of Collective Detection have been described. It was noted, in particular, the effect of the search grid in the performance of Collective Detection as a direct positioning and high sensitivity acquisition method. In this section we describe one of the main contributions of this study, which is the proposal of a methodology for the systematic and efficient implementation of Collective Detection/Acquisition (SECA).

In [22, 23, 119–122], the search grid to be applied in Collective Detection is defined only with the objective of not having an excessively coarse resolution in the code phase domain. In [22], in particular, it is noted that the different grid resolutions chosen have not been optimized to minimize the computational load. The proposed optimization starts with the transformation of the local horizontal search from the traditional North-East referential to a polar Rho-Theta one, which will allow simplifying the mathematics involved in the next steps of position-bias parametrization. The objective of the new algorithm is summarized in Figure 5.8 for the horizontal position search. As shown in this figure, the resolutions to be employed in the search process (δR for the radial component, and $\delta\theta$ for the angular one) are calculated from a set of parameters, Θ , that is defined in section 5.3.2. The same applies to the clock bias resolution.

5.3.1 Redefinition of Local Horizontal Plane

The position uncertainty range in [22, 23, 119–122] is defined in a NED frame. This, however, is not ideal for the definition of a search grid taking into account the satellite geometry, given that the satellites' azimuth angle would also have to be taken into account, as well as their elevation. In Figure 5.9, the maximum code phase variation over the North-East local plane for two satellites

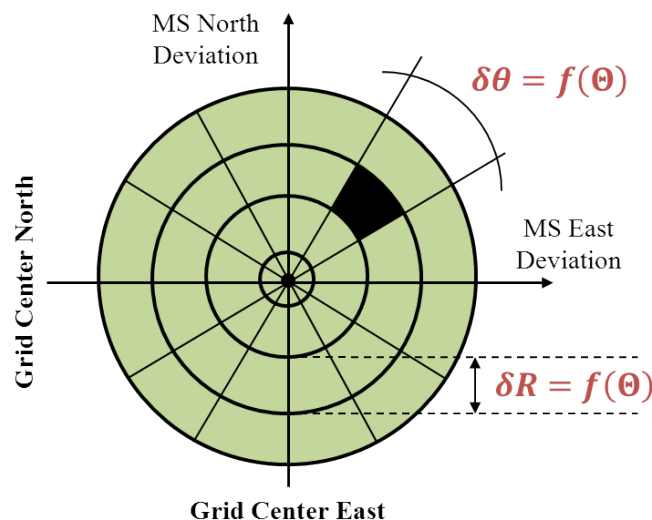


Figure 5.8 – Illustration of the principle of the proposed algorithm

at different azimuths is shown. The range considered in both dimensions is ± 10 kms. From these figures, it becomes clear the influence of the azimuth angle on the maximum code phase variation across the horizontal plane.

To avoid having to take into account the azimuth angle in the search grid definition we redefine the search grid into a polar R - θ coordinate system. This way we can re-write:

$$\begin{cases} \Delta N = R \cdot \cos(\theta) \\ \Delta E = R \cdot \sin(\theta) \end{cases} \quad (5.5)$$

and (5.1) becomes:

$$\begin{aligned} \Delta \rho_k(R, \theta, \Delta D, \Delta B) &= -R \cos(e l_k) [\cos(a z_k) \cos(\theta) + \sin(a z_k) \sin(\theta)] \\ &\quad + \sin(e l_k) \Delta D + c \cdot \Delta B \\ &= -R \cos(e l_k) \cos(a z_k - \theta) + \sin(e l_k) \Delta D + c \cdot \Delta B \end{aligned} \quad (5.6)$$

Leaving the vertical component aside for now, (5.6) becomes:

$$\Delta \rho_k(R, \theta, \Delta D, \Delta B) = -R \cos(e l_k) \cos(a z_k - \theta) + c \cdot \Delta B = \Delta \rho_{hor, position} + \Delta \rho_{bias} \quad (5.7)$$

This redefinition of the horizontal plane will be useful in the next step of finding the ideal search grid resolutions.

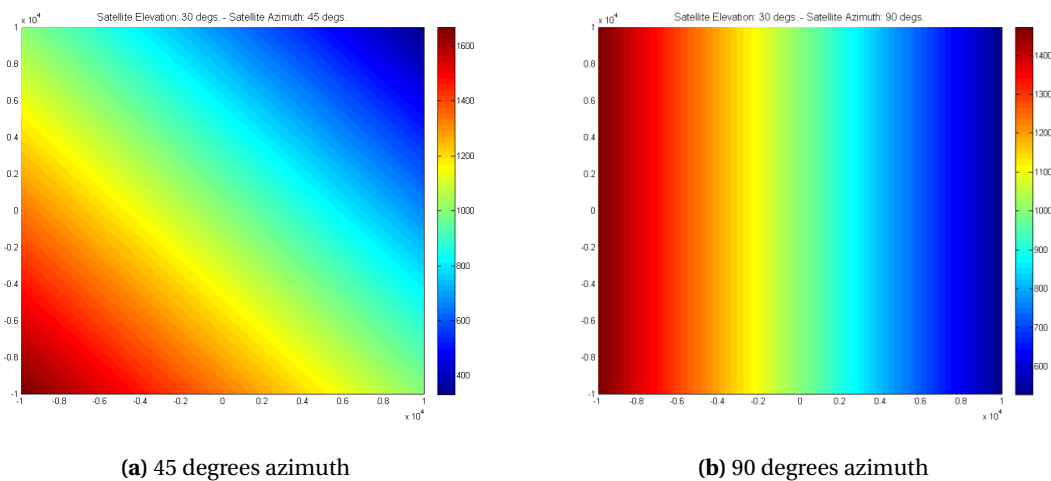


Figure 5.9 – Code phase change over a squared uncertainty range for a satellite at 30 degrees elevation. The satellite azimuth for the left plot is 45 degrees and 90 degrees for the right one.

5.3.2 Search Grid Definition

In order to optimize the search grid, we start by defining the maximum code phase error in chips, β , that can be considered acceptable within the Collective Detection search process. Recalling the relation between the code phase and the differential pseudorange, this requirement is then translated to:

$$\pm\beta = \frac{\pm\Delta\rho_{error,max}}{c \cdot T_{code}} \cdot N_{code} = \frac{\pm\Delta\rho_{error,max}}{c \cdot T_{chip}} \quad (5.8)$$

from which:

$$\Delta\rho_{error,max} = \beta \cdot c \cdot T_{chip} = \delta\rho/2 \quad (5.9)$$

where $\delta\rho$ represents the resolution in the pseudorange to which corresponds the maximum code phase error of β chips. This resolution is then translated into the position-clock search step as:

$$\delta\rho \geq \delta\rho_{hor,position} + \delta\rho_{bias} \quad (5.10)$$

meaning that the sum of the steps in both dimensions cannot exceed the pseudorange resolution. In fact, none of the steps in position or clock bias should exceed the pseudorange resolution, but this is also implied by the above condition. The partitioning of $\delta\rho$ can be equally divided between the two components or a weight component to unevenly partition the error between the two can be defined. This way:

$$\delta\rho = \delta\rho_{hor,position} + \delta\rho_{bias} = (1 - w_{bias})\delta\rho + w_{bias}\delta\rho \quad (5.11)$$

where $w_{bias} \in]0; 1[$ is the weight of the bias step, and $\delta\rho_{hor,position}$ and $\delta\rho_{bias}$ can now be expressed as function of $\delta\rho$ and w_{bias} .

Clock bias search resolution Starting with the bias component, defining δB as the resolution in the bias step, it results:

$$\delta\rho_{bias} = c \cdot \delta B = w_{bias}\delta\rho \quad (5.12)$$

from which

$$\delta B = w_{bias} \frac{\delta \rho}{c} = w_{bias} \cdot 2\beta \cdot T_{chip} \quad (5.13)$$

This resolution is then translated into a number of points to be searched by considering the total bias uncertainty. Assuming that no fine assistance information is available, the clock bias uncertainty is within a full code period of the incoming signal. Assuming a GPS-only Collective Detection implementation for the moment, the clock bias uncertainty range, $\Delta B_{dimension}$, will then be 1ms for the GPS L1 C/A signal. The number of points in the clock bias dimension, $n_{points,bias}$, is finally:

$$n_{points,bias} = \left\lceil \frac{\Delta B_{dimension}}{\delta B} \right\rceil = \left\lceil \frac{T_{code}}{w_{bias} \cdot 2\beta \cdot T_{chip}} \right\rceil = \left\lceil \frac{N_{code}}{w_{bias} \cdot 2\beta} \right\rceil \quad (5.14)$$

where $\lceil \cdot \rceil$ stands for the nearest integer rounded towards $+\infty$

Position search resolution For the position, starting with the radial dimension:

$$(1 - w_{bias})\delta \rho \geq \delta R \cos(e l_k) \cos(a z_k - \theta) \Leftrightarrow \delta R \leq \frac{(1 - w_{bias})\delta \rho}{\cos(e l_k) \cos(a z_k - \theta)} \quad (5.15)$$

The minimum values for the ratio on the right side of the inequality are obtained when $\theta = a z_k$, and the lowest satellite elevation from the set of satellites in view is considered. This way:

$$\delta R = \frac{(1 - w_{bias})\delta \rho}{\cos_{max}(e l_k)} = \frac{(1 - w_{bias})\delta \rho}{\cos(e l_{min})} \quad (5.16)$$

Through this relation, the constellation geometry rises as a factor to take into account in the definition of the search grid resolution. The number of points to be searched for the radial dimension, $n_{points,radius}$, is then:

$$n_{points,radius} = \left\lceil \frac{\Delta R_{dimension}}{\delta R} \right\rceil \quad (5.17)$$

where $\Delta R_{dimension}$ corresponds to the maximum horizontal search range. This definition of the position uncertainty range also comes as more intuitive than the squared search range, as it is defined as a circle with the BS position as center, and radius $\Delta R_{dimension}$.

For the angular resolution, a similar approach can be followed. In order not to exceed the pseudorange error allocated to the position component, the resolution in the radial search, $\delta \theta$, must respect the following constraint:

$$\begin{aligned}
R \cos(e l_k) \cos(a z_k - (\theta + \delta \theta)) - R \cos(e l_k) \cos(a z_k - \theta) &\leq (1 - w_{bias}) \delta \rho \Leftrightarrow \\
\cos(a z_k - (\theta + \delta \theta)) - \cos(a z_k - \theta) &\leq \frac{(1 - w_{bias}) \delta \rho}{R \cos_{max}(e l_k)} = \frac{(1 - w_{bias}) \delta \rho}{R \cos(e l_{min})}
\end{aligned} \tag{5.18}$$

Noting that:

$$\cos(u) - \cos(v) = -2 \sin\left[\frac{1}{2}(u + v)\right] \sin\left[\frac{1}{2}(u - v)\right] \tag{5.19}$$

then (5.18) can be rewritten as:

$$2 \cdot \sin\left(a z_k - \theta - \frac{\delta \theta}{2}\right) \sin\left(-\frac{\delta \theta}{2}\right) \leq \frac{(1 - w_{bias}) \delta \rho}{R \cos(e l_{min})} \Leftrightarrow \sin\left(-\frac{\delta \theta}{2}\right) \leq \frac{(1 - w_{bias}) \delta \rho}{2R \cos(e l_{min})} \tag{5.20}$$

Note that the approximation $\sin(\delta \theta) = \delta \theta$ should not be used as $\delta \theta$ can amount to more than a few degrees, and that $\max\left|\sin\left(a z_k - \theta - \frac{\delta \theta}{2}\right)\right| = 1$ was used to obtain the second expression. This way:

$$\delta \theta = 2 \cdot \sin^{-1}\left(\frac{(1 - w_{bias}) \delta \rho}{2R \cos(e l_{min})}\right) \geq 2 \cdot \sin^{-1}\left(\frac{(1 - w_{bias}) \delta \rho}{2R_{max} \cos(e l_{min})}\right) \tag{5.21}$$

According to this relation, the angular resolution is a function of the search radius, being the finest at the maximum radius. If $R = 0$ (the center of the grid), then the resolution is infinite, meaning that only one point (the center itself) is used for this position uncertainty area.

It should also be noted that, by attributing only one weight to allocate the error between the bias and position domains, a combined error in the position domain resulting from an estimation error in both the radial and angular dimension is not considered. Therefore, a more complete solution would include an additional weight to properly consider the error allocation in all three dimensions. Nevertheless, in the following analysis, only one weight shall be considered.

Summarizing, four parameters define the search grid resolutions to be employed within the SECA algorithm (the set Θ in Figure 5.8):

1. The code phase uncertainty to be considered for each candidate grid point, β - if it is set too low, an excessive number of points may be obtained in the search grid;
 2. The weight of the bias error component in the error allocation, w_{bias} - if it is set too high, the error due to the clock bias becomes very significant due to the 1 to 1 impact on the pseudorange;
 3. The maximum range uncertainty around the BS, $\Delta R_{dimension}$; and
-

-
4. The lowest elevation angle from the set of satellites in view, $e l_{min}$.

The first two parameters can be selected freely, the third one depends on the assistance, and the fourth on the visible constellation and the mask angle.

The analysis of the impact of β , w_{bias} , and $e l_{min}$ in the overall algorithm performance are shown in Tables 5.2-5.4, and the impact of $\Delta R_{dimension}$ in the total number of points to be analyzed in Figure Y. From the analysis of the results shown in the three tables several conclusions can be drawn. First, it is notorious the influence of each of the three parameters in the total number of points analyzed. The dependence with $1/w_{bias}$ is approximately squared and with $1/\beta$ approximately cubic. Therefore the choice of the values for these two parameters should be carefully considered. Nevertheless, a definite decision about their values, can only be taken once the rest of the algorithm has been described as well. Now that the search grid has been defined, it is necessary to see how to handle the uncertainties in the estimated code phase (β).

5.3.3 Generation of Individual Detection Metrics

The value of β has a very important impact on the number of points to be searched. In section 5.2.5 it was mentioned that one way to handle a high code phase uncertainty in the Collective Detection search grid is to associate a range of code phases to each search point, in an averaging process. This approach is followed, in order to be able to freely adjust the value of β . For each point in the search grid the candidate code phase for each satellite is calculated as:

$$\begin{aligned} \Delta\rho_k(R_i, \theta_j, \Delta B_m) &= -R_i \cos(e l_k) \cos(a z_k - \theta_j) + c \cdot \Delta B_m \Rightarrow \\ \Rightarrow \zeta_k(R_i, \theta_j, \Delta B_m) &= \frac{[\rho_{BS,k} + \Delta\rho_k(R_i, \theta_j, \Delta B_m)]_{c \cdot T_{code}}}{c \cdot T_{chip}} \end{aligned} \quad (5.22)$$

However, knowing that this code phase can be within $\pm\beta$ chips of the true code phase, the individual detection metric for each satellite is obtained as the sum of the detection metrics for the surrounding range around the central code phase:

$$D_{individual,k}(R_i, \theta_j, \Delta B_m, \beta) = \sum_{\zeta=\zeta_k-\beta}^{\zeta_k+\beta} |S(\zeta)|^2 \quad (5.23)$$

This will naturally have repercussions in the algorithm sensitivity and will be addressed later in this section. The collective detection metric is still obtained as the sum of the individual detection metrics from (5.23).

Table 5.2 – Influence of the maximum allowable code phase estimation error, β , in the proposed SECA algorithm ($w_{bias} = 0.15$, $e l_{min} = 10\text{deg}$, $\Delta R_{dimension} = 10\text{km}$)

| Max. Allowable Code Phase Estimation Error (chip) | 0.1 | 0.5 | 1 | 2 | 5 | 10 |
|---|------------|------------|--------------|--------------|--------------|-------------|
| Radial Resolution (m) | 51,7 | 258,5 | 516,9 | 1033,8 | 2584,6 | 5169,1 |
| Number Points Radial Dimension | 195 | 40 | 21 | 11 | 5 | 3 |
| Clock Bias Resolution (m) | 8,8 | 44 | 87,9 | 175,8 | 439,6 | 879,2 |
| Number Points Bias Dimension | 34100 | 6820 | 3410 | 1705 | 682 | 341 |
| Finest Angular Resolution (deg) | 0,3 | 1,5 | 3,0 | 6 | 15 | 30 |
| Total number points scanned | 3E9 | 3E7 | 4.5E6 | 6.0E5 | 44330 | 6820 |

Table 5.3 – Influence of the weight allocated to the bias component on the pseudorange estimation error, w_{bias} , in the proposed SECA algorithm ($\beta = 5$, $e l_{min} = 10\text{deg}$, $\Delta R_{dimension} = 10\text{km}$)

| Bias weight | 0.1 | 0.15 | 0.2 | 0.25 | 0.3 |
|------------------------------------|--------------|--------------|--------------|--------------|--------------|
| Radial Resolution (m) | 2736,6 | 2584,6 | 2432,5 | 2280,5 | 2128,5 |
| Number Points Radial Dimension | 5 | 5 | 6 | 6 | 6 |
| Clock Bias Resolution (m) | 293,1 | 439,6 | 586,1 | 732,6 | 879,2 |
| Number Points Bias Dimension | 1023 | 682 | 511 | 409 | 341 |
| Finest Angular Resolution (deg) | 16,4 | 15 | 14,4 | 13,3 | 12,4 |
| Total number points scanned | 66495 | 44330 | 49567 | 39673 | 33077 |

Table 5.4 – Influence of the minimum elevation angle, $e l_{min}$, in the proposed SECA algorithm ($\beta = 5$, $w_{bias} = 0.15$, $\Delta R_{dimension} = 10\text{km}$)

| Minimum Elevation Angle (deg) | 10 | 20 | 30 | 45 | 60 |
|------------------------------------|--------------|--------------|--------------|--------------|--------------|
| Radial Resolution (m) | 2584,6 | 2690,9 | 2876,3 | 3522,7 | 4981,9 |
| Number Points Radial Dimension | 5 | 5 | 5 | 4 | 4 |
| Clock Bias Resolution (m) | 439,6 | 439,6 | 439,6 | 439,6 | 439,6 |
| Number Points Bias Dimension | 682 | 682 | 682 | 682 | 682 |
| Finest Angular Resolution (deg) | 15 | 15,7 | 17,1 | 21,2 | 30 |
| Total number points scanned | 44330 | 44330 | 42966 | 25916 | 25916 |

5.3.4 Search Grid Iterative Update

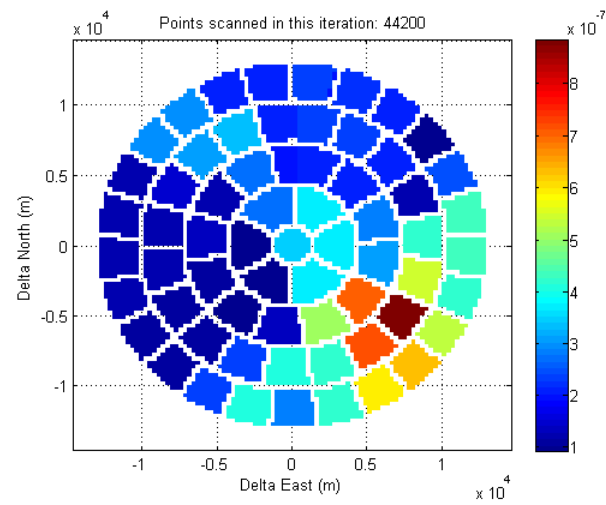
Again, if the value of β is set too low, a very high code phase resolution is obtained with the SRE search grid, but the number of points that will need to be considered may deem the method im-

Table 5.5 – Details of the application of the SECA algorithm for $\beta_0 = 5$, $\beta_{div.factor} = 10$, $w_{bias} = 0.15$, $e_{l_{min}} = 30\text{deg}$, and $\Delta R_{dimension} = 10\text{km}$

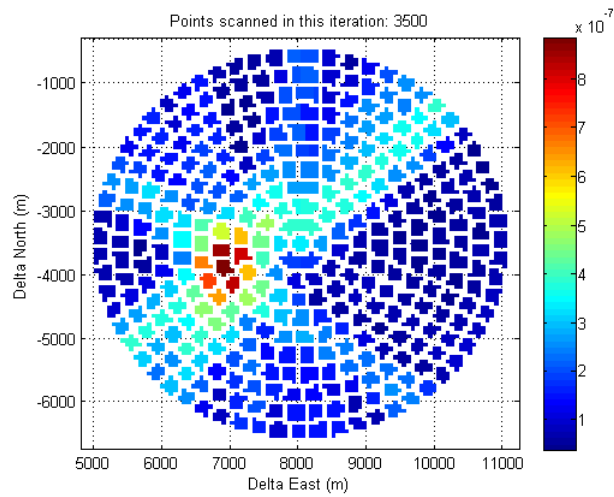
| Item | Iteration 1 | Iteration 2 | Iteration 3 |
|---------------------------------|----------------------|-------------|-------------|
| Radial Uncertainty (m) | $1 \cdot 10^4$ | 2922 | 292 |
| Radial Resolution (m) | 2922 | 292 | 29.2 |
| Clock Bias Uncertainty (m) | $\pm 1.5 \cdot 10^5$ | ± 220 | ± 22.0 |
| Clock Bias Resolution (m) | 440 | 44.0 | 4.4 |
| Finest Angular Resolution (deg) | 14.4 | 5.7 | 5.7 |

practical for execution. This way, a more conservative value for β can be set at first, and then refined, as the position and clock bias uncertainties are also reduced. In the examples shown in this chapter, an initial value of $\beta = 5$ is chosen and at each iteration it is divided by 10. Three iterations are run so that β goes from 5 to 0.5 to 0.05, approximately 1/16, the resolution that is obtained with the receiver which was used in the real data collections as will be seen in the following sections. At each new iteration, the uncertainty in clock bias and R is made equal to the resolution of the previous search, and the resolution of the new search is calculated as described in section 5.3.2, using the new value of β and the new uncertainties.

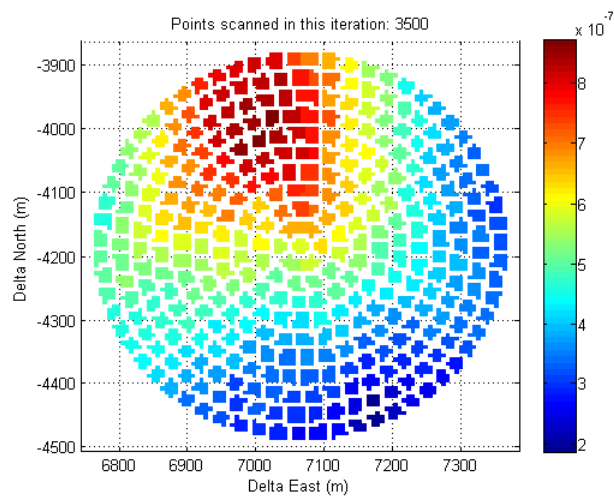
An example of application of the new algorithm through simulation is shown in Figure 5.10. The true MS position is set to $(\Delta N, \Delta E) = (-4000, 7000)$ and the clock bias to 1km. The bias weight chosen is 0.15, the minimum elevation angle considered was 30 degrees, and the radial uncertainty around the BS is set to 10km. A total of six strong signals are used for this simple illustration. Each plot shows the collective detection metrics for each iteration at the most likely clock bias. The total number of points scanned is 52.030, one order of magnitude less than the values in [22, 119] and even more for [23, 120–122], also not taking into account the vertical dimension in these methods. The details of the resolution and search range for each of the iterations are provided in Table 5.5. The assessment of the sensitivity performance of the new algorithm is carried in the next section.



(a) 1st iteration



(b) 2nd iteration



(c) 3rd iteration

Figure 5.10 – Example of application of the SECA algorithm (details in Table 5.5)

5.4 Performance of the SECA Approach

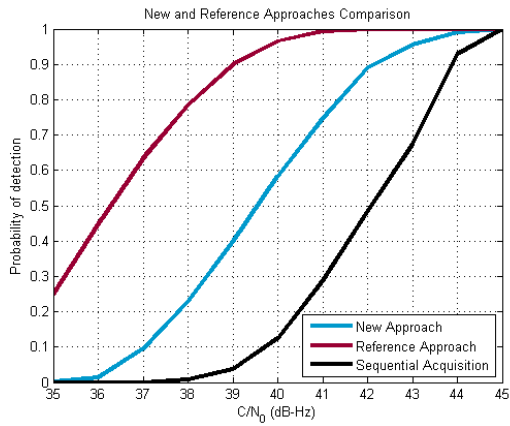
The performance assessment of Collective Detection in general is not an easy task as there are many factors that influence the overall method performance, in particular the number of satellites visible, their geometry, and the relation between their signal powers. Furthermore in the SECA approach also the parameters β and w_{bias} have an influence in the algorithm's performance, as seen in the previous section. The performance of the new approach is assessed here in comparison to the performance of the search grid from [22, 119]. The details of this search grid are shown in Table 5.6. Note that also the search grid from [23] could have been used but this grid is computationally much heavier with respect to the search grid from [22, 119] and a smaller position uncertainty range is covered with no noticeable improvements in positioning errors.

For this comparison, a fixed constellation of six GPS satellites is chosen, and the MS position is varied within the uncertainty area. All signals are generated at the same signal power and the mask angle used is 30 degrees. For this simple illustration only 1ms of signal is employed and processed by the SLD detector to generate the individual detection metrics sets. The simulation results are shown in Figures 5.11 and 5.12, where the evolution of the probability of detection and position error of both approaches with the incoming signals' power is shown. The signals are considered to be correctly acquired when their final code phase estimation is within ± 0.5 chips of their true code phase (calculated from the true MS position/clock bias and the satellites simulated positions). For reference, a curve representing the sequential acquisition of these signals is also shown, corresponding to the case when the maximum detection metric corresponds to the true code phase index. Note that the curves respect the correct acquisition of all signals in view.

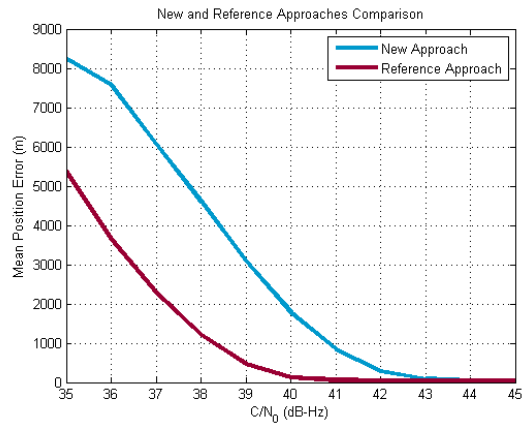
The main conclusion that can be drawn from the plots in Figures 5.11 and 5.12 is that the performance of both approaches is dependent on the true MS position and clock bias. This is particularly noticeable for the reference search grid, as in some positions the algorithm's performance is highly impaired. This is due to the fact that no averaging over a range of code phases is being applied, and the resolution of the first grid ("rough" in Table 5.6) does not assure a maximum code phase estimation error lower than half chip in this first step, so the true code phases can be missed in this step. Nevertheless, it can also be seen that in some cases the fixed grid performs better than the

Table 5.6 – Reference Collective Detection Search Grid

| Item | Rough | Medium | Fine |
|----------------------------|----------------------|------------|-----------|
| North/East Uncertainty (m) | $\pm 1 \cdot 10^4$ | ± 2000 | ± 900 |
| North/East Resolution (m) | 1000 | 100 | 30.0 |
| Clock Bias Uncertainty (m) | $\pm 1.5 \cdot 10^5$ | ± 1200 | ± 300 |
| Clock Bias Resolution (m) | 1000 | 100 | 30.0 |

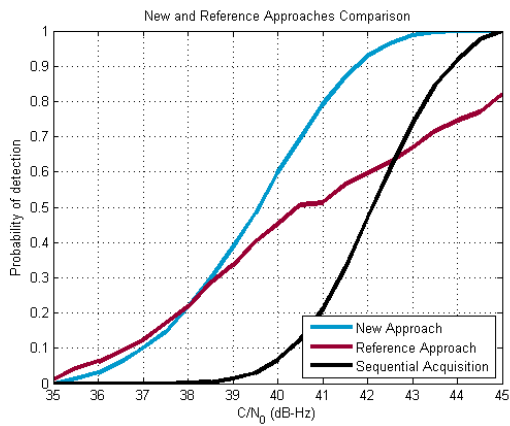


(a) Sensitivity Analysis

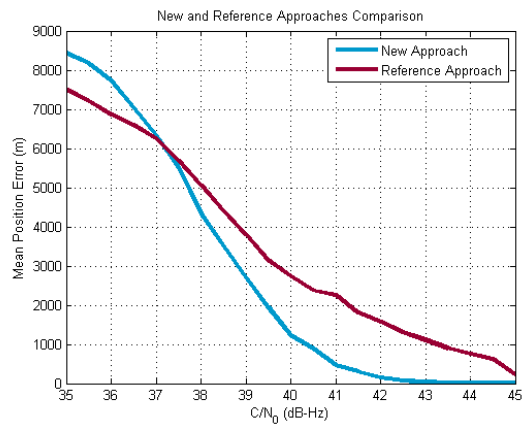


(b) Positioning Error

i) True MS coordinates (in meter): $(\Delta N, \Delta E, \Delta D, \Delta B) = (0, 0, 0, 0)$

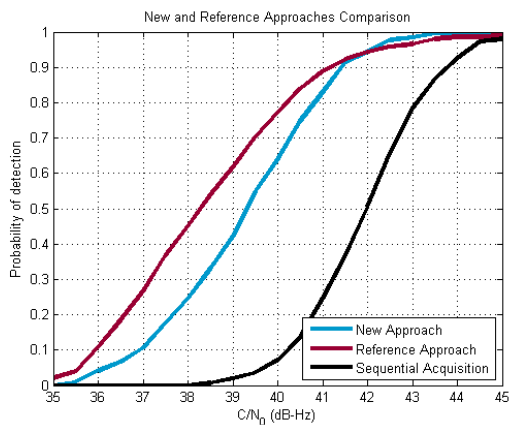


(c) Sensitivity Analysis

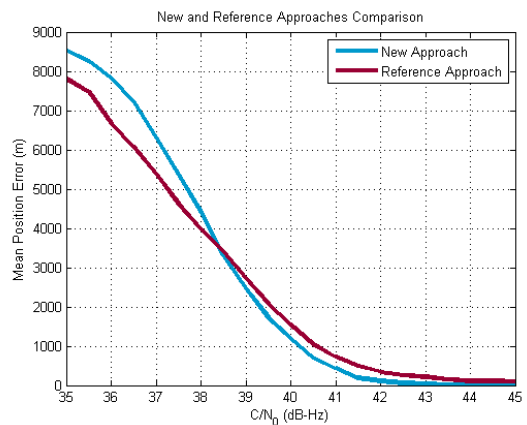


(d) Positioning Error

ii) True MS coordinates (in meter): $(\Delta N, \Delta E, \Delta D, \Delta B) = (0, 0, 0, 250)$



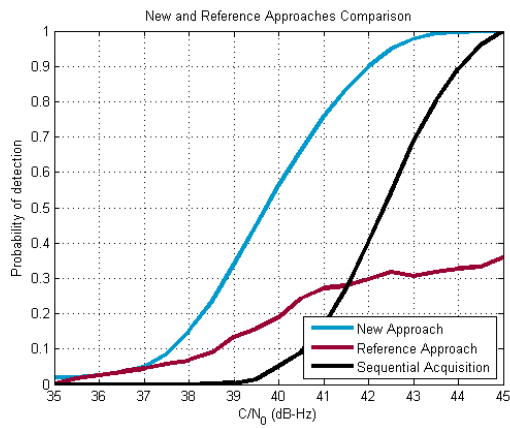
(e) Sensitivity Analysis



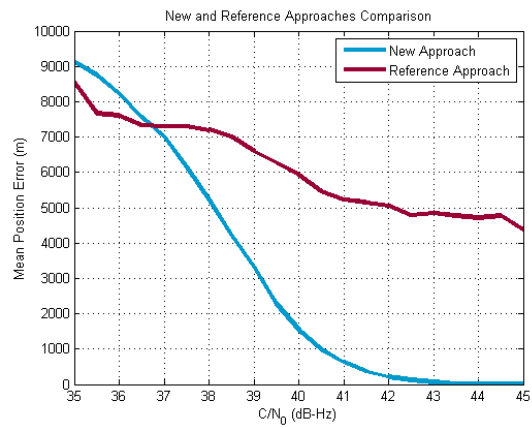
(f) Positioning Error

iii) True MS coordinates (in meter): $(\Delta N, \Delta E, \Delta D, \Delta B) = (0, 0, 0, 500)$

Figure 5.11 – SECA and reference Collective Detection approach comparison (1/2)

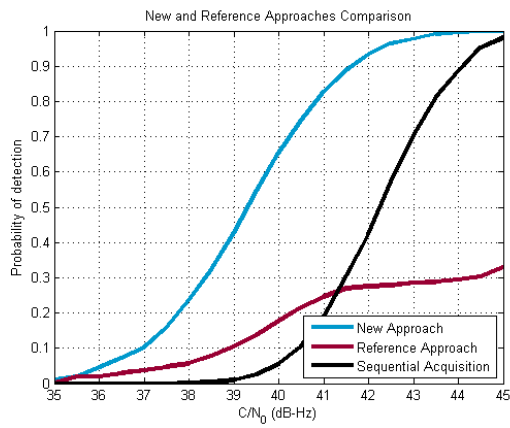


(a) Sensitivity Analysis

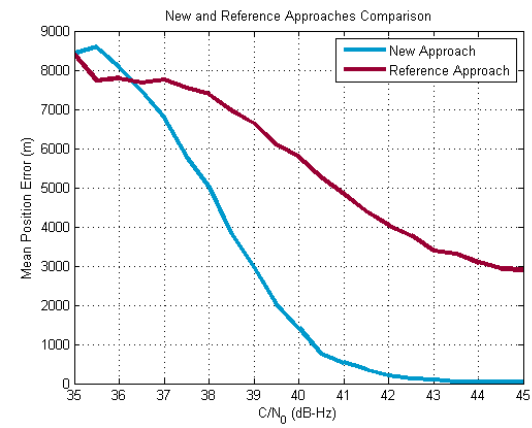


(b) Positioning Error

i) True MS coordinates (in meter): $(\Delta N, \Delta E, \Delta D, \Delta B) = (250, 250, 0, 0)$

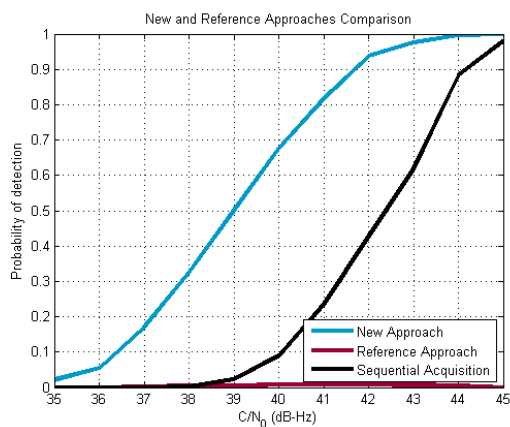


(c) Sensitivity Analysis

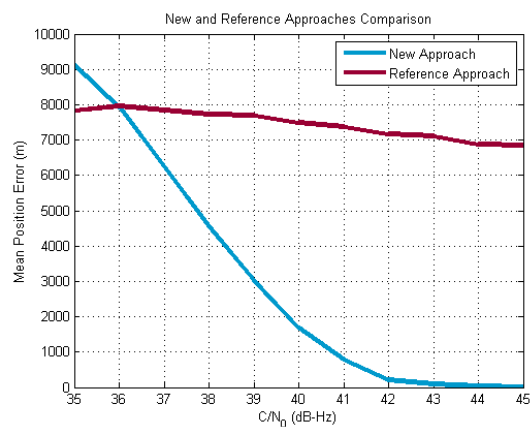


(d) Positioning Error

ii) True MS coordinates (in meter): $(\Delta N, \Delta E, \Delta D, \Delta B) = (500, 500, 0, 0)$



(e) Sensitivity Analysis



(f) Positioning Error

iii) True MS coordinates (in meter): $(\Delta N, \Delta E, \Delta D, \Delta B) = (500, 500, 0, 500)$

Figure 5.12 – SECA and reference Collective Detection approach comparison (2/2)

new approach. This occurs in the cases when the MS position and clock bias coincides precisely with one grid point. However, the averaging approach is more robust, keeping its performance practically independent of the MS true coordinates. In terms of complexity of execution, a computational gain of approximately five times is observed with the new approach, which scans 52.030 points compared to the 252.907 of the reference approach according to Table 5.6.

Through the analysis of the plots in Figures 5.11 and 5.12 it can be concluded that the proposed approach is effective in improving sensitivity over sequential acquisition methods, and that it is more robust and computationally effective than the reference method [22, 119]. In the section 5.5, the hybridization of the SECA approach with sequential acquisition techniques is addressed.

5.4.1 Influence of the Vertical Component

In light of the previous results, showing that Collective Detection, at best, provides a positioning error in the order of tens of meters (also confirmed by [22, 23, 119]), it can be expected that the vertical component can be safely neglected in the search process, and resort to 2D positioning. A reference vertical displacement could be provided by the BS, corresponding, for example, to the height of the BS antenna, which may be enough for the purposes of Collective Detection. This is also supported by the fact that the vertical error uncertainty will generally be much lower than its horizontal counterpart for land-based applications.

There may be, nevertheless, situations in which this assumption is not entirely correct (positioning within skyscrapers or tall buildings, for example), in which an uncertainty in the vertical component needs to be considered as well. In this case, a second weight can be introduced, $w_{vertical}$, to be added in (5.11), and the algorithm adapted accordingly from there. The vertical uncertainty should be provided by the BS jointly with the horizontal one. In any case, the vertical uncertainty is not considered in the examples shown here.

5.5 Hybridized Sequential-Vectorial SECA

Although the SECA algorithm has been designed to address the acquisition of all signals collectively, considering them as too weak to be detectable individually, it is often the case that one or more strong signals are present even in constrained environments. In these cases, it is desirable to make use of such strong signals in order to optimize the Collective Detection search process.

In [23] one proposal to do so has been introduced, by employing Singular Value Decomposition (SVD) of the geometry matrix in order to subtract the contribution of the strong signals and thus reduce the number of search dimensions, and it is mentioned that the computational gains are very significant with respect to the exclusively vectorial approach. In this section, the SECA algorithm is adapted to the case when one or two strong signals are present. This section starts with a review of the near-far problem in GNSS acquisition, originating exactly in the cases when both strong and weak signals are present. Then, the proposed hybridized algorithms are described and their performance compared at the end of this section.

5.5.1 Near-Far Problem in Acquisition

The families of PRN codes applied in GNSS signals (as the Gold codes for the GPS L1 C/A or the memory codes for the Galileo E1) ensure a fairly large cross-correlation protection between different codes. Nevertheless, in the presence of both strong and weak signals, this protection may not be enough, and the so-called *near-far problem* arises [71, 153, 155, 199, 200]. As an example, in Figure 5.13 the acquisition of a GPS L1 C/A signal at 20dB-Hz in the presence of another signal at 50dB-Hz is shown, employing the SLD detector (Figure 2.13, section 2.3.1) and 100ms coherent integration. Also in the plot of Figure 5.13, the same signal is acquired in the absence of the strong

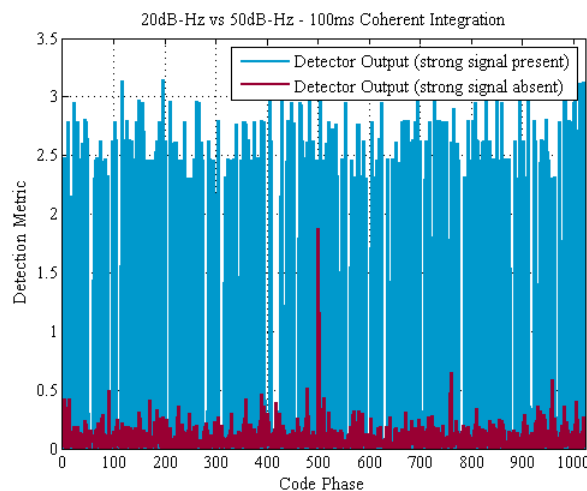


Figure 5.13 – Illustration of near-far effect in acquisition of a signal at 20dB-Hz in presence/absence of a signal at 50dB-Hz and 100ms coherent integration (SLD detector)

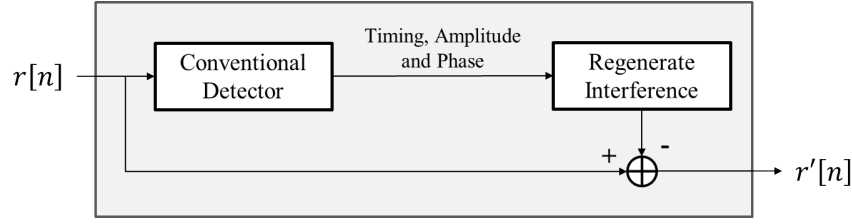


Figure 5.14 – Successive Interference Cancellation diagram

signal. From this figure, it becomes clear that acquisition in such cases must be handled carefully.

In such occasions, several techniques can be applied to prevent the strong signal from hindering the acquisition of the weaker one. This problem is widely addressed in the literature of communication systems to handle the Multiple Access Interference (MAI). Existing solutions include Successive Interference Cancellation (SIC) and Subspace Projection methods among others [199, 200]. The principle of SIC is simply to regenerate the strong signal that has been detected and remove it from the input signal, prior to the processing of the remaining signals (Figure 5.14).

5.5.2 Hybrid SECA in Presence of 1 Strong Signal

If one strong signal is identified in the set of signals in view, then its code phase, ζ_{strong} , is known. This way:

$$\zeta_{strong} = \frac{[\rho_{BS,strong} + \Delta\rho_{strong}]_{c \cdot T_{code}}}{c \cdot T_{chip}} \Leftrightarrow \Leftrightarrow \Delta\rho_{strong} = [\zeta_{strong} \cdot c \cdot T_{chip} - \rho_{BS,strong}]_{c \cdot T_{code}} \quad (5.24)$$

Inserting this relation in the pseudorange equation, we get:

$$\Delta\rho_{strong} = -R \cos(e l_{strong}) \cos(a z_{strong} - \theta) + c \cdot \Delta B \quad (5.25)$$

and from here:

$$c \cdot \Delta B = \Delta\rho_{strong} + R \cos(e l_{strong}) \cos(a z_{strong} - \theta) \quad (5.26)$$

which means that the MS clock bias search can be limited to $\Delta\rho_{strong} \pm R_{max} \cos(e l_{strong})$, therefore reducing the uncertainty search in the bias range. Furthermore, for a given candidate bias ΔB_m :

$$\Delta\rho_{strong} - c \cdot \Delta B_m = -R \cos(e l_{strong}) \cos(a z_{strong} - \theta) \quad (5.27)$$

from which:

$$R = -\frac{\Delta\rho_{strong} - c \cdot \Delta B_m}{\cos(e l_{strong}) \cos(az_{strong} - \theta)} \quad (5.28)$$

This way, for each candidate clock bias the candidate radius can be directly calculated from the candidate angle. The finest angular resolution can be employed, such that the total number of points of this approach is:

$$n_{points,total} = n_{points,bias} \cdot n_{points,angular} = \left\lceil \frac{\Delta B_{dimension}}{\delta B} \right\rceil \cdot \left\lceil \frac{2\pi}{\delta\theta_{finest}} \right\rceil \quad (5.29)$$

Depending on the algorithm configuration parameters, the number of points to be searched can be reduced with respect to the case when no strong signals are detected, or rather the computational effort can be used to reduce the initial value of β to enhance the detection sensitivity.

5.5.3 Hybrid SECA in Presence of 2 Strong Signals

If two strong signals are detected, it is also possible to further reduce the number of search points given that we will have two equations:

$$\begin{aligned} \Delta\rho_{strong,1} &= -R \cos(e l_{strong,1}) \cos(az_{strong,1} - \theta) + c \cdot \Delta B \\ \Delta\rho_{strong,2} &= -R \cos(e l_{strong,2}) \cos(az_{strong,2} - \theta) + c \cdot \Delta B \end{aligned} \quad (5.30)$$

To solve this set of equations, only one value needs to be assigned and the other two can be derived from it. Once again the finest radial resolution is chosen as the assigned value, and the candidate radius and clock bias are obtained as:

$$\begin{aligned} R &= \frac{\Delta\rho_{strong,2} - \Delta\rho_{strong,1}}{\cos(e l_{strong,1}) \cos(az_{strong,1} - \theta) - \cos(e l_{strong,2}) \cos(az_{strong,2} - \theta)} \\ c \cdot \Delta B &= \Delta\rho_{strong,1/2} + R \cos(e l_{strong,1/2}) \cos(az_{strong,1/2} - \theta) \end{aligned} \quad (5.31)$$

The number of points to be searched is therefore equal to:

$$n_{points,total} = n_{points,angular} = \left\lceil \frac{2\pi}{\delta\theta_{finest}} \right\rceil \quad (5.32)$$

So for each candidate θ , there will be only one pair $(R, \Delta B)$ that satisfies the above conditions.

5.5.4 Hybrid SECA in Presence of 3 or more Strong Signals

If three or more satellites are detectable by conventional acquisition methods, the user position and clock bias can be directly estimated, given that the vertical dimension is not being considered here. This direct positioning from acquisition is known as *snapshot positioning* [112–116,201]. The positioning accuracy of this technique is highly dependent on the accuracy of the strong signals' code phase estimations. If a signal oversampling factor of, for example, 16 times is considered, and assuming that the true code phase is the one which effectively produces the highest detection metric, a maximum code phase estimation error of $1/32$ chips is achieved. According to (5.2), such a code phase estimation error is translated into the pseudorange as an error of 9.4m. Depending on the constellation geometry, this pseudorange error will naturally be translated into different positioning errors. A quick assessment of the positioning accuracy of the snapshot approach in this case is shown in Figure 5.15. This simple analysis of the snapshot positioning error is obtained by randomly generating three satellite positions at elevations higher than 30 degrees and also randomly spread in azimuth. The pseudorange error is also randomly varied between 0 and 9.4m for each satellite. Although the horizontal scale of the histogram shown in Figure 5.15 is limited to 100m positioning error, it is noted that values of several hundreds of meters can be obtained for extremely adverse constellation configurations. The worst results are naturally obtained when the satellites are very close to each other in the sky plot. This may be the case also of positioning in harsh environments when only a very narrow portion of the sky is visible to the receiver, in which

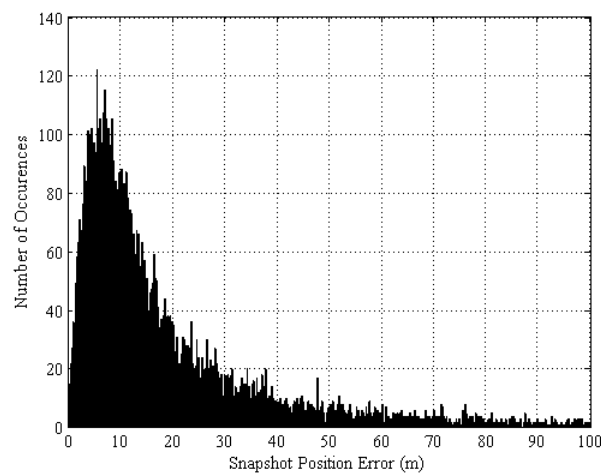


Figure 5.15 – Histogram of snapshot horizontal positioning errors for three satellites, maximum pseudorange error of 9.4m and 30 degrees mask angle

Table 5.7 – Details of full and hybrid SECA comparison ($e_{l_{min}} = 30\text{deg}$, $\Delta R_{dimension} = 10\text{km}$)

| Approach | Initial Code Phase Uncertainty (β_0) | Code Phase Uncertainty Dividing Factor | Number of Iterations | Total Number of Points |
|----------------------|--|--|----------------------|------------------------|
| Full | 5 | 10 | 3 | 52030 |
| Hybrid (1 Strong SV) | 0.5 | 10 | 2 | 85558 |
| Hybrid (2 Strong SV) | 0.05 | - | 1 | 2184 |

case similar positioning errors may be obtained.

5.5.5 Performance of Hybridized Algorithms

Having presented the different SECA algorithm versions in the presence of a different number of strong satellites, these approaches can now be compared also with the no-strong signals case, here referred to as *full* SECA. In the following examples the strong signals are generated only for testing the hybridized algorithms and are removed from the input signal prior to the Collective Detection search process in order to prevent the occurrence of cross-correlation effects. Therefore, their detection metrics are also not accounted for in the generation of the final combined detection metric. The details for the execution of each algorithm are shown in Table 5.7.

The results of the analysis of the three versions of the algorithm are shown in Figure 5.16. For this comparison, 1ms-long GPS L1 C/A signals are generated for each satellite and the number of satellites is always kept at 6, independently if there are strong signals in the set or not. From the plots shown in this figure it can clearly be seen the benefit for SECA of prior detection of strong signals, from both a sensitivity and positioning error point of view. For the same signal integration time,

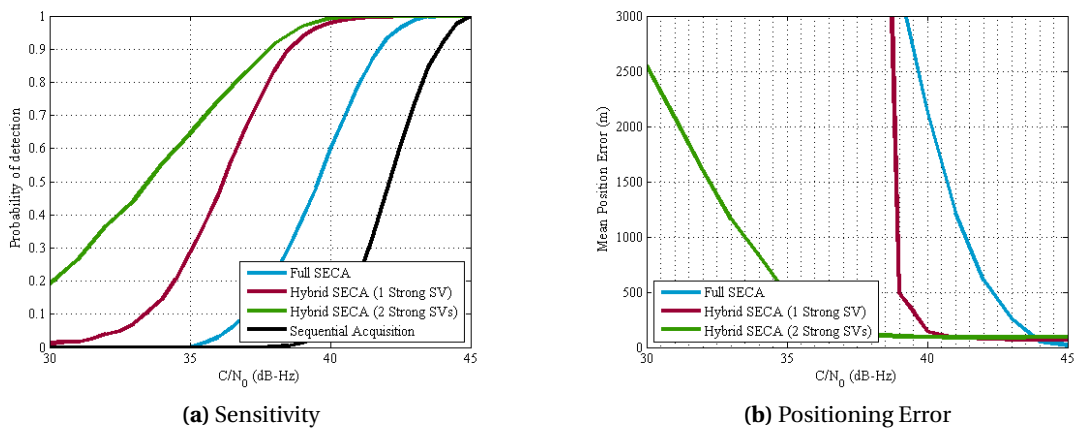


Figure 5.16 – Comparison of the full and hybrid versions of the SECA algorithm

number of signals, and satellite geometry, the hybrid detection methods can detect much weaker signals and significantly reduce the final positioning error with respect to the full algorithm version. Furthermore, the number of points to be evaluated can also be significantly reduced with respect to the full approach, especially when 2 strong signals are visible, as shown in Table 5.7. For the 1 strong satellite case, the number of points shown in Table 5.7 is even higher than for the full SECA application simply due to the value of β chosen, but for different configurations of its parameters it can lead to a smaller total number of points.

5.6 Combined GPS-Galileo SECA

With the advent of multi-constellation GNSS receivers, it is natural to consider that in the near future the application of SECA (or any other Collective Detection algorithm) will most likely be carried in the presence of signals originating from more than one constellation. One of the features that distinguish Collective Detection in this case is the possibility to combine information from satellites from different constellations at the acquisition level. The first advancement in this direction is described in [23], where a combined GPS+Locata Collective Detection implementation is shown. In the case here described we focus on the dual constellation GPS+Galileo and the L1 C/A and E1 Open Signal (OS) signals.

5.6.1 Considerations for Multi-GNSS Collective Detection

One factor that must usually be taken into account when handling more than one constellation is the time offset between both constellations, in this case commonly known as GPS-Galileo Time Offset (GGTO). This time offset, however, is not an issue in the Collective Detection approach, given that its principle is to differentially compute the pseudoranges from the BS measurements. This way, all sources of error common to the BS and MS, including the clock offset of GPS satellites, do not need to be considered in (5.1).

Also to be considered in a combined GPS and Galileo solution is the fact that the Galileo E1 OS spreading code period is four times longer than the GPS L1 C/A code. Depending on the input signal powers, this can originate large disparities in the magnitude of the individual detection metrics. To handle this, the coherent integration time for the acquisition of the GPS signals can be extended to 4ms. Furthermore, the fact that the Galileo E1 OS signal consists of two components (data and pilot) with each one being allocated 50% of the transmitted signal power, also impacts the final detection metric values. Applying the simplest channel combining technique (squaring the correlation outputs of both channels prior to summation [142]) a multiplication factor of 2 must be applied to the final Galileo detection metrics, prior to the Collective Detection processing. It should be also noted that, given the matching code and data bit period on the Galileo E1 OS signal, a correlation method robust to data bit transition within the correlation period should be applied. In the examples here described, two consecutive 4ms-long signal blocks of data are circularly correlated with a zero-padded local code of matching length, thus assuring insensitivity to the data bit transition [12].

One more factor to be considered in this context is the fact that, given the longer Galileo E1 OS codes the MS clock bias uncertainty is expanded by a factor of 4 with respect to the GPS-only case. This is therefore directly translated as an increase by the same factor for the number of points to be searched in this dimension. One practical solution to handle this issue without further increasing the complexity of the Collective Detection search process is to “fold” the Galileo detection metrics

twice, averaging the four points at “1ms distance” (1023 code phases) into just one, at a cost of a slight reduction in the method sensitivity.

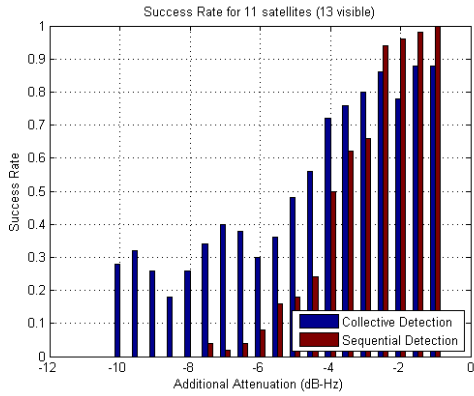
One last point to be noted concerns the application of the hybridized Collective Detection approaches, as well as snapshot positioning. Given the aforementioned 1ms ambiguity of the clock bias when considering the Galileo E1 OS signals, the algorithms described in the previous section cannot be directly applied to both GPS and Galileo satellites together. In the case of snapshot positioning, for example, if 3 strong satellites are detected, but from two different constellations (2 GPS and 1 Galileo or vice-versa), a solution cannot be obtained due to this clock bias ambiguity. Therefore, the minimum number of satellites required increases to 4 (or 5 in case the vertical component is also considered). For the case of the hybridized algorithms, further adaptations would be required but are not attempted here. This way, in the following examples only GPS satellites are considered in the preprocessing phase of the hybridized SECA algorithms, that is, imposing the conditions on the search space through (5.28) or (5.31). Likewise, the snapshot positioning solutions are also calculated based on GPS satellites only.

5.6.2 Real Data Results

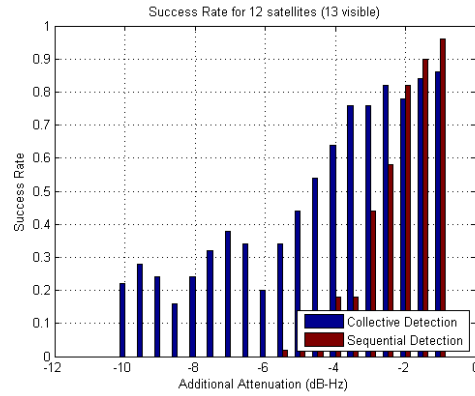
To illustrate the combined GPS+Galileo Collective Detection process, two experiments were carried at the *Institut Supérieur de l'Aéronautique et de l'Espace* (ISAE), in Toulouse. A Septentrio PolaRx3e TR Pro receiver capable of receiving and handling both GPS and Galileo signals was setup as BS, and a NordNav R30 receiver acting as MS was used to collect raw data at a position close by to the BS. The two sets of data were then post-processed to execute the Collective Detection approach. Two different scenarios were considered, one where the MS receiver is in an open-sky environment with relatively strong signals in view, and additional noise is injected to emulate weaker signals, and a second one where the MS receiver was in "light" indoor (close to a window). These two scenarios are analyzed separately.

Open Sky scenario By collecting the signals in an open sky scenario, weaker signals can be emulated in post-processing by adding extra Gaussian noise to the correlation outputs. This controlled scenario allows an easier comparison of the vectorial and sequential approaches. A total of 13 satellites were visible at the time of acquisition (9 GPS and 4 Galileo). The results for the acquisition of all satellites in view for 3 different mask angles values are shown in Figures 5.17-5.19. The parameters of the SECA algorithm are the same as shown in Table 5.5 ($\beta_0 = 5$, $\beta_{div.factor} = 10$, $w_{bias} = 0.15$, $e_{l_{min}} = 30deg$, and $\Delta R_{dimension} = 10km$)

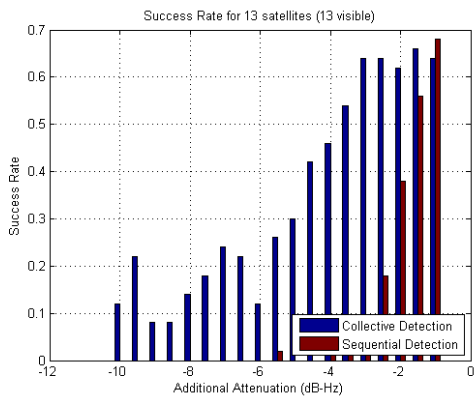
Several conclusions can be drawn from these plots. The clearest and most expected one is that for the highest injected noise powers, the proposed SECA approach performs above sequential detection. Next, it can also be noticed that for low injected noise powers, the performance of both ap-



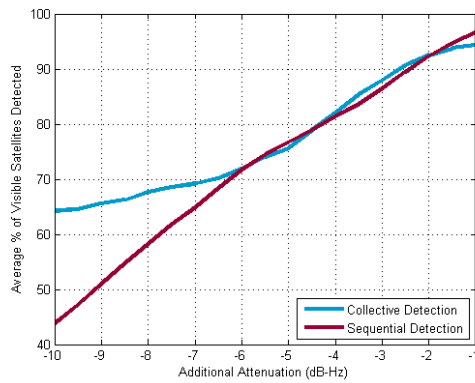
(a) Success rate for acquisition of 11 satellites (13 visible in total)



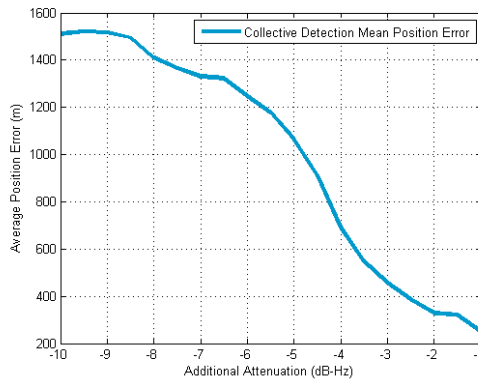
(b) Success rate for acquisition of 12 satellites (13 visible in total)



(c) Success rate for acquisition of 13 satellites (13 visible in total)

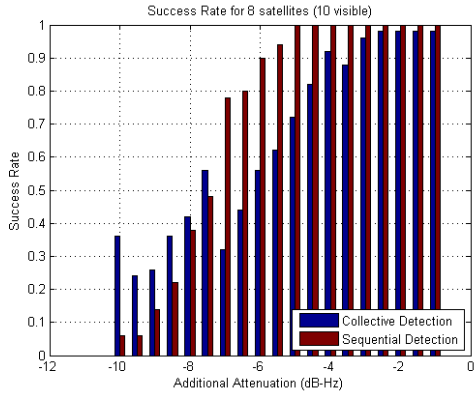


(d) Average percentage of satellites acquired

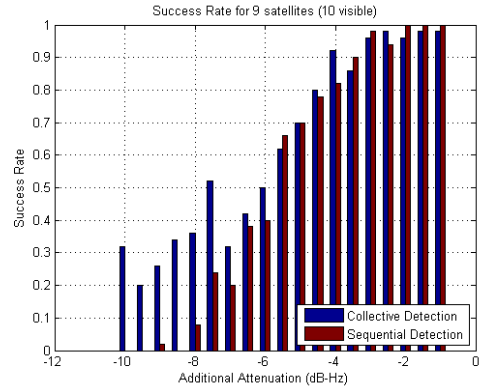


(e) Average Collective Detection positioning error

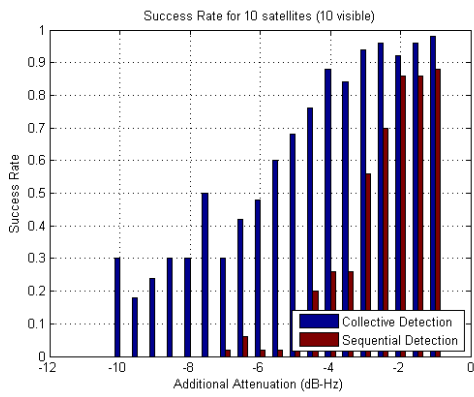
Figure 5.17 – Multi-Constellation Collective Detection performance assessment: 10 degrees mask angle



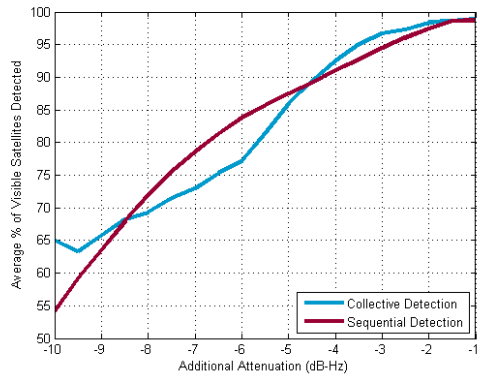
(a) Success rate for acquisition of 8 satellites (10 visible in total)



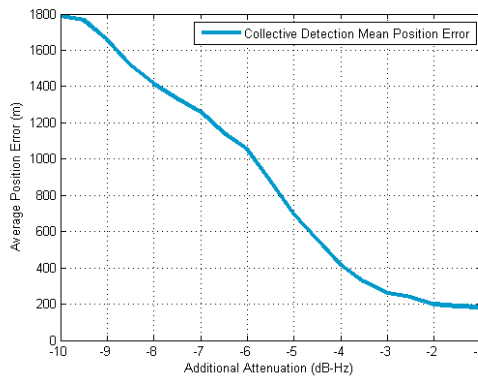
(b) Success rate for acquisition of 9 satellites (10 visible in total)



(c) Success rate for acquisition of 10 satellites (10 visible in total)

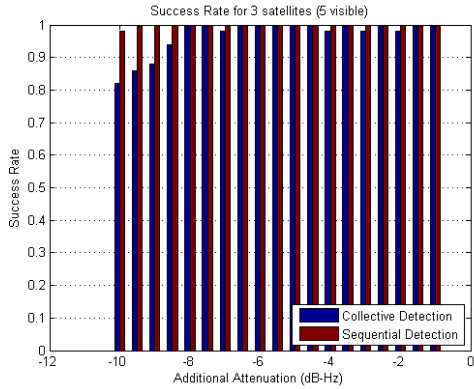


(d) Average percentage of satellites acquired

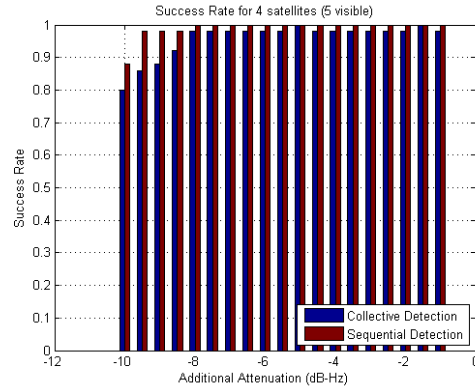


(e) Average Collective Detection positioning error

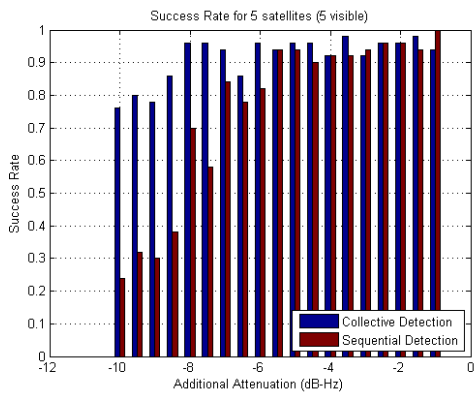
Figure 5.18 – Multi-Constellation Collective Detection performance assessment: 30 degrees mask angle



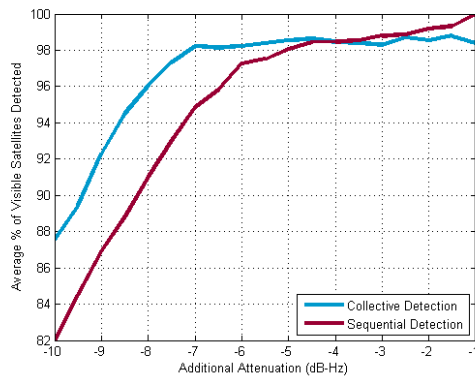
(a) Success rate for acquisition of 3 satellites (5 visible in total)



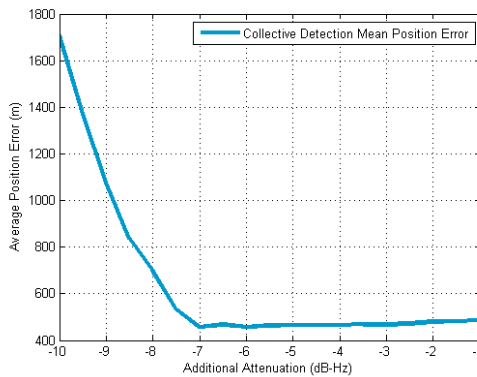
(b) Success rate for acquisition of 4 satellites (5 visible in total)



(c) Success rate for acquisition of 5 satellites (5 visible in total)



(d) Average percentage of satellites acquired



(e) Average Collective Detection positioning error

Figure 5.19 – Multi-Constellation Collective Detection performance assessment: 45 degrees mask angle

proaches is close, even slightly worse for the SECA approach in some cases. In terms of positioning error of the SECA approach, it can be seen that the average position errors are always considerable (few hundreds of meters). Comparing the errors obtained with the ones in [22, 23, 119–122], it can be concluded that this is in line with the typical performance of Collective Detection methods. In any case, the MS position uncertainty is decreased by one to two orders of magnitude with respect to the initial uncertainty (1E4 to 1E3 or 1E2).

Indoor scenario The second scenario considered in the analysis of the SECA algorithm consisted of collecting signals in a light indoor scenario. In this case the received signals at the MS are already significantly attenuated (or at least most of them), so no extra noise is injected, but rather the possibility of performing a number of noncoherent integrations in the generation of the individual detection metrics is included. The mask angle considered for this scenario is of 30 degrees, which, according to the sky plot shown in Figure 5.20 (obtained through the ephemeris data provided by the BS) implies that a total of eight satellites are considered in the SECA algorithm.

In this scenario a total of 100 data points (corresponding to a duration of 100 seconds given the 1Hz output of the BS data) are analyzed, and individual signals are detected based on a simple peak-to-peak threshold [4, 46, 47]. Given the considerations issued in the previous section regarding the hybridization of the SECA algorithm, only GPS signals are used to trigger the hybridized SECA versions. In case 3 or more GPS satellites are straight away detected, snapshot positioning is instead performed. The configurations used for the different algorithms shown in Table 5.7 are also applied here.

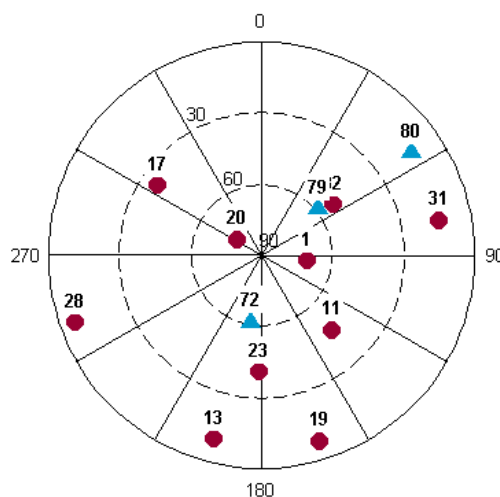


Figure 5.20 – Skyplot for indoor data collection (GPS satellites marked as circles and Galileo satellites as triangles)

The mean positioning errors obtained for each of the 4 approaches as function of the number of noncoherent integration performed are shown in Figure 5.21 either considering both GPS+Galileo satellites (Figure 5.21a) or only the set of GPS satellites (Figure 5.21b). It should be noted that, in order to produce meaningful results, a value is only shown in this figure if at least 10 points within the 100 point data set correspond to a given algorithm for a given number of noncoherent integrations executed, that is, it may happen that for one or two points in the data set a certain number of strong signals is detected, but this reduced number points cannot be considered as representative of the algorithm's performance, so they are excluded from the plots of Figure 5.21.

The first conclusion that can be drawn from these plots is the fact that the motivation to develop hybrid versions of the SECA algorithm is well justified, given that even for as low as 2 noncoherent integrations, 2 GPS signals are already detectable in at least 10% of the data set points. Nevertheless, it is not until 13 noncoherent integrations are performed that more than 2 GPS satellites are consistently detectable.

Next, the advantages of the hybrid versions of the SECA algorithm with respect to its full version are also well remarked in the plots shown, as the magnitude of the mean positioning errors obtained is significantly different for both cases. However, it is also clearly visible that even for the hybrid algorithms, the mean positioning errors are still quite high. Nevertheless, these errors in the order of hundreds of meters are also verified for the snapshot algorithm. This can be partially explained by examining the satellite sky plot for this data collection (Figure 5.20) and the fact that the GPS signals recurrently detected through sequential acquisition correspond to PRNs 17, 20, and 23, that clearly do not offer a good geometry for positioning. For reference, only the Galileo satellite PRN72 seems to actually be present in the MS collected data, which is in accordance with the geometry of the GPS satellites also identified in the collected data.

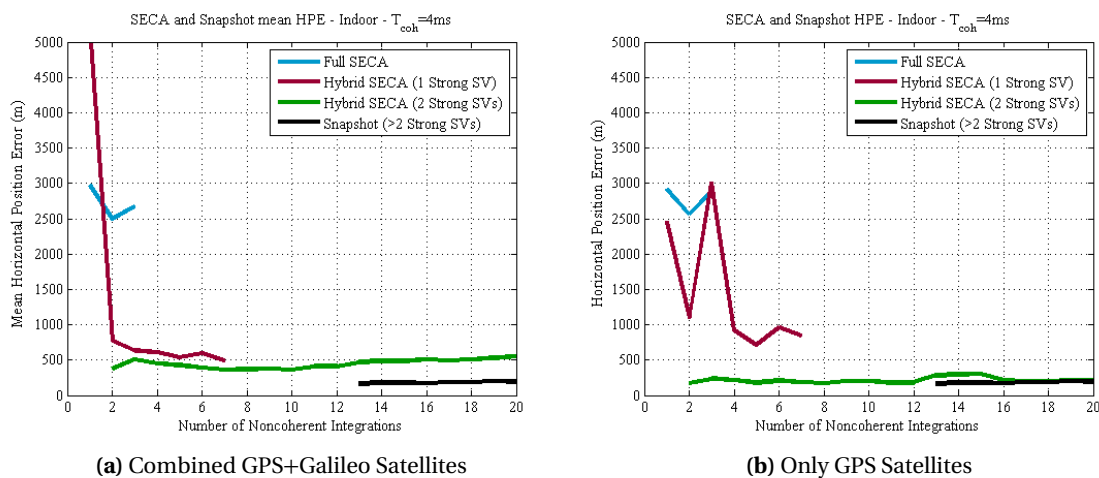


Figure 5.21 – Comparison of hybrid approach for different constellations

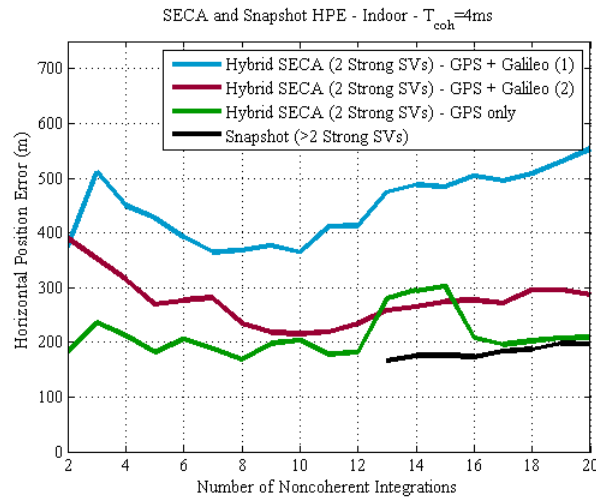


Figure 5.22 – Comparison of hybrid approach for different constellations

The third conclusion that can be drawn from these plots is the difference of performance of the hybrid SECA algorithm for the case of combined GPS+Galileo satellites with respect to the case of GPS only. This is most remarked for the hybrid algorithm with 2 "strong" signals previously identified. While for the GPS-only satellites the mean error is constantly around 200 meters, the combined set exhibits an error of around 500 meters, that is, more than double. After in-depth analysis it was concluded that this is for the most part due to folding of the Galileo satellites detection metrics prior to the SECA algorithm execution, in order to resolve the 4ms clock bias ambiguity mentioned in the previous section. If instead an exhaustive search is performed for this ambiguity (0 to 3), the multi-constellation SECA approach results are already significantly closer to those for the GPS-only satellites, as shown in Figure 5.22, where the line "GPS + Galileo (1)" corresponds to the folding approach and "GPS + Galileo (2)" to the exhaustive search. Given that for this particular algorithm the number of points to be analyzed is relatively low comparing with the other two SECA approaches, a multiplication by 4 of the number of points to be scanned should not amount to complexity issues. The biggest impact of the 4 times increase in number of points to be scanned, however, is the verified decrease in performance with respect to the GPS-only constellation, given the larger number of search points corresponding to a wrong combination of the parameters under estimation.

Finally, it is noted that for the GPS-only curve in Figure 5.22, the mean positioning errors obtained with the hybrid SECA algorithm after identification of two strong signals are quite close to the mean errors of the snapshot algorithm, requiring one more satellite to be detected individually. This way, it can be expected that further research on this topic will further clarify the benefits of the proposed approach. This research is currently taking place in the research group in order to consolidate the findings reported here. It will also be of interest to reassess the algorithm performance for the multi-constellation case when more Galileo satellites will be available.

5.7 Conclusion

In this chapter a new methodology for the systematic and efficient application of Collective Detection has been proposed. The new algorithm defines the user position/clock bias search grid based on the change of the shape of the user position uncertainty area to a circular uncertainty range, and takes into account the lowest elevation angle from the set of visible satellites as well as two user-defined parameters, the maximum allowable code phase estimation error during the Collective Detection search process and the maximum range from the BS. The new algorithm has proven to be computationally more efficient than a fixed-step squared search grid, and more reliable, keeping its performance independent of the user's true position and clock bias, thanks to the averaging of several points in the search process.

Two approaches for the hybridization of the proposed SECA algorithm with traditional sequential acquisition have also been presented. These were seen to be more effective in reaching higher sensitivity than the "full" SECA version, given the limitations imposed on the user uncertainty 4D search grid. Furthermore, the proposed algorithms were also tested in the acquisition of real GPS and Galileo signals, thus demonstrating the feasibility of multi-constellation Collective Detection. The results obtained in both scenarios considered (open-sky with extra added noise and light indoor) attest the capacity of the vectorial acquisition principle to acquire weaker signals than sequential algorithms. Furthermore, the results presented for the indoor data set show the capacity of the hybridized algorithms to provide a rough position estimation to the user even with only two signals detectable through sequential acquisition. Further analysis will be carried in the research group to consolidate the results presented here.

CONCLUSION AND FUTURE WORK

Satellite navigation is playing a role more and more important in the modern society. Nevertheless, with the new applications new challenges rose as well. In this thesis, one of the most crucial parts of the signal processing chain within a GNSS receiver has been studied, *signal acquisition*. After an exhaustive and in-depth introduction to the subject of GNSS acquisition in Chapter 2, the three following chapters presented the main contributions of this research. These contributions are summarized next, and some recommendations for future work follow.

6.1 Thesis Research Conclusions

Analysis and Compensation of the Doppler Effect in GNSS Acquisition In Chapter 3, the Doppler shift that is expected to be experienced by a user was seen to be one of the main design drivers for the acquisition module for different GNSS applications. In particular, not only its value, but also its variation during the signal observation time is important. Three separate scenarios of application were considered for evaluation, considered as low-, medium-, and high-dynamics.

For the low-dynamics case, when the Doppler offset can be considered to be constant during the acquisition time, the search grid resolution for the Doppler search has to be weighted with the computational efficiency of the correlation method to be applied. It was seen that the most computationally efficient correlation methods are subject to Doppler-derived attenuations higher than those for less efficient methods, and a methodology to alleviate these losses was proposed. By applying Spectral Peak Location (SPL) algorithms, the offset between the true and the closest FFT candidate frequencies can be estimated, and a fine search grid can be emulated with the otherwise less Doppler-robust methods. A new acquisition methodology was developed for the application of SPL algorithms in acquisition, and its merits were proven in the acquisition of both simulated and real GNSS signals. The obtained results and the simplicity of the SPL technique show that this

proposition is a promising solution for optimizing the sensitivity/complexity trade-off in the receiver design.

For the medium-dynamics case, defined as the situation when the Doppler change rate is not high enough to justify higher complexity solutions to attempt compensation, the analysis of this change rate on the SLD, NCD, and NCCD detectors was assessed. For the case of the SLD detector, it was established a limit for the coherent integration time, which ensures that the attenuations of the final detection metric are not higher than those which would be expected for a stationary Doppler. According to (3.17), this limit is $T_{coh} = \sqrt{\alpha^{-1}}$. For the NCD and NCCD detectors, a formula relating the maximum coherent integration time with the number of coherent outputs, depending on the expected dynamics and the maximum allowable attenuation for the coherent outputs, was obtained (equation (3.21)). It was equally seen that under the assumption of a chirp signal and initial offset frequency close to zero, the NCD detector is a more reliable choice than the NCDD in these scenarios. The second solution is more indicated for relatively low coherent integration times (10-20ms), so it can be applicable in standalone receivers, while the first one aims at very long coherent integration times (>100ms).

Finally, when the Doppler change rate is considered to be significant with respect to the coherent integration time, it was shown that the inclusion of a chirp-compensated FOC-loop in the NCD detector is capable of providing several dB additional sensitivity with respect to the uncorrected NCD detector (Figure 3.28 and Figure 3.29). The sensitivity enhancement of the proposed solution, however, is limited by the capability of the applied estimator to perform well at low coherent output SNRs. It was seen that for values of the sweep factor (γ) between 5 and 15%, the proposed solution can offer enhanced reliability with respect to the medium-dynamics assumption. Table 3.6 shows the preferable solution and detector to be applied as function of γ .

Sensitivity Characterization of Differential GNSS Detectors In Chapter 4, the performance of postcoherent differential detectors in the acquisition of weak GNSS signals was studied. First, we characterized statistically the PWD detector. Under the noise-only hypothesis, we made use of the fact that the output of pair-wise differential integration corresponds to a sum of independent Laplace random variables to propose a new expression for its characterization. Under the assumption that both signal and noise are present, it was shown that the approximation of the output of this detector by a Gaussian random variable matches closely its true distribution, and an expression for its probability of detection was derived. Given the complexity of following the similar procedure for the NCDD detector, we instead characterized this detector through its sensitivity loss with respect to the SLD detector. Firstly, the methodology to characterize a detector in this way was described, and subsequently a formula for assessing the sensitivity loss of the NCDD detector (combining both differential and squaring losses) with respect to the SLD detector was proposed. The theoretical results were validated by simulations, showing that this is a valid approach to follow

in such cases when the statistical analysis of the detectors is overly complex. The results obtained enabled the comparison of the NCDD and NCD detectors, allowing deciding on the most adequate integration strategy for achieving a predefined sensitivity level. It was confirmed that differential integration has in fact the potential to be preferable to noncoherent integration in the acquisition of weak signals. The user dynamics however, also need to be taken into consideration, as highlighted in Chapter 3. The theoretical conclusions were confirmed with the acquisition of real GPS L1 C/A signals, highlighting the potential of the NCDD detector in weak signal acquisition.

Systematic and Efficient Collective Acquisition of Multi-Constellation GNSS Signals In Chapter 5, a new methodology for a systematic and efficient application of Collective Detection has been proposed. This chapter deals with the situation of availability of a second receiver used as a Base Station and an assistance link providing the required data. The new algorithm defines the user position/clock bias search grid based on the change of the shape of the user position uncertainty area to a circular uncertainty range, and takes into account the lowest elevation angle from the set of visible satellites as well as two user-defined parameters, the maximum allowable code phase estimation error during the Collective Detection search process and the maximum range from the BS. The new algorithm has proven to be computationally more efficient than a fixed-step squared search grid, and more reliable, keeping its performance independent of the user's true position and clock bias (Figures 5.11 and), thanks to the averaging of several points in the search process.

Two approaches for the hybridization of the proposed SECA algorithm with traditional sequential acquisition have also been presented. These were seen to be more effective in reaching higher sensitivity than the "full" SECA version, given the limitations imposed on the user 4D uncertainty search grid. Furthermore, the proposed algorithms were also tested in the acquisition of real GPS and Galileo signals, thus demonstrating the feasibility of multi-constellation Collective Detection. The results obtained in both scenarios considered (open-sky with extra added noise and light indoor) attest the capacity of the vectorial acquisition principle to acquire weaker signals than sequential algorithms. Furthermore, the results presented for the indoor data set show the capacity of the hybridized algorithms to provide a rough position estimation to the user even with only two signals detectable through sequential acquisition. Further analysis will be carried in the research group to consolidate the results presented here.

6.2 Future Work Recommendations

In line with the research results here presented, several questions are also raised for future work:

- The analysis conducted regarding the dynamic scenarios in Chapter 3 assumes that the input signals are well-modeled by a chirp signal with a constant change rate, which certainly is not the
-

case for the acquisition of highly attenuated signals, requiring very long integration times. The most reliable way to test the proposed algorithms would be to create an experimental setup working with real signals and enabling the demonstration of the algorithm's actual performance in such scenarios.

- Also in the analysis of the dynamic scenarios in Chapter 3, it was seen that the performance on FOC loop-assisted acquisition schemes is highly dependent on the frequency estimator's capacity to perform well at low C/N_0 . This way, other estimators, more reliable than the one employed here, could be envisaged to be applied in such architectures, thus rendering them more reliable.
 - For the characterization of differential detectors carried in Chapter 4, one of the fundamental assumptions is that the data bit effect is aptly mitigated. However, if this is not the case, differential detectors can no longer be considered as preferable to the noncoherent one. This fact becomes particularly relevant for the acquisition of modern signals with matching code and data bit periods. Nevertheless, these signals also include a pilot channel which may be used to overcome this effect, given the knowledge of the secondary code phase. The assessment of the performance of differential detectors in this case was not carried in this thesis and, therefore, is also recommended for future work.
 - Regarding Collective Detection and the SECA algorithms proposed in Chapter 5, a more exhaustive analysis of their true performances is still required, especially under multi-constellation scenarios, as the results presented cannot be considered as fully conclusive. Further analysis shall be continued within the research group. Also to be considered in the future is the combination of signals from different frequency bands.
 - In what respects the proposed SECA algorithms, it is also noted that the configuration parameters used for executing the algorithms have an important influence on their overall performance (complexity, sensitivity, and positioning error). A study regarding the choice of the values for these configuration parameters should also be carried for optimal tuning of the algorithm. Also, the inclusion of a second weight to allocate the errors between the radial and angular dimension should be considered for a more robust design.
 - Today and in the near future, most of GNSS receivers will be connected and ready to receive different aids. The developed methods and analyses in this thesis could be integrated naturally in aided or assisted receiver. Depending on the application and additional available information, the Doppler shift may be compensated from a reference station or an Inertial Measurement Unit (IMU).
-

GPS AND GALILEO CIVIL SIGNALS STRUCTURE

The summary of the details of the current and planned GPS and Galileo signals are described in Tables A.1 to A.4 [26–28, 32–34].

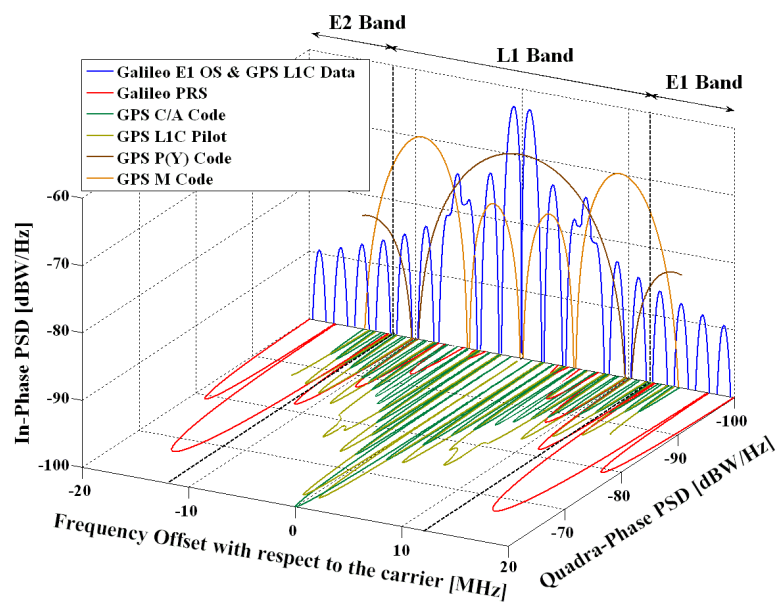


Figure A.1 – Spectrum of GPS and Galileo signals transmitted in the L1 band [33]

Table A.1 – GPS and Galileo signals in L1/E1 band ($f_c = 1575.42\text{MHz}$)

| GNSS System | GPS | | | | |
|----------------------------|------------|-----------------|-----------------|-------------|-----------|
| Service Name | C/A | L1C | | P(Y) Code | M-Code |
| Signal Component (Power %) | Data | Data (25%) | Pilot (75%) | Data | N/A |
| Modulation | BPSK | TMBOC(6,1,1/11) | | BPSK | BOC(10,5) |
| Subcarrier frequency (MHz) | - | 1.023 | 1.023 and 6.138 | - | 10.23 |
| Code frequency (MHz) | 1.023 | 1.023 | | 10.23 | 5.115 |
| Code family | Gold codes | Weil codes | | M-sequences | N/A |
| Primary PRN code length | 1023 | 10230 | | 6.19E12 | N/A |
| Secondary PRN code length | - | - | 1800 | - | N/A |
| Data rate (bps) | 50 | 50 | - | 50 | N/A |

| GNSS System | Galileo | | | |
|----------------------------|-----------------|----|-------------|-----------------------------|
| Service Name | OS | | | PRS |
| Signal Component (Power %) | Data (50%) | | Pilot (50%) | |
| Modulation | MBOC(6,1,1/11) | | | $\text{BOC}_{\cos}(15,2.5)$ |
| Subcarrier frequency (MHz) | 1.023 and 6.138 | | | 15.345 |
| Code frequency (MHz) | 1.023 | | | 2.5575 |
| Code family | Random codes | | | N/A |
| Primary PRN code length | 4092 | | | N/A |
| Secondary PRN code length | - | 25 | | N/A |
| Data rate (bps) | 250 | - | | N/A |

Table A.2 – GPS and Galileo signals in L5 ($f_c = 1176.45\text{MHz}$) / E5 ($f_c = 1191.795\text{MHz}$) bands

| GNSS System | | GPS | | | |
|----------------------------|--|-------------|--|-------|--|
| Service Name | | L5I | | L5Q | |
| Signal Component | | Data | | Pilot | |
| Modulation | | BPSK | | BPSK | |
| Subcarrier frequency (MHz) | | - | | - | |
| Code frequency (MHz) | | 10.23 | | | |
| Code family | | M-sequences | | | |
| Primary PRN code length | | 10230 | | | |
| Secondary PRN code length | | 10 | | 20 | |
| Data rate (bps) | | 50 | | - | |

| GNSS System | | Galileo | | | |
|----------------------------|--|---------------|-------|------|-------|
| Service Name | | E5a | | E5b | |
| Signal Component | | Data | Pilot | Data | Pilot |
| Modulation | | AltBOC(15,10) | | | |
| Subcarrier frequency (MHz) | | 15.345 | | | |
| Code frequency (MHz) | | 10.23 | | | |
| Code family | | M-sequences | | | |
| Primary PRN code length | | 10230 | | | |
| Secondary PRN code length | | 20 | 100 | 4 | 100 |
| Data rate (bps) | | 50 | - | 250 | - |

Table A.3 – GPS signals in L2 band ($f_c = 1227.60\text{MHz}$)

| GNSS System | GPS | | | |
|-----------------------------------|-------------|---------|-----------|-----------|
| Service Name | L2 CM | L2 CL | P(Y)-Code | M-Code |
| Signal Component | Data | Pilot | Data | N/A |
| Modulation | BPSK | | BPSK | BOC(10,5) |
| Subcarrier frequency (MHz) | - | - | - | 10.23 |
| Code frequency | 5.115kHz | | 10.23MHz | 5.115MHz |
| Code family | M-sequences | | | N/A |
| Primary PRN code length | 10230 | 767,250 | 6.19E12 | N/A |
| Secondary PRN code length | - | - | - | N/A |
| Data rate (bps) | 50 | - | 50 | - |

Table A.4 – Galileo signals in E6 band ($f_c = 1278.75\text{MHz}$)

| GNSS System | Galileo | | |
|-----------------------------------|--------------|-------------|---------------------------|
| Service Name | E6 CS | | E6 PRS |
| Signal Component (Power %) | Data (50%) | Pilot (50%) | Data |
| Modulation | BPSK | | BOC _{cos} (10,5) |
| Subcarrier frequency (MHz) | - | - | 10.23 |
| Code frequency (MHz) | 5.115 | 5.115 | 5.115 |
| Code family | Memory codes | | N/A |
| Primary PRN code length | 5115 | 5115 | N/A |
| Secondary PRN code length | - | 100 | N/A |
| Data rate (bps) | 1000 | - | N/A |

NORMAL-LAPLACE APPROXIMATION OF COHERENT DIFFERENTIAL
DETECTOR OUTPUT UNDER H_1 FOR $N_{DC} = 1$

In section 4.3.3 it was suggested that the output of the Coherent Differential Detector (CDD) can be approximated by a Normal-Laplace random variable. Given two independent random variables, Z and W , such that $Z \sim N(\mu, \sigma^2)$ and $W \sim \text{Laplace}(\lambda)$, their sum $Y = Z + W$ results in a Normal-Laplace distribution, whose PDF and CDF are given by [198]:

$$f_Y(y) = \frac{\phi(\gamma)}{2\lambda} \cdot [R(\sigma/\lambda - \gamma) + R(\sigma/\lambda + \gamma)] \quad (\text{B.1})$$

$$F_Y(y) = \Phi(\gamma) - \phi(\gamma) \cdot \frac{R(\sigma/\lambda - \gamma) + R(\sigma/\lambda + \gamma)}{2} \quad (\text{B.2})$$

with $\gamma = (y - \mu)/\sigma$, $\Phi(\cdot)$ and $\phi(\cdot)$ the CDF and PDF functions of a standard normal random variable, respectively, and $R(\cdot)$ the Mills ratio, defined as [198]:

$$R(z) = \frac{\Phi^c(\gamma)}{\phi(\gamma)} = \frac{1 - \Phi(\gamma)}{\phi(\gamma)} \quad (\text{B.3})$$

Given a threshold V_{th} , the tail probability of Y , equivalent to P_d in detection of a signal distributed according to $f_Y(y)$ is:

$$P_d = 1 - F_Y(V_{th}) \quad (\text{B.4})$$

This equation can be employed in the characterization of the output of the CDD detector under H_1 , considering the Gaussian and Laplace noise terms independent between themselves. For the case

of a single differential operation, the terms in (B.2) and (B.4) are given by:

$$\begin{aligned}\lambda &= \sigma_w^2 \\ \mu &= \mu_{S_{P_{WD}}^{H_1}} \approx |s_m|^2 \\ \sigma^2 &= \text{var}\{\Re\{w_{Y,m}\}\} \approx 2\sigma_w^2 \cdot |s_m|^2 \\ V_{th} &= -\sigma_w^2 \cdot \ln(P_{fa})\end{aligned}$$

where σ_w^2 is the coherent output noise variance and s_m is its useful signal component, function of the input signal power. Solving (B.4) for different values of $|s_m|$ provides the sensitivity curve of the CDD detector for this approximation.

BIBLIOGRAPHY

- [1] E. Kaplan and C. Hegarty, *Understanding GPS: Principles and Application*. Artech House, 2nd ed., 2006.
- [2] P. Misra and P. Enge, *Global Positioning System: Signals, Measurements and Performance*. Ganga-Jamuna Press, 2001.
- [3] J. Tsui, *Fundamentals of Global Positioning System Receivers: A Software Approach*. John Wiley & Sons, 2nd ed., 2005.
- [4] K. Borre, D. Akos, N. Bertelsen, P. Rinder, *et al.*, *A Software-Defined GPS and Galileo Receiver - A Single-Frequency Approach*. Birkhäuser, 2007.
- [5] M. Simon, *Spread Spectrum Communications Handbook*. McGraw-Hill, 1994.
- [6] C. O'Driscoll, *Performance Analysis of the Parallel Acquisition of Weak GPS Signals*. PhD thesis, National University of Ireland, 2007.
- [7] D. Borio, *A Statistical Theory for GNSS Signal Acquisition*. PhD thesis, Politecnico di Torino, 2008.
- [8] D. van Nee and A. Coenen, "New Fast GPS Code-Acquisition Technique Using FFT," *Electronic Letters*, vol. 27, no. 2, pp. 158–160, 1991.
- [9] D. Lin and J. Tsui, "Comparison of Acquisition Methods for Software GPS Receiver," in *Proceedings of the 13th International Technical Meeting of the Satellite Division of The Institute of Navigation (ION GPS 2000)*, (Salt Lake City, UT, USA), 2000.
- [10] N. Ziedan and J. Garrison, "Unaided Acquisition of Weak GPS Signals Using Circular Correlation or Double-Block Zero Padding," in *Proceedings of the 2004 IEEE/ION Position Location and Navigation Symposium (PLANS 2004)*, (Monterey, CA, USA), 2004.
- [11] N. Ziedan, *GNSS Receivers for Weak Signals*. Artech House, 2006.

-
- [12] M. Foucras, O. Julien, C. Macabiau, and B. Ekambi, "A Novel Computationally Efficient Galileo E1 OS Acquisition Method for GNSS Software Receiver," in *Proceedings of the 25th International Technical Meeting of The Satellite Division of the Institute of Navigation (ION GNSS 2012)*, (Nashville, TN, USA), 2012.
- [13] D. Akopian, "Fast FFT based GPS satellite acquisition methods," *IEEE Proceedings-Radar, Sonar and Navigation*, vol. 152, no. 4, pp. 277–286, 2005.
- [14] P. Sagiraju, G. Raju, and D. Akopian, "Fast acquisition implementation for high sensitivity global positioning systems receivers based on joint and reduced space search," *IET Radar, Sonar and Navigation*, vol. 2, no. 5, pp. 376–387, 2008.
- [15] T. Pany, *Navigation Signal Processing for GNSS Software Receivers*. Artech House, 2010.
- [16] J. Proakis, *Digital Communications*. McGraw Hill, 4th ed., 2005.
- [17] A. Schmid, *Advanced Galileo and GPS Receiver Techniques: Enhanced Sensitivity and Improved Accuracy*. Nova Science, 2009.
- [18] D. Barton, *Modern Radar System Analysis*. Artech House, 1988.
- [19] D. Borio, C. Gernot, F. Macchi, and G. Lachapelle, "The Output SNR and its Role in Quantifying GNSS Signal Acquisition Performance," in *Proceedings of the European Navigation Conference (ENC 2008)*, (Toulouse, France), 2008.
- [20] C. Strässle, D. Megnet, H. Mathis, and C. Bürgi, "The Squaring-Loss Paradox," in *Proceedings of the 20th International Technical Meeting of the Satellite Division of The Institute of Navigation (ION GNSS 2007)*, (Fort Worth, TX, USA), 2007.
- [21] R. DiEsposti, "GPS PRN Code Signal Processing and Receiver Design for Simultaneous All-in-View Coherent Signal Acquisition and Navigation Solution Determination," in *Proceedings of the 2007 National Technical Meeting of The Institute of Navigation (ION NTM 2007)*, (San Diego, CA, USA), 2007.
- [22] P. Axelrad, B. Bradley, J. Donna, M. Mitchell, *et al.*, "Collective Detection and Direct Positioning Using Multiple GNSS Satellites," *Journal of the Institute of Navigation*, vol. 58, no. 4, pp. 305–321, 2011.
- [23] J. Cheong, *Signal Processing and Collective Detection for Locata Positioning System*. PhD thesis, University of New South Wales, 2012.
- [24] B. Parkinson and J. Spilker Jr., *Global Positioning System: Theory and Applications*, vol. 1. American Institute of Aeronautics and Astronautics, 1996.
-

-
- [25] United States Government, "Official U.S. Government Information about the Global Positioning System (GPS) and related topics." www.gps.gov. Accessed: 27/02/2014.
- [26] *Navstar GPS Space Segment/Navigation User Interfaces (IS-GPS-200G)*. United States Government, 2012.
- [27] *Navstar GPS Space Segment/User Segment L5 Interfaces (IS-GPS-705C)*. United States Government, 2012.
- [28] *Navstar GPS Space Segment/User Segment L1C Interface (IS-GPS-800C)*. United States Government, 2012.
- [29] C. Hegarty and E. Chatre, "Evolution of the Global Navigation Satellite System (GNSS)," *Proceedings of the IEEE*, vol. 96, no. 12, p. 1902–1917, 2008.
- [30] *GLONASS Interface Control Document - Navigational Radiosignal in Bands L1, L2 (Edition 5.1)*. Russian Institute of Space Device Engineering, 2013.
- [31] Y. Urlichich, V. Subbotin, G. Stupak, V. Dvorkin, *et al.*, "GLONASS Modernization," *GPS World*, pp. 34–39, November 2011.
- [32] European Space Agency, "Navipedia - The Reference for Satellite Navigation Know-How." www.navipedia.net. Accessed: 27/02/2014.
- [33] J. Avila Rodriguez, *On Generalized Signal Waveforms for Satellite Navigation*. PhD thesis, Universität der Bundeswehr München, 2008.
- [34] *Galileo Open Service Signal in Space Interface Control Document (OS SIS ICD) Issue 1*. European Union, 2010.
- [35] *BeiDou Navigation Satellite System Open Service Performance Standard (Version 1.0)*. China Satellite Navigation Office, 2013.
- [36] *BeiDou Navigation Satellite System Signal In Space Interface Control Document - Open Service Signal (Version 2.0)*. China Satellite Navigation Office, 2013.
- [37] Indian Space Research Organization, "Navigation Satellites." www.isro.org/satellites/navigationssatellites.aspx. Accessed: 27/02/2014.
- [38] Indian Space Research Organization, "Indian Regional Navigation Satellite System." www.isro.gov.in/newsletters/contents/spaceindia/jan2012-jun2012/article5.htm. Accessed: 27/02/2014.
- [39] Quasi-Zenith Satellite System Service. www.qzs.jp/en/. Accessed: 27/02/2014.
-

-
- [40] Electronic Navigation Research Institute (Japan), "Development of QZSS." www.enri.go.jp/~sakai/qzss_e.htm. Accessed: 27/02/2014.
- [41] A. Wieser, "High-Sensitivity GNSS: The Trade-Off Between Availability and Accuracy," in *Proceedings of the 3rd Symposium on Geodesy for Geotech. & Struct. Engineering / 12th Symposium on Deformation Measurements*, (Baden, Austria), 2006.
- [42] R. Mautz, "The Challenges of Indoor Environments and Specification on some Alternative Positioning Systems," in *Proceedings of the 6th Workshop on Positioning, Navigation, and Communication (WPCN 2009)*, (Hannover, Germany), 2009.
- [43] G. Seco Granados, J. Lopez Salcedo, D. Jimenez Banos, and G. Lopez Risueno, "Challenges in Indoor Global Navigation Satellite Systems: Unveiling its core features in signal processing," *IEEE Signal Processing Magazine*, vol. 29, no. 2, pp. 108–131, 2012.
- [44] J. Hurd, J. Statman, and V. Vlnrotter, "High dynamic GPS receiver using Maximum-Likelihood estimation and frequency tracking," *IEEE Transactions on Aerospace and Electronics Systems*, vol. 23, no. 4, p. 425–437, 1987.
- [45] C. Yang, M. Miller, E. Blasch, and T. Nguyen, "Comparative Study of Coherent, Non-Coherent, and Semi-Coherent Integration Schemes for GNSS Receivers," in *Proceedings of the 63rd Annual Meeting of the Institute of Navigation*, (Cambridge, MA, USA), 2007.
- [46] J. Jung, "Implementation of Correlation Power Peak Ratio Based Signal Detection Method," in *Proceedings of the 17th International Technical Meeting of the Satellite Division of the Institute of Navigation (ION GNSS 2004)*, (Long Beach, CA, USA), 2004.
- [47] B. Geiger, C. Vogel, and M. Soudan, "Comparison Between Ratio Detection and Threshold Comparison for GNSS Acquisition," *IEEE Transactions on Aerospace and Electronics Systems*, vol. 48, no. 2, p. 1772–1779, 2012.
- [48] M. Sahmoudi, M. Amin, and R. Landry, "Acquisition of Weak GNSS Signals Using a New Block Averaging Pre-Processing," in *Proceedings of the 2008 IEEE/ION Position Location and Navigation Symposium (PLANS 2008)*, (Monterey, CA, USA), 2008.
- [49] J. Starzyk and Z. Zhu, "Averaging Correlation for C/A Code Acquisition and Tracking in Frequency Domain," in *Proceedings of the 44th IEEE Midwest Symposium on Circuits and Systems (MWSCAS 2001)*, (Dayton, OH, USA), 2001.
- [50] A. Coenen and Van Nee D., "Novel Fast GPS/GLONASS Code-Acquisition Technique Using Low Update Rate FFT," *Electronic Letters*, vol. 28, no. 9, pp. 863–865, 1992.
-

-
- [51] A. Polydoros and C. Weber, "A Unified Approach to Serial Search Spread Spectrum Code Acquisition - Part I: General Theory," *IEEE Transactions on Communications*, vol. COM-32, no. 5, pp. 542–549, 1984.
- [52] M. Sahmoudi, P. Esteves, M. Bousquet, L. Ries, *et al.*, "A New Frequency Offset Correction Approach for Enhancing Sensitivity of GNSS Receivers," in *Proceedings of the 24th International Technical Meeting of the Satellite Division of The Institute of Navigation (ION GNSS 2011)*, (Portland, OR, USA), 2011.
- [53] D. Kubrak, M. Monnerat, G. Artaud, and L. Ries, "Improvement of GNSS Signal Acquisition Using Low-Cost Inertial Sensors," in *Proceedings of the 21st International Technical Meeting of the Satellite Division of The Institute of Navigation (ION GNSS 2008)*, (Savannah, GA, USA), 2008.
- [54] T. Pany, J. Winkel, B. Riedl, M. Restle, *et al.*, "Performance of a Partially Coherent Ultra-Tightly Coupled GNSS/INS Pedestrian Navigation System Enabling Coherent Integration Times of Several Seconds to Track GNSS Signals Down to 1.5 dB-Hz," in *Proceedings of the 22nd International Technical Meeting of the Satellite Division of The Institute of Navigation (ION GNSS 2009)*, (Savannah, GA, USA), 2009.
- [55] P. Sagiraju, D. Akopian, and H. Valio, "Fine Frequency Estimation in Weak Signals for GPS Receivers," in *Proceedings of the 2006 National Technical Meeting of The Institute of Navigation (ION NTM 2006)*, (Monterey, CA, USA), 2006.
- [56] J. Betz, "Binary Offset Carrier Modulations for Radionavigation," *Journal of the Institute of Navigation*, vol. 48, no. 4, pp. 227–246, Winter 2001/02.
- [57] L. Lo Presti and B. Motella, "The math of ambiguity: what is the acquisition ambiguity function and how is it expressed mathematically?," *Inside GNSS*, no. June, pp. 20–28, 2010.
- [58] D. Rovelli, P. Crosta, P. Lacone, M. Rovini, *et al.*, "Acquisition Speed-Up Engine for GNSS Signals," in *5th ESA Workshop on Satellite Navigation Technologies and European Workshop on GNSS Signals and Signal Processing (NAVITEC 2010)*, (Noordwijk, The Netherlands), 2010.
- [59] V. Eerola, S. Pietilä, and H. Valio, "A Novel Flexible Correlator Architecture for GNSS Receivers," in *Proceedings of the 2007 National Technical Meeting of The Institute of Navigation (ION NTM 2007)*, (San Diego, CA, USA), 2007.
- [60] D. Djebourri, A. Djebbari, and M. Djebourri, "Robust GPS Satellite Signal Acquisition Using Lifting Wavelet Transform," *Telecommunications and Radio Engineering*, vol. 15, no. 1, pp. 47–52, 2006.
-

-
- [61] G. Heckler and J. Garrison, "Implementation and Testing of an Unaided Method for the Acquisition of Weak GPS C/A Code Signals," *Journal of the Institute of Navigation*, vol. 56, no. 4, pp. 241–259, 2009.
- [62] W. Zhang and M. Ghogho, "Improved Fast Modified Double-Block Zero-Padding (FMDBZP) Algorithm for Weak GPS Signal Acquisition," in 18th *European Signal Processing Conference (EUSIPCO 2010)*, (Aalborg, Denmark), 2010.
- [63] P. Sagiraju, S. Aghaian, and D. Akopian, "Reduced complexity acquisition of GPS signals for software embedded applications," *IEE Proceedings-Radar, Sonar and Navigation*, vol. 153, no. 1, pp. 69–78, 2006.
- [64] C. Yang and S. Han, "Block-Accumulating Coherent Integration over Extended Interval (BACIX) For Weak GPS Signal Acquisition," in *Proceedings of the 19th International Technical Meeting of the Satellite Division of The Institute of Navigation (ION GNSS 2006)*, (Fort Worth, TX, USA), 2006.
- [65] H. Mathis, P. Flammant, and A. Thiel, "An Analytic Way to Optimize the Detector of a Post-Correlation FFT Acquisition Algorithm," in *Proceedings of the 16th International Technical Meeting of the Satellite Division of The Institute of Navigation (ION GPS/GNSS 2003)*, (Portland, OR, USA), 2003.
- [66] J.-K. Kim, J.-B. Kim, S. Lee, J. Lee, *et al.*, "Acquisition Complexity Reduction by Multi-stage Partial Cross-Correlation Technique for GPS Receiver," in *Proceedings of the International GNSS Society Symposium (IGNSS 2011)*, (Sydney, Australia), 2011.
- [67] D. Borio and L. Lo Presti, "A Reconfigurable GNSS Acquisition Scheme for Time-Frequency Applications," *EURASIP Journal on Advances in Signal Processing*, vol. 2008, no. Article no. 149, 2008.
- [68] P. Esteves, M. Sahmoudi, L. Ries, and M.-L. Boucheret, "Accurate Doppler-Shift Estimation for Increased Sensitivity of Computationally Efficient GNSS Acquisition," in *Proceedings of the European Navigation Conference (ENC 2013)*, (Vienna, Austria), 2013.
- [69] F. Harris, "On the Use of Windows for Harmonic Analysis with the Discrete Fourier Transform," *Proceedings of the IEEE*, vol. 66, no. 1, pp. 241–259, 1978.
- [70] R. Lyons, *Understanding Digital Signal Processing*. Prentice Hall, 3rd ed., 2010.
- [71] F. van Diggelen, *A-GPS: Assisted GPS, GNSS, and SBAS*. Artech House, 2009.
-

-
- [72] M. Psiaki, "Block Acquisition of Weak GPS Signals in a Software Receiver," in *Proceedings of the 14th International Technical Meeting of the Satellite Division of The Institute of Navigation (ION GPS 2001)*, (Portland, OR, USA), 2001.
- [73] L. Lo Presti, M. Fantino, P. Mulassano, and X. Zhu, "Acquisition systems for GNSS signals with the same code and bit rates," in *Proceedings of the 2008 IEEE/ION Position Location and Navigation Symposium (PLANS 2008)*, (Monterey, CA, USA), 2008.
- [74] L. Lo Presti, X. Zhu, M. Fantino, and P. Mulassano, "GNSS Signal Acquisition in the Presence of Sign Transition," *IEEE Journal of Selected Topics in Signal Processing*, vol. 3, no. 4, pp. 557–570, 2009.
- [75] S. Jeon, H. So, G. Kim, and K. Kwon, "Bit Transition Cancellation Signal Acquisition Method for Modernized GPS and Galileo Signal," in *Proceedings of the 24th International Technical Meeting of The Satellite Division of the Institute of Navigation (ION GNSS 2011)*, (Portland, OR, USA), 2011.
- [76] M. Monnerat, R. Couty, N. Vincent, O. Huez, *et al.*, "The Assisted GNSS, Technology and Applications," in *Proceedings of the 17th International Technical Meeting of The Satellite Division of the Institute of Navigation (ION GNSS 2004)*, (Long Beach, CA, USA), 2004.
- [77] J. Leclère, C. Botteron, and P. Farine, "Resource and Performance Comparisons for Different Acquisition Methods that can be Applied to a VHDL-based GPS Receiver in Standalone and Assisted Cases," in *Proceedings of the 2010 IEEE/ION Position Location and Navigation Symposium (PLANS 2010)*, (Indian Wells, CA, USA), 2010.
- [78] T. Pany, B. Riedl, J. Winkel, *et al.*, "Coherent Integration Time: The Longer the Better," *Inside GNSS*, no. November/December, pp. 52–61, 2009.
- [79] H. Niedermeier, B. Eissfeller, J. Winkel, T. Pany, *et al.*, "DINGPOS: High Sensitivity GNSS platform for deep indoor scenarios," in *2010 International Conference on Indoor Positioning and Indoor Navigation (IPIN 2010)*, (Zürich, Switzerland), 2010.
- [80] R. Watson, G. Lachapelle, R. Klukas, S. Turunen, *et al.*, "Investigating GPS Signals Indoors with Extreme High-Sensitivity Detection Techniques," *Journal of the Institute of Navigation*, vol. 52, no. 4, pp. 199–214, Winter 2005-2006.
- [81] F. Dosis, R. Lesca, G. Boiero, and G. Ghinamo, "A test-bed implementation of an acquisition scheme for indoor positioning," *GPS Solutions*, vol. 14, no. 3, pp. 241–253, 2010.
- [82] D. Kubrak, M. Monnerat, G. Artaud, and L. Ries, "Performance Analysis of Sensor-Aided GNSS Signal Acquisition in Signal Degraded Environments," in *Proceedings of the 2008 National Technical Meeting of The Institute of Navigation (ION NTM 2008)*, (San Diego, CA, USA), 2008.
-

-
- [83] J. Holmes and C. Chen, "Acquisition Time Performance of PN Spread Spectrum Systems," *IEEE Transactions on Communications*, vol. COM-25, no. 8, pp. 778–784, 1977.
- [84] U. Ahmad, C. Sik, S. Park, and L. Dong Sun, "Sample Fraction & Doppler Effect Compensation Algorithm for Acquisition of Weak GPS Signals," in *Proceedings of the 2011 International Technical Meeting of The Institute of Navigation (ION ITM 2011)*, (San Diego, CA, USA), 2011.
- [85] M. Chansarkar and L. Garin, "Acquisition of GPS Signals at Very Low Signal to Noise Ratio," in *Proceedings of the 2000 National Technical Meeting of The Institute of Navigation (ION NTM 2000)*, (Anaheim, CA, USA), 2000.
- [86] D. Borio and D. Akos, "Noncoherent Integrations for GNSS Detection: Analysis and Comparisons," *IEEE Transactions on Aerospace and Electronic Systems*, vol. 45, no. 1, pp. 360–375, 2009.
- [87] L. Andrews and R. Phillips, *Mathematical Techniques for Engineers and Scientists*. SPIE Press, 2003.
- [88] S. Lowe, "Voltage Signal-to-Noise ratio (SNR) nonlinearity resulting from incoherent summations," tech. rep., Telecommunications and Mission Operations Progress Report 42-137, 1999.
- [89] M. Zarrabizadeh and E. Sousa, "A Differentially Coherent PN Code Acquisition Receiver for CDMA Systems," *IEEE Transactions on Communications*, vol. 45, no. 11, pp. 1456–1465, 1997.
- [90] J. Iinati and A. Pouttu, "Differentially Coherent Code Acquisition in Doppler," in *Proceedings of the IEEE Vehicular Technology Conference*, (Amsterdam, The Netherlands), 1999.
- [91] I. Choi, S. Park, D. Cho, S. Yun, *et al.*, "A Novel Weak Signal Acquisition Scheme for Assisted GPS," in *Proceedings of the 15th International Technical Meeting of the Satellite Division of the Institute of Navigation (ION GPS 2002)*, (Portland, OR, USA), 2002.
- [92] D. Cho, C. Park, and S. Lee, "An Assisted GPS Acquisition Method Using L2 Civil Signal in Weak Signal Environment," *Journal of Global Positioning Systems*, vol. 3, no. 1-2, 2004.
- [93] H. Elders Boll and U. Dettmar, "Efficient Differentially Coherent Code/Doppler Acquisition of Weak GPS Signals," in *IEEE 8th International Symposium on Spread Spectrum Techniques and Applications (ISSSTA 2004)*, (Sydney, Australia), 2004.
- [94] A. Schmid and A. Neubauer, "Differential Correlation for Galileo/GPS Receivers," in *Proceedings of IEEE International Conference on Acoustics, Speech, and Signal Processing (ICASSP 2005)*, (Philadelphia, PA, USA), 2005.
-

-
- [95] A. Schmid, C. Günther, and A. Neubauer, "Adaptive Phase Correction Loop for Enhanced Acquisition Sensitivity," in *Proceedings of the 18th International Technical Meeting of the Satellite Division of the Institute of Navigation (ION GNSS 2005)*, (Long Beach, CA, USA), 2005.
- [96] A. Schmid, A. Neubauer, and C. Günther, "Frequency Offset Estimation for Galileo/GPS Receivers Based on Differential Correlation," in *Proceedings of the 13th IEEE Workshop on Statistical Signal Processing (SSP 2005)*, (Novosibirsk, Russia), 2005.
- [97] W. Yu, B. Zheng, R. Watson, and G. Lachapelle, "Differential Combining for Acquiring Weak GPS Signals," *Signal Processing*, vol. 87, pp. 824–840, 2006.
- [98] C. Yang, T. Nguyen, E. Blasch, and M. Miller, "Post-Correlation Semi-Coherent Integration For High-Dynamic and Weak GPS Signal Acquisition," in *Proceedings of the 2008 IEEE/ION Position Location and Navigation Symposium (PLANS 2008)*, (Monterey, CA, USA), 2008.
- [99] A. Ayaz, "Analysis of Differential Acquisition Methods by Using Monte-Carlo Simulations," in *Proceedings of the 18th International Technical Meeting of the Satellite Division of the Institute of Navigation (ION GNSS 2005)*, (Long Beach, CA, USA), 2005.
- [100] K. Sun and L. Presti, "A Differential Post Detection Technique for Two Steps GNSS Signal Acquisition Algorithm," in *Proceedings of the 2010 IEEE/ION Position Location and Navigation Symposium (PLANS 2010)*, (Indian Wells, CA, USA), 2010.
- [101] M. Villanti, P. Salmi, and G. Corazza, "Differential Post Detection Integration Techniques for Robust Code Acquisition," *IEEE Transactions on Communications*, vol. 55, no. 11, pp. 2172–2184, 2004.
- [102] S. Shanmugam, "Improving GPS L1 C/A Code Correlation Properties Using a Novel Multi-Correlator Differential Detection Technique," in *Proceedings of the 19th International Technical Meeting of the Satellite Division of the Institute of Navigation (ION GNSS 2006)*, (Fort Worth, TX, USA), 2006.
- [103] S. Shanmugam, *New Enhanced Sensitivity Detection Techniques for GPS L1 C/A and Modernized Signal Acquisition*. PhD thesis, University of Calgary, 2008.
- [104] J. Avila Rodriguez, T. Pany, and B. Eissfeller, "A Theoretical Analysis of Acquisition Algorithms for Indoor Positioning," in *2nd ESA Workshop on Satellite Navigation Technologies and European Workshop on GNSS Signals and Signal Processing (NAVITEC 2004)*, (Noordwijk, The Netherlands), 2004.
- [105] W. Liu, J. Li, G. Rui, and F. Wang, "Optimization and Convenient Evaluation Model of Differential Coherent Post Detection Integration," in *Proceedings of the 24th International Technical*
-

-
- Meeting of the Satellite Division of The Institute of Navigation (ION GNSS 2011)*, (Portland, OR, USA), 2011.
- [106] P. Esteves, M. Sahmoudi, N. Ziedan, and M.-L. Boucheret, "A New Adaptive Scheme of High-Sensitivity GNSS Acquisition in Presence of Large Doppler Shifts," in *Proceedings of the 25th International Technical Meeting of The Satellite Division of the Institute of Navigation (ION GNSS 2012)*, (Nashville, TN, USA), 2012.
- [107] P. Esteves, M. Sahmoudi, and M.-L. Boucheret, "Sensitivity Characterization of Differential Detectors for Acquisition of Weak GNSS Signals," *Submitted to IEEE Transactions in Aerospace and Electronic Systems*.
- [108] B. Li, J. Zhang, P. Mumford, and A. Dempster, "How good is Assisted GPS?," in *Proceedings of the International GNSS Society Symposium (IGNSS 2011)*, (Sydney, Australia), 2011.
- [109] N. Harper, *Server-side GPS and assisted-GPS in Java*. Artech House, 2010.
- [110] J. DeSalas and F. van Diggelen, "Cell-Phone Location without Ephemeris," *GPS World*, pp. 28–33, February 2011.
- [111] J. DeSalas and F. van Diggelen, "GNSS Position Computation without Ephemeris "Single Shot MS Based"," in *Proceedings of the 23rd International Technical Meeting of The Satellite Division of the Institute of Navigation (ION GNSS 2010)*, (Portland, OR, USA), 2010.
- [112] G. López-Risue no and A. Seco Granados, "Measurement and Processing of Indoor GPS Signals Using a One-Shot Software Receiver," in *2nd ESA Workshop on Satellite Navigation Technologies and European Workshop on GNSS Signals and Signal Processing (NAVITEC 2004)*, (Noordwijk, The Netherlands), 2004.
- [113] D. Jiménez-Ba nos, N. Blanco Delgado, G. López-Risue no, A. Seco Granados, *et al.*, "Innovative Techniques for GPS Indoor Positioning Using a Snapshot Receiver," in *Proceedings of the 19th International Technical Meeting of The Satellite Division of the Institute of Navigation (ION GNSS 2006)*, (Fort Worth, TX, USA), 2006.
- [114] A. Schmid, "Single Shot Positioning," in *Proceedings of the International GNSS Society Symposium (IGNSS 2007)*, (Sydney, Australia), 2007.
- [115] D. Dötterböck and B. Eissfeller, "A GPS/Galileo Software Snap-Shot Receiver for Mobile Phones," in *Proceedings of the 13th International Association of Institutes of Navigation (IAIN 2009)*, (Stockholm, Sweden), 2009.
- [116] S. Carrasco Martos, G. López-Risue no, D. Jiménez-Ba nos, and E. Gill, "Snapshot Software Receiver for GNSS in Weak Signal Environments: An Innovative Approach for Galileo E5," in
-

Proceedings of the 23rd International Technical Meeting of The Satellite Division of the Institute of Navigation (ION GNSS 2010), (Portland, OR, USA), 2010.

- [117] J. Sennott, "A flexible GPS software development system and timing analyzer for present and future microprocessors," *Navigation*, vol. 31, no. 2, pp. 84–95, 1984.
- [118] E. Copps, G. Geier, W. Fidler, and P. Grundy, "Optimal processing of GPS signals," *Navigation*, vol. 27, no. 3, pp. 171–182, 1980.
- [119] P. Axelrad, J. Donna, and M. Mitchell, "Enhancing GNSS Acquisition by Combining Signals from Multiple Channels and Satellites," in *Proceedings of the 22nd International Technical Meeting of the Satellite Division of The Institute of Navigation (ION GNSS 2009)*, (Savannah, GA, USA), 2009.
- [120] J. Cheong, "Towards Multi-Constellation Collective Detection for Weak Signals: A Comparative Experimental Analysis," in *Proceedings of the 24th International Technical Meeting of the Satellite Division of The Institute of Navigation (ION GNSS 2011)*, (Portland, OR, USA), 2011.
- [121] J. Cheong, J. WU, A. Dempster, and C. Rizos, "Efficient Implementation of Collective Detection," in *Proceedings of the International GNSS Society Symposium (IGNSS 2011)*, (Sydney, Australia), 2011.
- [122] J. Cheong, A. Dempster, and C. Rizos, "Hybrid of Collective Detection with Conventional Detection for Weak Signal Acquisition," in *Proceedings of the International GNSS Society Symposium (IGNSS 2011)*, (Sydney, Australia), 2011.
- [123] United States and European Governments, "Agreement on the Promotion, Provision and Use of Galileo and GPS Satellite-Based Navigation Systems and Related Applications." http://ec.europa.eu/enterprise/policies/satnav/galileo/files/2004_06_21_eu_us_agreement_en.pdf, 2004. Accessed: 30/11/2013.
- [124] G. Hein, J.-A. Avila Rodriguez, J. Betz, C. Hegarty, *et al.*, "MBOC: The New Optimized Spreading Modulation Recommended for GALILEO L1 OS and GPS L1C," in *Proceedings of the 2006 IEEE/ION Position Location and Navigation Symposium (PLANS 2006)*, (San Diego, CA, USA), 2006.
- [125] J.-A. Avila Rodriguez, G. Hein, S. Wallner, J.-L. Issler, *et al.*, "The MBOC Modulation: A Final Touch for the Galileo Frequency and Signal Plan," *Inside GNSS*, no. September/October, pp. 43–58, 2007.
- [126] V. Heiries, J.-A. Avila Rodriguez, M. Irsigler, G. Hein, *et al.*, "Acquisition Performance Analysis of Candidate Designs for the L1 OS Optimized Signal," in *Proceedings of the 18th International*
-

-
- Technical Meeting of the Satellite Division of the Institute of Navigation (ION GNSS 2005)*, (Long Beach, CA, USA), 2005.
- [127] V. Heiries, D. Roviras, L. Ries, and V. Calmettes, "Analysis of Non Ambiguous BOC Signal Acquisition performance," in *Proceedings of the 17th International Technical Meeting of the Satellite Division of the Institute of Navigation (ION GNSS 2004)*, (Long Beach, CA, USA), 2004.
- [128] E.-S. Lohan, "Statistical analysis of BPSK-like techniques for the acquisition of Galileo signals," *AIAA Journal of Aerospace Computing, Information, and Communication*, vol. 3, pp. 234–243, 2006.
- [129] A. Burian, E.-S. Lohan, V. Lehtinen, and M. Renfors, "Complexity considerations for unambiguous acquisition of Galileo signals," in *Proceedings of the 3rd Workshop on Positioning, Navigation, and Communication (WPCN 2006)*, (Hannover, Germany), 2006.
- [130] E.-S. Lohan, "Analytical Performance of CBOC-modulated Galileo E1 signal using sine BOC(1,1) receiver for mass-market applications," in *Proceedings of the European Navigation Conference (ENC 2008)*, (Toulouse, France), 2008.
- [131] M. Samad and E.-S. Lohan, "MBOC Performance in Unambiguous Acquisition," in *Proceedings of European Navigation Conference - Global Navigation Satellite Systems (ENC-GNSS 2009)*, (Naples, Italy), 2009.
- [132] E.-S. Lohan, "Analytical Performance of CBOC-modulated Galileo E1 signal using sine BOC(1,1) receiver for mass-market applications," in *Proceedings of the 2010 IEEE/ION Position Location and Navigation Symposium (PLANS 2010)*, (Indian Wells, CA, USA), 2010.
- [133] L. Martin, V. Leblond, G. Guillotel, and V. Heiries, "BOC(x,y) signal acquisition techniques and performances," in *Proceedings of the 16th International Technical Meeting of the Satellite Division of The Institute of Navigation (ION GPS/GNSS 2003)*, (Portland, OR, USA), 2003.
- [134] N. Hoult, E. Aguado, and P. Xia, "MBOC and BOC(1,1) Performance Comparison," *Journal of Navigation*, vol. 61, pp. 613–627, 2008.
- [135] F. Macchi, M. Petovello, and G. Lachapelle, "Consequences of MBOC Approximation by BOC Modulation," in *Proceedings of the 21st International Technical Meeting of the Satellite Division of The Institute of Navigation (ION GNSS 2008)*, (Savannah, GA, USA), 2008.
- [136] F. Dovis, L. Lo Presti, M. Fantino, P. Mulassano, *et al.*, "Comparison between Galileo CBOC Candidates and BOC(1,1) in Terms of Detection Performance," *International Journal of Navigation and Observation*, vol. 2008, no. Article ID 793868, 2008.
-

-
- [137] S. Carrasco Martos, D. Jiménez-Ba nos, and G. López-Risue no, “Galileo E5a/E5b Acquisition Techniques for Weak Signal Environments,” in *4th ESA Workshop on Satellite Navigation User Equipment Technologies (NAVITEC 2008)*, (Noordwijk, The Netherlands), 2008.
- [138] N. Shivaramaiah, *Enhanced Receiver Techniques for Galileo E5 AltBOC Signal Processing*. PhD thesis, University of New South Wales, 2012.
- [139] N. Shivaramaiah and A. Dempster, “An Analysis of Galileo E5 Signal Acquisition Strategies,” in *Proceedings of the European Navigation Conference (ENC 2008)*, (Toulouse, France), 2008.
- [140] D. Borio, C. Mongrédién, and G. Lachapelle, “New L5/E5a Acquisition Algorithms: Analysis and Comparison,” in *IEEE 10th International Symposium on Spread Spectrum Techniques and Applications (ISSSTA 2008)*, (Bologna, Italy), 2008.
- [141] N. Martin, M. Revol, and H. Guichon, “First results of the implementation of the coherent E5 AltBOC processing,” in *Proceedings of the 5th European Workshop on GNSS Signals and Signal Processing (SIGNALS 2011)*, (Toulouse, France), 2011.
- [142] T. Ta, F. Dovis, D. Margaria, and L. Lo Presti, “Comparative study of joint data/pilot strategies for high sensitivity Galileo E1 open service signal acquisition,” *IET Radar Sonar Navigation*, vol. 4, no. 6, pp. 764–779, 2010.
- [143] D. Borio, C. O’Driscoll, and G. Lachapelle, “Coherent, Non-Coherent and Differentially Coherent Combining Techniques for the Acquisition of New Composite GNSS Signals,” *IEEE Trans. on Aerospace and Electronic Systems*, vol. 45, no. 3, pp. 1227–1240, 2009.
- [144] D. Borio and L. Lo Presti, “Data and Pilot Combining for Composite GNSS Signal Acquisition,” *International Journal of Navigation and Observation*, vol. 2008, no. Article ID 738183, 2008.
- [145] D. Borio, C. O’Driscoll, and G. Lachapelle, “Composite GNSS signal acquisition over multiple code periods,” *IEEE Trans. on Aerospace and Electronic Systems*, vol. 46, no. 1, pp. 193–206, 2010.
- [146] K. Sun and L. Lo Presti, “Channels Combining Techniques for a Novel Two Steps Acquisition of New Composite GNSS Signals in Presence of Bit Sign Transitions,” in *Proceedings of the 2010 IEEE/ION Position Location and Navigation Symposium (PLANS 2010)*, (Indian Wells, CA, USA), 2010.
- [147] B. Siddiqui, J. Zhang, M. Bhuiyan, and E. Lohan, “Joint Data-Pilot acquisition and tracking of Galileo E1 Open Service signal,” in *Proceedings of the International Conference on Ubiquitous Positioning Indoor Navigation and Location Based Service (UPINLBS 2010)*, (Helsinki, Finland), 2010.
-

-
- [148] C. Yang, C. Hegarty, and M. Tran, "Acquisition of the GPS L5 signal using coherent combining of I5 and Q5," in *Proceedings of the 17th International Technical Meeting of the Satellite Division of the Institute of Navigation (ION GNSS 2004)*, (Long Beach, CA, USA), 2004.
- [149] F. Bastide, O. Julien, C. Macabiau, and B. Roturier, "Analysis of L5/E5 acquisition, tracking and data demodulation thresholds," in *Proceedings of the 15th International Technical Meeting of the Satellite Division of the Institute of Navigation (ION GPS 2002)*, (Portland, OR, USA), 2002.
- [150] C. Hegarty, "Optimal and near-optimal detector for acquisition of the GPS L5 signal," in *Proceedings of the 2006 National Technical Meeting of The Institute of Navigation (ION NTM 2006)*, (Monterey, CA, USA), 2006.
- [151] C. Hegarty, M. Tran, and A. van Dierendonck, "Acquisition algorithms for the GPS L5 signal," in *Proceedings of the 16th International Technical Meeting of the Satellite Division of The Institute of Navigation (ION GPS/GNSS 2003)*, (Portland, OR, USA), 2003.
- [152] K. Seals, W. Michalson, P. Swaszek, and R. Hartnett, "Analysis of Coherent Combining for GPS L1C Acquisition," in *Proceedings of the 25th International Technical Meeting of The Satellite Division of the Institute of Navigation (ION GNSS 2012)*, (Nashville, TN, USA), 2012.
- [153] D. Margaria, B. Motella, and F. Dovis, "On the Impact of Channel Cross-Correlations in High-Sensitivity Receivers for Galileo E1 OS and GPS L1C Signals," *International Journal of Navigation and Observation*, vol. 2012, no. Article ID 132078, 2012.
- [154] M. Foucras, O. Julien, C. Macabiau, and B. Ekambi, "Probability of Secondary Code Acquisition for Multi-Component GNSS Signals," in *Proceedings of the 6th European Workshop on GNSS Signals and Signal Processing (SIGNALS 2013)*, (Neubiberg, Germany), 2013.
- [155] Z. Yang, Z. Huang, and S. Geng, "Codes cross-correlation analysis and data/pilot code pairs optimization for Galileo E1 OS and GPS L1C," *Chinese Journal of Aeronautics*, vol. 26, no. 3, pp. 751–765, 2013.
- [156] D. Borio, "M-Sequence and Secondary Code Constraints for GNSS Signal Acquisition," *IEEE Transactions on Aerospace and Electronic Systems*, vol. 47, no. 2, pp. 928–945, 2011.
- [157] N. Shivaramaiah, A. Dempster, and C. Rizos, "Exploiting the secondary codes to improve signal acquisition performance in Galileo receivers," in *Proceedings of the 21st International Technical Meeting of the Satellite Division of The Institute of Navigation (ION GNSS 2008)*, (Savannah, GA, USA), 2008.
- [158] G. Corazza, C. Palestini, R. Pedone, and M. Villanti, "Galileo Primary Code Acquisition Based on Multi-hypothesis Secondary Code Ambiguity Elimination," in *Proceedings of the 20th In-*
-

-
- ternational Technical Meeting of the Satellite Division of The Institute of Navigation (ION GNSS 2007)*, (Fort Worth, TX, USA), 2007.
- [159] Y. Tawk, A. Jovanovic, J. Leclère, C. Botteron, *et al.*, “A New FFT-Based Algorithm for Secondary Code Acquisition for Galileo Signals,” in *Proceedings of IEEE Vehicular Technology Conference (VTC 2011)*, (San Francisco, CA, USA), 2011.
- [160] C. Macabiau, L. Ries, F. Bastide, and J.-L. Issler, “GPS L5 Receiver Implementation Issues,” in *Proceedings of the 16th International Technical Meeting of the Satellite Division of The Institute of Navigation (ION GPS/GNSS 2003)*, (Portland, OR, USA), 2003.
- [161] C. Hegarty, M. Tran, and A. van Dierendonck, “Acquisition Algorithms for the GPS L5 Signal,” in *Proceedings of the 16th International Technical Meeting of the Satellite Division of The Institute of Navigation (ION GPS/GNSS 2003)*, (Portland, OR, USA), 2003.
- [162] B. Zheng and G. Lachapelle, “Acquisition Schemes for a GPS L5 Software Receiver,” in *Proceedings of the 17th International Technical Meeting of the Satellite Division of the Institute of Navigation (ION GNSS 2004)*, (Long Beach, CA, USA), 2004.
- [163] F. Macchi, *Development and Testing of an L1 Combined GPS-Galileo Software Receiver*. PhD thesis, University of Calgary, 2010.
- [164] F. Macchi Gernot, M. Petovello, and G. Lachapelle, “Combined Acquisition and Tracking Methods for GPS L1 C/A and L1C Signals,” *International Journal of Navigation and Observation*, vol. 2010, no. Article ID 190465, 2010.
- [165] C. Gernot, S. Shanmugam, K. O’Keefe, and G. Lachapelle, “A Novel L1 and L2C Combined Detection Scheme for Enhanced GPS Acquisition,” in *Proceedings of the 20th International Technical Meeting of the Satellite Division of The Institute of Navigation (ION GNSS 2007)*, (Fort Worth, TX, USA), 2007.
- [166] C. Gernot, K. O’Keefe, and G. Lachapelle, “Assessing Three New GPS Combined L1/L2C Acquisition Methods,” *IEEE Transactions on Aerospace and Electronic Systems*, vol. 47, no. 3, pp. 2239–2247, 2011.
- [167] C. Gernot, *Development of Combined GPS L1/L2C Acquisition and Tracking Methods for Weak Signals Environments*. PhD thesis, University of Calgary, 2009.
- [168] T. Ta and S. Ngo, “A novel signal acquisition method for GPS dual-frequency L1 C/A and L2C receivers,” in *Proceedings of the 2011 International Conference on Advanced Technologies for Communications (ATC 2011)*, (Da Nang, Vietnam), 2011.
-

-
- [169] F. Rosa, H. Hurskainen, J. Nurmi, M. Dettratti, *et al.*, “GRAMMAR: Challenges and Solutions for Multi-Constellation Mass Market User Receivers,” in *Proceedings of the 2010 Ubiquitous Positioning Indoor Navigation and Location Based Service (UPINLBS 2010)*, (Helsinki, Finland), 2007.
- [170] K. Hurskainen, E.-L. Lohan, J. Nurmi, S. Sand, *et al.*, “Optimal dual frequency combination for Galileo mass market receiver baseband,” in *Proceedings of the 2009 IEEE Workshop on Signal Processing Systems (SiPS 2009)*, (Tampere, Finland), 2009.
- [171] F. Bastia, L. Deambrogio, C. Palestini, M. Villanti, *et al.*, “Hierarchical Code Acquisition for Dual Band GNSS Receivers,” in *Proceedings of the 2010 IEEE/ION Position Location and Navigation Symposium (PLANS 2010)*, (Indian Wells, CA, USA), 2010.
- [172] H. Al Bitar, *Advanced GPS signal processing techniques for LBS services*. PhD thesis, Institut Polytechnique de Toulouse, 2007.
- [173] H. El Natour, A.-C. Escher, C. Macabiau, and M.-L. Boucheret, “A new algorithm to reduce AGPS acquisition TTFF,” in *Proceedings of the 2006 National Technical Meeting of The Institute of Navigation (ION NTM 2006)*, (Monterey, CA, USA), 2006.
- [174] J. Arribas, P. Closas, and C. Fernández-Prades, “Joint Acquisition Strategy of GNSS Satellites for Computational Cost Reduction,” in *5th ESA Workshop on Satellite Navigation Technologies and European Workshop on GNSS Signals and Signal Processing (NAVITEC 2010)*, (Noordwijk, The Netherlands), 2010.
- [175] Y.-C. Lin and S.-S. Jan, “Linear Composite Code Acquisition Method for GNSS,” in *Proceedings of the 2010 IEEE/ION Position Location and Navigation Symposium (PLANS 2010)*, (Indian Wells, CA, USA), 2010.
- [176] N. Sokolova, D. Borio, B. Forsell, and G. Lachapelle, “Doppler Rate Measurements in Standard and High Sensitivity GPS Receivers: Theoretical Analysis and Comparison,” in *2010 International Conference on Indoor Positioning and Indoor Navigation (IPIN 2010)*, (Zürich, Switzerland), 2010.
- [177] F. van Graas, A. Soloviev, M. de Haag, and S. Gunawardena, “Closed-Loop Sequential Signal Processing and Open-Loop Batch Processing Approaches for GNSS Receiver Design,” *IEEE Journal of Selected Topics in Signal Processing*, vol. 3, no. 4, pp. 571–586, 2009.
- [178] M. Tahir, M. Fantino, and L. Lo Presti, “Characterizing Different Open Loop Fine Frequency Estimation Methods for GNSS Receivers,” in *Proceedings of the 2011 International Technical Meeting of The Institute of Navigation (ION ITM 2011)*, (San Diego, CA, USA), 2011.
-

-
- [179] X. Tang, E. Falletti, and L. Lo Presti, "Fast Nearly ML Estimation of Doppler Frequency in GNSS Signal Acquisition Process," *Sensors*, vol. 13, pp. 5649–5670, 2013.
- [180] D. Borio, L. Camoriano, L. Lo Presti, and M. Fantino, "DTFT-based frequency lock loop for GNSS applications," *IEEE Transactions in Aerospace and Electronic Systems*, vol. 44, pp. 595–612, 2008.
- [181] S. Kay, "A Fast and Accurate Single Frequency Estimator," *IEEE Transactions on Information Theory*, vol. 37, pp. 1987–1990, 1989.
- [182] D. Lin and J. Tsui, "Acquisition Schemes for Software GPS Receiver," in *Proceedings of the 11th International Technical Meeting of the Satellite Division of The Institute of Navigation (ION GPS 1998)*, (Nashville, TN, USA), 1998.
- [183] E. Jacobsen and P. Kootsookos, "Fast, Accurate Frequency Estimators," in *Streamlining Digital Signal Processing: A Tricks of the Trade Guidebook* (R. Lyons, ed.), pp. 107–114, Wiley-IEEE Press, 2nd ed., 2007.
- [184] E. Jacobsen and P. Kootsookos, "Fast, accurate frequency estimators," *IEEE Signal Processing Magazine*, vol. 24, no. 3, pp. 123–125, 2008.
- [185] E. Jacobsen, "On Local Interpolation of DFT Outputs," Accessible at <http://www.ericjacobsen.org/FTinterp.pdf> (last accessed 31 January 2013).
- [186] B. Quin, "Estimating frequency by interpolation using Fourier coefficients," *IEEE Transactions on Signal Processing*, vol. 42, no. 5, pp. 1264–1268, 1994.
- [187] B. Quin, "Estimation of frequency, amplitude, and phase from the DFT of a time series," *IEEE Transactions on Signal Processing*, vol. 45, no. 3, pp. 814–817, 1997.
- [188] M. Macleod, "Fast nearly ML estimation of the parameters of real or complex single tones or resolved multiple tones," *IEEE Transactions on Signal Processing*, vol. 46, no. 1, pp. 141–148, 1998.
- [189] C. Candan, "A Method for Fine Resolution Frequency Estimation from three DFT samples," *IEEE Signal Processing Letters*, vol. 18, no. 6, pp. 351–354, 2011.
- [190] T. Pany, E. Göhler, M. Irsigler, and J. Winkel, "On the State-of-the-Art of Real-Time GNSS Signal Acquisition - A Comparison of Time and Frequency Domain Methods," in *2010 International Conference on Indoor Positioning and Indoor Navigation (IPIN 2010)*, (Zürich, Switzerland), 2010.
-

-
- [191] V. Calmettes, A. Dion, and E. Boutillon, "Reconfigurable GPS-Galileo Receiver for Satellite Based Applications," in *Proceedings of the 20th International Technical Meeting of the Satellite Division of The Institute of Navigation (ION GNSS 2007)*, (Fort Worth, TX, USA), 2007.
- [192] V. Calmettes, A. Dion, E. Boutillon, and E. Liegeon, "Fast Acquisition Unit for GPS/GALILEO Receivers in Space Environment," in *Proceedings of the 2008 National Technical Meeting of The Institute of Navigation (ION NTM 2008)*, (San Diego, CA, USA), 2008.
- [193] J. Zhike, "Efficient and Flexible Numerical Controlled Oscillators for Navigational Receivers," US Patent No. 7,830,951 B2, 2010.
- [194] G. Lank, I. Reed, and G. Pollon, "A Semicoherent Detection and Doppler Estimation Statistic," *IEEE Transactions on Aerospace and Electronic Systems*, vol. 9, no. 2, pp. 151–165, 1972.
- [195] S. Kotz, T. Kozubowski, and T. Podgorski, *The Laplace Distribution and Generalizations: A Revisit with Applications to Communications, Economics, Engineering, and Finance*. Birkhäuser, 2001.
- [196] A. Papoulis and S. Pillai, *Probability, Random Variables and Stochastic Processes*. McGraw-Hill, 4th ed., 2002.
- [197] C. Taillie, *Statistical Distributions in Scientific Work, Volume 4 - Models, Structures and Characterizations*. D. Reidel Publishing Company, 1981.
- [198] W. Reed, "The Normal-Laplace distribution and its relatives," in *Advances in Distribution Theory, Order Statistics, and Inference* (N. Balakrishnan, E. Castillo, and J. Sarabia, eds.), pp. 61–74, Birkhäuser, 2006.
- [199] E. Glennon and A. Dempster, "A Review of GPS Cross Correlation Mitigation Techniques," in *Proceedings of the International Symposium on GNSS/GPS (IGNSS 2004)*, (Sydney, Australia), 2004.
- [200] P. Madhani, P. Axelrad, K. Krumvieda, and J. Thomas, "Application of Successive Interference Cancellation to the GPS Pseudolite Near-Far Problem," *IEEE Transactions on Aerospace and Electronics Systems*, vol. 39, no. 2, p. 481–488, 2003.
- [201] B. Peterson, R. Hartnett, and G. Ottman, "GPS Receiver Structures for the Urban Canyon," in *Proceedings of the 1995 International Technical Meeting of The Institute of Navigation (ION ITM 1995)*, (Palm Springs, CA), 1995.
-